Planetary Plasma Modeling and Ion Escape

by

H. L. Egan

B.S., Michigan State University, 2013

A thesis submitted to the

Faculty of the Graduate School of the

University of Colorado in partial fulfillment

of the requirements for the degree of

Doctor of Philosophy

Department of Astrophysical and Planetary Science

2019

This thesis entitled:
Planetary Plasma Modeling and Ion Escape
written by H. L. Egan
has been approved for the Department of Astrophysical and Planetary Science

Prof. David Brain

Kevin France

Zachary Berta-Thompson

Fran Bagenal

Jed Brown

Date

The final copy of this thesis has been examined by the signatories, and we find that both the content and the form meet acceptable presentation standards of scholarly work in the above mentioned discipline.

Egan, H. L. (Ph.D., Astrophysical and Planetary Science)

Planetary Plasma Modeling and Ion Escape

Thesis directed by Prof. David Brain

In this thesis I use global plasma simulations to explore the star-planet interaction for Mars and Mars-like exoplanets, with an emphasis on the relationship to ion escape.

I compare the results of five global Martian plasma models run with identical input conditions to each other and corresponding MAVEN data, in order to assess the effect of the different physical assumptions and numerical implementations. I show that no one model outperforms all others in every data comparison, necessitating the careful selection of model for the type of physics one is analyzing. There are clear morphological differences in ion behavior in the tail and southern hemisphere, as well as in the location of various plasma boundaries.

I then apply a hybrid plasma model to the study of a generic Mars-like planet in the habitable zone of a typical M-dwarf star. I systematically vary the stellar input conditions and examine the changing plasma environment and ion escape. Both ion loss morphology and overall rates vary significantly, and in cases where the stellar wind pressure was increased, the ion loss begins to be diffusion or production limited. A quasi-parallel interplanetary magnetic field drives asymmetrically draped field lines and correspondingly asymmetric ion escape.

I use the same hybrid model to explore the effects of intrinsic planetary magnetic field strength on ion outflow, for both current Mars and a Mars-like exoplanet. The presence of an intrinsic magnetic field enhances escape to a certain point before beginning to inhibit it, depending on the polar cone angle and the magnetic standoff distance. I argue that ion escape reflects a balance between the competing effects of magnetic shielding at the equator and enhanced escape at the poles.

Dedication

To love the journey is to accept no such end

Acknowledgements

I would like to express my deep gratitude to my thesis advisor Dave Brain, for his support and guidance throughout this process, unwavering belief in me and my work, and willingness to stand up for me when I needed it. Above all else I appreciate how he convinced me to stay in science by never telling me I should, but by helping me rediscover what it was I loved about science in the first place.

I would also like to thank my thesis committee for their outside advice and assistance as well as my collaborators for their technical assistance and valuable feedback. The support staff at LASP and APS has also been invaluable throughout this process.

I also wish to thank my APS classmates and CSGF fellows, for their friendship, support, and entertaining scientific discussions. There are far too many to list here, but I certainly wouldn't have made it through without you all.

Finally, I'd like to thank my family and those closest to me. My parents have always been my biggest cheer-leaders and never fail to support me in whatever direction I'm currently headed in. Their love and support means the world. My closest friends and teammates have helped me through the hardest times in this long process and taught me so much about myself along the way; I don't know what I'd do without them.

Contents

Chapter

Tables

Table

Figures

Figure

Chapter 1

Planetary Habitability, Atmospheric Evolution and Escape

One of the most exciting scientific questions of our time is "Is there life on other planets?". Answering this question will likely take decades of work and draw on fields as disparate as microbiology, geology, and astrophysics. Here I discuss the role of planetary science and astrophysics in understanding the processes relevant for creating an environment capable of sustaining life, both in our own solar system and around other stars quite different than our Sun.

The presence of water has long been considered a necessary ingredient for life to begin. While some posit the existence of subsurface ocean life on bodies such as Europa [e.g. Kargel et al., 2000]; for life to be remotely detectable this water must exist on the surface in a liquid form [e.g Rasool and de Bergh, 1970, Kasting et al., 1988]. The presence of liquid water requires both a substantial atmosphere, in order to prevent the rapid evaporation and loss of oceans, and a temperature between the freezing and boiling points of water, so that the oceans can be liquid rather than steam or ice. Understanding the atmosphere of a planet and its climate is thus very important to habitability.

Atmospheres change over time due to their interaction with the surface, oceans, space environment, solar forcing, and global biome. These systems are all coupled and change non-linearly. Our own solar system shows multiple examples of substantial atmospheric evolution over time; Venus became extremely hot due to the runaway greenhouse effect and has lost most of its water [Dayhoff et al., 1967, Kulikov et al., 2006], while Mars used to have a substantial atmosphere and liquid surface water but is now a cold dry planet with minimal atmosphere [Anders and Owen, 1977, Jakosky and Phillips, 2001]; Section 1.4 describes the observational evidence leading to such con-

clusions. Both of Earth's nearest neighbors illustrate the importance of understanding atmospheric loss.

Habitability is also becoming a relevant question for planets outside our solar system. Exoplanet discovery missions such as Kepler [Borucki et al., 2010] and the Transiting Exoplanet Survey Satellite (TESS) [Ricker et al., 2015] have allowed the discovery of thousands of extra-solar planets, including dozens of small, rocky planets. The closest star to us, Proxima Centauri, hosts a planet with a minimum mass of 1.3 times the mass of the Earth [Anglada-Escudé et al., 2016], and the nearby Trappist system is home to seven transiting Earth sized planets [Gillon et al., 2017, 2016]. Both Proxima Centari-b and 4 of the Trappist-1 exoplanets fall within the Habitable Zones (HZs) of their host stars; or regions around a star where a planet's temperature would allow liquid water to exist [Kasting et al., 1993, Kopparapu et al., 2013]. However, as seen in our own solar system, habitability is complex and requires the careful analysis of many inner-connected processes, including atmospheric escape.

Atmospheric volatiles that are not sequestered in the surface may be lost through escape to space. In order to be lost to space a given particle must have enough energy to overcome the gravitational potential of the planet. Section 1.2 discusses various processes responsible for energizing atmospheric particles and the subsequent escape. Because the escape processes are intrinsically linked to the coupling of the planet and the stellar environment, we first summarize the regions involved in this interaction (Section 1.1). I then discuss how escape can be measured (Section 1.3) and linked to understanding of the overall atmospheric evolution (Section 1.4).

1.1 Planetary Environments

In this section we describe planetary regions that are relevant to escape. We put a specific emphasis on the Martian environment, due to to its extreme atmospheric evolution, wealth of observable data, and connection with the models run in Chapters 3-5. We break down the section into a discussion of the neutral atmosphere, ionosphere, and magnetosphere. These regions are depicted schematically in Figure 1.1; however, as described in the following subsections the three

regions are highly coupled and also have significant spatial overlap.

1.1.1 Neutral Atmosphere

To first order the structure of the neutral atmosphere is controlled by the pressure and temperature variation with altitude. The exosphere is the outermost portion of the atmosphere where densities are so low that collisions are infrequent. Below the exosphere is the thermosphere, a region where collisions become important and temperatures increase with altitude. The lower boundary of this region is the mesopause where the temperature reaches a minimum. The homopause, or region where the atmosphere begins to be well mixed rather than diffusively separated is another important boundary in this region. These layers are shown with a typical temperature profile for the Martian atmosphere in Figure 1.2

The Martian upper atmosphere was first sampled during the descents of Viking Lander 1 and 2 [McElroy et al., 1976, Nier et al., 1972, 1976], and followed up from direct measurements from a variety of landers [Magalhães et al., 1999, Schofield et al., 1997] and orbiters [Bougher et al., 1999, Tolson et al., 2005, Tolson et al., 2000, Bhardwaj et al., 2015, Stone et al., 2018, Jakosky, 2017, Mahaffy et al., 2015]. Meanwhile, stellar occultations [Krasnopolsky et al., 1991, Bertaux et al., 2006, Forget et al., 2009, Gröller et al., 2015] and dayglow observations [Anderson, 1974, Krasnopolskii, 1975, Stewart, 1972, Leblanc et al., 2006, Huestis et al., 2010, Evans et al., 2015] have provided additional information on the thermal structure. The thermal structure is consistent with heating by UV radiation and cooling through CO_2 radiation at 15 μm and thermal conduction, indicating that the Martian exosphere temperature depends linearly on solar EUV flux [Bougher et al., 2009, González-Galindo et al., 2009, Stone et al., 2018]. Because Mars has a thin atmosphere, atmospheric circulation and heat transfer is weak, creating strong diurnal variations [Bougher et al., 2009, Gröller et al., 2018, Stone et al., 2018]. Seasonal heating and dust storms have strong effects on the neutral structure and vertical transport of H [Bougher et al., 2006, Van den Acker et al., 2002, Bhattacharyya et al., 2017, Hollingsworth et al., 1997]. There is also significant thermal variability due to waves; this has key implications for atmospheric mixing and subsequent escape

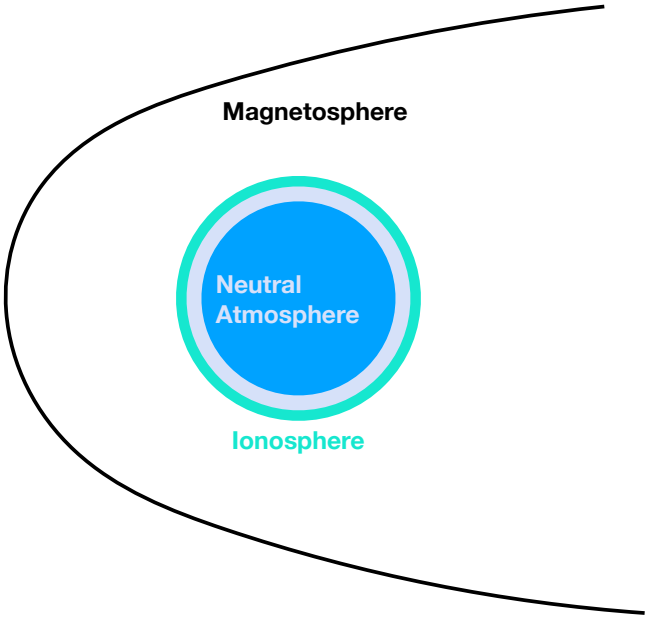

Figure 1.1: Schematic representation of the relationship of the magnetosphere, ionosphere, and neutral atmosphere for an unmagnetized planet. Note that these three regions are not necessarily spatially distinct, as described in the following subsections.

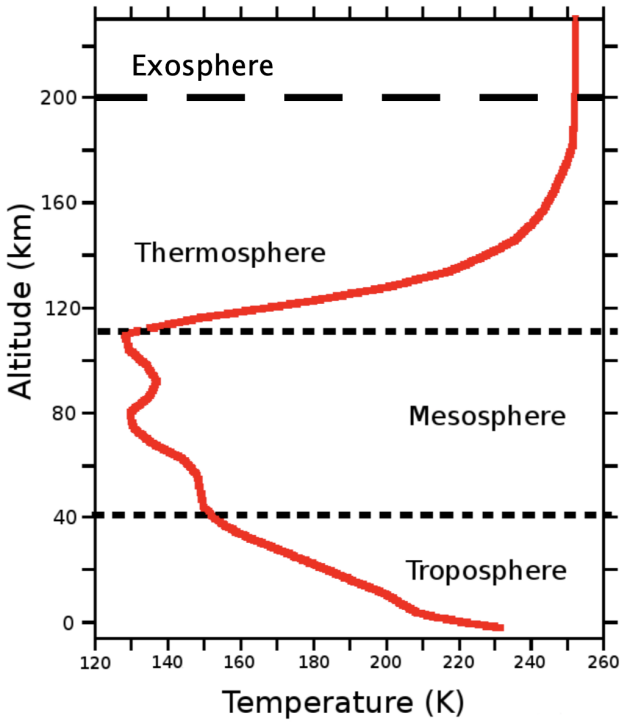

Figure 1.2: Schematic example of a temperature profile for the Martian neutral atmosphere [adapted from González-Galindo et al., 2008].

[Slipski et al., 2018, Stone et al., 2018, England et al., 2017].

Planetary escape typically proceeds from a point where particles experience largely ballistic trajectories rather than collisional ones. This transition between the exosphere and the thermosphere is typically called the exobase, where the mean free path ($l = 1/\sigma n(z)$, σ is the collisional cross section and $n(z)$ is the number density) is equal to the scale height ($H = k_B T/mg$, k_B is the Boltzmann constant, T is the temperature, m is the species mass, and g is the gravitational acceleration at the surface).

1.1.2 Ionosphere

The ionosphere is a layer of plasma formed by the photo-ionization of the upper atmosphere via stellar radiation or energetic particle impact ionization. As the plasma is only partially ionized, it is spatial coincident with parts of the neutral upper atmosphere. This region is important due to its role in coupling the neutral upper atmosphere to the magnetosphere.

In the dayside of the Martian atmosphere photo-ionization dominates over particle precipitation [Kallio and Janhunen, 2001]. Photo-ionization of a neutral species M can proceed via

$$hv + M \rightarrow M^+ + e^- \tag{1.1}$$

when the photon energy hv exceeds the ionization potential of species M. The most important wavelengths for producing photo-ionization of species which typically make up neutral upper atmospheres are in the Extreme Ultra-violet (EUV).

The production rate of ions for a species M at an altitude z is given by

$$Q_M(z) = \int_0^{\lambda_M} F_\lambda(z) n_n(z) \sigma_\lambda d\lambda \tag{1.2}$$

where λ_M is the ionization threshold, $F_\lambda(z)$ is the photon flux of wavelength λ at altitude z, $n_n(z)$ is the neutral density, and σ_λ is the photo-ionization cross section at wavelength λ. The photon flux at an altitude z for some incident flux $F_{\lambda 0}$ is given by

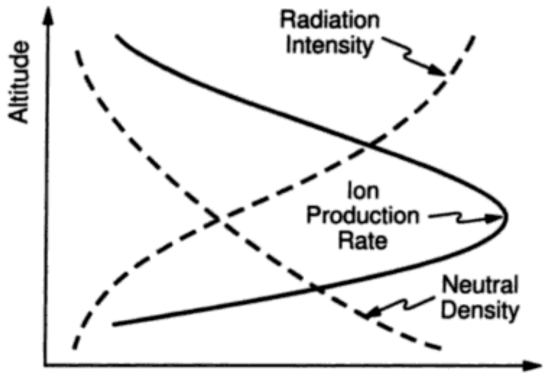

Figure 1.3: Ion Production, adopted from Baumjohann and Treumann [1996]

$$F_\lambda(z,\chi) = F_{\lambda 0} e^{-\tau_\lambda} \tag{1.3}$$

where the optical depth τ_λ is given by

$$\tau_\lambda = \frac{1}{\cos(\chi)} \int_z^\infty n_n(z')\sigma_\lambda dz' \tag{1.4}$$

where χ is the Solar Zenith Angle (SZA) or angle between the subsolar line and the vertical. The production rate of ions is thus reflected by a balance of the neutral atmosphere available for ionization and the radiation intensity of the EUV flux. This is shown schematically in Figure 1.3.

In the assumption of an isothermal atmosphere the optical depth can be approximated by

$$\tau_\lambda \approx \frac{1}{\cos(\chi)} n_n(z) H_n \sigma_\lambda \tag{1.5}$$

where H_n is the scale height of the isothermal neutral atmosphere. The resulting production rate can be written

$$Q(\chi, z') = Q_0 \exp[1 - z' - \sec(\chi) * e^{-z'}] \tag{1.6}$$

for $z' = (z - z_0)/H$. This approximation is called a Chapman layer profile [Chapman and Zirin, 1957].

When ion production via photoionization, electron impact ionization, and chemistry is balanced by loss from ion-neutral reactions and electron-ion recombination, the system is said to be in photochemical equilibrium. Near the density peak of the Martian ionsphere photochemical equilibrium holds because timescales for plasma transport processes ($\tau = H^2/D$, H is the scale height, D is the plasma diffusion coefficient) are much longer than timescales for photochemical processes ($\tau = 1/(\alpha N)$, α is the dissociative recombination coefficent, N_e is the electron density) [Schunk and Nagy, 2009, Martinis et al., 2003]. This peak electron density region, also known as the M2 layer, occurs at altitudes of around 100-150 km depending on SZA [Fox and Yeager, 2006]. As the electron density decreases exponentially above this layer, diffusive processes and production of O_2^+ and O^+ become important [Rishbeth and Garriott, 1969].

The ionosphere of Mars has been observed via radio occultation [Hinson et al., 1999, Withers et al., 2008], radar experiments on Mars Express and Mars Reconnaissance Orbiter [Pätzold et al., 2005, Gurnett et al., 2005], and in situ probes on the two Viking landers and MAVEN [Nier and McElroy, 1977, Jakosky et al., 2015c, Benna et al., 2015]. Due to the simultaneous measurements of the neutral atmosphere and plasma properties, the in situ measurements from the MAVEN mission are particularly important to understanding the ionosphere. Neutral atmosphere variability [Mendillo et al., 2017, Withers et al., 2018], wave activity [Gurnett et al., 2010, Fowler et al., 2018], solar irradiance variability [Dubinin et al., 2017, 2018], solar wind variability [Shinagawa and Cravens, 1989, Dubinin et al., 2008, 2018], and crustal field presence [Withers et al., 2005, Nielsen et al., 2007, Mitchell et al., 2001] are all found to produce ionospheric variability.

An important part of the coupling between the ionosphere and the larger magnetospheric system is the conductivity of the ionosphere. In an ionosphere with large scale magnetic structure the conductivity of the plasma becomes highly anisotropic, due to current carrying ions and electrons moving along magnetic fields. This magnetic structure can come from an intrinsic magnetic field or the draping of stellar wind magnetic field lines, further described in Section 1.1.3.

$$\sigma_P = \frac{n_e e}{B}\left(\frac{\omega_i \nu_{in}}{\omega_i^2 + \nu_{in}^2} + \frac{\omega_e \nu_{en}}{\omega_e^2 + \nu_{en}^2}\right) \tag{1.7}$$

$$\sigma_H = \frac{n_e e}{B}\left(-\frac{\omega_i^2}{\omega_i^2 + \nu_{in}^2} + \frac{\omega_e^2}{\omega_e^2 + \nu_{en}^2}\right) \tag{1.8}$$

$$\sigma_\parallel = n_e e^2\left(\frac{1}{m_i \nu_{in}} + \frac{1}{m_e \nu_{en}}\right) \tag{1.9}$$

Equations 1.7, 1.8, and 1.9 give expressions for the Pedersen, Hall, and field-aligned conductivities, where ω is the cyclotron frequency, n is the number density, ν is the collision frequency, and the subscripts i, e, and n indicated ions, electrons, and neutrals respectively. Studies of ionspheric conductivities at Mars find very strong Hall and Pedersen conductivities in magnetically undisturbed regions and more complicated behavior near crustal fields [Opgenoorth et al., 2010, Riousset et al., 2014].

1.1.3 Magnetosphere

The magnetosphere is typically defined as the region around a magnetized planet where the planetary magnetic field strongly affects charged particle motion. The magnetosphere is important because any escaping particle is subject to the forces from the magnetospheric environment; this is particularly relevant for charged particle escape from the ionosphere. An induced magnetosphere is produced at any unmagnetized planet with a substantial conducting ionosphere, as the conducting ionosphere creates an effective magnetic obstacle. Here we use the term magnetosphere to broadly include both intrinsic and induced magnetospheres, referring to the whole region where the solar wind magnetic field is affected by draping around the magnetic obstacle. Figure 1.4 shows a comparison of an intrinsic and induced magnetosphere, and their typical magnetic topology.

Just outside the magnetosphere is the bow shock created by the interruption of the supersonic solar wind flow by the planetary obstacle. The shape and size of this boundary is determined by the obstacle size and the alfven Mach number of the inflowing plasma [Spreiter et al., 1966]. Bow

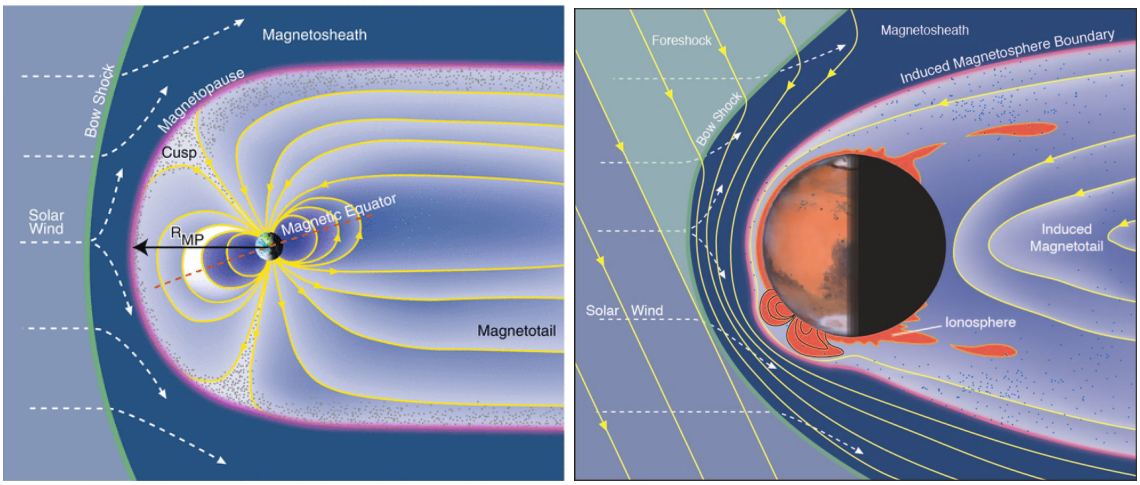

Figure 1.4: Schematic examples of an intrinsic magnetosphere (left) and an induced magnetosphere (right) of small, terrestrial planets. Adapted from Bagenal [2013].

shocks have been observed at Earth [Fairfield, 1971], Mars [Riedler et al., 1989], and Venus [Bridge et al., 1967].

Within the magnetosphere, magnetized planets have a magnetopause boundary that is defined by the balance of the dynamic pressure from the solar wind and the magnetic pressure of the intrinsic dipole. Outside the magnetopause but within the bow shock is the magnetosheath, or region of shocked solar wind plasma. Within the magnetopause is the plasmasphere, or the region of cool plasma trapped by the magnetic dipole.

Unmagnetized planets share a similar structure, but due to the lack of dominant magnetic field the physics controlling various boundaries within the magnetosphere differs. The Magnetic Pileup Boundary (MPB) is characterized by the pileup of the IMF as it drapes around the planet, while the Induced Magnetosphere Boundary (IMB) is marked by a transition from solar wind to planetary plasma [Nagy et al., 2004a]. Outside of the IMB/MPB but within the bow shock is the magnetosheath, in analog to the magnetized systems.

The region in the wake of the planet is called the magnetotail. In the magnetotail, draping of magnetic field lines around the magnetosphere create a current sheet. At unmagnetized planets the current sheet has both twisting and flapping motions [DiBraccio et al., 2017, DiBraccio et al., 2018, Chai et al., 2019], which may be associated with changes in response to upstream IMF or solar wind pressure, kink-like flapping due to waves propagating along the current sheet, or reconnection of crustal fields [Luhmann et al., 2015]. Magnetized planets also have current sheets that show flapping motions [Speiser and Ness, 1967], this motion is strongly influenced by reconnection events [Nakamura et al., 2006].

It is important to understand magnetospheric processes and variability in order to relate measured plasma populations back to intrinsic escape physics. Both the stellar drivers (see Chapter 4) and the intrinsic planetary magnetic field (see Chapter 5) have a critical impact on the magnetosphere and subsequent escape.

1.2 Escape Processes

A variety of processes are responsible for driving planetary atmospheric escape. This section summarizes the physics responsible for each process, the relevance for solar system planets, and observations of such escape with a specific focus on escape from Mars.

1.2.1 Thermal Escape

One common source of escape energy for a particle is its thermal motion. For this energy to lead to escape, the velocity of the particle must exceed the escape velocity. Thus, the escape rate for a population of particles is dependent on its thermal distribution near the exobase.

1.2.1.1 Jeans Escape

For a population in thermodynamic equilibrium, the probability density function follows a Maxwell-Boltzmann distribution given by

$$f(v) = 4\pi v^2 \left(\frac{m}{2\pi k_B T}\right)^{3/2} e^{-\frac{m|v|^2}{2k_B T}} = \frac{GMm}{r_{exo} k T_{exo}} \tag{1.10}$$

where m is the mass of the particle, v is the velocity, k_B is the Boltzmann constant, and T is the thermodynamic temperature.

In slow-steady state escape the particle population maintains thermodynamic equilibrium such that only the high energy tail of the distribution escapes; this process is known as Jeans escape [Jeans, 1925, Chamberlain, 1963]. If we assume that all particles that exceed the escape velocity above the exobase escape, this leads to a straightforward escape flux prediction

$$\Phi = \frac{n(z_0) v_0}{\sqrt{\pi}} \left(\frac{{v_{esc}}^2}{{v_T}^2} + 1\right) e^{-\frac{{v_{esc}}^2}{{v_T}^2}} \tag{1.11}$$

where $n(z_0)$ is the number density at the exobase, $v_T = \sqrt{2kT/m}$ is the mean thermal velocity, and $v_{esc} = \sqrt{2GM/r}$ is the escape velocity. Non-thermal energy distributions will affect this escape rate, and the applicability of this process for different species. Jeans escape occurs at all

terrestrial planets including Earth [Hunten and Donahue, 1976, Pierrard, 2003, Romantan et al., 1981, Lindenfield and Shizgal, 1979], Mars [Hunten and Donahue, 1976, Liu and Donahue, 1976, Brain et al., 2016, Pierrard, 2003], and Venus [Hunten and Donahue, 1976, Brain et al., 2016].

1.2.1.2 Hydrodynamic Escape

Jeans escape can only be maintained in situations where the escape velocity is much larger than the mean thermal velocity; if these values approach each other the thermal equilibrium assumption is broken, and the atmosphere becomes weakly bound. The departure from this assumption can be assessed using the escape parameter λ, defined as

$$\lambda = \left(\frac{{v_{esc}}^2}{{v_T}^2}\right)^2 = \frac{E_{grav}}{E_{therm}} \tag{1.12}$$

where E_{grav} is the gravitational escape energy and E_{therm} is the thermal energy. Jeans escape occurs when $\lambda \gg 1$, while hydrodynamic escape occurs for $\lambda \lesssim 1$. While hydrodynamic escape is likely only currently occuring in the solar system at Pluto due to its low surface gravity [Krasnopolsky, 1999, Tian and Toon, 2005], hydrodynamic escape may have played a role in the evolution of young, hydrogen-rich Earth [Pepin, 1991, Tian et al., 2008], Venus [Kasting and Pollack, 1983], and Mars [Pepin, 1991].

1.2.2 Non-Thermal Escape

While lighter species commonly escape thermally, the lower velocity for a heavier species at a fixed temperature means that heavier species need additional energy sources to escape the gravitational potential of the planet. As secondary atmospheres are typically composed of heavier species, studying non-thermal loss processes is very important for assessing atmospheric evolution and habitability.

Non-thermal loss processes have been studied extensively for solar system planets including Earth [e.g Strangeway et al., 2005], Mars [e.g Lundin et al., 1989a, Barabash et al., 2007b, Brain et al., 2015], Venus [e.g NordströM et al., 2013, Barabash et al., 2007a], and Titan [Wahlund et al.,

2005, Gurnett et al., 1982, e.g]. This loss takes a variety of observed forms including photochemical escape [Jakosky et al., 1994, Fox and Hać, 2009], charge exchange [Chamberlain, 1977], sputtering [Jakosky et al., 1994, Lammer and Bauer, 1993, Leblanc and Johnson, 2001], ion pickup [Luhmann and Kozyra, 1991a], ion bulk escape [Brain et al., 2010], and the polar wind [Banks and Holzer, 1968, Yau et al., 2007]. These processes are summarized schematically in Figure 1.5.

1.2.2.1 Ion Pickup and Plume Escape

Because a stellar wind carries a magnetic field (B_{sw}) with some velocity (U_{sw}) past a planet, it produces a motional electic field given by

$$E = -U_{sw} \times B_{sw} \tag{1.13}$$

While the intrinsic magnetic field of magnetized planets prevents the motional electric field from substantially affecting the planet's atmosphere due to the slow down and deflection of the solar wind around the magnetic obstacle, the motional electric field strongly affects planetary ions at unmagnetized planets, accelerating particles to speeds that may exceed the escape velocity. Any ions accelerated by this force and gyrating around interplanetary magnetic field lines are referred to as "pickup ions". Planetary pickup ions that are accelerated from the day side of an unmagnetized planets can form a coherent structure known as the plume; this escape process was first identified in numerical simulations of the Mars plasma environment [Connerney et al., 2015, Brecht and Ledvina, 2006, Jarvinen et al., 2016, Luhmann and Schwingenschuh, 1990, Fang et al., 2008b, Najib et al., 2011b, Dong et al., 2014].

Plume escape has been found to be an important process at Mars [Dong et al., 2015b, Curry et al., 2015, Dubinin et al., 2011], Venus [Curry et al., 2015, Luhmann et al., 2006, Dubinin et al., 2011, McEnulty, 2012], and Titan [Ledvina et al., 2004, Michael et al., 2005]. Studies at Mars have found that plume fluxes are affected by seasonal variability [Dong et al., 2017c], solar wind variations [Dubinin et al., 2017], and ion production mechanism [Curry et al., 2013].

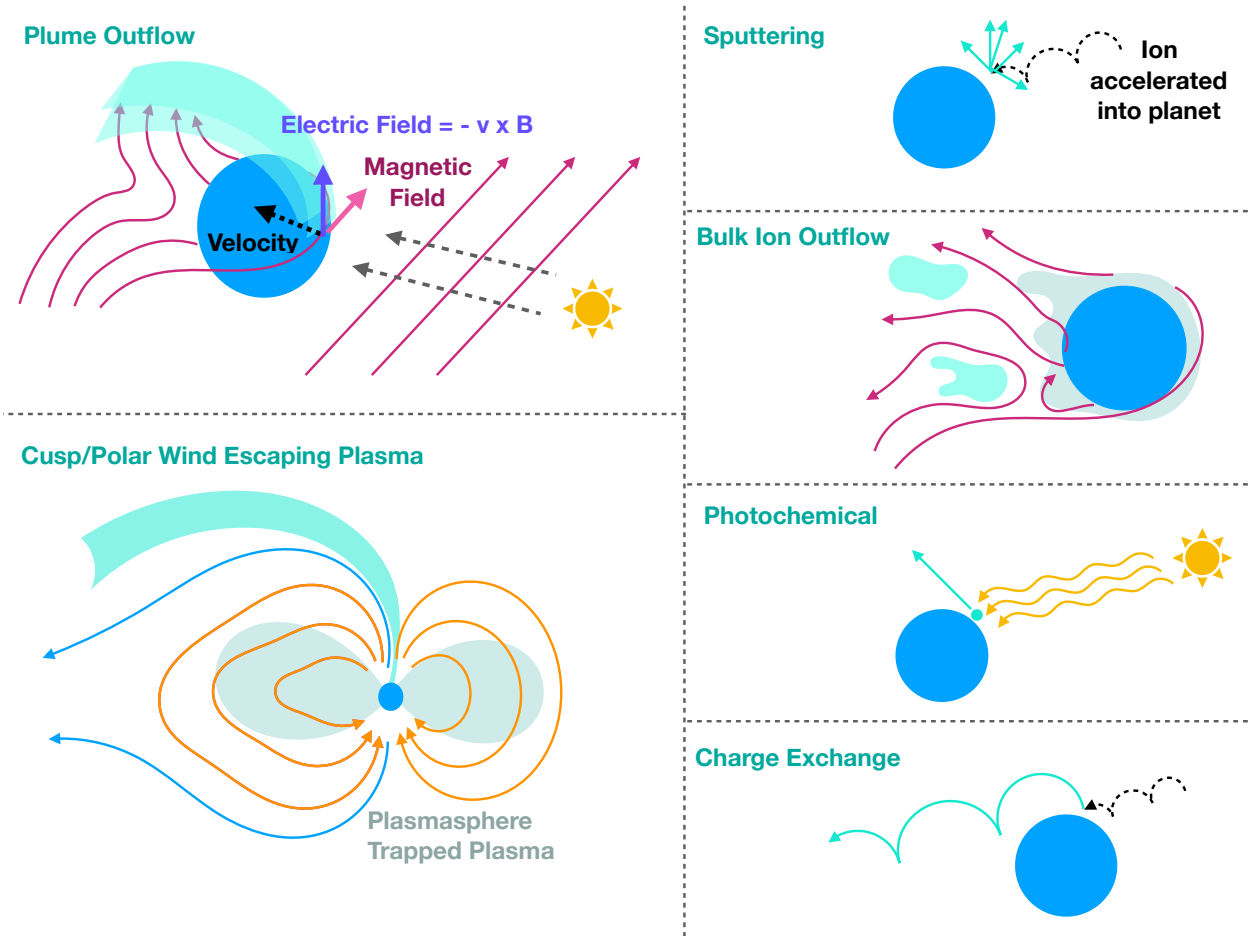

Figure 1.5: Schematic diagrams of non-thermal escape processes.

1.2.2.2 Photochemical Escape

Photochemical escape converts energy from absorbed X-ray photons to kinetic energy by dissociating a molecule. The effectiveness of this mechanism depends on the energy released by the chemical reaction. Dissociative recombination of $O_2{}^+$ is an effective escape mechanism at Mars because the reaction

$$O_2^+(v, J) + e \rightarrow O^* + O^* + \Delta E \tag{1.14}$$

has multiple channels with exothermicities that exceed the escape energy necessary for the planet ($\sim$ 1.97 eV), two of which have branching ratios large enough to lead to substantial escape [Fox and Hać, 2009]. The larger escape energy at Earth and Venus prevents photochemical escape from being an effective driver of O escape. Photo-chemical escape of C and N may also have been important at Mars through the photodissociation of CO and N_2 [Fox, 1993, Fox and Bakalian, 2001, Bakalian and Hartle, 2006, Cui et al., 2019].

Photochemical escape has long been understand to be an important escape process at Mars [McElroy, 1972, McElroy et al., 1977]. While photochemistry is important to the thermospheric structure at Venus [Sze and McElroy, 1975, Krasnopolsky, 2011], it is not a significant source of escape [Yatteau, 1983, Krasnopolsky, 2011]. Photochemical escape may also be important at Titan due to photochemical production of H from hydrocarbons [Strobel, 1982].

1.2.2.3 Charge Exchange

Charge exchange occurs when a fast ion exchanges charge with a slow neutral, creating an energetic neutral atom (ENA) and a slow ion. The ENA can then escape on a ballistic trajectory, where the ion was subject to forces from the plasma environment and corresponding magnetic field. Furthermore, charge exchange between an H^+ solar wind ion and a heavier neutral (e.g. O) will remove momentum and add mass to the plasma flow.

Charge exchange was first postulated as a mechanism necessary to explain some magneto-

spheric phenomena by Cole [1966]. Chamberlain [1977] then applied the mechanism to a planetary corona model to understand how charge exchange modifies the exosphere and can lead to increased H^+ escape. Charge exchange has been found to be an important mechanism in affecting the exospheric structure and loss of Hydrogen at Earth [Yung et al., 1989, Shizgal and Arkos, 1996, He, 1995, Maher and Tinsley, 1977], Mars [Chen, 2003, Shizgal and Arkos, 1996, Jin et al., 2006, Dubinin et al., 2011], and Venus [Kumar et al., 1983, Shizgal and Arkos, 1996, Dubinin et al., 2011].

1.2.2.4 Sputtering

The extreme energy input from fast ions impacting the atmosphere can knock many atoms out of the atmosphere via elastic collisions in a process known as sputtering. While sputtering of Io's atmosphere by Jupiter's plasmasphere has long been a well studied process [Smyth and Combi, 1988], the sputtering of the Martian ionosphere by pickup ions accelerated by the solar wind motional electric field was first suggested by [Luhmann and Kozyra, 1991b]. Sputtering has been postulated to be an important process for removing neutral oxygen at Mars [Luhmann et al., 1992] and Venus [Luhmann et al., 2008]. Furthermore, sputtering may be a key process for removing heavier elements such as Argon, of which isotopic abundances provide a record of atmospheric loss [Jakosky et al., 1994, Johnson et al., 2000, Hutchins et al., 1997]. The energy input from sputtering may also enhance the exobase temperature [Kozyra et al., 1982, Johnson, 1989], although there are currently no supporting observations for Mars or Venus.

1.2.2.5 Ion Bulk Escape

Ion bulk escape is defined as the coherent detachment of portions of the ionosphere en masse. This has been proposed to be a process operating at Venus [Wolff et al., 1980] and Mars [Penz et al., 2004] due to the Kelvin-Helmholtz instability. Initial observations suggest this process may be happening at both planets [Brace et al., 1982, Cloutier et al., 1999], but it is difficult to disambiguate the signature from other escape mechanisms. Additionally, the presence of crustal fields at Mars may lead to episodic detatchment of magnetic flux ropes and the corresponding

plasma [Brain et al., 2010].

1.2.2.6 Cusp Escape and the Polar Wind

Because ions are constrained to gyrate around magnetic field lines, ion escape proceeds more directly along magnetic field lines that are connected directly to the stellar wind. For magnetized planets this only occurs at poles, while for planets like Mars magnetic topology is sensitive to the locations of remnant crustal fields. Additionally, electron pressure gradients along magnetic cusp regions act to drag heavier ions up along the cusps as well, due to the larger scale height of lighter electrons. When electron pressure forces act to drive increased ion outflow along magnetic cusps the process is called the polar wind, originally coined by Axford [1968].

The polar wind was first modelled by Banks and Holzer [1968], and observed at Earth by Hoffman [1970], Brinton et al. [1971] and Hoffman et al. [1974]. The polar wind has been found to be an important ion supply to the Earth plasmasphere [Huddleston et al., 2005]; however, its still a matter of debate to what extent the polar wind ions eventually leave the system or are recycled back into the ionosphere [Seki et al., 2001, Huddleston et al., 2005, Slapak et al., 2017].

At Mars the remnant crustal fields provide a laboratory for understanding escape along very localized magnetic cusps, independent of global morphology. Crustal magnetic fields have been found to have a key impact on ion escape, some of which is due to crustal fields being directly open to the solar wind [Lundin et al., 2011, Ma et al., 2014, Dong et al., 2015b, Fang et al., 2010, 2015b, Ramstad et al., 2016a]. These results necessitate detailed studies of the local magnetic topology in order to connect cusp processes with measured particle distributions.

1.3 Measuring Atmospheric Escape and Evolution

There are a variety of methods used to measure atmospheric escape, from in-situ measurements, to transits and occultations, to isotopologue abundance measurements. Atmospheric evolution can also be measured through its relationship with geology, both in the weathering of surface features and in the geochemical record, but we here summarize measurements that may be obtained

directly from the atmosphere itself.

1.3.1 In-Situ Measurements

In-situ measurements of escaping ions are a key method for understanding planetary escape. These measurements typically involve counting ions within some mass per charge or velocity per charge bins to assess the plasma distribution. These measurements can then be extrapolated to ion outflow rates or combined with other plasma measurements to drive planetary plasma models (see Chapter 2).

There are many challenges in extrapolating in-situ measurements to global escape rates. The first is instrumental; it is extremely difficult to measure the entire plasma distribution in all directions for a non-spinning spacecraft. Therefore it is quite possible for a given instrument to miss a plasma population with coherent velocity structure due to a pointing issue. Second, even with a perfectly complete plasma distribution, a single spacecraft only takes measurements at a given point in space and time. While statistical averages can be built up over many orbits, this then introduces another difficulty in the intrinsic variability of escape due to both stellar driving and planetary properties.

Despite these difficulties, in situ measurements from various spacecraft have been used to estimate global ion escape rates from Mars [Nilsson et al., 2011, Lundin et al., 1990, Lundin and Dubinin, 1992, Jakosky, 2017], Venus [Barabash et al., 2007a, Fedorov et al., 2011, Lundin, 2011, NordströM et al., 2013, Brain et al., 2015], Earth [Seki et al., 2001, Strangeway et al., 2005], and Titan [Yelle et al., 2008, Coates et al., 2012]. Escape variability has also been studied to understand the influence of the stellar wind driving [Lundin et al., 2008, Ramstad et al., 2017, 2015b, Nilsson et al., 2010], crustal field location [Ramstad et al., 2016b], space weather [Mayyasi et al., 2018], solar cycle variation [Lundin et al., 2013], and seasonal variability [Dong et al., 2017c, Rahmati et al., 2018]. Figure 1.6 shows an example of plasma measurements made by the STATIC instrument on MAVEN, looking at seasonal variability of plume escape.

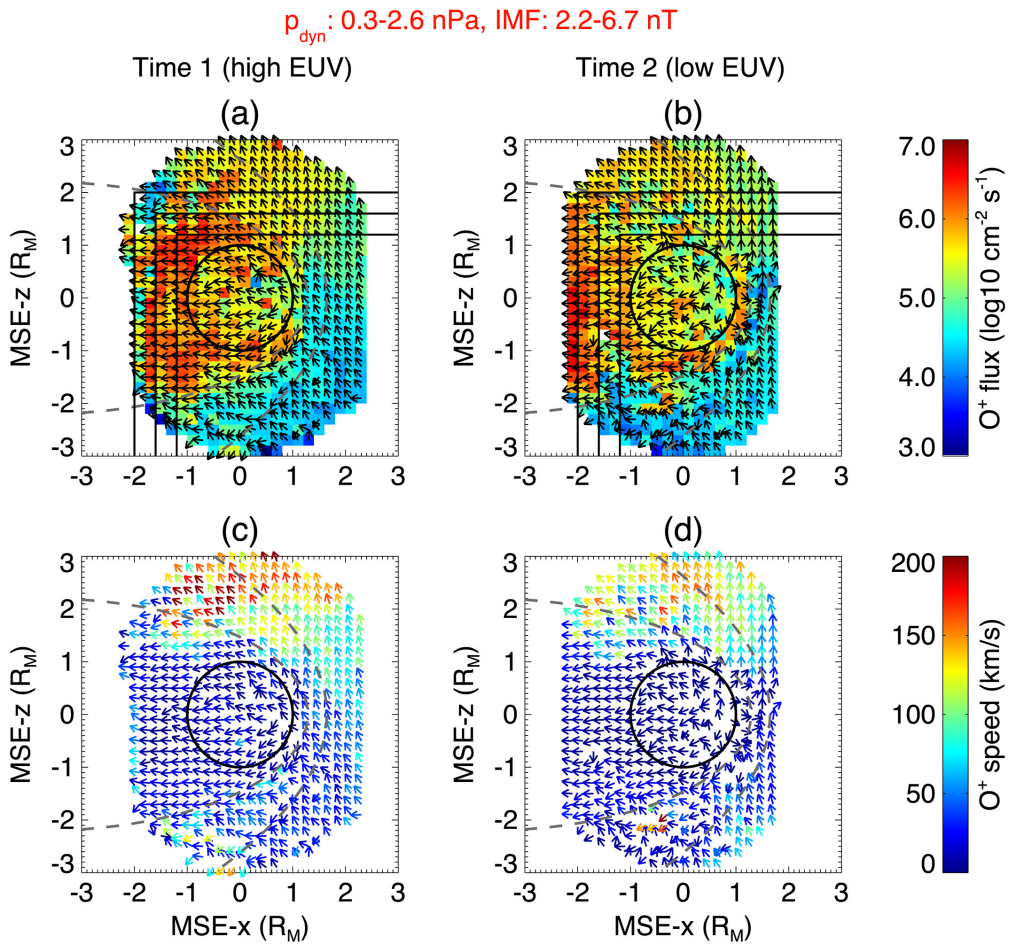

Figure 1.6: O_2^+ flux and velocity maps from MAVEN, used to estimate ion escape rates. Observed total escape rates are of order 10^{25} s^{-1}. [Adapted from Dong et al., 2017c].

1.3.2 Emission and Absorption

While direct plasma measurements are an important tool in detecting atmospheric escape, they are limited by taking a measurement at a single point in space and necessitating an in-situ spacecraft. In contrast, atmospheres may also be observed in the emission and absorption of light. Atmospheric emission can come from processes such as scattering of solar light and dayglow emission from electronic transitions of ionized species. Absorption of light can happen from re-absorption of scattered emission or occultation of a background source; such a source can be a distant star or the star the planet is directly orbiting.

Radiative transition of H atoms in the thermosphere and corona have been observed in the 121.6nm Lyman alpha line at Mars with Mariner 6 and 7 [Anderson, 1974], Mars 2, 3, and 5 [Babichenko et al., 1977, Dostovalov and Chuvakhin, 1973], Mariner 9 [Anderson, 1974], Mars Express [Chaufray et al., 2008, Chaffin et al., 2014], the Hubble Space Telescope [Bhattacharyya et al., 2015, Clarke et al., 2014], and MAVEN [Chaffin et al., 2018]; these observations were then used to infer the H escape rate. Similar observations have also been made at Venus [Wallace, 1969]. One example of this process is shown in Figure 1.7 for Mars using MAVEN IUVS data.

Observations of exoplanet planet atmospheres largely use the transit technique, where small portions of a star's light are blocked out by an occulting planet as it orbits the star. While the planet itself cannot be resolved, different portions of the atmosphere can be observed by using different wavelengths and considering the ingress and egress portions of the occultation separately from the main transit. This technique has been used to identify H escape for hot Jupiters such as HD 209458b [Vidal-Madjar et al., 2003] and HD 189733b [Lecavelier Des Etangs et al., 2010]. Other species including Helium (via the the 1083 nm triplet) [Nortmann et al., 2018, Allart et al., 2018], Sodium (via the 588 nm doublet) [Charbonneau et al., 2002, Redfield et al., 2008, Vidal-Madjar et al., 2011], and Magnesium (via the 280 nm doublet) [Haswell et al., 2012, Vidal-Madjar et al., 2013] have also been observed escaping hot gas giant exoplanets. Figure 1.8 shows an example of how the Ly-α transit of HD 189733b can be used to infer a corresponding escape rate.

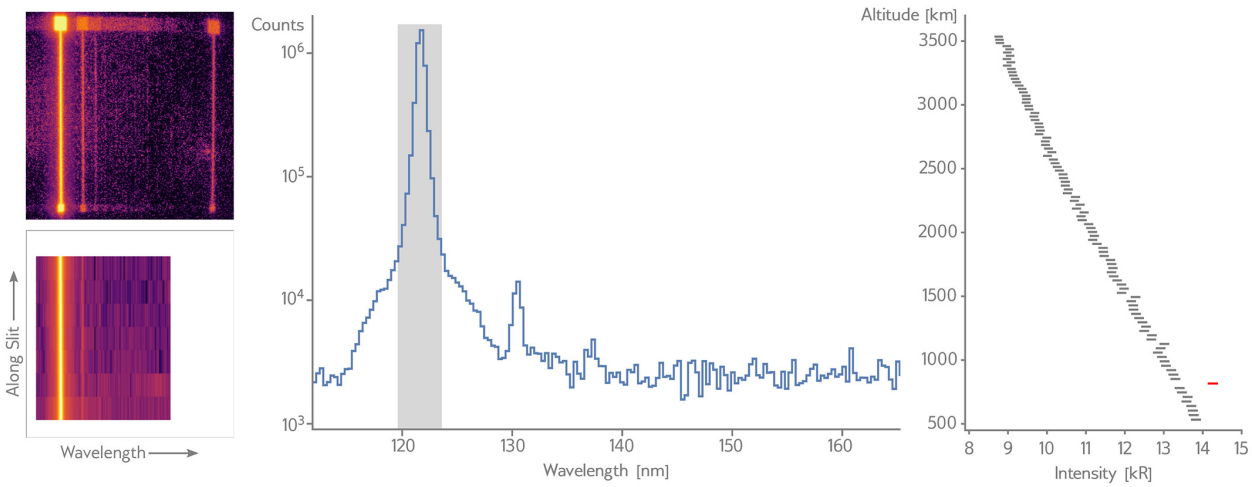

Figure 1.7: Example of the data reduction pipeline used to measure the hydrogen corona at Mars, moving from the native IUVS spectral image (left), to averaging the spectra along the slit and integrating over the Ly-α line, to creating a Hydrogen altitude profile (right). These profiles can then be used with coronal models to estimate the escape rate [adapted from Chaffin et al., 2018].

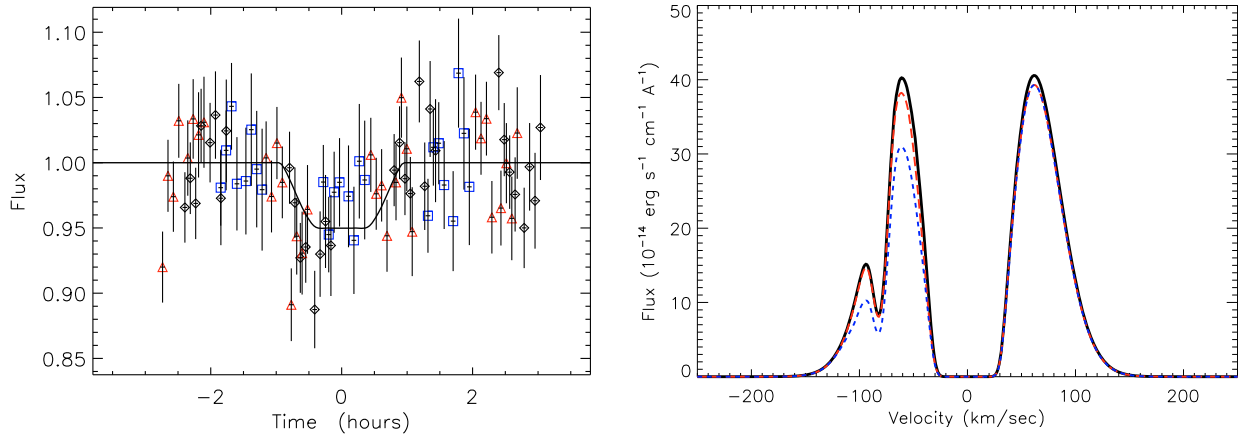

Figure 1.8: Ly-α transit of HD189733b (left) and corresponding reconstructed spectra (right) with colored dashed lines indicating different possible H escape rates [adapted from Lecavelier Des Etangs et al., 2010].

1.3.3 Isotope Abundances

Both methods discussed so far involve measuring atmospheric escape as it is currently happening. In contrast, measuring isotopic abundance ratios allows one to measure the effect that atmospheric escape has had on an atmosphere.

Two isotopologues (e.g. Deuterium and Hydrogen) will escape using the same processes, however, the slight mass difference will allow the lighter isotope to escape more easily. Thus, measuring the current abundance ratio in comparison to some original reference point can be used to estimate the amount of atmosphere that has escaped. The critical factors for connecting the current isotopic measurements with escape magnitude are the current abundance ratio, the outgassed abundance ratio, and the height difference between the homopause (or the point at which the atmosphere starts being diffusively separated rather than well mixed) and the exobase.

The deuterium to hydrogen ratio, or D/H, has been measured for Venus [Bertaux and Clarke, 1989, Donahue and Hodges, 1992, de Bergh et al., 1991] and Mars [Owen et al., 1988, Krasnopolsky et al., 1998, Villanueva et al., 2015]. Enrichment of these values with respect to Vienna Standard Mean Ocean Water (VSMOW) values implies that both planets have lost substantial amounts of water. Additionally, abundance measurements of heavy isotopes such as Argon have been measured for both Mars [e.g Biemann et al., 1976, Atreya et al., 2013] and Venus [Hoffman et al., 1979] using high precision mass spectroscopy. Due to the heavy mass and lack of signficant chemistry, sputtering is the only loss mechanism for argon; these measurements thus have key implications in constraining the efficiency of sputtering [Jakosky et al., 1994, Slipski and Jakosky, 2016].

1.4 Connecting Escape to Atmospheric Evolution

Although the aforementioned escape rates and isotope measurements have given us a much better picture of the current atmospheric loss, there is still substantial uncertainty in how to extrapolate a planet's atmosphere back in time. The planet's climate, atmosphere, ionosphere, and magnetosphere, are a set of non-linear coupled systems that also co-evolve with the Sun. It

is thus a non-trivial problem to predict a planet's long-term atmospheric evolution. Similarly, it is difficult to assess the capability of an observed exoplanet to retain a potential atmosphere over long timescales.

First estimates for the integrated atmospheric loss over time for Mars were obtained by simply multiplying the current loss rate by the system age; this lead to discrepancies with the amount of water required to produce geomorphic features [Yung et al., 1988, Liu and Donahue, 1976, McElroy et al., 1977]. Luhmann et al. [1992] was the first to use models of the EUV flux and solar-wind conditions over time to estimate variable loss over time, and found that loss rates could be orders of magnitude greater than they are today. Other models [e.g. Chassefire et al., 2013, Barabash et al., 2007, Boesswetter et al., 2010, Lammer et al., 2003] have since been developed that use more detailed physics to estimate total loss. Results from the MAVEN and MEX missions have also been used to inform estimations of current loss rates and variability [Jakosky et al., 2018, Lillis et al., 2017, Ramstad et al., 2018]; however, there are still major uncertainties related to the changing solar conditions over time, influence of obliquity, non-linear effects related to atmospheric composition, and early-epoch boundary conditions. Figure 1.9 shows an example of the estimated evolution and uncertainties of the solar wind, escape rate, and surface pressure at Mars.

Understanding exoplanet atmospheric evolution typically inverts this question; rather than starting with present day atmosphere and working backwards to understand the initial planet condition, exoplanet studies typically start with a given atmosphere and evolve it forward over time to see if the planet is capable of maintaining the atmosphere over geologic timescales. Atmospheric escape models have been developed to understand the observed gap in exoplanets with radii between super-Earths and mini-Neptunes [Owen and Wu, 2017, Ginzburg et al., 2018, Biersteker and Schlichting, 2018] as well as the potential habitability of observed exoplanets [Anglada-Escudé et al., 2016, Meadows et al., 2018, Gillon et al., 2017, Dong et al., 2018] with respect to atmospheric evolution. Some models [e.g. Barnes et al., 2018] couple atmospheric escape estimates to simple analytic models of a variety of planetary properties. In order for such models to be useful we must understand the variability of and build intuition from solar system models, which can be better

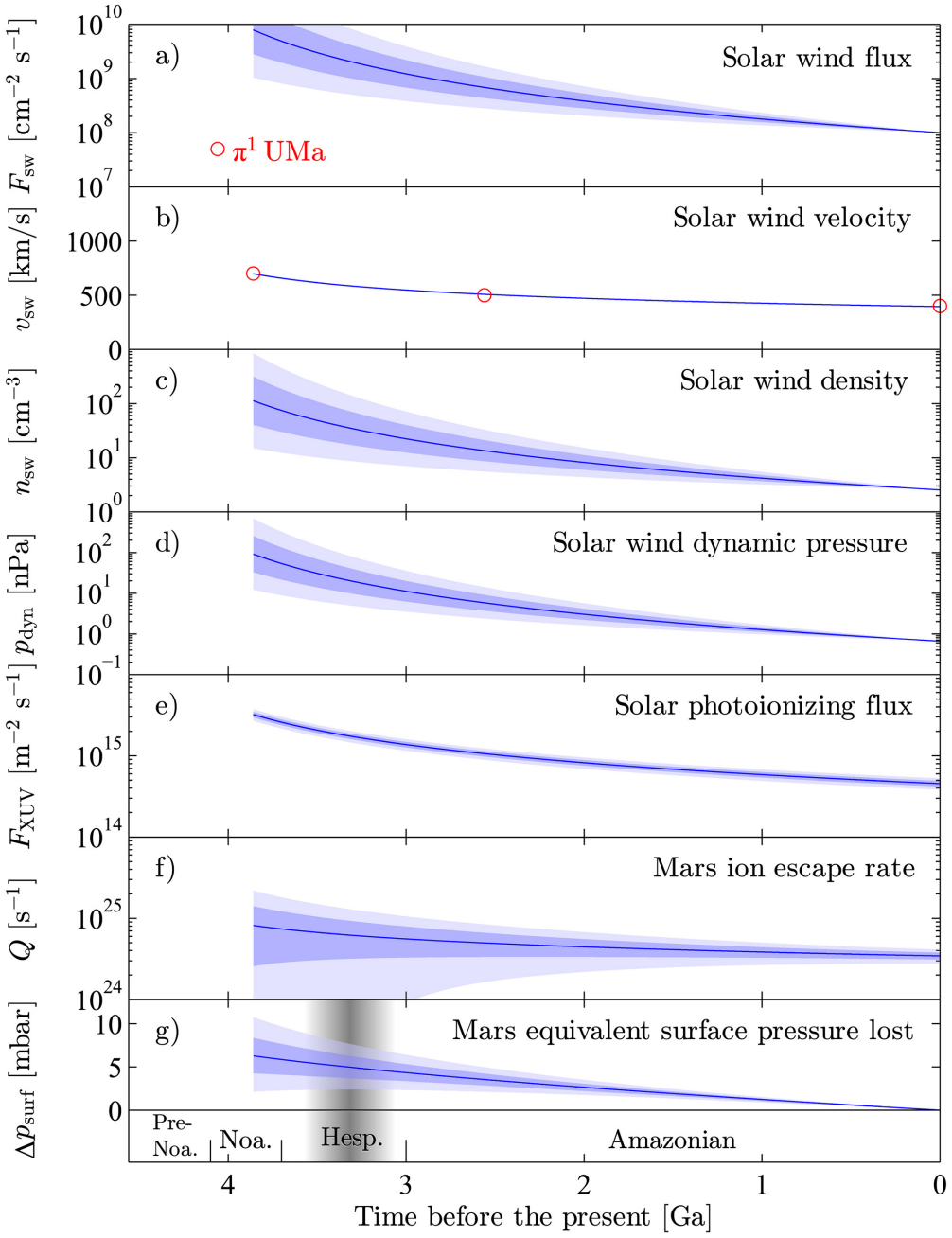

Figure 1.9: Evolution of solar wind drivers, Martian escape rate, and Martian surface pressure over time [adapted from Ramstad et al., 2018].

constrained with current observations.

1.5 Overview

In this thesis I explore the relationship of various planetary plasma environments and ion loss using computer simulations. This has key implications for understanding atmospheric evolution and overall planetary habitability.

In Chapter 2 I discuss the role of computer simulations in understanding planetary plasma environments as well as the underlying assumptions in adopting various models. Chapter 3 describes a comparison of some of these plasma models, with specific applications to the Martian plasma environment. In addition to intra-model comparison I also compare the models to data from the MAVEN spacecraft. This additional contextualization allows us to build confidence in the models and consider what physical assumptions discussed in Chapter 2 are valid or invalid for understanding a given process. Chapter 3 is published in its entirety as Egan et al. [2018].

Chapter 4 explores the relationship of the star with planetary ion escape, specifically the influence of an M-dwarf as compared to a G-type star. In order to be able to generalize these results, each input model parameter that changes as a result of the change in stellar type is varied individually. Specifically we look at the role of interplanetary magnetic field, magnetic and dynamic solar wind pressure, and EUV magnitude. We find that changing the orientation of the IMF drastically changes the plasma environment and introduces extreme atmospheric asymmetry. Additionally, ion escape can become limited by the supply of ions to the ionosphere in cases of extreme energetic input. This chapter is published in its entirety as Egan et al. [2019].

In Chapter 5 I explore the relationship between planetary magnetic field and habitability by answering the question "Do magnetic fields shield planets from ion escape?". I find that weak magnetic fields can enhance ion escape rather than shielding it due to southern hemisphere shielding, up until the point where the intrinsic magnetosphere boundary reaches the induced magnetosphere boundary. I also fit scaling relations for ion escape rates and power loss with planetary magnetic field, and discussed the ranges over which these scaling laws are appropriate.

Finally, Chapter 6 summarizes the conclusions of the previous three chapters and discusses future extensions of this work. Together, these chapters explore a variety of ideas related to atmospheric evolution through ion escape.

Chapter 2

Planetary Plasma Modeling

Many of the aforementioned atmospheric escape processes critically depend on the plasma environment of the planet. The dynamic interaction of a stellar wind and planetary obstacle leads to a wide variety of physical phenomena and plays an important role in the energization of planetary particles and atmospheric escape.

Computer models can greatly assist our understanding of these physical processes when used in conjunction with data. These models are useful as they allow one to probe the state of the whole system and its drivers at once, rather than a single point at space and time from in situ spacecraft measurements. Plasma models such as magnetohydrodynamic (MHD) [e.g Kallio et al., 1998, Ma et al., 2002, 2013b, Terada et al., 2009], hybrid [e.g Brecht and Ferrante, 1991, Kallio and Janhunen, 2002, Terada et al., 2002, Modolo et al., 2005a, Simon and Motschmann, 2009, Jarvinen et al., 2009], and test particle/direct simulation Monte-Carlo (DSMC) methods [e.g Cravens et al., 2002, Fang et al., 2008, Luhmann et al., 2006], have all been used to understand ion escape in the context of the terrestrial planets. Using plasma simulations that have been validated in the solar system planetary context can also add to understanding of ion loss in exoplanetary systems as well as young solar system planets [e.g Johansson et al., 2011, Terada et al., 2009b, Boesswetter et al., 2010].

These models have been used to understand an extensive array of plasma processes and interactions, including plasma boundaries [Najib et al., 2011a, Bertucci et al., 2005, Bößwetter et al., 2004], spatial ion distribution [Kallio and Barabash, 2012b, Najib et al., 2011a], ion escape

[Brecht et al., 2016, Brecht and Ledvina, 2014, Dong et al., 2015c, Kallio et al., 2006b, 2010, Fang et al., 2010], magnetic topology [Liemohn et al., 2006] energetic neutral atoms (ENAs) [Kallio et al., 2006a, Gunell et al., 2006, Wang et al., 2016, 2014], and X-ray emission [Gunell et al., 2004]. Transient processes including CMEs [Ma et al., 2017, Dong et al., 2015a], changes in dynamic pressure [Ma et al., 2014], changes in solar EUV flux [Modolo et al., 2006, Modolo et al., 2005b], seasonal variation [Dong et al., 2015], and crustal field rotation [Ma et al., 2014, Fang et al., 2015a] have also been topics of study.

2.1 Model Paradigms

A plasma is made up of ionized gas where electrodynamic forces dominate the statistical properties of the medium. The motion of an individual ion or electron is determined by the Lorentz force:

$$m\frac{d\vec{v}}{dt} = q\left(\vec{E} + \vec{v} \times \vec{B}\right) \tag{2.1}$$

while the fields themselves are determined via Maxwell's equations:

$$\nabla \cdot \vec{B} = 0 \tag{2.2}$$

$$\nabla \cdot \vec{E} = \frac{\rho}{\epsilon_0} \tag{2.3}$$

$$\nabla \times \vec{E} = \frac{\partial \vec{B}}{\partial t} \tag{2.4}$$

$$\nabla \times \vec{B} = \mu_0 \vec{J} + \mu_0 \epsilon_0 \frac{\partial \vec{E}}{\partial t} \tag{2.5}$$

Solving the equations of motion self-consistently with the evolution of the fields for every ion and electron in a plasma is infeasible; therefore, the study of plasmas necessitates assumptions and simplifications to understand real systems. Here we present some of the models through which plasmas are understood and the corresponding underlying assumptions.

2.1.1 Magnetohydrodynamics

For a magnetohydrodynamic (MHD) model, the fundamental assumption is that the plasma may be treated as a quasi-neutral fluid, and that the fields and fluid fluctuate on the same time and length scales. Therefore we can justify the introduction of the Navier-Stokes fluid equations for continuity, momentum and energy. Furthermore, in a non-relativistic plasma the displacement current $\epsilon_0\mu_0\partial\vec{E}/\partial t$ can be neglected.

The conservative form of the ideal MHD equations are therefore

$$\frac{\partial \rho}{\partial t} + \nabla \cdot \rho\vec{u} = 0 \tag{2.6}$$

$$\frac{\partial \rho\vec{u}}{\partial t} + \nabla \cdot (\rho\vec{u}\vec{u}) = \vec{J} \times \vec{B} - \nabla P \tag{2.7}$$

$$\frac{d}{dt}\left(\frac{P}{\rho^\gamma}\right) = 0 \tag{2.8}$$

$$\frac{\partial \vec{B}}{\partial t} = \nabla \times (\vec{u} \times \vec{B}) \tag{2.9}$$

here ρ is the density, $\vec{u}$ is the fluid velocity, $\vec{B}$ is the magnetic field, J is the current, and P is the isotropic pressure. To arrive at this set of equations, Ohm's law has been adopted as the closure equation of $\vec{E}$. Generalized Ohm's law is given by

$$\vec{E} + \vec{u} \times \vec{B} - \eta\vec{J} = \frac{1}{en}\vec{J} \times \vec{B} - \frac{1}{en}\nabla \cdot P_e + \frac{m_e}{ne^2}\left[\frac{\partial \vec{J}}{\partial t} + \nabla \cdot (\vec{J}\vec{u} + \vec{u}\vec{J})\right] \tag{2.10}$$

The inclusion of various terms in the more generalized form of Ohm's law leads to variants from ideal MHD including Hall MHD (inclusion of the $J \times B$ term) and electron-pressure MHD (inclusion of the $\nabla \cdot P_e$ term).

In the interaction of planetary plasma with solar wind plasma, there are multiple ion species which must be taken into account. A first approximation is to use a multi-species MHD model where a different continuity equation is solved for each species and the electron fluid assumes charge neutrality from the sum of all the species. This allows the number densities of the species to vary with respect to one another, but not relative motions. A multi-fluid MHD model solves a different

momentum equation for each species rather than just a different continuity equation. Thus, effects associated with finite ion gyroradii can be included. In the study of space plasmas one must take care to select a model with appropriate approximations for the region or process of study.

A variety of MHD models have been used in the study of Mars [e.g Kallio et al., 1998, Ma et al., 2002, 2013b, Terada et al., 2009, Dong et al., 2014], Venus [e.g Benna et al., 2009, Terada et al., 2009, Shinagawa et al., 1991, Ma et al., 2013b, Biernat et al., 2000], Titan [e.g Ma et al., 2007, Ledvina and Cravens, 1998, Cravens et al., 1998, Ma et al., 2004], Earth [e.g. Spreiter et al., 1966, Ogino, 1986, Tanaka, 1995], Mercury [e.g. Kabin et al., 2000, Ip and Kopp, 2002], comets [e.g. Sagdeev et al., 1986, Schmidt-Voigt, 1989, Gombosi, 1988, Cravens, 1989], and exoplanets [e.g Dong et al., 2018, 2017b,a, Cohen et al., 2014].

2.1.2 Hybrid

While the MHD paradigm treats all charged particle populations as fluid, in a hybrid model the ions are treated as macroparticles representing a group of ions with the same velocity, mass, and location. The electrons are then treated as a charge neutralizing fluid. This formulation allows the simulation of kinetic effects associated with finite ion gyroadii and non-thermal velocity distributions.

Each ion macroparticle obeys the Lorentz force such that

$$m_i \frac{d\vec{v_i}}{dt} = q_i(\vec{E} + \vec{v_i} \times \vec{B}) \ , \tag{2.11}$$

where $\vec{E}$ and $\vec{B}$ are the electric and magnetic fields respectively.

The current density is calculated from the magnetic field via Ampere's Law

$$\vec{J} = \nabla \times \vec{B}/\mu_0 \ , \tag{2.12}$$

and the electric field can then be found using Ohm's law (Equation 2.10). Finally, the magnetic field is then propagated using Faraday's Law (Equation 2.4).

Because ions are treated as particles, this approach automatically includes Hall effects, finite ion gyroradii effects, and counter-streaming as the ions are not frozen into the magnetic field. It

can also be easily expanded to include multiple ion species. The ion velocity distribution may also be fully three-dimensional, rather than strictly Maxwellian.

Hybrid models have been used to study ion escape from Mars [e.g. Kallio and Janhunen, 2002, Kallio et al., 2010, Dival et al., 2012, Brecht and Ledvina, 2010, Brecht and Ferrante, 1991, Brecht et al., 2016, Ledvina et al., 2017, Modolo et al., 2016, 2006], Venus [e.g. Brecht and Ferrante, 1991, Jarvinen et al., 2009, 2013], Mecury [e.g. Kallio and Janhunen, 2003, Trávníček et al., 2007, Müller et al., 2011], Titan [e.g. Kallio et al., 2007, Ledvina et al., 2005, Modolo and Chanteur, 2008], Earth [e.g. Swift, 1996, Lin, 2002], and comets [e.g. Bagdonat and Motschmann, 2002, Motschmann and Kührt, 2006, Koenders et al., 2015, Delamere, 2006].

2.1.3 Test-Particle

Test-particle schemes are used to examine kinetic effects associated with ion or electron motion, without the computational expense of a fully hybrid or kinetic model. Particles are integrated via the Lorentz force (Equation 2.11) through a background of fields, such that the particle motion does not feed back on the fields or the other particles. The background fields may be calculated analytically or solved for via an MHD or Hybrid simulation. This approach is not self-consistent, nor does it treat wave-particle interactions; however, it is a useful tool for understanding the behaviour of a particular population of particles in situations where kinetic effects are important but time variations in the background fields are not.

Test particle models have been used to study ion loss from Mars [Curry et al., 2014, Liemohn et al., 2013, Leblanc and Johnson, 2002, Curry et al., 2013, Cravens et al., 2002], Venus [Luhmann et al., 2006, Phillips et al., 1987, Curry et al., 2015, Kulikov et al., 2006], and Titan [Ledvina et al., 2005, Regoli et al., 2016].

2.2 Planetary Properties

In each paradigm care must be taken in the choices related to the inner boundary, or planetary properties. In reality, the planetary properties are dynamic, three-dimensional, and cannot

be strictly separated from the plasma environment and coupling between each region (neutral atmosphere, ionosphere, magnetosphere) is bilateral. However, computational constraints prohibit a fully self-consistent treatment of the entire planetary atmosphere and solar-wind interaction; therefore, approximations must be made.

2.2.1 Neutral Atmosphere

As discussed in Sections 1.1.1 and 1.1.2, the neutral atmosphere plays a key role in the development and variability of the ionosphere; however, neutral species are not explicitly included in any of the model paradigms described above.

To first approximation the neutral atmosphere can be described as a 1-D spherically symmetric background; where the only coupling to the plasma model is in the production rate of various species. Such models have been successfully used to model the Martian plasma environment far from the inner boundary [e.g. Ma et al., 2004b, Brecht and Ledvina, 2012, Harnett and Winglee, 2006, Najib et al., 2011, Riousset et al., 2013, Modolo et al., 2006]. One-dimensional models can also be motivated via neutral model simulations [e.g. Bougher et al., 2000] or observations [e.g. Mahaffy et al., 2015], and can also include the effects of chemistry, both hot and cold components, and a sputtered exosphere/corona. Figure 2.1 depicts the altitude profiles for a typical 1-D neutral background at Mars.

Due to the spatial and temporal variability of the neutral atmosphere, many global plasma models have begun to include a one-way coupling from a three dimensional neutral model. Three-dimensional neutral atmosphere models [e.g. Bougher et al., 2000, 2009] self-consistently solve for time-dependent neutral-ion densities, neutral temperatures, and neutral winds. These values can then be interpolated onto the overlapping portion of the plasma model and then analytically extended over the rest of the domain [see e.g. Dong et al., 2014]. Including a bi-directional coupling where the plasma model feeds back onto the neutral model is beyond current computational feasibility [Kallio et al., 2011].

In addition to the production of ions, the neutral background can affect the ionosphere

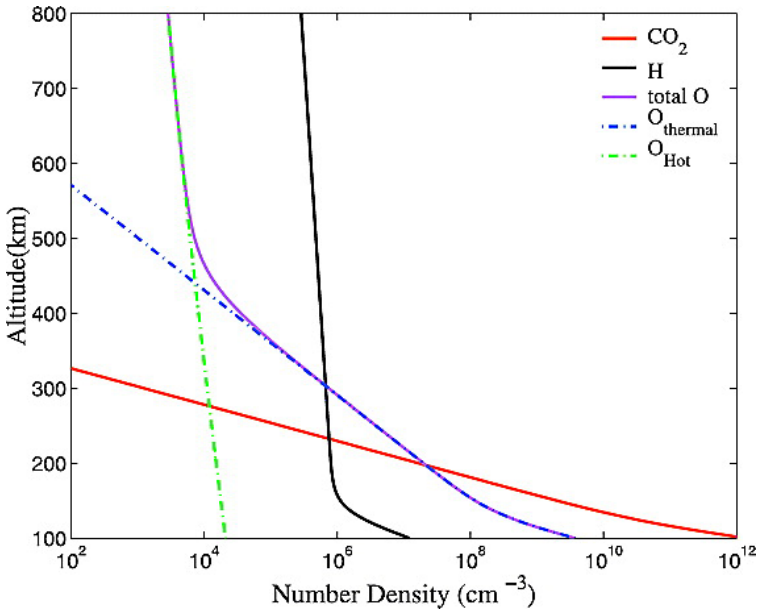

Figure 2.1: 1-D neutral atmosphere for solar minimum conditions at Mars [Ma et al., 2004b]

through ion-neutral drag. This can be implemented in multi-species MHD or Hybrid models by combining the ion-neutral collisional cross section with the velocity difference between the ions and neutrals; the exact formulation of this term is model dependent.

2.2.2 Ionosphere

Accurate simulation of the ionosphere within a global magnetosphere model has many of the same challenges as the neutral atmosphere. The typical scale size of the ionosphere is the scale height of the heaviest species; this is much smaller than the simulation domain required to simulate the entire magnetosphere. Chemistry also plays an important role in the production and loss of ionospheric species. Finally, any variability in the neutral atmosphere as driven by winds or waves also impacts the ionospheric variability.

The simplest method of treating the ionosphere is to introduce a hard lower boundary around the exobase and define a background density (for MHD models) or ion production rate (for hybrid models). While these models can be used to model the greater magnetosphere region and compare favorably with in-situ data [Kallio et al., 2006, Jarvinen et al., 2018], they are not self-consistent and rely on tunable parameters that influence resulting escape rates [Jarvinen et al., 2009]. This method can be extended by defining a region over which to produce ions or define a background density, rather than a simple spherical boundary.

A second option is to use a secondary model to define the conditions at the lower boundary. Here the complexity comes from treating the coupling of the models; each model will have different relevant time and spatial scales and there is a substantial region where their influences overlap. Many implementations simplify the coupling by treating it as uni-directional.

Finally, some models treat the ionosphere by varying grid-spacing and time-stepping and solving a limited selection of chemical reactions on a subset of the overall grid. This method is used by both MHD [Ma et al., 2014] and Hybrid [Brecht et al., 2016] models; however, even such sophisticated methods do not fully treat the ionosphere in all its complexity.

2.2.3 Magnetic Field

For both magnetized and unmagnetized planets, a choice must be made at the lower boundary for the behavior of the magnetic field. For unmagnetized planets, there is a distinction between the interaction of the IMF and a planet with or without a substantial ionosphere, as described in Chapter 1.1.3. For a planet like Mars or Venus the IMF drapes around the planet due to the conducting ionosphere, which is numerically implemented as a superconducting shell at some altitude. This shell enforces a zero magnetic field normal to the shell, and thus infinite conductivity of the shell itself. Actual ionospheres have finite conductivity; however, it is high enough such that diffusion of the magnetic field on the time-scale of the simulations is negligible [Opgenoorth et al., 2010, Riousset et al., 2014]. For magnetized planets a minimum magnetic field value is enforced at the boundary. This is also the approach for planets like Mars where remnant crustal fields are present; spherical harmonic models of the distribution of crustal fields [Arkani-Hamed, 2004, Cain et al., 2003] are used to set the magnetic field of the boundary.

2.3 Stellar Driving

Stellar driving can be broken into two main components: the radiation energy from the stellar spectrum and the mechanical energy from the stellar wind. The impact of the radiative energy is to ionize and heat the neutral background, producing the ionosphere. Meanwhile the mechanical energy creates the dynamic interaction of the planet and the stellar wind. Both the stellar wind and stellar spectrum change on both short and long time scale due to stellar variability. Furthermore, the properties of the star (e.g. age, stellar type) critically affect the resulting spectra and winds.

To first order the stellar wind can be described by the Parker model of the solar wind and magnetic spiral. A Parker wind is one-dimensional solution for the radial expansion of a corona driven wind with pressure going to zero at infinity. A solution for this system is given by

$$\left(\frac{u^2}{u_c^2} - 1\right) - \ln \frac{u^2}{u_c^2} = 4 \ln \frac{r}{r_c} + 4 \left(\frac{r_c}{r} - 1\right) \tag{2.13}$$

where r_c is the critical radius where the wind becomes super-sonic, u is the radial velocity, and u_c is the coronal sound speed, or $u_c = 2T_c/m_p$. From conservation of mass, the density of the stellar wind decreases as r^2 at large distances. The interplanetary magnetic field (IMF) can be approximated by assuming a steady-state configuration where the stellar gravitation and the acceleration of the solar wind flux can be neglected beyond some distance b, the tangential velocity is given by the rate of stellar rotation Ω, and the magnetic field lines are frozen into the plasma. Then the magnetic field streamlines in the ecliptic plane can be given by

$$\frac{r}{b} - 1 - \ln\frac{r}{b} = \frac{u_{sw}}{\Omega b}(\phi - \phi_0) \tag{2.14}$$

where u_{sw} is the velocity of the stellar wind.

Despite these simple approximations, the actual solar wind is highly variably on many scales in both space and time. These variations can be small rotations in the IMF, density, or speed, or large events due to coronal mass ejections (CMEs) or stellar flares. Stellar outflows can be modelled using stellar wind reconstruction models [e.g. van der Holst et al., 2014]; however, these become increasingly uncertain at large distances from the star or long times from a measurement and require careful observation of the solar corona.

Despite the near constant variability in the solar wind, planetary plasma models are typically run using constant upstream stellar wind conditions. Typically the velocity, density, temperature, and IMF are all specified at one end of the simulation domain. This produces good agreement with in-situ observations at times where the solar wind is relatively steady [Kallio et al., 2006, Jarvinen et al., 2018, Egan et al., 2018, Ma et al., 2015]. Time-dependent studies of CMEs have also been performed to understand the impact of these events on the planetary plasma environment [Dong et al., 2015a, Ma et al., 2017, Romanelli et al., 2018].

Chapter 3

Model Challenge

This chapter has been published in its entirety as "Egan, H., Ma, Y., Dong, C., Modolo, R., Jarvinen, R., Bougher, S., et al. (2018). Comparison of global Martian plasma models in the context of MAVEN observations. Journal of Geophysical Research: Space Physics, 123, 3714 3726."

Abstract: Global models of the interaction of the solar wind with the Martian upper atmosphere have proved to be valuable tools for investigating both the escape to space of the Martian atmosphere and the physical processes controlling this complex interaction. The many models currently in use employ different physical assumptions, but it can be difficult to directly compare the effectiveness of the models since they are rarely run for the same input conditions. Here we present the results of a model comparison activity, where five global models (singlefluid MHD, multifluid MHD, multifluid electron pressure MHD, and two hybrid models) were run for identical conditions corresponding to a single orbit of observations from the Mars Atmosphere and Volatile EvolutioN (MAVEN) spacecraft. We find that lowaltitude ion densities are very similar across all models and are comparable to MAVEN ion density measurements from periapsis. Plasma boundaries appear generally symmetric in all models and vary only slightly in extent. Despite these similarities there are clear morphological differences in ion behavior in other regions such as the tail and southern hemisphere. These differences are observable in ion escape loss maps and are necessary to understand in order to accurately use models in aiding our understanding of the Martian plasma environment.

3.1 Introduction

Mars presents a richly complicated and time variable obstacle to the solar wind, consisting of both a conducting ionosphere and localized crustal magnetic fields, but no global dipole field. The interaction region between the undisturbed solar wind and the lower ionosphere hosts a wide variety of physical processes and plays an important role in the energization of planetary particles, atmospheric escape, and upper atmospheric phenomena such as aurora.

Computer models can greatly assist our understanding of these physical processes when used in conjunction with data. The first models of Martian gas dynamics were Spreiter et al. [1970] and Dryer and Heckman [1967]. Since then the number of models capable of simulating the Martian magnetosphere has proliferated greatly, and now includes a variety of MHD [Ma et al., 2015, Dong et al., 2015, Najib et al., 2011a, Terada et al., 2009a, Harnett and Winglee, 2007], Hybrid [Brecht et al., 2016, Kallio and Janhunen, 2002, Boesswetter et al., 2010, Modolo et al., 2016], and test particle [Cravens et al., 2002, Fang et al., 2008a, Liemohn et al., 2013] models.

These models have been used to understand an extensive array of Martian plasma processes and interactions. Plasma boundaries [Najib et al., 2011a, Bertucci et al., 2005, Bößwetter et al., 2004], spatial ion distribution [Kallio and Barabash, 2012b, Najib et al., 2011a], ion escape [Brecht et al., 2016, Brecht and Ledvina, 2014, Dong et al., 2015c, Kallio et al., 2006b, 2010, Fang et al., 2010], magnetic topology [Liemohn et al., 2006] energetic neutral atoms (ENAs) [Kallio et al., 2006a, Gunell et al., 2006, Wang et al., 2016, 2014], and X-ray emission [Gunell et al., 2004] have all been studied using Martian plasma models. Transient processes including CMEs [Ma et al., 2017, Dong et al., 2015a], changes in dynamic pressure [Ma et al., 2014], changes in solar EUV flux [Modolo et al., 2006, Modolo et al., 2005b], seasonal variation [Dong et al., 2015], and crustal field rotation [Ma et al., 2014, Fang et al., 2015a] have also been topics of study. Long term Martian evolution has also been examined through estimation of early conditions and the corresponding escape rates [Terada et al., 2009a].

The wide variety of models presents a unique challenge in cross-validation of results. In

addition to different implementations and numerical methods, each model type makes different implicit physical assumptions. This means that the study of a particular plasma process may be more or less valid with the use of a particular model. The strengths and weaknesses of various models have been discussed previously in the literature [Ledvina et al., 2008]. Directly comparing model results provides a complementary approach to the aforementioned discussion, to determine how the fundamental differences affect the interpretation of simulations.

Here we perform a model comparison challenge where we run a variety of models with the same input conditions to understand the strengths and weaknesses of each one. Running a model challenge allows the comparison across a variety of model types in a one-to-one manner and isolates the effects of different physics from the effects of the input conditions.

Model challenges are a commonly used tool across a variety of disciplines (e.g. Kim et al. [2016], Hurrell [1995]). Within the Martian modelling community, one such model challenge has previously been performed [Brain et al., 2010]; however, substantial model development has occurred in the interim, and it is useful to provide an updated effort and expand the types of analysis performed. Here we evaluate different quantities, beyond boundaries and global escape rates. Additionally we compare to Mars Atmospheric Volatile EvolutioN (**Maven**) [Jakosky et al., 2015a] data from a single orbit with upstream conditions that correspond to our model inputs. This provides a baseline measurement for comparison in the region of the spacecraft orbit. In particular, **Maven** adds critical information due to its simultaneous measurements of particles and fields.

In this paper we report the results from such a model comparison challenge. We identified a suitable **Maven** orbit, extracted the upstream solar wind drivers, and ran a variety of models using nearly identical input conditions. In Section 3.2 we describe the input conditions and codes. Our results are shown in Section 3.3, where we focus on the plasma boundaries (3.3.1), low altitude ion behaviour (3.3.2), southern hemisphere (3.3.3), and global escape (3.3.4). We conclude with a discussion and summary in Section 3.4, as well as brief projection of our future work.

3.2 Methods

3.2.1 Orbit

This model challenge was designed such that the results can be compared to data from a specific MAVEN orbit. The trajectory of the chosen orbit (#2349, 2015/12/14) is depicted in Fig. 3.1. The coordinates are labeled in the Mars Solar Orbital (MSO) coordinate system; $+\vec{x}$ is the direction from Mars to the sun, $+\vec{z}$ is perpendicular to the orbital plane of Mars, and $+\vec{y}$ is the completion of a right-handed coordinate system. This orbit is almost entirely in the terminator plane, with periapsis near dawn at the equator. The sub-solar longitude is 170°, indicating that the dominant crustal fields are on the dayside of the planet as the dominant crustal fields are centered around a geographic longitude of 180°.

Fig. 3.1 also shows data from the Solar Wind Electron Analyzer (SWEA) [Mitchell et al., 2016], Solar Wind Ion Analyzer (SWIA) [Halekas et al., 2015], Suprathermal and Thermal Ion Composition (STATIC) [McFadden et al., 2015], and the Magnetometer (MAG) [Connerney et al., 2015] rotated into MSO coordinates. **Maven** exits and enters the upstream solar wind at times 17:12 and 20:24 respectively. At times 17:30-18:30 both STATIC and SWIA show a group of highly energetic ions whose energy increases with altitude in the northern hemisphere, commonly refered to as the ion plume. Periapsis occurs around 18:43 where many heavy ions are measured. The outbound portion of the orbit shows another section of heavy ions from times 19:05-19:25. The model results for these regions will be explored in Section 3.3.

3.2.2 Upstream Boundary

The upstream boundary conditions (Table 3.1) were calculated from period of orbit #2349 **Maven** is in the upstream solar wind, and are listed in Table 3.1. These conditions are relatively moderate, not representing an extreme event, and are consistent between the inbound and outbound portion of the orbit. The interplanetary magnetic field (IMF) is almost entirely in the $+\vec{y}$ direction, perpendicular to the solar wind velocity.

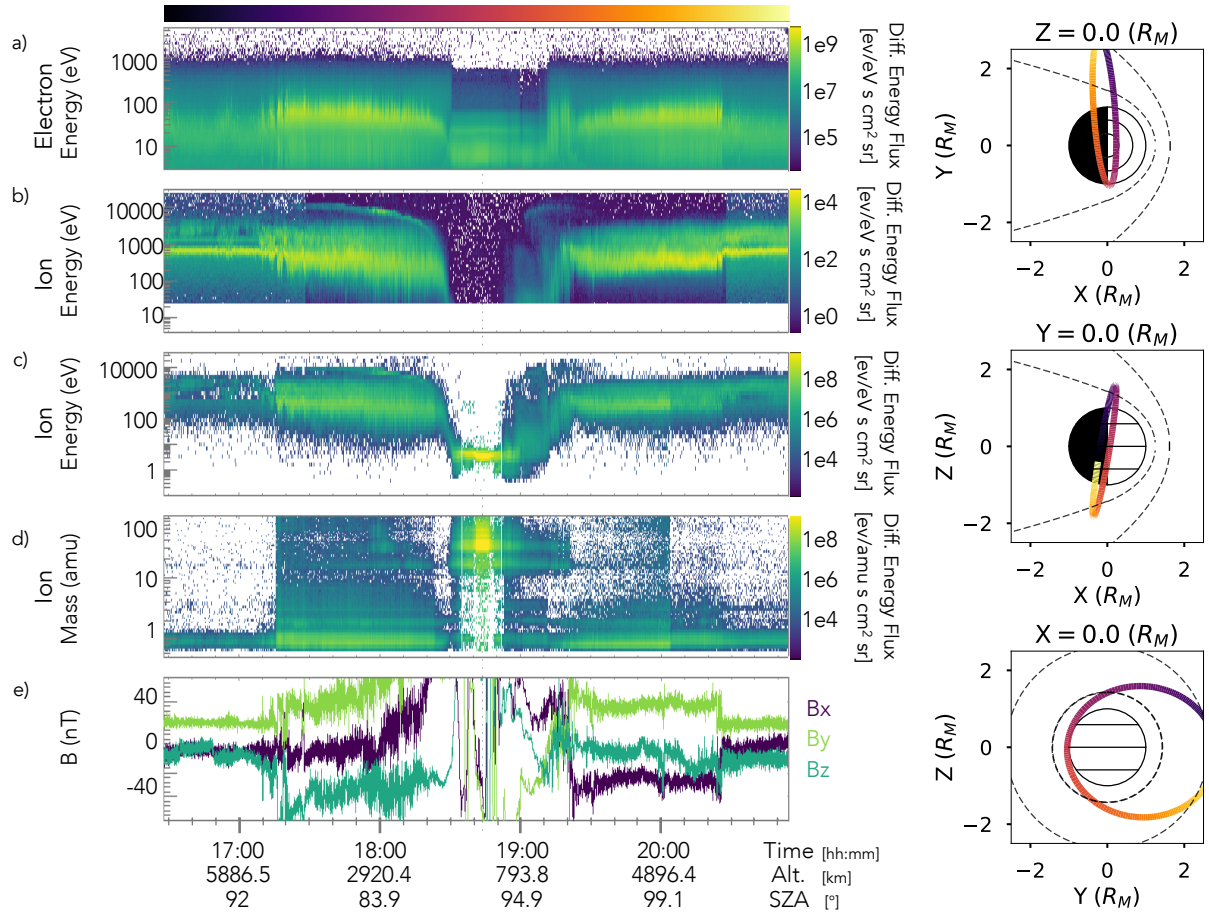

Figure 3.1: Trajectory and data from the **Maven** orbit (2349, 12/14/2015) that the upstream conditions are drawn from. **Left:** Panels show a) electron flux per energy as measured by SWEA, b) ion flux per energy as measured by SWIA, c) ion flux per energy as measured by STATIC, d) ion flux per mass as measured by STATIC, e) and magnetic field as measured by MAG. The x-axis is labeled by time, altitude, and Solar Zenith Angle (SZA). **Right:** Trajectory of **Maven** orbit in MSO coordinates. Empirical boundaries [Trotignon et al., 2006b] are plotted as dashed lines, and the color corresponds to the time bar on the left.

Table 3.1: Upstream conditions and derived parameters extracted from **Maven** data, used to drive the models. Here P_{dyn} is the dynamical pressure and v_A is the Alfven speed.

v	$[-350, 0, 0]$ km/s
n_p	4.9 cm^{-3}
n_α	0.14 cm^{-3}
T_p	59200 K
B	$[-0.74, 5.46, -0.97]$ nT
P_{dyn}	0.5 nPa
v_A	55 km/s

3.2.3 Models

As shown in Table 3.2, a wide variety of models were run for this model challenge, with different codes and underlying physical assumptions. Each model will be referred to by the tag given in the first column to minimize confusion between similar models. In this section we describe the models, some of the relevant implementation details, and any differences in the parameters used to run the simulations. Although multiple crustal field models were used, this will not cause a significant difference in the results.

3.2.3.1 MHD Models

The three magnetohydrodynamics (MHD) models were all run within the BATS-R-US (Block Adaptive-Tree Solar wind Roe-type Upwind Scheme) code [Ma et al., 2004a, Glocer et al., 2009b, Najib et al., 2011a]. The BATS-R-US platform has a non-uniform spherical grid to maximize resolution near the planet while minimizing computation time. The radial resolution varies from 10 to 600 km, and the angular resolution varies between 1.875 and 3.75. The simulated domain extends from -24 to +8 R_M (where R_M is the radius of Mars) in the x-direction, and -16 to +16 in the y and z directions. Local time stepping is utilized such that the time step can vary dynamically between cells while satisfying the Courant condition.

Within this platform, 3 separate simulations were performed with increasing complexity. The first, BATSRUS-MS [Ma et al., 2004a], is a multi-species run where ions H^+, O^+,O_2^+, and CO_2^+ were included and treated as a single fluid. This model solves a single momentum and energy equation but separate continuity equations for each species. BATSRUS-MF, the second model [Najib et al., 2011a], includes the same ion species but each each species is treated as a separate fluid with its own continuity and momentum equations. BATSRUS-MF+Pe [Ma et al., 2013a] includes the same ion species as independent fluids, and also solves an equation for the electron pressure analogous to the energy equation that dictates ion pressure (see details in Ma et al. [2011]), allowing the electron temperature to differ from the ion temperature.

For all three simulations the lower boundary of the code is set at 100 km above the planet, and the O^+, O_2^+, and CO_2^+ densities are set by the photo-equilibrium values. The velocity condition at the lower boundary is reflexive, leading to an approximately zero value. Crustal fields were included as modeled by Cain et al. [2003].

3.2.3.2 Hybrid Models

The two hybrid simulations were run using two different codes: HELIOSARES [Modolo et al., 2016], and RHybrid [Jarvinen and Sandroos, 2013]. As hybrid codes they both treat ions

	Model type	Crustal Fields	Highest Resolution (km)	Inner Boundary (km)
BATSRUS-MS [(1)]	MHD	Yes	10	100
BATSRUS-MF [(2)]	MHD	Yes	10	100
BATSRUS-MF+PE [(3)]	MHD	Yes	10	100
HELIOSARES [(4)]	Hybrid	Yes	60	110
RHybrid [(5)]	Hybrid	No	113	300

Table 3.2: A summary of the models used in this model challenge along with some of the relevant parameters. (1) Ma et al. [2004a], (2) Najib et al. [2011a], (3) Ma et al. [2013a], (4) Modolo et al. [2016], (5) Jarvinen and Sandroos [2013]

as macroparticles that evolve kinetically according to the Lorentz force, while the electrons are implemented as a charge neutralizing fluid. A macroparticle does not represent a single physical particle, rather a group of particles with a given density and the same properties. Fields are advanced by accumulating particle moments according to macroparticle shape functions onto a grid using a cloud-in-cell technique and then solving the magnetic and electric field equations accordingly. In order to improve particle statistics, multiple independent time steps were averaged together to create the datasets that were analysed here. Both models include planetary H^+, O^+, and O_2^+, He^{++}, and H^+. Although CO_2+ is included in the HELIOSARES simulation, due to the limited resolution compared to the ion scale height it is not included in further analysis. The RHybrid model does not include CO_2+.

This HELIOSARES run uses a cartesian grid with a resolution of 60 km, and a lower boundary at 110 km, and bounds $X = [-2.7R_M, 2.1R_M]$, $Y, Z = \pm 4.7R_M$. Crustal fields are included via the Cain et al. [2003] model. HELIOSARES also implements a particle splitting technique to limit numerical noise that results from having large particles; when a macroparticle with a statisical weight ≥ 3 times the solar wind density exceeds 700 km in altitude, it is split into two child particles with the same velocity and half the statistical weight. Solar wind and ionospheric electrons are modelled as two separate fluids, with densities set by the solar wind ion density and ionospheric ion density respectively. The solar wind electron population is assumed to be adiabatic with polytropic index $\gamma_{sw} = 5/3$, while the ionospheric population follows a polytropic equation varying smoothly between isobaric and adiabatic as $\gamma_{ion} = a(1 + (a/\gamma_{sw})^4)^{-1/4}$ where $a = (\log(n_e))^{-1}$ and n_e is the ionospheric electron density.

To initialize the simulation, ion macroparticles are loaded to match ionspheric profiles computed assuming photo-equilibrium. For the first 2500 timesteps, planetary ion motion is inhibited to allow a bow shock to develop before direct interaction of the solar wind with the ionosphere. Additionally, this HELIOSARES run was simulated using a different thermosphere, exoshere, and photoionization rates than are discussed in Section 3.2.4. Full 3D models for the exosphere and thermosphere generated for solar median, LS=90 using LMD-MGCM (Laboratoire de Météorologie

Dynamique Martian General Circulation Model) [González-Galindo et al., 2007] were utilized. Although they are not identical to the models used for the rest of the simulations, they are similar when averaged radially and should not greatly affect the presented results. The photoproduction is based on the EUVAC (EUV model for Aeronomic Calculations) model [Richards et al., 1994], which takes into account 27 wavelength groups, combine with the ionization and absorption cross sections for each species from Schunk and Nagy [2000]. The computed photoionization frequencies are similar, with less than 20% difference from the other models.

This RHybrid run uses a cartesian grid with a resolution of 113 km, bounds $X, Y, Z = \pm 4 R_M$, and does not include crustal fields. Resistivity and electron velocity are set as zero at the altitude of 300 km and below. All ions are absorbed and removed from the simulation at the altitude of 200 km and below. Ionospheric O^+ and O_2^+ ions are emitted upwards from a spherical shell at 400 km with the temperature of 2×10^4 K. The emission has a maximum flux at noon and cos(SZA) (Solar Zenith Angle) dependence towards terminator where the flux reaches 10% of the noon value and is constant for the nightside. Total ionospheric emission rates are $1.4 \times 10^{25} s^{-1}$ for O^+ and $2 \times 10^{25} s^{-1}$ for O_2^+. Photoionization of the exospheric monatomic oxygen and hydrogen neutral coronas are included at the altitude of 400 km and above in the dayside. The total photoionization rate in the simulation domain is $2.15 \times 10^{24} s^{-1}$ for hydrogen and $2.67 \times 10^{23} s^{-1}$ for monatomic oxygen. The exospheric neutral profiles and ionospheric emission rates are the same as in earlier studies such as Brain et al. [2010], Kallio et al. [2010], Jarvinen et al. [2016b].

Details of the numerical algorithm used by RHybrid are described by Kallio and Janhunen [2003] with the following exceptions. In RHybrid the electron velocity is determined directly at grid cell nodes, which means no cell volume average to node interpolation is needed. The electric current density is evaluated at the edges of the grid cell faces instead of the grid cell nodes [Pohjola and Kallio, 2010]. Further, no ion macroparticle cloud splitting and joining nor adaptive mesh refinements are used in RHybrid.

3.2.4 Inner Boundary

For all models except HELIOSARES, a 3D neutral atmosphere and 1D exosphere were used. The 3D neutral atmosphere was computed using the Mars Global Ionosphere-Thermosphere Model (MGITM) [Bougher et al., 2015] for subsolar latitude of 90 at moderate EUV (F10.7=130). MGITM uses Martian physical parameters, ion-neutral chemistry, and radiative processes in order to simulate the dynamical structure of the Mars from the surface to the exosphere. The exosphere is implemented via 1D profiles for hydrogen and oxygen, with oxygen containing both a hot and cold component. Photoionization rates were also calculated using MGITM, and the additional rate coefficients were set from Schunk and Nagy [2000].

3.3 Results

3.3.1 Boundaries

The interaction of the solar wind with the Martian plasma environment produces several boundaries and transitions within the plasma, including the bow shock, the Magnetic Pileup Boundary (MPB) due to the pileup of the IMF as it drapes around the planet, and the Induced Magnetosphere Boundary (IMB) marked by a transition from solar wind to planetary plasma [Nagy et al., 2004b]. here has been some discussion that has found to the MPB and IMB to be coincident; however, here we just consider the MPB.

Fig. 3.2 shows slices of H^+, O^+, and magnetic field magnitude in the Y=0 and Z=0 planes for each model. Overplotted in white are the locations of the empirical bow shock and MPB boundaries [Trotignon et al., 2006b].

Each model well predicts the magnetic standoff distance and the position of the bow shock along the Mars-Sun line. Along the wings of the bow shock the H^+ and magnetic field magnitude slices show that all the BATSRUS models show a more extended shock region than the conic fits, while both hybrid models show a more compressed shock region. The shock boundary in all of the models is symmetric with respect to Y and Z except in HELIOSARES, which shows some

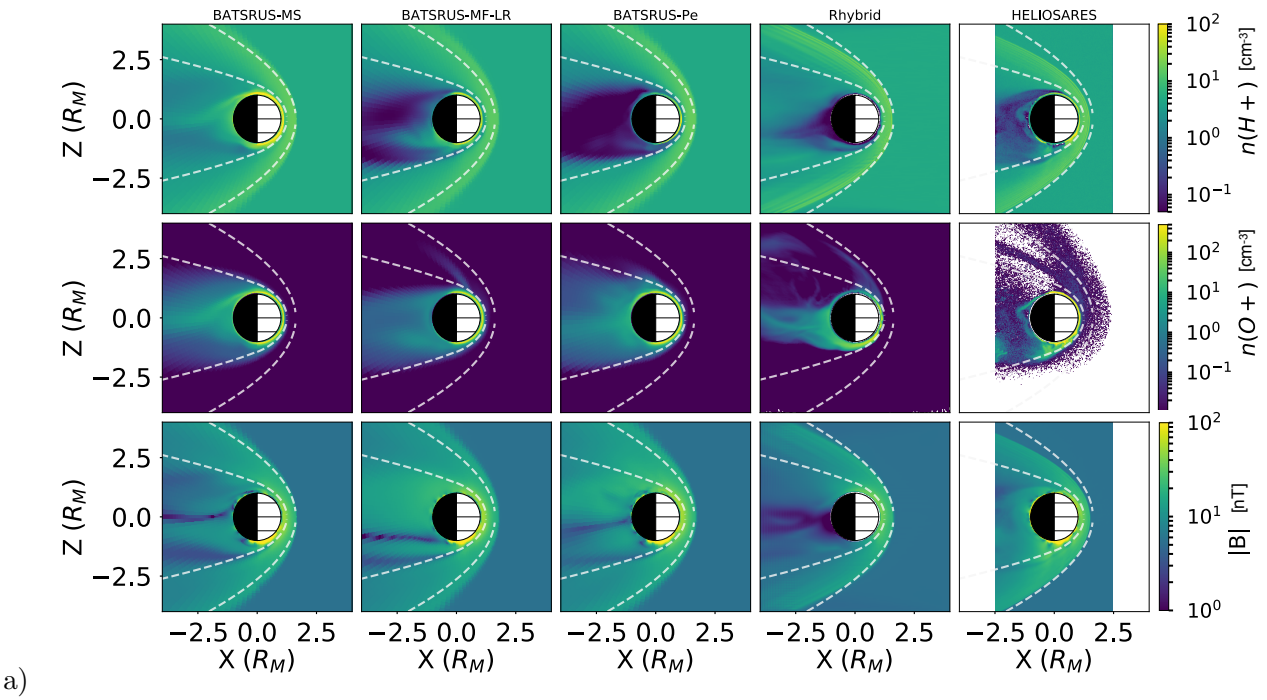

a)

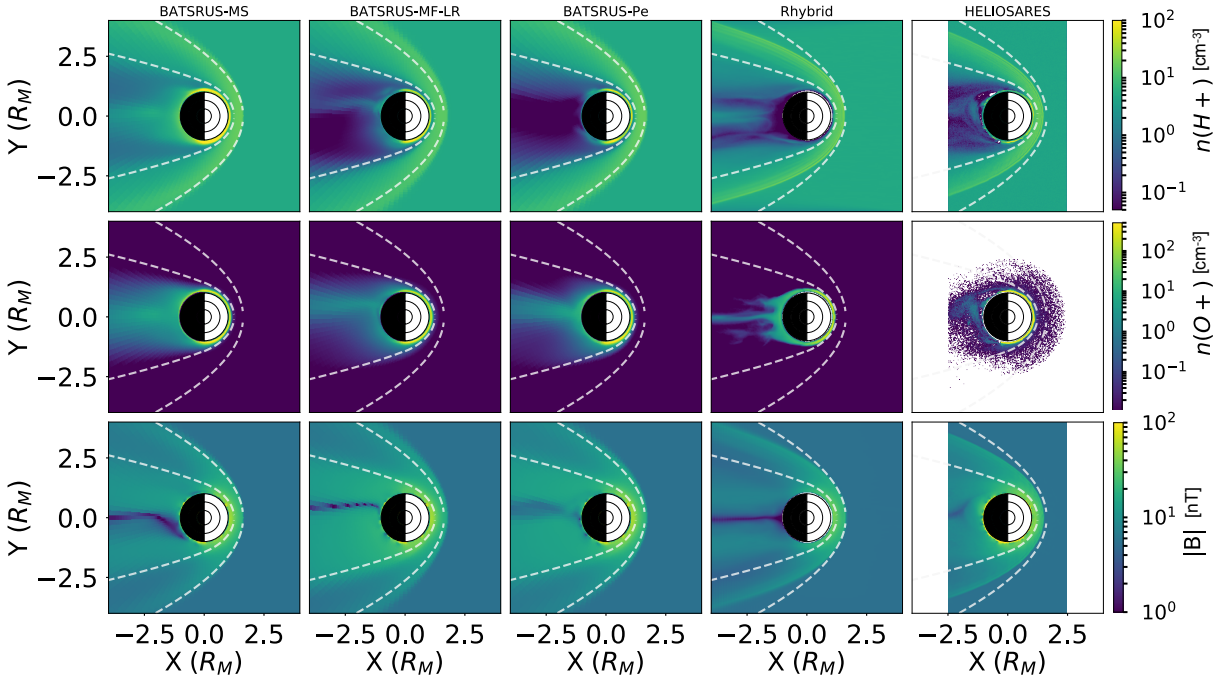

b)

Figure 3.2: Slices in the XZ (**top**) and XY (**bottom**) planes. From top to bottom the rows show H^+ number density, O^+ number density, and magnetic field magnitude. The columns indicate the model, from left to right: BATSRUS-MS, BATSRUS-MF, BATSRUS-MF+Pe, RHybrid, HELIOSARES. The empty space in the HELIOSARES data occurs because a slightly smaller domain is simulated while the plotting limits are kept constant. Each column uses identical color space limits.

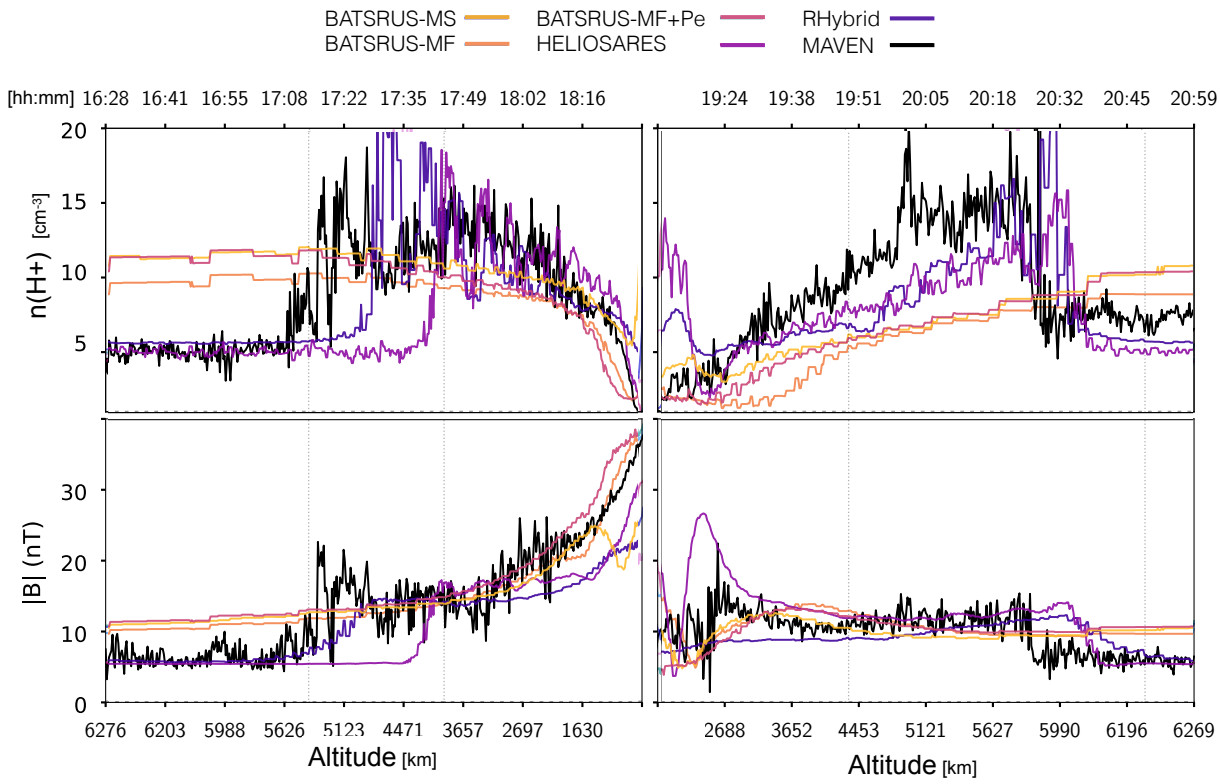

Figure 3.3: Flythrough of model results of the inbound and outbound portion of the orbit (#2349, 12/14/15) excluding periapsis with corresponding **Maven** data. Panels show H^+ number density and magnetic field magnitude. The location at which the orbit passes through the analytic boundary locations [Trotignon et al., 2006b] for the bow shock and MPB/IMB are plotted as vertical dashed lines.

asymmetry with respect to Z, opposite the direction of the convection electric field. This general lack of asymmetry is driven by an almost entirely +y oriented IMF.

The asymmetry in HELIOSARES with respect to Z is likely driven by the motional electric field, which points inward in the $-\vec{z}$ hemisphere and outward in $+\vec{z}$ hemisphere, and electron pressure gradient. As described in Simon et al. [2007]

The transition to planetary plasma (depicted by O^+) along the subsolar line occurs simultaneously with the empirical boundary location for all models. In the X-Z plane (3.2a), the BATSRUS-MS and BATSRUS-Pe models show little asymmetry in O^+ number density and well reproduce the empirical boundary location, while BATSRUS-MF and HELIOSARES show strong Z asymmetry, and RHybrid only shows planetary plasma along the plume and current sheet outside the ionosphere. All models show very little asymmetry in the X-Y plane (3.2b).

Fig. 3.3 confirms the intuition gained with slices, but by flying through the models we are also able to compare with **Maven** data from this orbit. On the inbound portion of the orbit the **Maven** data show a bow shock at roughly the same location as the empirical boundary, but the outbound crossing happens lower in altitude than the empirical crossing. This indicates the presence of some some combination of asymmetry and time variability. As the shocked region is relatively extended in the MHD models, none of them show a bow shock crossing in this flythrough, instead **Maven**'s orbit encounters only modeled magnetosheath and lower. Thus, both the H^+ number density and the magnetic field magnitude appear to be larger than both the data and hybrid models the RHybrid and HELIOSARES models both show a clear shock crossing that is lower in altitude than the inbound **Maven** crossing, but very similar on the outbound crossing.

3.3.2 Low Altitude

Maven enters the ionosphere on Mars' northern hemisphere along the the terminator plane. Measurements in this region from the Neutral Gas and Ion Mass Spectrometer (NGIMS) [Mahaffy et al., 2015] are shown along with model results in Fig. 3.4. RHybrid is not shown here due to the absence of ionosphere in the run.

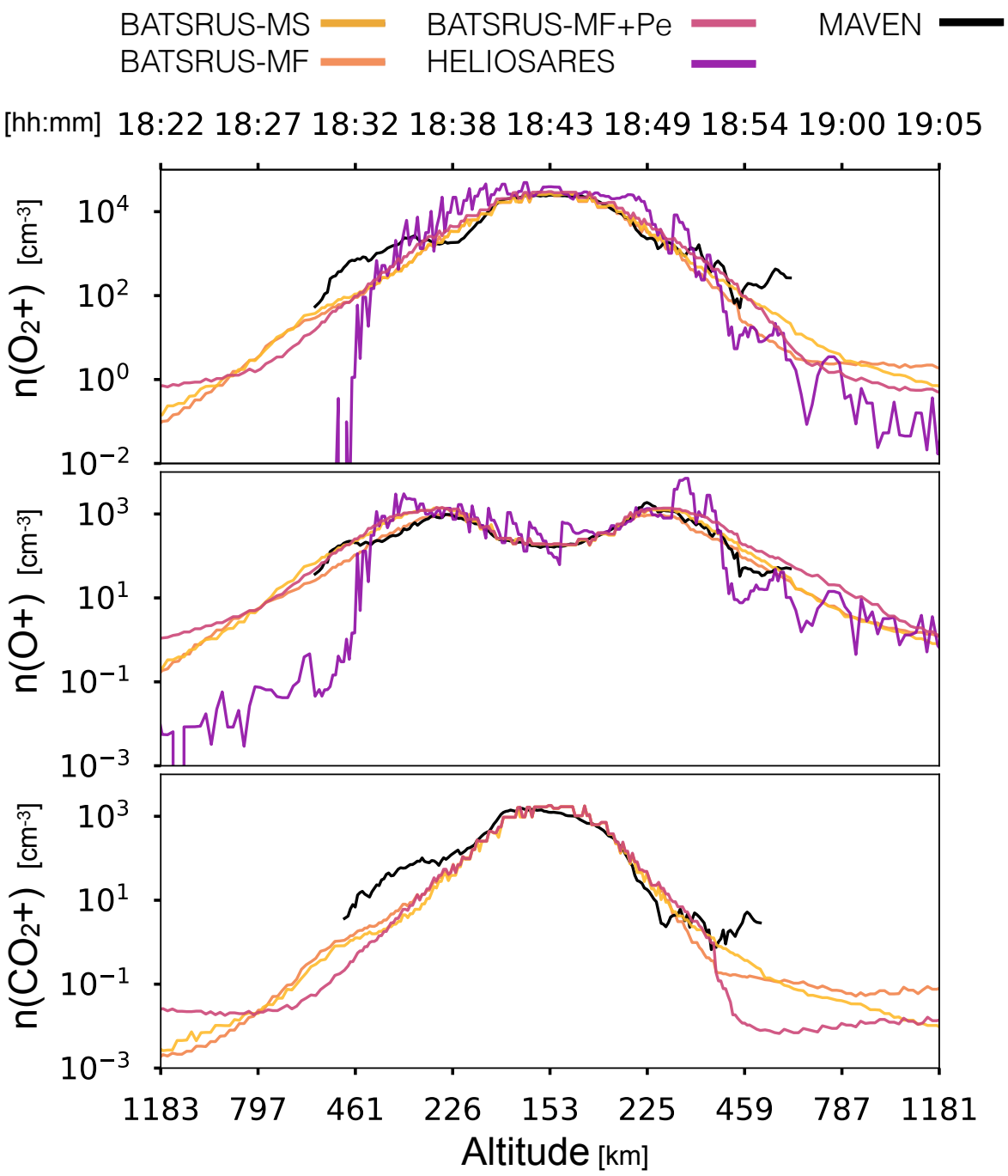

Figure 3.4: Flythrough of model results at low altitudes with corresponding **Maven** data from orbit #2349 (12/14/15). Panels show O_2^+, O^+, CO_2^+ number densities from top to bottom. RHybrid results are excluded due to the lack of ionosphere. No HELIOSARES results are shown for CO_2^+ because it was not included in the model.

At the lowest altitudes there is strong agreement across all models and data for O^+, O_2^+, and CO_2^+, indicating that the ion production physics is well represented in each model. Previous studies, including Ma et al. [2015] also found good agreement in ionospheric densities between data and models. The difference in shapes of the heavy ion profiles are indictative of different dominant heights. The relative steepness in decline with altitude between ions is and shape of the distributions are consistent with predicted scale heights. The jaggedness of the HELIOSARES profiles is due to the limited resolution of the grid that the ion macroparticles are deposited onto. The shallow drop off of the HELIOSARES densities on the outbound segment relative to the inbound segment is due to contributions from the southern hemisphere slow escaping ions (see Section 3.3.3).

For each ion, the inbound portion of the **Maven** data shows some excess number density relative to the to steep drop off shown by the models, likely due to time and spatial variability not captured by the models.

3.3.3 Southern Hemisphere

Cold ion escape likely plays an important role in heavy ion loss on Mars [Fränz et al., 2015, Dong et al., 2015c]. Here we discuss differences betwen the models in the southern (-z) hemisphere where an extended population of cold ions connects to the tail. This region of the tail is not affected by the northern pickup ions, which we will discuss in a future paper.

As shown in Fig. 3.5, all models show a region of planetary ions that extends from the southern hemisphere towards the tail. These ions are cold and have near zero bulk velocity. HELIOSARES shows slightly higher number densities than the BATSRUS and RHybrid models and the region extends farther in the -z direction.

Fig. 3.5 also shows vectors of the magnetic field. From this figure it is clear that the topology varies substantially in this region across the models. The top panel shows a draped field configuration in the BATSRUS and RHybrid models, while the field in the HELIOSARES model appears toroidal where the ion densities are highest. In the YZ plane (**middle panels**) the HELIOSARES model again appears toroidal in the tail, while the BATSRUS models all show

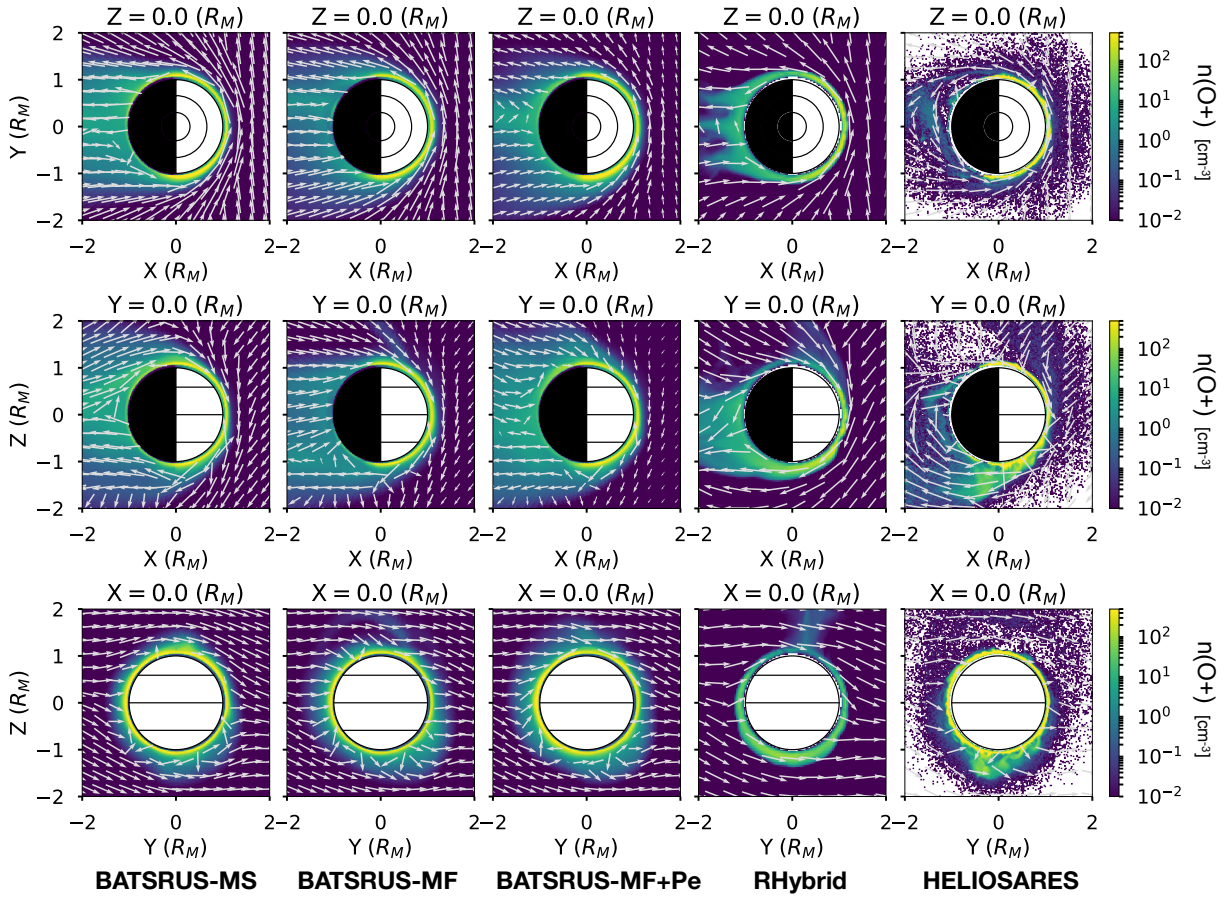

Figure 3.5: Slices of O^+ number density with magnetic field vectors overlaid. Panels show (top to bottom) planes $Z = -1.3R_M$, $Y = 0$, $X = 0$, and (left to right) simulations BATSRUS-MS, BATSRUS-MF, BATSRUS-MF+Pe, RHybrid, and HELIOSARES. All colorbars are consistent and labeled to the right.

magnetic field vectors predominately in the $\pm x$ direction.

From examining the field line topology in three dimensions the magnetic field in HELIOSARES appears coiled in the southern hemisphere, forming a channel for slow ion escape. This differs from the magnetic topology in BATSRUS which appears more like a basic current sheet model created by a draped IMF. These differences are likely related to differences in the obstacle boundary and conductivity.

3.3.4 Global Escape

One of the foremost areas of interest to the Martian community is the rate at which ions are lost to space, and the channels this escape proceeds through. Global ion escape has been measured [Lundin et al., 1989b, Barabash et al., 2007c], as has variance in escape with solar wind and EUV [Ramstad et al., 2015a], and variance with crustal fields [Ramstad et al., 2016a]; for full review of global ion escape at Mars see Dubinin et al. [2011]. Brain et al. [2015] has mapped the spatial distribution of inflowing and outflowing ion fluxes by averaging data across many orbits. Here we present similar maps to Brain et al. [2015] but of the entire system at a single instance in time as simulated by the models.

Fig. 3.6 shows maps of the modelled ion fluxes at $1.8R_M$ across latitude and longitude in the Mars-Solar-Electric field (MSE) coordinate system; $+\vec{x}$ is the direction from Mars to the sun, $+\vec{z}$ is along the upstream solar wind motional electric field, and $+\vec{y}$ is the completion of a right-handed coordinate system. The maps are created by defining a set of points in a spherical shell, equally spaced in five degree increments in latitude and longitude, and probing the net ion flux at each point in each model without averaging or interpolation.

On the dayside (centered on longitude = 0), all models have inbound heavy ion flux. In BATSRUS-MS this is symmetrical around latitude = 0 and longitude = 0. In the BATSRUS-MF, BATSRUS-MF+Pe, RHybrid, and HELIOSARES models the dayside inbound ion flux is confined to the southern hemisphere.

This symmetry breaking is related to the plume presence in the BATSRUS-MF, BATSRUS-

MF+Pe, RHybrid, and HELIOSARES models. The plume feature is seen as a dark blue (outbound flux) feature at high latitudes ($> 45°$ directly above the northern pole) centered around longitude $-30°$, and as a channel connecting to the tailward outbound flux centered at longitude $180°$. Furthermore, due to the limited number of heavy ions at large radii on the dayside, the H^+ dynamics dictate the ion flux for BATSRUS-MS.

All models except HELIOSARES show predominately outbound flux in the tail. RHybrid shows only outbound flux, while all the BATSRUS models have regions where ions are inflowing. These inflow regions are present in the same locations at lower altitudes (down to $1.1R_M$) but shrink at higher altitudes (out to $\sim 3.0R_M$). They are also correlated to the magnetic field vector at this point. This indicates that they are likely related to the dynamics of the current sheet and the presence of crustal fields, as only RHybrid does not include crustal fields. As the the dynamics of these regions are sensitive to tail plasma proccesses, crustal field implementation, and low altitude nightside ions, and our orbit does not probe this region, we leave further study to future work.

We find that the modelled maps are qualitatively similar to maps created from **Maven** data [Brain et al., 2015]. The dayside shows predominately inward flux, while the tail shows outward flux. Northern MSE latitude shows relatively more outward flux than the southern MSE latitude region. However, coverage of this space is still relatively incomplete due to the limited amount of **Maven** orbits there have been, so further conclusions and more detailed model-data comparison are not yet possible.

By summing across all latitude/longitude bins and weighting by area, global ion fluxes can be calculated for a given radius for each model. The rates for $R = 1.8R_M$ are shown in Table 3.3, along with observed rates calculated by Brain et al. [2015] and [Ramstad et al., 2015a]. A full comparison with all observed rates is beyond the scope of this paper, we just show Brain et al. [2015] for comparison with the escape maps and [Ramstad et al., 2015a] for a recent result calculated for comparable solar wind conditions. For a full comparison of ion escape rates at Mars, see Dubinin et al. [2011].

These results are very constant with radius for all models and are very similar for such a large

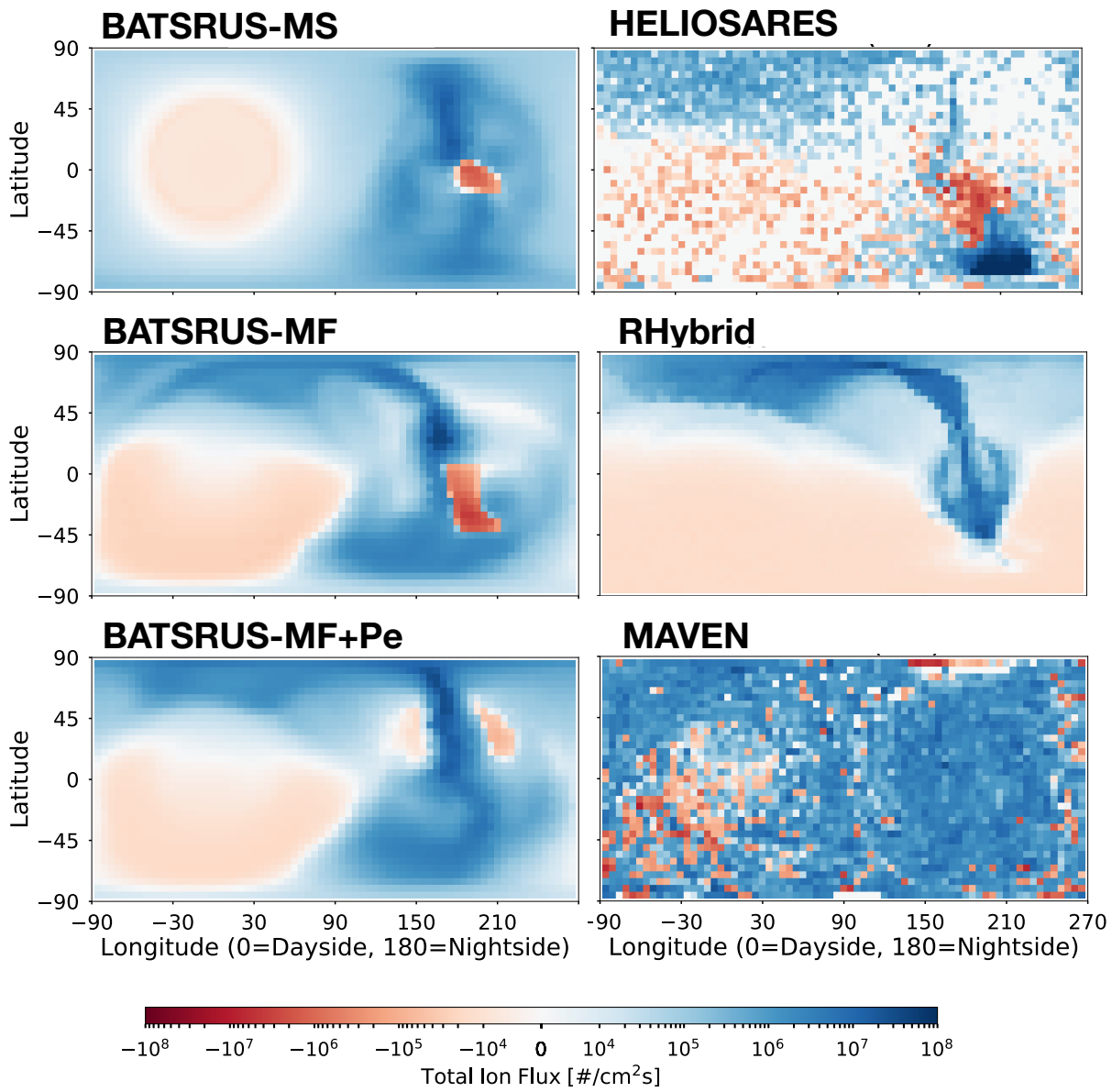

Figure 3.6: Total heavy ion flux maps for (Left to right, top to bottom) BATSRUS-MS, RHybrid, BATSRUS-MF+Pe, BATSRUS-MF+Pe, HELIOSARES, **Maven** data. Axes limits and colorbar are identical for each panel (except the **Maven** panel which is labeled separately), with blue indicating outward flux and red indicating inward flux. The map created from **Maven** data is adopted from [Brain et al., 2015].

Table 3.3: Calculated model escape rates in comparison with observed escape rates

Model/Survey	O^+ Flux	O_2^+ Flux	Total Flux
BATSRUS-MS	1.0	1.1	2.1
BATSRUS-MF	0.6	1.8	2.4
BATSRUS-MF+Pe	1.3	2.1	3.4
RHybrid	1.1	1.1	2.2
HELIOSARES	2.3	0.9	3.2
Brain et al. [2015]	-	-	1.6
Ramstad et al. [2015a]	-	-	2.1 ± 1.1

variation in escape maps. There is greater agreement between these rates than those calculated by Brain et al. [2010], indicating some level of convergence over time across models. These rates are also within a factor of three of those calculated by Brain et al. [2015], though those rates are for a wide variety of solar wind conditions and planetary orientation, and also include all heavy ion species. When compared to rates calculated by Ramstad et al. [2015a] for similar solar wind and EUV conditions our calculated rates are all within the appropriate range ($2.1 \pm 1.1 \times 10^{24} s^{-1}$).

3.4 Conclusion

Five models of the Martian magnetosphere have been run for nearly identical input conditions (aside from the small variations discussed in section 3.2); these models were then compared to each other and to **Maven** data. The input conditions were chosen to reflect the upstream drivers of **Maven** orbit #2349, an orbit chosen because the solar wind data is steady and typical, while the rest of the orbit probes other interesting regions. Model flythroughs along the orbit trajectory, slices through different regions, spherical ion flux maps, and global escape rates were obtained for each dataset.

Most models showed little boundary asymmetry due to the IMF being nearly completely in the $+\vec{y}$ direction. The overall extent of the shocked region was larger in the fluid models than both the empirical boundaries and the **Maven** results, while the hybrid models matched the outbound crossing very well.

From comparing NGIMS ion data to model flythroughs at low altitude it is clear that all models that have an inner boundary lower than $\sim$ 200 km do a good job modelling the low altitude day-side ions. Both overall normalization and scale heights are well recreated by all the BATSRUS models as well as HELIOSARES.

The outflow of cold ions in the southern hemisphere varied substantially across models. More study of the effects of lower boundary conditions and the impact they have on the magnetic topology and ion outflow in tail could impact ion escape estimates. However, although this outflow was much denser and more localized in the HELIOSARES model than the BATSRUS models, overall global escape rates were relatively constant.

Future efforts on this front are still necessary. This model challenge focused specifically on one orbit with a moderate solar wind and +y directed IMF. Changing input conditions will vary how the solar wind interacts with the ionosphere and likely how variations in model physics appear. Furthermore, we have limited our analysis to certain regions, and delayed comparison of the plume region for a future paper. More analysis and comparisons with data from additional **Maven** orbits will be necessary to probe other regions such as the tail.

Chapter 4

Stellar Influence

This chapter has been published in its entirety as "Hilary Egan, Riku Jarvinen, David Brain, Stellar influence on heavy ion escape from unmagnetized exoplanets, Monthly Notices of the Royal Astronomical Society, Volume 486, Issue 1, June 2019, Pages 12831291" and is reproduced here with minor changes.

Abstract: Planetary habitability is in part determined by the atmospheric evolution of a planet; one key component of such evolution is escape of heavy ions to space. Ion-loss processes are sensitive to the plasma environment of the planet, dictated by the stellar wind and stellar radiation. These conditions are likely to vary from what we observe in our own Solar system when considering a planet in the habitable zone around an M-dwarf. Here, we use a hybrid global plasma model to perform a systematic study of the changing plasma environment and ion escape as a function of stellar input conditions, which are designed to mimic those of potentially habitable planets orbiting M-dwarfs. We begin with a nominal case of a solar wind experienced at Mars today, and incrementally modify the interplanetary magnetic field orientation and strength, dynamic pressure, and Extreme Ultraviolet input. We find that both ion-loss morphology and overall rates vary significantly, and in cases where the stellar wind pressure was increased, the ion loss began to be diffusion or production limited with roughly half of all produced ions being lost. This limit implies that extreme care must be taken when extrapolating loss processes observed in the Solar system to extreme environments.

4.1 Introduction

Recent developments in exoplanet observation techniques have allowed the discovery of thousands of extra-solar planets, including dozens of small, rocky planets that are potentially habitable. The closest star to us, Proxima Centauri, hosts a planet with a minimum mass of 1.3 M_E [Anglada-Escudé et al., 2016], and the nearby Trappist system is home to seven transiting Earth sized planets, three or four of which are in the habitable zone (HZ) of the star [Gillon et al., 2017, 2016]. Analysis of the Kepler data has shown that planetary systems are common around M-dwarfs [Kopparapu, 2013], and these systems also show the best promise of observing exoplanet atmospheres [Shields et al., 2016].

As planetary atmospheres affect the surface temperature and prevent rapid water loss, atmospheric evolution of terrestrial planets around M-dwarfs is a topic of key importance. Atmospheric evolution can encompass a broad variety of processes, including volcanic out-gassing, sequestration, and loss to space. One component of loss to space is thermal loss, where particles with a thermal energy exceeding the escape velocity of the planet escape; however, heavier elements with higher escape velocities will have more difficult escaping thermally. Non-thermal processes, including those that act on ions, act to increase the energy available to a given particle and therefor provide additional paths to escape for heavy ions.

Non-thermal loss processes have been studied extensively for solar system planets including Earth [e.g Strangeway et al., 2005], Mars [e.g Lundin et al., 1989a, Barabash et al., 2007b, Brain et al., 2015], Venus [e.g NordströM et al., 2013, Barabash et al., 2007a], and Titan [Wahlund et al., 2005, Gurnett et al., 1982, e.g]. This loss takes a variety of observed forms including photo-chemical escape [Jakosky et al., 1994, Fox and Hać, 2009], charge exchange [Chamberlain, 1977], sputtering [Jakosky et al., 1994, Lammer and Bauer, 1993, Leblanc and Johnson, 2001], ion pickup [Luhmann and Kozyra, 1991a], ion bulk escape [Brain et al., 2010], and the polar wind [Banks and Holzer, 1968, Yau et al., 2007].

Further understanding of ion loss from terrestrial solar system planets has been developed

using 3D global plasma models. These models are useful as they allow one to probe the state of the whole system and its drivers at once, rather than limited in situ observations from spacecraft. Plasma models such as magnetohydrodynamic (MHD) [e.g Kallio et al., 1998, Ma et al., 2002, 2013b, Terada et al., 2009], hybrid [e.g Brecht and Ferrante, 1991, Kallio and Janhunen, 2002, Terada et al., 2002, Modolo et al., 2005a, Simon and Motschmann, 2009, Jarvinen et al., 2009], and test particle/direct simulation Monte-Carlo (DSMC) methods [e.g Cravens et al., 2002, Fang et al., 2008, Luhmann et al., 2006], have all been used to understand ion escape in the context of the terrestrial planets.

Due to the relative abundance of planetary systems and constraints from the signal to noise ratio in most observing techniques, the most potentially observable planets that meet this criteria are found in the habitable zone around M-dwarfs. These environments are likely to be extreme due to the enhanced EUV [France et al., 2016] and the closer radius of the habitable zone relative to solar. Each of these factors is likely to have a distinct effect on the ion loss of the planet, and it is necessary to understand how they work in conjunction.

Using plasma simulations that have been validated in the solar system planetary context can add to understanding of ion loss in exoplanetary systems as well as young solar system planets [Johansson et al., 2011, Terada et al., 2009b, Boesswetter et al., 2010]. Exoplanets may differ from solar system planets in their intrinsic properties such as size, composition, or magnetic field, as well as the external conditions dictated by the interaction with the host star. Cohen et al. [2015] explore the influence of an M-dwarf star on a Venus-like planet in the habitable zone, concentrating on the impact the possible sub- and super-alfvenic stellar wind. Garcia-Sage et al. [2017] examine the influence of a magnetic field in the protection of a planet from atmospheric escape in the habitable zone of red dwarf Proxima Centauri using a 1D polar wind outflow model.

Here we explore the case of an unmagnetized planet orbiting in the habitable zone of a generalized M-dwarf system. Although magnetospheres are classically considered necessary to prevent solar wind erosion of atmospheres, this may not necessarily be the case. Estimates of ion escape from Mars, Venus, and Earth all show similar rates [Strangeway et al., 2005, Brain et al.,

2013], despite Earth's strong intrinsic magnetic field and the lack thereof at Mars and Venus. Thus it is still worth considering and very necessary to study the plasma environment and ion escape of unmagnetized planets.

Here we present a systematic study of the changing plasma environment and planetary ion escape as a function of stellar input conditions. The input conditions have been selected to incrementally change from typical solar wind today to the stellar wind at potentially habitable planets orbiting M-dwarfs. We begin with a base case of Mars today, and alter the interplanetary magnetic field (IMF) orientation, dynamic and magnetic pressure, and EUV flux. Section 4.2 describes the choices in stellar input conditions, Section 4.3 describes the model, Section 4.4 gives our results, Section 4.5 further discusses the limitations and implications of our results, and Section 4.6 summarizes our conclusions.

4.2 Stellar Parameters

Both the intrinsic stellar parameters and the habitable zone location drive differences in the stellar influence on terrestrial planet escaping atmospheres. Here we describe some of the general differences and motivate our selection of parameters. Our initial base case (R0), is the same as that studied by Egan et al. [2018], and is an example of a typical solar wind experienced by Mars. The final case (R4), is identical to the case considered for Trappist-g by Dong et al. [2018], where the stellar wind was reconstructed using the Alfven Wave Solar Model [van der Holst et al., 2014].

4.2.1 Quasi-Parallel IMF

For unmagnetized planets, much of the interaction with the solar wind is dictated by the direction of the IMF. Because ions are constrained to gyrate around magnetic fields, both solar particle inflow and planetary ion outflow will change due to the influence of the IMF. An interaction with the solar wind and unmagnetized planets (eg. Venus and Mars) is typically sketched with magnetic field lines roughly perpendicular to the direction of solar wind flow piling up around the induced ionosphere and then slipping past the planet. However, configurations where the magnetic

field is more aligned than perpendicular with the solar wind flow occur in the inner solar system due to the Parker spiral structure of the IMF and occur at exoplanets orbiting close to their host stars. Aligning the magnetic field with the solar wind flow will create regions where ions can flow directly away from the planet along field lines normal to the planet surface, dramatically changing the ionospheric interaction [Johansson et al., 2011, Liu et al., 2009, Zhang et al., 2009]. Furthermore, the radial magnetic field results in vanishing upstream convection electric field, which is the large-scale energy source for ion pickup [e.g. Jarvinen and Kallio, 2014].

Additionally, a shock is unstable when the angle between the magnetic field and the local shock normal $< 15°$ [Treumann and Jaroschek, 2008b,a]. A quasi-parallel magnetic field will satisfy this condition for an entire hemisphere of the bow shock, thus making the interaction quite different than the quasi-perpendicular IMF. Because quasi-parallel shocks do not form stable well-defined surfaces and can reflect ions in an extended foreshock region, kinetic effects associated with finite ion gyroradii and the ion velocity distribution become important [Treumann and Jaroschek, 2008b,a]. This makes hybrid models well-suited to simulating such an interaction.

As M-dwarfs are relatively dimmer than the Sun, the habitable zone must be correspondingly closer in. In addition to causing increased stellar fluxes, this will also likely lead to more radially oriented IMFs as expected from a Parker spiral model. MHD simulations of M-dwarf stellar winds such as Garraffo et al. [2017] also show radially oriented IMFs in the corresponding habitable zones. Although it is not universally true that all exoplanets in the HZ of an M-dwarf will experience a radial IMF, it is a significant departure from what the potentially habitable solar system planets (Venus, Earth, and Mars) experience so it is helpful to investigate its effects.

Here we consider a quasi-parallel magnetic field, with $\alpha = 18.2$ (R1), which in the context of the solar system is similar to the nominal Parker spiral angle at Mercury. Considering a perfectly radial field is both somewhat unlikely to the slight variability in both the solar wind and the IMF, and more difficult computationally due to instabilities in the ionospheric interaction and vanishing upstream convection electric field. Additionally, although the Parker spiral angle for the Trappist-1 exoplanets would be far less than the chosen value, this value is motivated by the solar wind

reconstruction model used by Dong et al. [2018].

This choice does, however, neglect the influence of the large orbital velocities these planets must have, which will be comparable to the stellar wind velocity. Thus the corresponding angle of the stellar wind as seen by the planet and the magnetic field will also change. The results we present here neglect this effect for ease in comparison of results, however, future work could study the influence of the planetary orbital velocities.

4.2.2 Solar Wind Strength

Solar wind momentum is key source of energy input into the planetary plasma environment. Observations of terrestrial planets have shown that ion loss is dependent on solar wind dynamic pressure [Ramstad et al., 2017, Brain et al., 2017].

It is not currently possible to measure the stellar wind of stars besides our Sun directly, so investigations into these effects rely on stellar wind reconstructions using MHD solar wind models [e.g. Vidotto et al., 2015, Garraffo et al., 2017].

The steady state stellar wind may vary extensively across a single orbit for a close in planet [Garraffo et al., 2017, 2016]. Furthermore, space weather may also increase variability. Previous models of exoplanet ion loss have investigated the steady state loss rates for two cases: maximum total pressure, and minimum total pressure [e.g. Dong et al., 2018], effectively varying the magnetosonic mach number.

Here we consider the scaling of stellar wind in two parts, increasing the overall pressure, and varying the ratio of magnetic to dynamic pressure. We first scale the overall pressure by a factor of roughly 4×10^3 (R2), and then increase the solar wind density by a factor of 100 (R3), decreasing the ratio of magnetic to dynamic pressure. This mimics an overall increase due to the increased flux expected for a closer habitable zone distance and then a possibly extreme dynamic pressure dominated scenario. While an actual planet ma33y experience extreme variation in stellar wind due to both orbital variation and the intrinsic variability of the wind, here we select two interesting cases for study.

4.2.3 EUV Input

Another critical component of the stellar interaction with a planetary atmosphere is the input in the UV and Extreme UV (EUV). In addition to photoionization of planetary neutrals, EUV photons are absorbed in the upper atmosphere leading to heating, and in some cases thermal driven hydrodynamic escape [Hunten et al., 1987]. In cases where heavy elements like Oxygen are gravitationally bound to the atmosphere, EUV input is still correlated with ion escape rates [Ramstad et al., 2017].

EUV flux will also increase due to the proximity of the habitable zone, similarly to the stellar wind flux. Furthermore, observations show that M-dwarfs have EUV fluxes of 10-1000 times that of solar [France et al., 2016]. Here we chose to scale I_{EUV} by a factor of 100 (R4). Although we do not directly simulate the stellar radiation environment, our overall ion production rate scales directly with I_{EUV}. For further description of this implementation see Section 4.3. While stellar activity may dominate the EUV flux experienced by the planet, we here examine a steady state case.

4.2.4 Summary of Models

Table 4.1 summarizes the stellar parameters used for our suite of simulations. Each simulation builds upon the changes of the last, such that R2 contains the same adjustments as R1, R3 contains the R2 and R1 adjustments and so on. We also list a variety of relevant plasma scales that further illustrate the differences and similarities between the models.

Stellar wind speed (u): Input speed of the incident stellar wind in the $-x$ direction.

Temperature (T): Temperature of the incident solar wind Hydrogen ions.

Number Density ($n(H_+)$): number density of the incident solar wind Hydrogen ions.

IMF (B): Incident stellar wind magnetic field vector, in PSE coordinates (described in Section 4.3).

Production Rate (Q): Total production rate for a given ion (described further in Section

Simulation	R0 : Nominal	R1 : Parallel-IMF	R2 : Total-Pressure	R3 : Density	R4 : EUV
u (km/s)	350	350	**604**	604	604
T (K)	5.91e4	5.91e4	**1.26e6**	1.26e6	1.26e6
$n(H^+)$ (cm^{-3})	4.85	4.85	**6.44e2**	**5.79e3**	5.79e3
B (nT)	[-0.74, 5.46, -0.97]	**[-5.31, 0.44, -1.51]**	**[-149, 13, -42]**	[-149, 13, -42]	[-149, 13, -42]
$Q(O^+)$ ($10^{25}/s$)	2	2	2	2	**200**
$Q(O_2{}^+)$ ($10^{25}/s$)	1.4	1.4	1.4	1.4	**140**
$\|B\|$ (nT)	5.59	5.59	**155**	155	155
α (°)	82.4	**18.2**	18.2	18.2	18.2
v_A (km/s)	55.3	55.3	**133**	**44.4**	44.4
M_A	6.3	6.3	**4.5**	**13.6**	13.6
P_B/P_{dyn}	0.02	0.02	0.02	**0.005**	0.005
$r(O^+)$ (km)	10364	**3266**	**203**	203	203
$r(O_2{}^+)$ (km)	20728	**6532**	**406**	406	406
$\bar{E}(O^+)$ (keV)	19.5	1.6	4.9	4.9	4.9
$\bar{E}(O_2{}^+)$ (keV)	38.9	3.2	9.8	9.8	9.8

Table 4.1: Parameters used to drive each simulation. Simulations are labelled R0 through R4. Parameters that are directly configured in the simulation are listed on top, while derived parameters are listed below. Numbers in **bold** are changed from the preceding simulation.

4.3).

IMF Angle (α): angle between the upstream stellar wind velocity and the IMF, smaller angle indicates a more parallel interaction.

Alfven Speed ($v_A = B/\sqrt{\mu_0 \rho}$, μ_0 := magnetic permitivity, ρ := density): Alfven speed in the incident solar wind

Alfven Mach Number ($M_A = u/v_A$): Determines the nature of the bow shock.

Magnetic to dynamic pressure ratio ($P_B/P_{dyn} = (B^2/2\mu_0)/(1/2\rho u^2)$): Ratio of the incident solar wind magnetic pressure and dynamic pressure, influences how the magnetic field lines drape around the planet.

Ion Gyroradius ($r = mv_\perp/qB$, $v_\perp$:= velocity component perpendicular to the magnetic field): dictates the radius at which an ion moving with the velocity of the upstream solar wind gyrates in the upstream magnetic field. This has an influence on the trajectory of escaping particles when the radius is comparable to the size of the planet (3390 km).

Ideal Gyro-Averaged Pickup Energy ($\bar{E} = 2(1/2m_i v_\perp)$) ideal energy of an ion gyrating in the solar wind averaged over a gyroperiod, see discussion in Jarvinen and Kallio [2014].

4.3 Methods

The following simulations were performed using RHybrid [Jarvinen and Sandroos, 2013], a hybrid global plasma model for planetary magnetospheres. In a hybrid model the ions are treated as macroparticle clouds that are evolved according to the Lorentz equation, while the electrons are treated as a charge neutralizing fluid. This allows the simulation to include ion kinetic effects which are important in situations where the ion gyroradius is large compared to the scale size of the system.

Each ion macroparticle represents a group of ions that have the same velocity (v_i), central position (x_i), charge (q_i), and mass (m_i) obeying the Lorentz force such that

$$m_i \frac{d\vec{v_i}}{dt} = q_i(\vec{E} + \vec{v_i} \times \vec{B}) \ , \tag{4.1}$$

where $\vec{E}$ and $\vec{B}$ are the electric and magnetic fields respectively. The electron charge density then follows from the quasi-neutral assumption when summed over all ion species.

The current density is calculated from the magnetic field via Ampere's Law

$$\vec{J} = \nabla \times \vec{B}/\mu_0 \,, \tag{4.2}$$

and the electric field can then be found using Ohm's law

$$\vec{E} = -\vec{U_e} \times \vec{B} + \eta \vec{J} \,, \tag{4.3}$$

, where the η is explicit resistivity profile used to add diffusion in the propagation of the magnetic field [Ledvina et al., 2008]. This value was chosen to be $\eta = 0.02\mu_0 \Delta x^2/\Delta t$, such that the magnetic diffusion time scale $\tau_D = \mu_0 L_B^2/\eta = 50\Delta t$, for the magnetic length scale $L_B \approxeq \Delta x$. This is a similar value as used in earlier work [Egan et al., 2018, Jarvinen and Sandroos, 2013], and ensures that the magnetic field diffuses on timescales longer than the timestep Δt. The explicit resistivity allows some diffusion to stabilize the numerical integration and is greater than the inherent numerical resistivity of the code for the chosen resolution. At the same time η is kept small enough to keep the solution from becoming smoothed out by diffusion. Note that the resistivity is not explicitly included in the Lorentz force.

Finally, the magnetic field is then propagated using Faraday's Law

$$\frac{\partial \vec{B}}{\partial t} = -\nabla \times \vec{E} \,. \tag{4.4}$$

See Jarvinen and Sandroos [2013] and references therein for details of the numerical scheme.

The lower boundary is located at 250 km altitude and is implemented as a super-conducting sphere. This mimics the effect of the electromagnetic properties of the induced magnetosphere.

In the RHybrid runs analyzed in this work the emission of ionospheric ions in the induced magnetosphere is implemented using a Chapman profile which arises naturally when considering an isothermal atmosphere that is ionized by plane-parallel, monochromatic radiation in the EUV

[Chapman and Zirin, 1957]. The production rate of ions is given by

$$q(\chi, z') = Q_0 \exp[1 - z' - \sec(\chi) * e^{-z'}] \,, \tag{4.5}$$

where z' is the normalized height parameter given by $z' = (z - z_0)/H$ where χ is the solar zenith angle, z_0 is the reference height, and H is the scale height. In each simulation we use a reference height of 300 km and a scale height of 16 km. We also add an additional constant ionization source behind the planet that is continuous across the terminator to mimic other ionization sources and prevent divergence caused by extremely low densities.

We note that this is not a self-consistent ionospheric model, merely a convenient way to inject ions with a reasonable distribution with altitude than is dependent on solar zenith angle. While the scale height is used to inject particles we are not modeling the ionospheric processes themselves, justifying the comparably large resolution. We discuss the impact of this choice in Section 4.5.

Each simulation is run on a 240^3 grid, with boundaries ± 4 RM in X, Y, and Z leading to an overall resolution of $\Delta x = 113$ km. Each simulation was run for 60,000 time steps with $\Delta t = 0.005$, or ~ 3 solar wind crossing times. The final results analyzed for this paper were averaged over several timesteps once the simulation reached steady state, in order to improve statistics in low particle density regions.

The coordinate system used to present results throughout this paper is Planet Stellar Electric (PSE) coordinate system. This planet-centered system is used so that despite varying the direction of the IMF, the corresponding direction of the motional electric field ($E_{SW} = -u \times B$) remains constant.The PSE coordinates are then defined such that $-\hat{x}$ is defined to be in the direction of the solar wind, $\hat{z}$ is the direction of the convection electric field, and $\hat{y}$ is the completion of a right handed coordinate system. The simulation runs were performed in the same coordinate system as in our earlier study [Egan et al., 2018], which is similar to the PSO (Planet Stellar Orbital) system. Transformation from PSO to PSE is a rotation around the X axis.

Much of the subsequent analysis was performed using the volumetric analysis package yt [Turk et al., 2011] and visualization system Paraview [Ayachit, 2015].

4.4 Results

4.4.1 Magnetic Field Morphology

As discussed in Section 4.2, the planetary interaction with the IMF and the resulting magnetic field configuration has key implications for ion escape. This intuition is confirmed in Figure 4.1 which shows magnetic field lines traced through each simulation domain with slices of $O_2{}^+$ number density.

The top two simulations in Figure 4.1 show the difference between the quasi-perpendicular (left) and quasi-parallel (right) IMF. While the magnetic field lines pile up symmetrically in the quasi-perpendicular run, the pile-up is only significant in the +y hemisphere in the quasi-parallel run. In the -y hemisphere the magnetic field is much more bent close to the planet, leading to an offset s-shaped current sheet behind the planet.

The location of the quasi-parallel shock determines where the magnetic field lines slip past the planet from their draped configuration to the current sheet. This location also corresponds to region where there is the greatest local curvature in the magnetic field close to the planet. While this region is symmetrically oriented over the +z pole in the R0 model, in the R1 model the region is offset towards the unstable shock side with the s-type current sheet.

Comparing simulations R1 and R2, the s-type current sheet becomes more extreme and the bend closer to the center of the planet gets much sharper. Additionally, some field lines that were clearly draped around the magnetic barrier in R1 appear to connect deeper in the magnetic barrier near the inner boundary (ionospheric obstacle) in R2. These differences are due to the much stronger magnetic field in the latter simulation. Because the magnetic field pressure is much stronger in the latter simulation it can more easily overcome the plasma pressure at low altitudes, embedding further field lines into the inner boundary. These field lines are thus less able to slip past the planet, extending the extent of the S-type current sheet. As the magnetic field lines are pushed much deeper in the ionospheric region this may make our results sensitive to the conditions at the lower boundary.

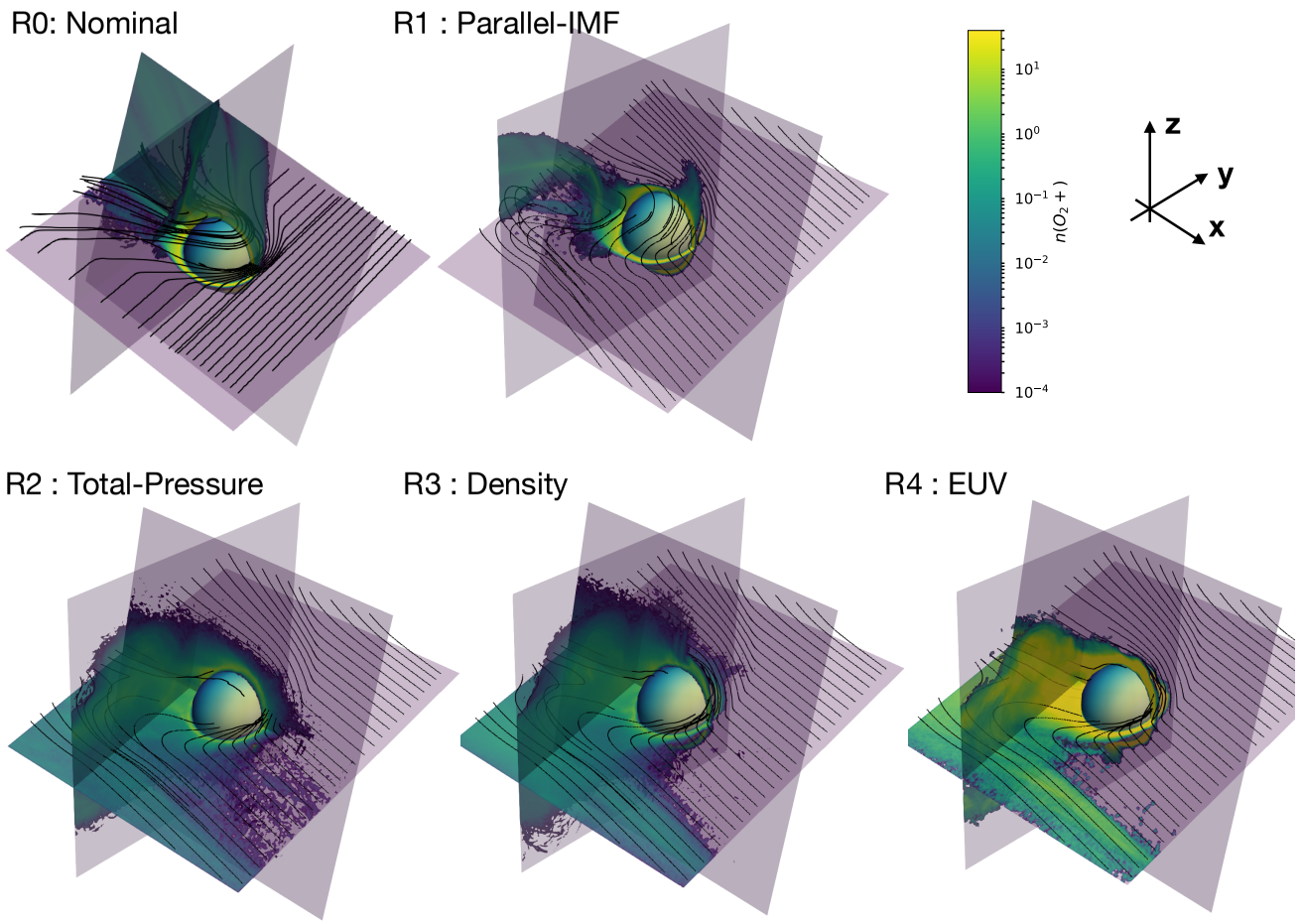

Figure 4.1: Each panel shows slices of $O_2{}^+$ number density in the Z= 0, X=-1, and Y=0 planes with magnetic field lines traced in white. Panels show simulation R0, R1, R2, R3, and R4 from left to right, top to bottom. Note that the planes are not exactly aligned in each simulation due to the changing angle between induced electric field and magnetic field.

Simulations R3 and R4 show similar magnetic field morphologies to R2, despite the increases in solar wind density and ionospheric production rates, respectively.

4.4.2 Ion Morphology

While overall ion loss rates are important for atmospheric evolution, this loss occurs through a variety of different processes, and it is important to understand the variation in each channel. Here we examine the overall ion morphology, and draw parallels to the ion escape channels seen at solar system objects and the different forces that govern the particle motion.

As discussed in section 4.4.1, changing the IMF orientation from quasi-perpendicular to quasi-parallel drives asymmetry in the solar wind access near the ionosphere. In addition to creating an S-type current sheet, this asymmetry makes one hemisphere of the bow shock unstable as shown in Figure 4.2, where slices of H^+ number density, H^+ velocity magnitude, and magnetic field magnitude are shown for each simulation. In each slice the solar wind flows from right to left, with the solar wind motional electric field normal to the plane.

The unstable bow shock is evident in each row; the upper half of the bow shock shows sharply delineated boundary, while the lower half is ill-defined. This allows solar wind approaches the planet at a much higher velocity in lower hemisphere. This not only drives more energy transfer to the ionosphere, but drives ion pickup due to the $v \times B$ force from this location. The instability always occurs on the hemisphere where the magnetic field vector relative to the normal becomes less that 15°.

Figure 4.3 shows slices of the ${O_2}^+$ and O^+ number density for each simulation in the YZ plane. Comparing the first two panels illustrates the effect of the s-shaped configuration of the induced magnetosphere; while R0 shows symmetric acceleration in the direction of the motional electric field, R1 shows ions accelerated preferentially from the unstable shock hemisphere. While the ions in simulation R0 maintain their trajectory in the $+z$ direction along the symmetric current sheet, the ions in simulation R1 are redirected towards the asymmetric current sheet in the $-y$ hemisphere by the $J \times B$ force.

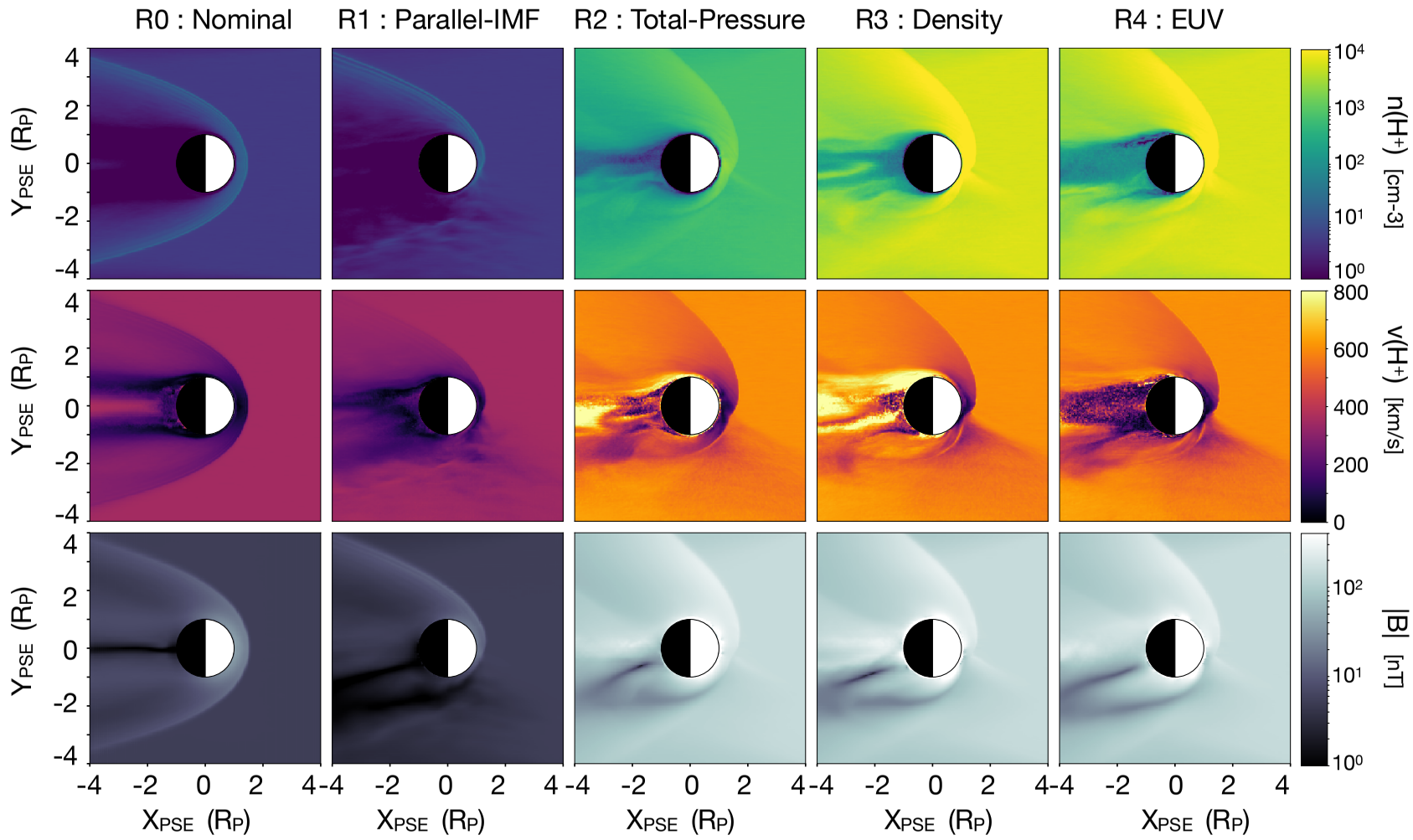

Figure 4.2: Slices through the simulation domain at Z=0, showing the impact of the quasi-parallel shock. Here, the motional electric field is pointed out of the plane and the solar wind flows from right to left. Panels show H+ number density (top), H+ velocity (middle), and magnetic field magnitude (bottom) with identical color scales across all panels. From left to right the columns show simulations R0, R1, R2, R3, and R4.

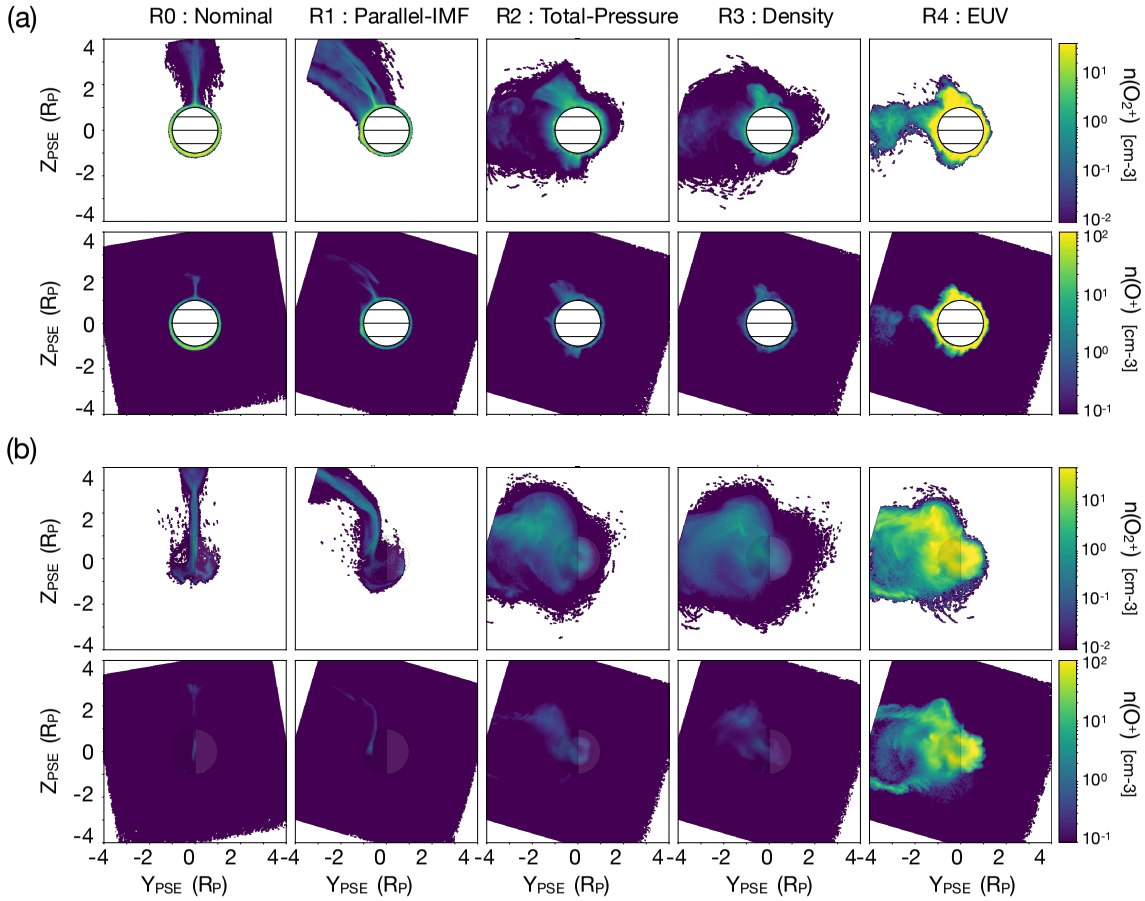

Figure 4.3: Slices through the simulation domain at X=0 (a) and X=-1.5, showing heavy ion escape. Here, the motional electric field is pointed up and the solar wind flows normal to the page. Panels show O2+ number density (top), and O+ number density (bottom) with identical color scales across all panels. From left to right the columns show simulations R0, R1, R2, R3, and R4. The tilted box effects occur due to rotating the simulation domain into the PSE coordinate system.

The morphology of escaping ions looks substantially less organized in the transition from R1 to R2. While the initial acceleration locations are the same, the outflow is much less collimated to the specific current sheet channel. This is due to much smaller gyroradii and changes in the current sheet configuration. As seen in Table 2, the large increase in the solar wind magnetic field with a modest increase in solar wind velocity drastically shortens the ion gyroradius to be much smaller than the size of the planet. Thus coherent motion on the scale of the planet is unlikely and the motion of even heavy ions like $O_2{}^+$ show magnetized behaviour. Furthermore, the changes in the current sheet discussed in section 4.4.1 have expanded the area from which ions are initially accelerated, broadening the eventual escape distribution. There is also a population of heavy ions that move upstream, after being quickly accelerated from low latitudes on the day side. This is a relatively small population of particles as denoted by the low number densities, and do not contribute much to the overall escape.

Despite roughly an order of magnitude increase in solar wind number density from R2 to R3, the ion escape morphology remains roughly the same. This is likely a consequence of the similar magnetic field morphology. Similarly, when increasing the ion production rate by two orders of magnitude from R3 to R4, although the overall ion escape rates differ, the morphology of the escape again remains constant. This is a consequence of the magnetic field morphology dominating the spatial distribution of ion escape and of the ion supply limited escape rather than energy limited escape. The escape limitations are further discussed in the following section.

4.4.3 Ion Escape

Table 4.2 lists a variety of metrics relating to ion escape rates for each simulation for both $O_2{}^+$ and O^+. Each of the escape properties were calculated by considering integrating the normal ion flux or power over a sphere located at $3.5R_P$. This radius was chosen such that it is far enough from the planet that all ions are escaping and do not return back to the planet while not being affected by the simulation boundary. These results are roughly constant over $\pm 1R_P$. The inflow power was calculated by integrating over the entire $+x$ simulation face. We chose to use the entire

simulation face because the size of the bow shock approaches the size of the simulation domain.

Here we concentrate on the relative differences between the models, rather than the absolute magnitudes. Although this model has been validated by observations in solar system contexts [Jarvinen et al., 2009, Jarvinen and Sandroos, 2013], the specific escape rates are heavily dependent on the lower boundary conditions. As we are considering a generic exoplanet around an M-dwarf and there on not observed atmospheric constraints for any terrestrial exoplanets, we focus instead on the relative effects of the stellar wind conditions.

Each stage of stellar property changed increases the net escape flux of both $O_2{}^+$ and O^+, except for R2 to R3 (increasing the stellar wind dynamic pressure). The transition from quasi-perpendicular to quasi-parallel increases the amount of solar wind that can penetrate directly into the ionosphere. Increasing the solar wind strength in R1 to R2 increases the amount of energy that is put into the system, and the strength of the magnetic field used in the $v \times B$ and $J \times B$ forces to accelerate the ions.

While the transition from R2 to R3 increases the solar wind dynamic pressure, and thus the total amount of energy available to the system, this does not translate to increased escape flux. Figure 4.2 shows that the increased density allows the solar wind to penetrate the ionosphere at higher velocity in some regions, which leads to an increased $v \times B$ force. However, the increased force does not lead to overall increased escape, because the escape is now production/diffusion limited.

The escape fraction column of Table 4.2 lists the fraction of total planetary ions injected that escape the planet. While R0 and R1 have escape fractions of a few percent, R2 and R3 show that roughly 50% of all injected ions are escaping. This limits the effect of the increased ion pickup force. The limit on ion escape is no longer the energy injected into the system, but the supply of ions from the planet that are available to escape.

This is further illustrated in the transition to R4 when the ion production rate is increased. While the overall escape flux increases, the fraction of injected planetary ions decreases. This means that the escape is less limited by the available supply of planetary ions to the system due

to diffusion through the lower atmosphere or production via photo-ionization.

The next columns in Table 4.2 list the escape power, total inflow power, and the coupling constant k, defined as the ratio of the escape power to the inflow power. The escape power follows roughly the same trends as the escape flux, except when comparing R0 and R1. In this case while the escape flux increases for a quasi-parallel IMF, the escape power slightly decreases. This is because the R1 heavy ions are not accelerated as much by the $v \times B$ force after leaving the planet, due to the much small perpendicular velocity component.

The power coupling constant k generally decreases as the stellar wind drivers are increased. The decrease from R0 to R1 corresponds to the decrease in escape power for the same stellar wind as discussed earlier. The power coupling also decreases from R1 to R2 as although the escape power increases, it does not increase as much as the solar wind power due to the limit of available ions. This effect is exacerbated in transition from R2 to R3, when the solar wind power continues to increase but the escape flux and power stay roughly constant. Finally, when the EUV is increased in R4 the power coupling constant increases, however, only to a rate comparable to R2, not as high as R0. Noting that the nominal case of R0 corresponds to the largest coupling constant is of key importance, because it implies that current observations of ion loss cannot be scaled indefinitely to more extreme conditions due to ion production/diffusion limitations. Thus, current observations may represent a more extreme case in solar wind power coupling.

The final columns in Table 4.2 list the average ion escape energy, or the escape power divided by the escape rate. For simulations R0 and R1 the energies are quite comparable to the average ion pickup energy expected given the solar wind parameters, as listed in Table 4.1. For simulations R2-R4, however, the ions greatly exceed the estimates. This is because convection electric field is much stronger at lower altitudes than in the solar wind due to the increased dynamic pressure, leading to strong acceleration. The magnetic field draping allows there to be a larger component of the magnetic field perpendicular to the inflow velocity, plasma pressure balance ensures that the magnetic field pileup leads to strong magnetic fields, and higher bulk velocities are present closer to the planet as discussed in Section 4.4.2.

Simulation	Escape Flux (10^{24} #/s)		Escape Fraction		Escape Power (10^{10} W)		Inbound Power (10^{11} W)	Power Coupling	Escape Energy (keV)	
	O^+	$O_2{}^+$	O^+	$O_2{}^+$	O^+	$O_2{}^+$			O^+	$O_2{}^+$
R0 : Nominal	0.6	0.6	0.04	0.03	0.2	0.3	2.5	0.02	31	20.8
R1 : Parallel-IMF	0.9	1.1	0.06	0.05	0.1	0.1	2.5	0.01	5.6	6.9
R2 : Total-Pressure	6.4	9.6	0.45	0.48	4.5	1.4	1.7e3	0.001	91	44
R3 : Density	6.8	9.4	0.49	0.47	5.5	1.1	1.5e4	0.0001	73	50
R4 : EUV	400	410	0.29	0.21	190	404	1.5e4	0.003	61	29

Table 4.2: Ion escape flux, fraction of injected planetary ions that escape, escape power, power coupling to solar wind, and average escape energy for each simulation.

4.5 Discussion

4.5.1 Model Limitations

One additional potential short-coming of the model we have applied here is that the ionospheric emission is driven by a predefined Chapman ion production profile. Accurately resolving ionospheric dynamics in the same domain as the global magnetosphere is computationally very challenging due to the large range of spatial and temporal scales; however, some simulation platforms include a one-way coupling from an ionosphere implementation to the global model, [e.g. Glocer et al., 2009a, Brecht et al., 2016, Modolo et al., 2016].

We have also chosen to use a constant resistivity value above the lower boundary and zero resistivity at the lower boundary; however, a self-consistent model would couple the ionospheric electrodynamics and modulate the effective resistivity throughout the domain. Ionospheric resistivity is known to affect global thermosphere structure [Roble et al., 1982] and ionospheric-magnetospheric coupling [Ridley et al., 2004] through mechanisms such as current closure, atmospheric Joule heating, and Alfven wave dissipation. Furthermore, resistivity is dependent on auroral precipitation [Robinson et al., 1987, Fuller-Rowell and Evans, 1987] and EUV flux [Moen and Brekke, 1993], both of which change across our simulations.

Modeling the ionospheric emission as a predefined production profile with a constant resistivity and the inner boundary as a super conducting sphere allows us to analyze stellar wind interactions of unmagnetized planets without an additional layer of uncertainty from a coupling between ionospheric photo-chemistry, ionospheric electrodynamics, and global kinetic plasma models. These ionospheric models, while important, are poorly constrained with current upper atmospheric profiles of exoplanets. Furthermore, as the ion escape rates listed in Table 3 are not self-consistently resolved based on ionospheric photochemistry they should be taken as rough order of magnitude estimates. Further study should separately assess the variations of ionospheric production and electrodynamics with the change in stellar parameters considered here.

4.5.2 Implications of Changing Ion Loss Morphology

In general, as the stellar input conditions are varied the morphology of the outflowing ions changes. The nominal case R1 showed symmetric tail and plume outflow from the nightside and mid-latitude dayside respectively. They were both collimated along the current sheet but well-defined as two different outflow channels. The R2 showed asymmetric outflow in both the tail and the plume due to the quasi-parallel shock and S-type current sheet. Models R3 and R4 showed outflow where the plume and tail were no longer distinct channels and were not well collimated.

One immediate result from this is semantic; applying definitions of different ion outflow channels from solar system planetary science to exoplanets must be carefully considered. Although the initial acceleration mechanisms may be distinct, the outflow channels may not be.

Observable signatures may also vary as a result of different ion morphology. Although the possibility of observing such low density escape is far off, it is worth considering the wealth of different geometries that are possible.

Finally, different ion outflow morphologies may also have key implications for tidally locked planets. If heavy ions are preferentially accelerated from one hemisphere due to a quasi-parallel stellar wind interaction, rather than the day side of the planet, this may set up a diffusion limited scenario for escaping ions, or drive asymmetries in the environment at lower altitudes.

4.5.3 Ionospheric Loss Rate Implications

Ion loss rates derived from simulations are often used to assess whether a planet is potentially habitable [e.g. Barnes et al., 2016]. While such rates may be validated by observations in solar system planetary contexts [Jarvinen et al., 2009, Jarvinen and Sandroos, 2013], the specific escape rates are heavily dependent on the ionospheric emission rates near the inner boundary, as discussed in Section 4.5.1. Thus, beyond noting that the rates we find in our simulation cases R0-R3 are comparable to current ion loss rates derived for Earth, Venus, and Mars [Strangeway et al., 2005] and are thus relevant for discussing atmospheric evolution, we have focused our discussion on the

relative difference in loss rates.

Atmospheric loss rates for the stellar parameters considered here may vary by several orders of magnitude; however, there is not a straightforward coupling between energy input and output, due to the complex coupling between the planet and the stellar wind. These results also imply that these systems are likely not energy limited. Instead, ion escape rates are likely limited by ion production or diffusion of the relevant species to the exobase.

4.6 Conclusions

The plasma environment for potentially habitable planets around M-dwarfs is markedly different that the environment experienced by solar system planets like Venus, Earth, or Mars. Here we have presented a systematic study of the difference in environment and implications on magnetic field morphology and ion loss. The differences we considered were a quasi-parallel IMF orientation (R1), overall stellar wind pressure (R2), ratio of magnetic pressure to dynamic pressure in the solar wind (R3), and EUV input (R4).

We found that both the ion loss morphology and overall loss rates were dictated by the plasma environment and magnetic field morphology. In cases where the stellar wind pressure was increased, the ion loss began to be diffusion- or production-limited with roughly half of all produced ions being lost. Because of this limit, the coupling of solar wind power to escaping ion power decreased in these extreme cases, despite the overall increase in ion loss. It is thus important to consider under what conditions scaling laws derived by observations of terrestrial planets begin to break down when applied to more extreme environments.

Going forward, careful models of stellar winds for relevant systems will become increasingly important to constrain the plasma environment for potentially habitable exoplanets. Furthermore, it will be important to consider the dynamics of these systems, not only through an orbit of a steady state solar wind, but the intrinsic variability of any wind.

Chapter 5

Planetary Magnetic Field Control of Ion Escape from Weakly Magnetized Planets

5.1 Introduction

Atmospheric escape is capable of shaping a planets atmospheric composition and total mass, and thus the planet's long-term habitability. Loss to space of atmospheric particles is thought to have played a key role in the atmospheric evolution of both Mars [e.g. Anders and Owen, 1977, Jakosky and Phillips, 2001, Jakosky et al., 2018] and Venus [e.g. Dayhoff et al., 1967, Kulikov et al., 2006]. This evolution may have prevented these planets from being currently habitable like the Earth, despite their likely similarities in initial formation. As we begin to discover an abundance of exoplanets, it is important to understand the processes that shape their evolution, including atmospheric escape. This will be particularly interesting for potentially habitable terrestrial planets, such as Proxima-b [Anglada-Escudé et al., 2016, Meadows et al., 2018] and those in the Trappist-1 system [Gillon et al., 2017, Dong et al., 2018].

Hydrogen atmospheres accreted early in a planet's life are thought to escape due to the thermal energy of the particles, either slowly through Jeans escape or quickly due to a thermal wind [Hunten, 1973]. In both of these processes a significant portion of the particle velocity distribution exceeds escape velocity due to their thermal motion. This thermal energy can be gained from photo-heating [e.g. Yelle, 2004], giant impacts [Liu et al., 2015], or core-accretion [Ginzburg et al., 2016]. Thermally-driven atmospheric escape is thought to lead to the gap between super-earths and mini-neptunes [Owen and Wu, 2017, Ginzburg et al., 2018, Biersteker and Schlichting, 2018].

Although thermal loss is an important process for dictating the evolution of the primary atmosphere or hydrogen nebula of a planet, secondary atmospheres created by planetary outgassing are composed of gravitationally bound heavier species and have more difficulty escaping thermally after the primary atmosphere has been lost. Additional energy sources such as photochemical production [McElroy et al., 1977, Hunten, 1982], sputtering [Haff and Watson, 1979, Hunten, 1982], charge exchange [Chamberlain, 1977], or ion escape are necessary to drive significant escape of secondary atmospheres over the course of a planets lifetime [Hunten, 1982]. Ion escape encompasses the collection of escape channels where escape occurs through loss of ionized species, including ion pickup [e.g. Luhmann and Kozyra, 1991a], ion bulk escape [e.g. Brain et al., 2010], and the polar wind [e.g. Banks and Holzer, 1968, Yau et al., 2007]. Both the energization of the particles through these processes and their eventual escape trajectories (or lack thereof) are critically affected by the dynamic plasma environment created by the interaction of the planet and the stellar wind.

The strength of a planet's magnetic field is a critical factor in shaping a planetary plasma environment. In the solar system the only clearly habitable planet, Earth, has a strong intrinsic magnetic field driven by an internal dynamo, while Venus and Mars do not. This has led many to speculate that an intrinsic magnetic field is a critical component required to shield the planet from atmospheric erosion due to the solar wind [Driscoll and Bercovici, 2013, Lundin et al., 2007, do Nascimento et al., 2016, Driscoll, 2018], we call this the magnetic umbrella hypothesis. However, present measurements of escape rates suggest that all three planets are losing their atmosphere at similar rates [Strangeway et al., 2005], and the magnetic umbrella hypothesis has been called into question [Kasting, 2012, Brain et al., 2013]. Understanding the complex interplay between the planetary plasma environment, solar wind driving, and ion loss is thus of critical importance.

Some investigation into the effects of an intrinsic magnetic field on ion loss has been made using global plasma models. Dong et al. [2017b] compared escape rates from Proxima-b using a multi-species MHD model with a magnetized and an unmagnetized case and found larger escape rates in the unmagnetized case, while Garcia-Sage et al. [2017] found using a polar wind outflow

model that the higher ionizing radiation levels of EUV radiation fluxed of M dwarfs compared to Earth may increase the effectiveness of the polar wind by orders of magnitude. Global hybrid modeling work from Kallio and Barabash [2012a] looked at ion escape from a Mars type planet with a global dipole of 0, 10, 30, and 60 nT, and found maximum ion escape from the 10 nT case. Gunell, Herbert et al. [2018] combined empirical measurements at Earth, Mars, and Venus with semi-analytic models to analyze the influence of planetary magnetic field over a large range of magnetic field values, finding multiple peaks in escape rate over the range that varied in strength and value by planet. Sakai et al. [2018] found an increased escape rate for a weakly magnetized Mars (100 nT) compared to an unmagnetized Mars in a multi-species MHD model. In combination these results suggest that there is much more to learn about about ion escape as it relates to planetary magnetic fields.

Weakly magnetized planets are an especially interesting regime as they represent the transition from unmagnetized planets with induced magnetospheres to magnetized planets with intrinsic magnetospheres. In the weak-field limit the scale size of the stellar wind interaction region is not dramatically changed. However, a global planetary magnetic field is typically approximated to the first order as a magnetic dipole centered at the planet, this introduces a new axis of symmetry. Furthermore, some studies indicate that planets around M-dwarfs may be weakly magnetized [Gaidos et al., 2010]. Analysis of the Kepler data has shown that planetary systems are common around M-dwarfs [Kopparapu, 2013], and these systems also show the best promise of observing exoplanet atmospheres [Shields et al., 2016]. Thus it is important to understand what effect weak magnetic fields will have on the subsequent ion escape.

Here we study the influence of weak planetary magnetic fields on the plasma environment of a planet and subsequent ion loss through a series of hybrid plasma simulations. Section 5.2 describes our methods, Section 5.4 details influence of the magnetic field on the planetary plasma environment, Section 5.5 describes the corresponding influence on ion escape, Section 5.6 contains a discussion of the results, and Section 5.7 summarizes the conclusions.

5.2 Methods

To analyze the effects of planetary magnetic field strength on ion escape we have run seven simulations of the solar wind interaction with increasingly magnetized planets. These simulations were performed using the hybrid plasma model RHybrid [Jarvinen et al., 2018]. In a hybrid model the ions are treated as macroparticle clouds while the electrons are treated as a charge-neutralizing fluid. By treating ions as macroparticles ion kinetic effects associated with finite ion gyroradii are included, while treating the electrons as a fluid allows simulating a much larger volume than a corresponding fully kinetic approach.

Each ion macroparticle represents a group of ions that have the same velocity (v_i), central position (x_i), charge (q_i), and mass (m_i). Each cloud has the same shape and size as a grid cell and clouds move inside the grid cells obeying the Lorentz force such that

$$m_i \frac{d\vec{v_i}}{dt} = q_i(\vec{E} + \vec{v_i} \times \vec{B}) \, , \tag{5.1}$$

where $\vec{E}$ and $\vec{B}$ are the electric and magnetic fields respectively. The electron charge density then follows from the quasi-neutral assumption with all ion species accumulated in the grid and total new charge density assumed to be zero in each cell.

Amperes law is used to calculate the current density from the magnetic field

$$\vec{J} = \nabla \times \vec{B}/\mu_0 \, , \tag{5.2}$$

and then the electric field is found using Ohm's law

$$\vec{E} = -\vec{U_e} \times \vec{B} + \eta \vec{J} \, , \tag{5.3}$$

where the η is the explicit resistivity profile, and U_e is the electron fluid velocity. The value of η was chosen to be $\eta = 0.02\mu_0\Delta x^2/\Delta t$, such that the magnetic diffusion time scale becomes $\tau_D = \mu_0 L_B^2/\eta = 50\Delta t$, for the magnetic length scale $L_B \simeq \Delta x$. This choice adds diffusion in the propagation of the magnetic field [Ledvina et al., 2008], stabilizing the numerical integration, while

Table 5.1: Upstream conditions used to drive the models. Here u is the stellar wind velocity, n_p is the stellar wind H^+ number density, T_p is the stellar wind H^+ temperature, B_{sw} is the interplanetary magnetic field (IMF), P_{sw} is the dynamical pressure, and v_A is the Alfven speed.

u	$[-350, 0, 0]$ km/s
n_p	4.9 cm^{-3}
T_p	59200 K
B_{sw}	$[-0.74, 5.46, -0.97]$ nT
P_{sw}	1.0 nPa
v_A	55 km/s

ensuring that the magnetic field diffuses on timescales longer than the timestep Δt . Note that the resistivity is not explicitly included in the Lorentz force. Finally, the magnetic field is advanced using Faraday's Law

$$\frac{\partial \vec{B}}{\partial t} = -\nabla \times \vec{E} \, . \tag{5.4}$$

Jarvinen et al. [2018] and references therein contain details of the numerical scheme. Highly parallelized RHybrid and its sequential predecessor code HYB have been used to study ion escape from Mars [Kallio and Janhunen, 2002, Kallio et al., 2010, Dival et al., 2012], Venus [Jarvinen et al., 2009, 2013], Mecury [Kallio and Janhunen, 2003], Titan [Kallio et al., 2007], and exoplanets around M-dwarfs [Egan et al., 2019].

The results presented in this paper are in the Planet Stellar Orbital (PSO) coordinate system, such that the planet is at the origin, the x direction points from the planet against the undisturbed upstream stellar wind velocity vector, the z direction is perpendicular to the orbital plane of the planet, and y is the completion of a right-handed coordinate system. The physical distances are shown in planetary radii (R_p) that correspond to 3390 km (= 1 Martian radius).

The externally forced stellar wind and interplanetary magnetic field (IMF) was chosen to be the same as in Egan et al. [2018] and is a case of a nominal solar wind interaction with Mars. The corresponding parameters are listed in Table 5.1. Note that the magnetic field is largely in the +y direction and thus the corresponding motional electric field is largely in the +z direction.

The ion production representative of the planetary ionosphere is implemented via Chapman profiles such that

$$q(\chi, z') = Q_0 \exp[1 - z' - \sec(\chi) * e^{-z'}] \,, \tag{5.5}$$

where z' is the normalized height parameter given by $z' = (z - z_0)/H$, χ is the solar zenith angle, z_0 is the reference height, and $H = 16$ km is the scale height. Such a profile assumes an isothermal atmosphere that is ionized by plane-parallel, monochromatic radiation in the EUV. This is a simplified method to inject planetary ionospheric ions in the simulation using a pre-defined production rate and spatial emission profile near the exobase and the inner boundary of the model; limitations arising from such a choice are discussed in Section 5.6. The peak location of ion production occurs at an altitude of $z_0 = 300$ km, while the ion absorption lower boundary occurs at 150 km. The global emission rates Q_0 for each ion are picked to correspond to nominal values at Mars today ($Q_0(O_2^+) = 2 \times 10^{25}$ s^{-1}, $Q_0(O^+) = 1.4 \times 10^{25}$ s^{-1}) [Jarvinen et al., 2016a, 2018, Egan et al., 2018, 2019].

The planetary magnetic field is enforced at the planet surface, and in the non-magnetized case is implemented as a super-conducting sphere. The range of planetary magnetic fields runs from unmagnetized to an equatorial surface dipole field of $B_p = 150$ nT, which corresponds to approximately 1/400th of the Earths equatorial surface magnetic field. The magnetic dipole is aligned with the z axis such that equatorial dipole field point along $+z$.

Each simulation was run on a 240^3 grid, with boundaries at $\pm 5 R_P$ in the Y and Z directions and $[-6, +4]$ in the X direction. This leads to a corresponding resolution of $\Delta x = 141$ km, which is comparable to an estimate of the ion gyroradius for O^+ ($\gamma = m v_\perp / qB \sim 390$ km). Each simulation was run for 100,000 time steps with $\Delta t = 0.01 s$ (satisfying the Courant condition), corresponding to roughly 8 stellar wind crossing times through the simulation domain.

5.3 Unmagnetized and Magnetized Planetary Paradigms

For unmagnetized planets with some atmosphere, the conductivity of the ionosphere induces a magnetosphere which acts to stand off the stellar wind in the absence of a planetary magnetic

field. This creates a transition region that includes the Magnetic Pileup Boundary (MPB) due to the pileup of the IMF as it drapes around the planet and the Induced Magnetosphere Boundary (IMB) marked by a transition from stellar wind to planetary plasma [Nagy et al., 2004a]. The dynamics of ion escape are thus dominated by the plasma environment associated with the induced magnetosphere.

As the stellar wind directly interacts with the ionosphere at unmagnetized planet, the stellar wind motional electric field accelerates pickup ions into a plume [Cloutier et al., 1974, Luhmann and Kozyra, 1991a, Dong et al., 2015]. Additionally, cold ions can flow out on the night-side of the planet in tail escape [Frnz et al., 2015, Engwall et al., 2009].

For magnetized planets the intrinsic magnetic field acts to stand off the incoming stellar wind through a balance of the magnetic pressure and incoming stellar wind dynamic pressure. For a planetary magnetic field given by a dipole this pressure balance can be used to define the magnetic standoff distance Rs as follows

$$R_s = R_P \left(\frac{P_B}{P_{sw}} \right)^{1/6} = R_P \left(\frac{2B_P^2}{\mu_0 \rho_{sw} u_{sw}^2} \right)^{1/6} \tag{5.6}$$

where the additional factor of 2 in the numerator comes from the compression of the magnetic field at the magnetopause [Cravens, 2004]. Because the stellar wind has less direct access to the ionosphere, the dynamics of the escaping ions are dictated by the plasma environment associated with the intrinsic magnetosphere and the topology of the field lines.

Magnetic topology is defined by the structure of magnetic field lines and their relationship to the surrounding environment. Open magnetic field lines have one end connected to the planet with the other connected directly to the stellar wind, while closed field lines have both foot-points connected to the planet. As a planet's magnetic field increases, the area of the ionosphere that is magnetically connected to the stellar wind via open field lines can be expected to decrease.

The locations of closed and open field lines can be estimated analytically for magnetized planets using the magnetic stand-off distance. Because the magnetic standoff distance is associated

with the last closed field line, the latitude of the polar cap, or region of open field lines is thus given by

$$\theta_c = \arcsin\left(\sqrt{\frac{R_p}{R_s}}\right) \tag{5.7}$$

and the corresponding polar cap solid angle is then

$$\Omega_c = 4\pi(1 - \cos(\theta_c)) = 4\pi(1 - \sqrt{1 - R_p/R_s}). \tag{5.8}$$

When the standoff distance becomes less than the planet radius the polar cap angle becomes saturated at 4π, or twice the angle of an entire hemisphere.

As ions are constrained to gyrate around magnetic field lines, magnetic topology has key implications for determining ion escape rates. At strongly magnetized planets ions escape along open field lines at the poles in a process known as cusp escape [Lockwood et al., 1985]. If the ions are accelerated due to the electron pressure gradients along the poles it is called the polar wind [Banks and Holzer, 1968, Yau et al., 2007].

The transition between magnetized and unmagnetized systems is a transition between these two paradigms; unmagnetized planets are dominated by induced magnetosphere dynamics and direct acceleration of planetary ions via the stellar wind motional electric field, while magnetized planets are dominated by their intrinsic magnetospheres and global magnetic topology. The following results sections explore this transition in plasma environments and the corresponding changes ion escape.

5.4 Plasma Environment

In this section we analyze the structure of the plasma environment and magnetic topology near the planet in our set of runs with an increasing planetary magnetic field strength. Even a moderate change in environment and topology associated with a weakly magnetized planet can affect the ion dynamics near the planet and thus the ion outflow.

5.4.1 Tail Twisting

The tail magnetic morphology is critically affected by both the IMF and the dipole structure. In an unmagnetized planet the stellar wind magnetic field drapes around the planet in a roughly symmetric fashion, creating a central current sheet within the induced magnetosphere. Observations at Mars have shown that the current sheet is very dynamic with local variations ascribed to both twisting and flapping motions [DiBraccio et al., 2017, DiBraccio et al., 2018, Chai et al., 2019], which may be associated with changes in response to upstream IMF or stellar wind pressure, kink-like flapping due to waves propagating along the current sheet, or reconnection of crustal fields [Luhmann et al., 2015]. For magnetized planets the intrinsic dipole field also creates a current sheet in the tail oriented perpendicularly to the dipole axis. This current sheet also experiences flapping motion [Speiser and Ness, 1967] and is strongly influenced by reconnection events [Nakamura et al., 2006].

In this set of simulations the dipole axis and the IMF are roughly perpendicular, making the topology of the current sheet sensitive to the relative strengths of these fields. Figure 5.1 shows slices through the tail at $x = -2$ for each simulation for both O_2^+ number density and the x-component of the magnetic field, which illustrate the location of the current sheet. As the field strength increases the tail becomes more twisted such that the central area is dominated by the dipole contribution while farther out is dominated by the IMF draping. This structure shows the transition in relative influences of the induced and intrinsic magnetospheres, as well as the effect on ion escape morphology.

5.4.2 Magnetic Topology Mapping

Figure 5.2 shows magnetic field line tracing through our models with orange lines indicating closed field lines and blue indicating open field lines. The lines were traced in both directions from a spherical shell at 400 km altitude. These field line tracings reflect the above intuition where stronger magnetic fields create larger regions with more closed magnetic field lines.

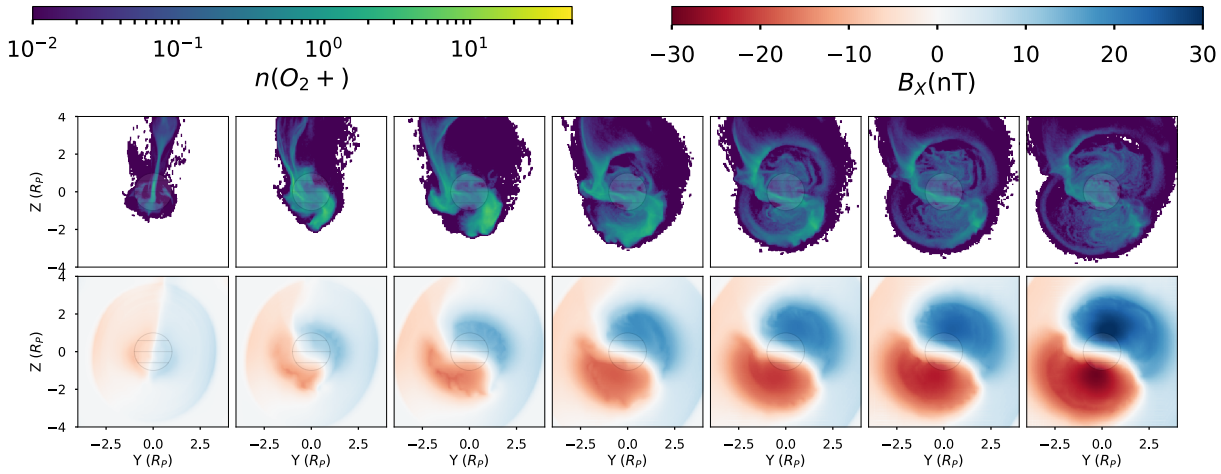

Figure 5.1: Slices through the tail at $X = -2$ for each simulation (0, 10, 25, 50, 75, 100, 150 nT from left to right). Top row shows O_2^+ number density while the bottom row shows the x-component of the magnetic field. The gradual twisting of the tail represents a shift from being IMF draping dominated (symmetric about Y) to dipole dominated (symmetric about Z).

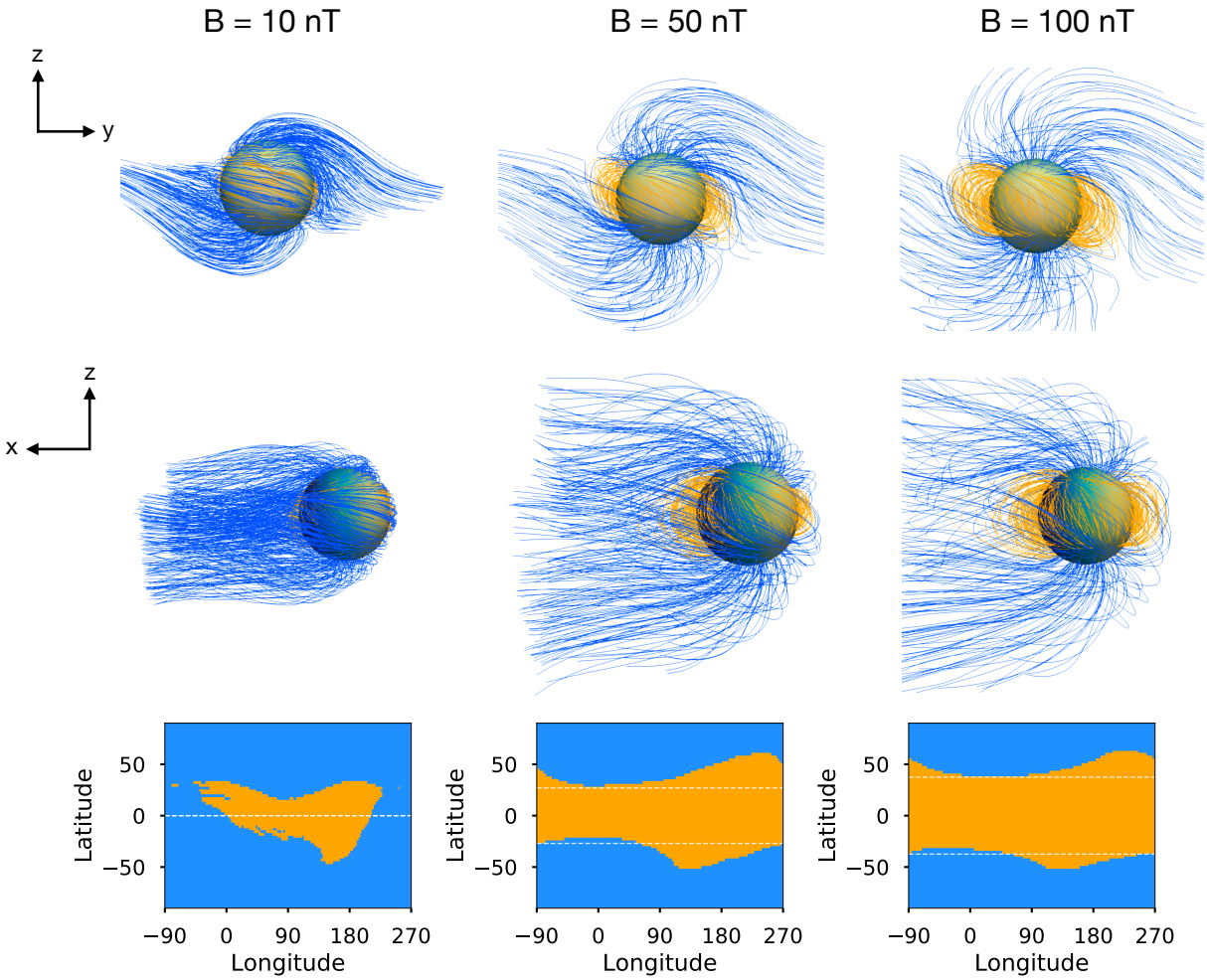

Figure 5.2: Magnetic field line traces for three representative simulations with planetary magnetic fields of 10 nT (**left**), 50 nT (**center**), and 100 nT (**right**). Top row shows the planet as viewed from the star and middle row shows planet as viewed within the orbital plane; in both cases the motional electric field points upwards. Bottom row is a latitude-longitude map of the field line tracings, with white dashed lines indicating the analytic critical latitude. Closed magnetic field lines are indicated in orange while open magnetic field lines are illustrated in blue. The planet is colored by stellar-zenith angle.

Because the magnetization of the planet is weak, the interplanetary magnetic field (IMF) carried by the stellar wind has a large impact on the structure of the magnetosphere. This is similar to what has been found at Mercury [Slavin, 2004, Luhmann et al., 1998, Kabin et al., 2000] and Ganymede [Kivelson et al., 1997] where the external magnetic field induces polar alignment. Figure 5.2 shows this influence where the $+y$ oriented IMF causes the open field lines at the poles to twist towards the dawn ($+y$) and dusk ($-y$) sides in the northern and southern hemispheres respectively, such that at larger distances the field lines align with the IMF.

The closed field lines attached to the planet on both sides also show twisting to align with the IMF. This causes the closed field lines to attach asymmetrically in longitude; a field line attached at a dawnward longitude in the northern hemisphere will close on the duskward longitude in the southern hemisphere. As the magnetic field strength increases, this effect decreases due to the larger strength of the planetary field in comparison to the IMF.

The lower portion of Figure 5.2 shows a latitude-longitude map of the field line topology at the same altitude where the field line tracings began, with dashed lines indicating the critical latitude θ_c given by Equation 5.7. While field lines outside $\pm\theta_c$ are indicated as open within the analytic formulation described earlier, the field line mapping shows significant area of closed field lines outside this region, particularly for the lowest magnetic field strength (10 nT) and on the night side (longitude ~ 180). This occurs because of the aforementioned asymmetries, as well as the neglect of the induced magnetospheric pressure in the analytic formulation.

5.4.3 Magnetic Standoff

In the upper panel of Figure 5.3 the magnetic topology is compared across magnetic field strength by assessing the area of the polar cap open to the stellar wind, an estimate of the region from which ions may escape. The "full field line trace" is calculated by summing the solid angle of all open field lines identified in the tracing associated with Figure 5.2. The "axially symmetric field trace" is calculated finding the region of closed field lines along the noon longitude and assuming a polar axis symmetry. The "analytic cap area" is calculated assuming a polar axially symmetric

system with a critical latitude given by Equation 5.7. The discrepancy between the two calculated values is due to the lack of symmetry in the system because of day-night variation, and symmetry breaking induced by the IMF as discussed in the following subsection. Both values are useful to show due the physical accuracy (topology area) and directness of the comparison with the analytic value (symmetric area).

In general the analytic formulation overestimates the polar cap solid angle, especially at small magnetic field values. This occurs because the analytic estimate must be completely open for all field values where the magnetic field pressure is less than the stellar wind pressure. However, this once again neglects the influence of the induced magnetosphere.

We also show a best fit scaling relationship between the polar cap angle and magnetic field for the full field line trace, where $\Omega_c \propto {B_p}^{-0.34}$. A scaling law exponent of $-1/3$ can be recovered by expanding Equation 5.8 around small values of R_p/R_s, and then substituting Equation 5.6 for R_s. This scaling matches well even to small magnetic field values ($B_P \sim 10$ nT).

The bottom panel of Figure 5.3 shows the transition from induced to intrinsic magnetospheres through a variety of metrics designed to assess standoff of the stellar wind by the planet. The analytic stand-off altitude (Equation 5.6) is calculated assuming pressure balance between the incoming stellar wind and the intrinsic magnetosphere of the planet. This is most clearly related to the pressure equilibrium point (the altitude along the sub-stellar line at which the magnetic pressure is equivalent to the stellar wind pressure); however, the pressure equilibrium point occurs at much higher altitude in the magnetosheath due to the expected thickness of the transition region, corresponding to a few proton gyroradii ($\gamma_{H^+} \sim 730$ km) [Cravens, 2004].

The analytic stand-off altitude is also closely related to the magnetic topology, as shown in Equation 5.7. Here, rather than calculating the latitude associated with the last closed field line, we show the altitude along the sub-stellar line of the last closed field line. This matches fairly well with the analytic stand-off distance but occurs slightly higher due to the the same asymmetry and induced field pressure support as described in Section 5.4.2.

Finally, we show a measure of the magnetospheric boundary through identification of the

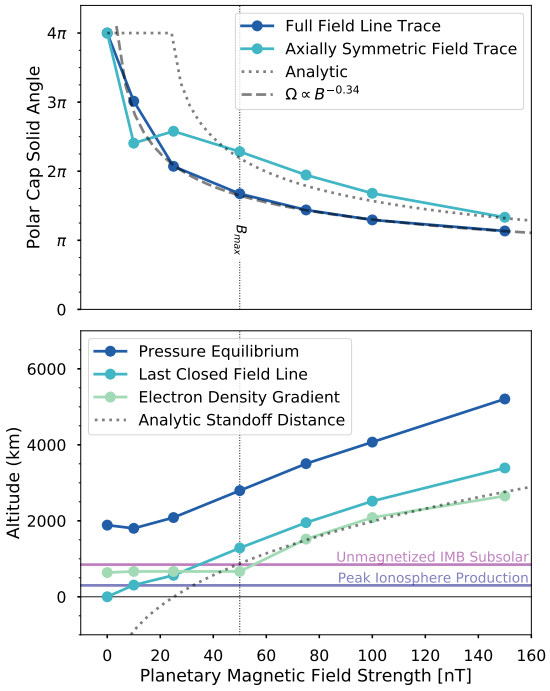

Figure 5.3: Polar cap solid angle (**top**) and standoff altitude and proxies thereof along the sub-stellar line (**bottom**) plotted over planetary magnetic field. Dotted lines indicate analytic approximations while solid lines with points are calculated from the simulations. Horizontal lines indicate empirical boundaries measured for Mars [Trotignon et al., 2006a] and the peak ionosphere production location in the simulations and the vertical line indicates magnetic field associated with peak ion outflow (see Section 5.5).

steepest gradient in electron number density, a method used to identify the induced magnetospheric boundary at unmagnetized planets [Vogt et al., 2015]. At unmagnetized planets this can be thought of as the "top" of the ionosphere, where there is a transition from planetary to stellar wind plasma. At magnetized planets this becomes the outer region of the plasmasphere (see Section 5.5.3), where closed magnetic field lines can confine plasma. This measurement thus has a clear relationship to the closed field line boundary, while also having a well defined meaning for unmagnetized planets.

In Figure 5.3 we see that the last closed field line and electron density gradient altitudes agree fairly well with each other and the analytic standoff distance at higher magnetic field strengths. At lower magnetic field strengths, the electron density gradient flattens out due to the intrinsic gradient associated with the ionosphere. This transition occurs where the magnetic stand-off crosses the unmagnetized induced magnetosphere boundary (847 km) [Trotignon et al., 2006a]. Critically, this point is also identical to the magnetic field associated with maximum ion outflow as shown in Section 5.5.

This transition between induced and intrinsic magnetospheres is shown schematically in Figure 5.4. The induced magnetosphere boundary remains constant with magnetic field as it is determined by the ionospheric conductivity and pressure support against the stellar wind. For the weakest magnetic fields ($B_P < 50$ nT) the induced magnetosphere is the dominant source of pressure support against the stellar wind, the last closed field lines occur below the boundary, and the electron density gradient is then associated with the induced boundary. At stronger magnetic fields ($B_P > 50$ nT) the intrinsic magnetosphere is the dominant source of pressure support against the stellar wind, the last closed field lines occur above the induced magnetosphere boundary, and the electron pressure gradient is associated with trapped plasma within the closed magnetic field line region. The transition point occurs when the intrinsic magnetosphere standoff distance reaches the induced magnetosphere models; for this set of simulations this occurs at $B_P = 50$ nT. In the following section we will discuss the implications this pattern has for ion escape.

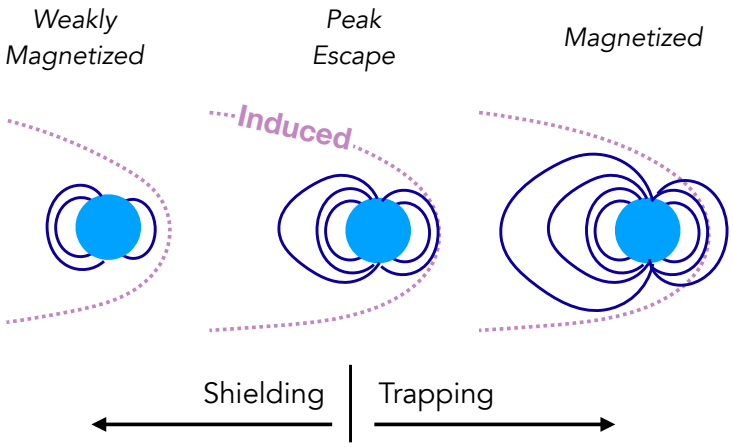

Figure 5.4: Schematic depiction of the relationship of the induced (**pink dashed**) and intrinsic (**blue solid**) magnetospheric boundaries. The different regimes are responsible for different patterns of ion escape, as discussed in Section 5.5.

5.5 Ion Escape

As discussed in Section 5.4, the transition between unmagnetized and magnetized planets affects the stand-off of the stellar wind and the opening angle of the polar cap, which in turn affect the pickup ion and cusp escape processes. Here we analyze the trends in ion escape rates and energy and connect them to the influence of the surrounding plasma environment.

5.5.1 Escape Rates and Energies

Figure 5.5 shows the escape rate, escape power, and average ion escape energy (escape rate divided by escape power) for each simulation run. These parameters are calculated as

$$\Phi = \int n_i(\vec{u_i} \cdot \vec{\hat{r}})r^2 d\Omega \tag{5.9}$$

$$P_{esc} = \int m_i n_i {u_i}^2(\vec{u_i} \cdot \vec{\hat{r}})r^2 d\Omega \tag{5.10}$$

$$\bar{E} = P_{esc}/(\mu\Phi) \tag{5.11}$$

respectively, where n_i is the ion number density, u_i is the ion velocity, m_i is the ion mass, and μ is the ion mass expressed in units of the proton mass. We calculate these rates by integrating over a sphere far from the planet such that the sphere is large enough ($r = 4.0R_P$) that the flux value is insensitive to changes in radius, and all outbound flux escapes and does not return to the planet, even for our most strongly magnetized simulation cases.

We find that the escape rate increases for magnetic fields up to $B_P = 50$ nT and then begins to decrease again, with a maximum variation of a factor of ~ 3. The magnetic field associated with peak escape rate (B_{max}) is equivalent to the magnetic field where the induced magnetosphere altitude equals the intrinsic magnetosphere altitude. This divides the ion escape trends into different regimes illustrated in Figure 5.6; weaker escape associated with predominately induced magnetospheres, stronger escape associated with magnetic shielding and equivalent induced and intrinsic

magnetospheres, and weaker escape associated with strong magnetospheres and plasmasphere trapping. Each of these regimes will be explored more fully in the following subsections. Additionally, we show a power law fit for simulations $B_P \geq 50$ nT where we find that the escape rate scales as ${B_P}^{-0.67}$.

Escape power shows a steady decrease with magnetic field, and a power law scaling of ${B_P}^{-0.60}$ for $B_P \geq 50$ nT. Average escape energy is calculated by dividing integrated escape power over the spherical shell by integrated escape flux. For both O_2^+ and O^+ Figure 5.5 shows the reduced escape energy is highest for small magnetic field values before reaching an asymptote at around 50 nT.

Both power laws calculated for escape rate and escape power have clear lower limits at $B_p = 50\ nT$, a point we define as B_{max}. These power laws also likely have upper limits that may prevent their extension to very strongly magnetized systems like Earth, as indicated by the various shaded regions in Figure 5.5. This is discussed further in Section 5.6.4.

Figure 5.7 shows a histogram of the full velocity distribution of escaping particles through the $R = 4.0\ R_P$ sphere, weighted by area $\times\ n_i \times v_i$ and normalized such that the integral over the distribution is 1. Dashed lines indicate the average escape energies. This figure shows that the decrease in escape energy with increasing magnetic field is caused by a corresponding decrease in high energy particles in the tail of the velocity distributions. As the magnetic field begins to stand off the stellar wind, fewer ions are exposed to the strong motional electric field, and thus fewer ions are accelerated to high velocities.

5.5.2 Southern Hemisphere Shielding

The increase in escape rate with increasing magnetic field is caused by stellar wind standoff in the southern hemisphere decreasing the flux of pickup ions accelerated towards the planet and preciptating in the inner boundary. While the motional electric field in the northern hemisphere causes ion pickup and the plume feature, in the southern hemisphere the motional electric field accelerates the ions into the planet, preventing their escape. This effect is illustrated in Figure 5.6, with the direction of the motional electric field indicated by the green arrow. While particles

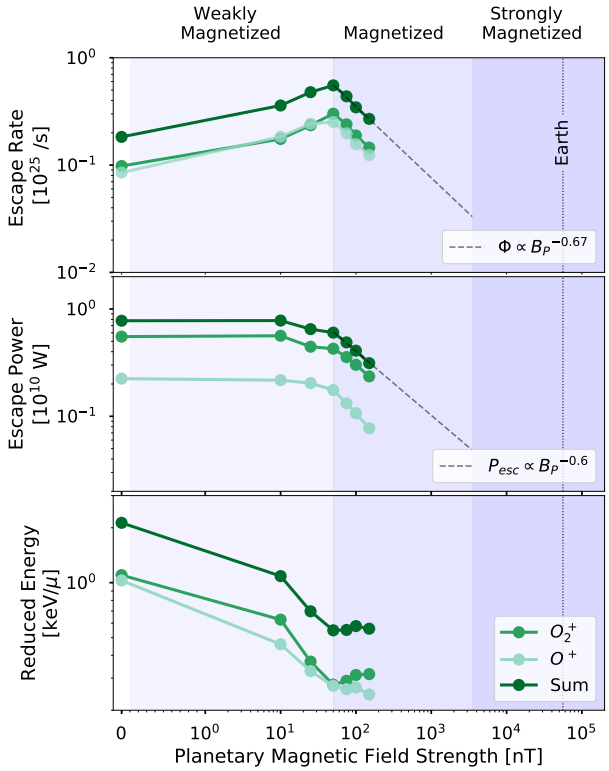

Figure 5.5: Ion escape rates (**top**), escape power (**middle**), and average ion escape energies (**bottom**) over planetary magnetic field strength for O_2^+,O^+, and the sum of both ions. Relative escape rates are normalized to the escape rate of the unmagnetized case. Power law fits to the sum are shown in with a dashed line for the escape rate and escape power for $B_p \geq 50$ nT.

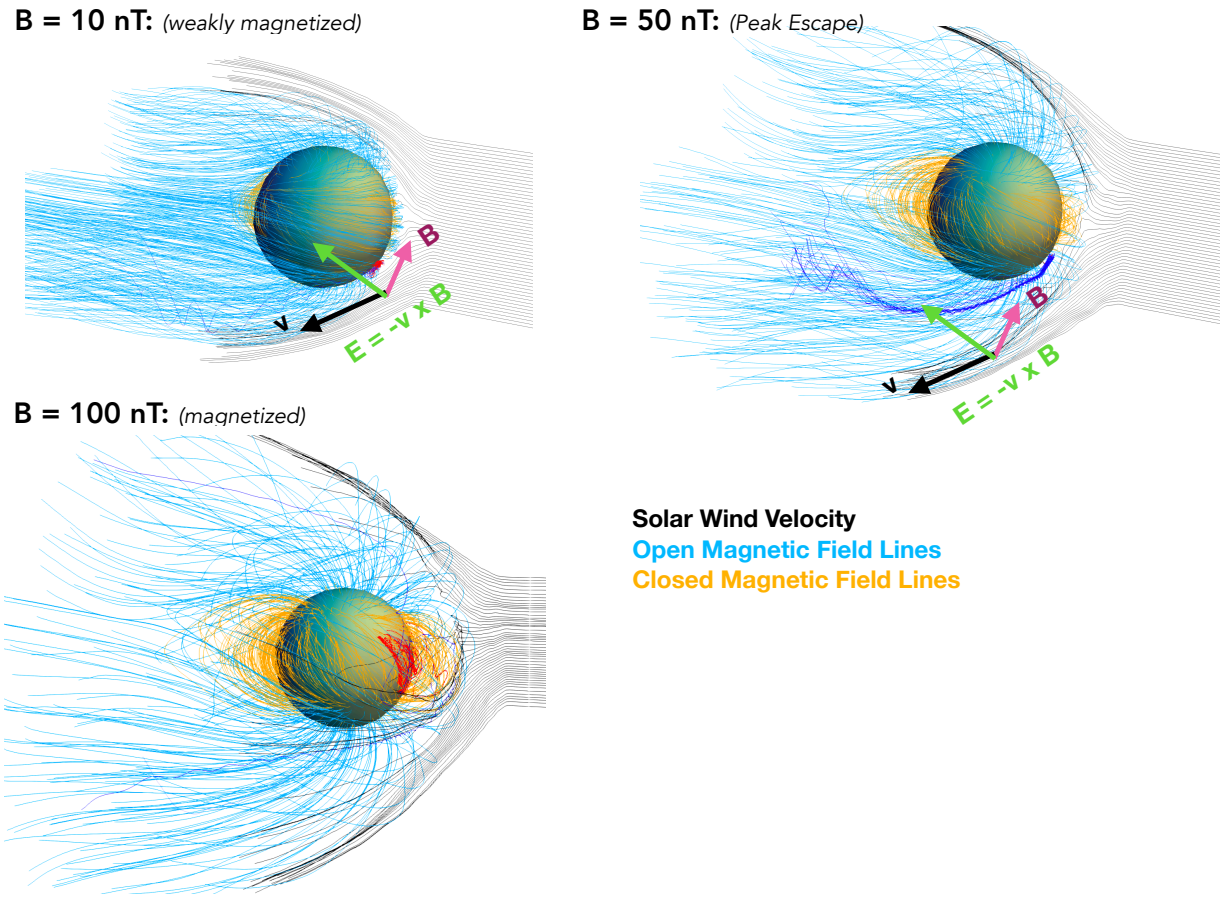

Figure 5.6: Three example particle trajectory tracings for 10, 50, and 100 nT simulations. Particle tracings are shown in red (trapped) or dark blue (escaping), and magnetic field lines are shown in light blue (open) and orange (closed). While this location was picked primarily as an illustrative example for these three simulations, it is representative of overall ion escape trends discussed in Sections 5.5.2 and 5.5.3.

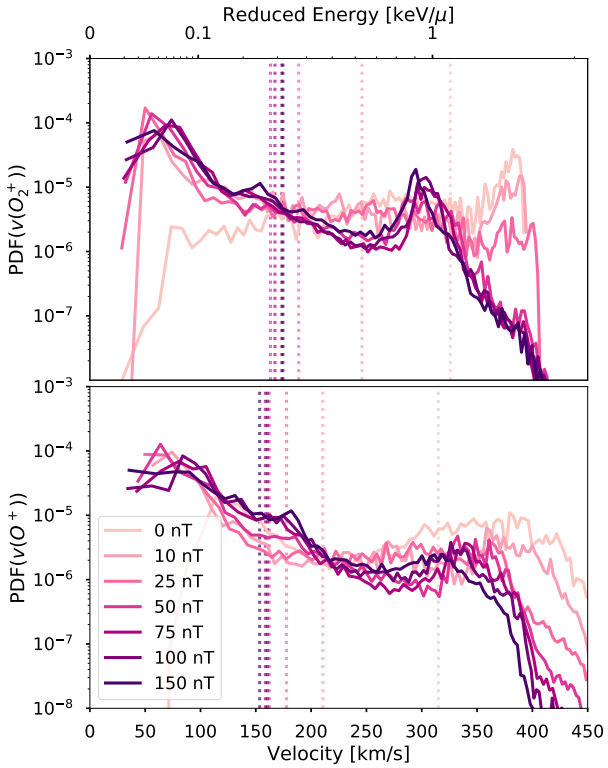

Figure 5.7: Velocity distribution of escaping O_2^+ (**top**) and O^+ (**bottom**) ions weighted by number density and velocity, such that integrating over the distribution is equivalent to the escape power. Each color shows a different magnetic field. The dashed lines indicate the weighted average of each distribution (equivalent to the average reduced escape energy plotted in Figure 5.5).

injected in the southern hemisphere of the 10 nT simulation are accelerated towards the planet and do not escape, particles injected in the same location in the 50 nT simulation do escape due to the increased stand-off of the stellar wind.

Figure 5.8 shows slices of the total motional electric field, total electron velocity, and ratio of the fluid velocity and the ion velocity for the 10, 50, and 100 nT simulations. In the 10 nT case strong electric fields due to high electron velocities permeate the region of planetary ions. In the 50 and 100 nT cases the increasing magnetic pressure slows the stellar wind down much more before reaching the planet, decreasing the magnitude of the motional electric field. The ions in these more strongly magnetized cases can then flow farther from the planet along open field lines before being exposed to the strong electric field, and are thus accelerated down-tail rather than into the planet. This effect will saturate roughly when the standoff distance reaches the altitude of the IMB at the terminator, which is illustrated occurring at 50 nT in Figure 5.3.

5.5.3 Plasmasphere Trapping

The decrease in escape rate at higher magnetic field strengths is due to plasmasphere trapping, where ions become trapped within the closed field line regions. This is depicted in Figure 5.6 where particles escape in the 50 nT simulation, but are confined within the closed magnetic field line in the 100 nT simulation. This effect is related to the decrease in polar cap solid angle illustrated in the lower panel of Figure 5.3. As more area of the planet is wrapped in stronger closed magnetic field lines, ions will have greater difficulty escaping these closed field regions.

As the magnetic field of the planet increases creating a region of closed magnetic field lines, the planet develops a region of plasma protected from stellar wind. This toroidal region of dense cold plasma connects to the top of the ionosphere and is known at Earth as the plasmasphere. The development of the plasmasphere is shown in Figure 5.9, where higher densities of planetary ions occur within the planetary dipole field where the motional electric field becomes small. Because the magnetic field stands off the stellar wind, the motional electric field becomes very small within the the plasmasphere. The ion motions are then dominated by gyromotion along the magnetic field

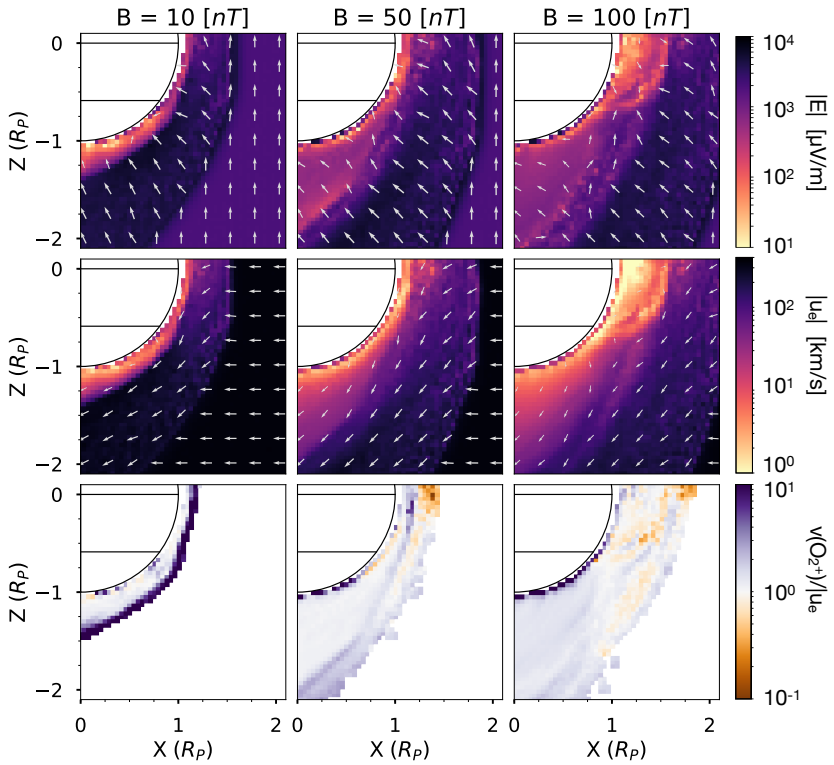

Figure 5.8: Slices in the $y = 0$ plane of motional electric field magnitude (**top**), electron velocity magnitude (**center**), and ratio of the O_2^+ velocity to the electron velocity (**bottom**) for the 10 nT (**left**), 50 nT (**center**), and 100 nT (**right**) simulations, showing the effectiveness of the 50 and 100 nT fields in standing off the stellar wind preventing strong planet-oriented electric fields. White arrows indicate direction of the corresponding vector fields.

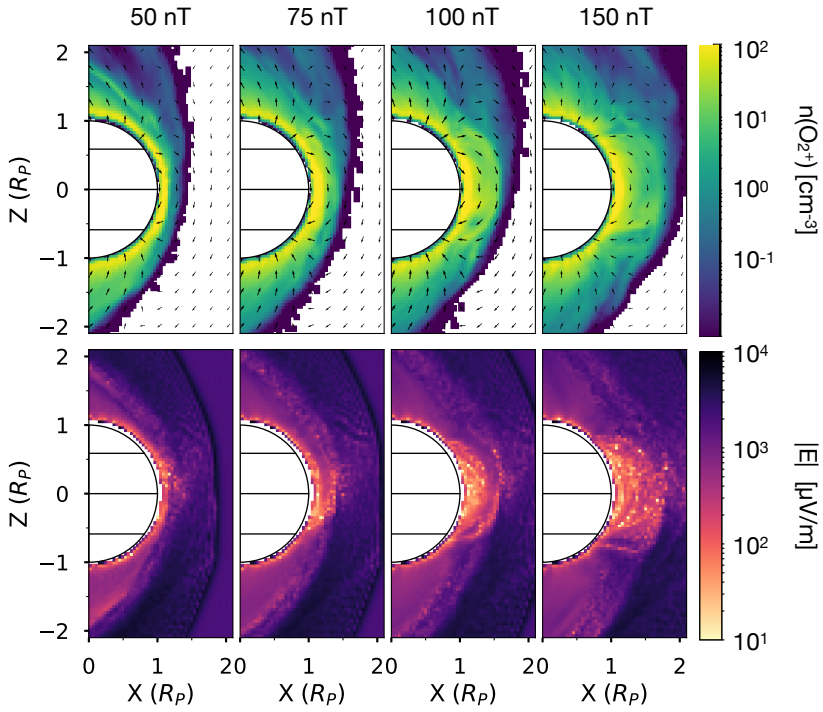

Figure 5.9: Slices in the $y = 0$ plane showing the development of the plasmasphere. O_2^+ number density (**top**) and motional electric field magnitude (**bottom**) for the 50, 75, 100, and 150 nT simulations are shown from left to right, with black arrows over-plotted indicating the direction of the magnetic field.

lines, and thus the ions are trapped within the plasmasphere.

Figure 5.5 shows a best fit scaling relation for the escape rate of the plasmasphere trapping dominated simulations ($\geq$ 50 nT), where $\Phi \propto {B_P}^{-2/3}$ or $\Phi \propto \Omega_c^2$. This is a steeper relationship than typically expected where $\Phi \propto \Omega_c$ [e.g. Gunell, Herbert et al., 2018]. This is likely due to the production rate variation with stellar zenith angle. Because more ions are produced in the equatorial region, the relationship of escape rate with polar cap angle will be steeper than $\Phi \propto \Omega_c$. Thus, the escape rate relationship with magnetic field will be sensitive to the ion production in relation to the magnetic field topology. This is further discussed in Section 5.6.

5.5.4 Mass Flux and Power Coupling

Though intrinsic magnetic fields were long thought to shield atmospheres from being stripped by interaction with a stellar wind, it has also been pointed out recently that intrinsic fields increase the cross-sectional area through which a planet interacts with the wind, and therefore the amount of energy or momentum it could collect from the wind to drive escape [Brain et al., 2013]. A common technique used to discuss the relationship between input and output from a given reservoir is through the idea of a coupling efficiency. This idea has also been used in the context of planetary atmospheres where the mass loss rate ($\dot{M}_{out}$) or the escaping power (P_{out}) are coupled to the mass flux ($\dot{M}_{in}$) or power input (P_{in}) from the stellar wind with some efficiency ϵ [e.g. Strangeway et al., 2005, Dubinin et al., 2006, Ramstad et al., 2017, Egan et al., 2019]. The key questions then become how to define and parameterize the inflow flux/power and identifying the typical efficiency of various processes.

We put this framework in a more general form by including a correlation constant k such that $\dot{M}_{out} = \epsilon(\dot{M}_{in})^k$ (or $P_{out} = \epsilon(P_{in})^k$), where $k = 1$ indicates a traditional linear coupling with a constant efficiency.

We define the inflow properties by scaling the stellar wind parameters with an interaction area defined by the cross-sectional area of the bow shock at the terminator ($x = 0$) as

$$\dot{M}_{in} = A(\rho_{sw} u_{sw}) \tag{5.12}$$

and

$$\dot{P}_{in} = A(\rho_{sw} u_{sw}^3) \tag{5.13}$$

where ρ_{sw} and u_{sw} are the density and velocity of the undisturbed stellar wind. The area A is calculated by identifying the shock boundary in the $x = 0$ plane and summing the corresponding area in the $x = 0$ plane within the boundary. We identify the boundary in this way rather than an area calculated using a symmetric shock radius R_{shock} such that $A = \pi R_{shock}^2$ to account for bow shock asymmetry. As the magnetic field increases the effective obstacle size presented by the planet also increases; this then increases the cross sectional area of the bow shock. The outflow properties are determined in the same method described in earlier in Section 5.5.1.

The resulting inflow and outflow fluxes and power for each simulation are shown in Figure 5.10, as well as the cross sectional areas calculated for each simulation. We find that the cross sectional area increases with magnetic field as roughly $A \propto {B_P}^{0.41}$ or $A \propto R_S^{1.23}$ (by Equation 5.6).

Neither the mass flux nor the power are coupled with a linear efficiency, nor does either relationship show a constant power law correlation over the entire range. This is indicative of the same change in ion escape processes as described in the preceding sections on escape trends, despite a constant scaling in cross-sectional area. For the higher magnetic field values where plasmasphere trapping is the dominant process affecting escape, the mass flux and power correlations have indexes of $k = -1.60$ ($\epsilon = -0.48$) and $k = -1.43$ ($\epsilon = 25.8$) respectively. As the inflow mass (power) scales with area ($A \propto {B_P}^{0.41}$) and the outflow mass (power) scales as $\propto {B_P}^{-0.66}$ ($\propto {B_P}^{-0.6}$), both correlation constants follow straightforwardly.

5.6 Discussion

5.6.1 Stellar Driving Dependence

All the simulations shown in this paper were run with the same nominal Martian solar wind driving; however, stellar winds are dynamic and can dramatically change ion loss [Ramstad et al., 2017, Brain et al., 2017]. Here we discuss the impact of our choice in stellar wind on our results.

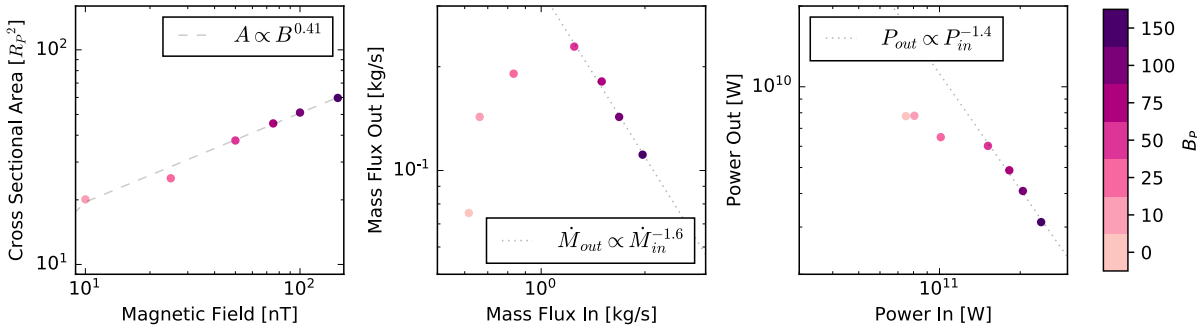

Figure 5.10: Coupling of the inflow and outflow mass fluxes (**center**) and power (**right**). Outflow properties are calculated over a spherical shell far from the planet, while inflow properties are calculated assuming a constant inflow from the stellar wind over an interaction region determined by the cross-sectional area at the terminator (**left**). Dashed lines indicate a coupling of the form $\dot{M}_{out} = \epsilon(\dot{M}_{in})^k$ (or $P_{out} = \epsilon(P_{in})^k$).

As shown in Equation 5.6, the stellar wind pressure controls the standoff distance associated with an intrinsic magnetosphere. The induced magnetosphere boundary has also been shown to depend weakly on dynamic pressure and extreme ultra-violet input, but much less so than the intrinsic magnetosphere [Ramstad et al., 2017]. As the magnetic field associated with the peak escape rate, B_{max}, occurs when the intrinsic magnetosphere reaches the induced magnetosphere, it will also scale with stellar wind pressure as $B_{max} \propto P_{sw}^{1/2}$. Therefore a planet experiencing a stellar wind pressure increase by orders of magnitude, as may be likely for a planet in the habitable zone around an M-dwarf [Vidotto et al., 2015, Garraffo et al., 2017], will have a much larger B_{max}.

As shown in Section 5.4, due to the relative strengths of the planetary dipole and the IMF, the IMF critically affects the magnetic topology of the system. The IMF can be described by a magnitude, the clock angle ϕ (angle in the YZ plane, perpendicular to the sub-stellar line), and the cone angle θ (angle between the IMF and the sub-stellar line). Our study has assumed an IMF that is perpendicular to the dipole axis, thus a motional electric field that is aligned with the dipole axis. In the opposite case where the IMF is aligned with the dipole axis, the southern hemisphere shielding effect would be mitigated as the motional electric field will stand-off or accelerate into the plasmasphere rather than the poles. Thus, there is a critical dependence on the IMF clock angle relative to the dipole axis, necessitating further study for different configurations.

Similarly, the angle between the dipole magnetic field axis and the sub-stellar line also impacts the escape rate relations we have shown here. The ion production method we have chosen is dependent on the stellar zenith angle, such that the highest production occurs at the sub-stellar point. A dramatically different configuration would occur for a planetary pole aligned with this peak in ion production; however, this is a less likely scenario due to spin-orbit alignment. Further, planets orbiting close to their stars have fast orbital velocities. In the case when the orbital velocity is the same as the stellar wind speed, the upstream stellar wind vector and the sub-stellar line have an angle of 45°.

5.6.2 Model Limitations

In a global hybrid model like RHybrid, specific escape rates depend on the inner boundary ionospheric emission rates. The emission rate of inospheric ions is a free parameter, which is fixed by comparing a model to in situ observations from solar system planets [e.g. Jarvinen et al., 2009, 2018]. While we show escape rates here that are comparable to current escape rates at Mars [Lundin et al., 1990, Jakosky, 2017, Brain et al., 2015], we caution against the over-interpretation of these rates due to their dependence on the lower boundary, and instead concentrate on the relative differences.

Furthermore, our implementation of ionospheric emission is driven by a predefined Chapman ion production profile. Currently, accurately resolving ionospheric dynamics on the same domain as the global magnetosphere is computationally infeasible. Although some simulations suites include a one way coupling of an ionosphere implementation to a global magnetosphere [e.g. Glocer et al., 2009a, Brecht et al., 2016, Modolo et al., 2016], we chose to restrict our ionospheric production to a simple approximation. This allows us to focus on the magnetospheric physics associated with an increasing magnetic field, without introducing an additional layer of uncertainty from coupling an additional model.

We have also neglected to include an ionospheric electrodynamics model, and instead use a constant resistivity value above the lower boundary and zero resistivity at the lower boundary. Global thermospheric structure [Roble et al., 1982] and ionospheric-magnetospheric coupling [Ridley et al., 2004] are both affected by ionospheric electrodynamics through mechanisms such as current closure, atmospheric Joule heating, and Alfven wave dissipation.

Impact ionization, neutral structure, and resistivity are all affected by auroral precipitation [Cravens et al., 1995, Deehr et al., 1980, Tinsley, 1979, Robinson et al., 1987, Fuller-Rowell and Evans, 1987], which will change with magnetic field strength. In the weakly magnetized cases we have chosen here the polar cap solid angle (and the corresponding precipitation per area) varies by a factor of a few across the simulations. While this is likely to become important at large magnetic

field strengths (see Section 5.6.2), it is likely a secondary effect behind the basic ion production method we use here.

5.6.3 Comparison With Existing Results

In general our conclusions agree with similar results from previous analytic and numerical studies, but add a deeper understanding of the physics controlling the transition from unmagnetized to weakly magnetized planets.

An analytic study by Gunell, Herbert et al. [2018] showed a similar peak in ion escape rates at the point where the standoff radius reaches the IMB; however, their model enforces a sharp transition in escape processes at this point rather than a gradual build up. This study also uses the typical assumption of linear dependence of ion escape with the polar cap angle, whereas we find a stronger dependence.

Kallio and Barabash [2012a] used a hybrid model to study weakly magnetized planets and found a peak ion escape rate for a Mars-like planet with a 10 nT magnetic field. Our peak escape rate occurs at a higher point due to the stronger stellar wind conditions. Furthermore, the same group studied the magnetic morphology of the same system and found similar trends in tail twisting and IMF control; however, the effects were weaker due to the relative weakness of the IMF in comparison with the dipole strengths for a similar stellar wind pressure [Kallio et al., 2008].

Blackman and Tarduno [2018] studied the impact of magnetic fields on stellar wind erosion of planetary atmospheres using an analytic estimation of the maximum escape rate for a given system. This model assumes there is a direct relationship between the inbound and outbound mass flux, an assumption our results contradict in the weakly magnetized regime; however, they largely concentrate on magnetic fields estimated for ancient Earth, which are larger than those studied here.

Other studies examining the escape rates of exoplanets with and without magnetic fields have been performed [e.g. Dong et al., 2017b]; however, these results are not directly comparable as the magnetic fields studied are much stronger than the range considered here.

5.6.4 Limits of Derived Scaling Laws

In Table 5.2 we summarize the scaling laws we have fit for various parameters from the simulations with $B_P \geq 50$ nT, along with estimations for the lower and upper limits of the power law applicability. Although we can calculate error bars on the scaling relations from the model results, these errors do not reflect the sensitivity of the calculated power law to the model assumptions. Instead, here we discuss some of the main parameters and assumptions these laws are most sensitive to.

As shown in Section 5.4.3, the polar cap solid angle should scale as ${B_P}^{-1/3}$ for large magnetic field values. This matches our calculated scaling law very well, even to small magnetic field values leading us to place an approximate lower limit of $R_S \sim R_P$. While magnetic topology is a fairly straightforward feature to interpret from our models, it is also sensitive to the magnetic dipole orientation with respect to the IMF and sub-stellar line. This relationship does not have a clear upper limit for reasonable values of planetary magnetic field; however, as the polar cap region becomes smaller care must be taken to understand the asymetries and dependence on IMF [e.g. Kabin et al., 2004, Merkin and Goodrich, 2007]

We find a mass loss rate that scales more strongly with magnetic field than predicted, likely due to the variation in ion production with SZA. This result is quite sensitive to the ion production mechanism, as well as the magnetic topology. From the simulations here we have shown the lower limit will be $R_S \simeq R_{IMB}$ or equivalently $B_P \simeq B_{max}$.

The upper limit is more difficult to estimate. First, the power law will become more shallow with decreasing polar cap angle, likely approaching the predicted $\dot{M} \propto \Omega \propto B^{-1/3}$ relationship. Additionally, as the polar cap angle becomes small, cusp dynamics associated with ionospheric electrodynamics and energization from particle precipitation will become more dominant. Strangeway et al. [2005] showed that cusp ionospheric outflow at the Earth is associated with polar cap Poynting flux and electron precipitation leading to Joule dissipation and electron heating, causing increased ion upwelling and subsequent outflow. Both of these effects are associated with a large

power input to a small polar cap area coupling to the ionosphere.

A polar cap solid angle an order of magnitude smaller than our base case will occur at $\Omega_c \sim 0.1 \times 4\pi$, or $P_B \sim (5.26)^6 P_{SW}$. For this set of simulations this would occur for magnetic fields of $B_P \sim 3500$ nT, which is still much smaller than the Earth's surface field, where cusp escape processes are known to be relevant [Li et al., 2012]. While the escaping ion flux may in fact continue to decrease past this point, the dominant physical mechanisms are likely to be quite different due to the intensity of precipitating particle flux in the small auroral region and the scale of the electrodynamic systems.

As shown in Figure 5.5, the average escape energy per particle becomes constant with increasing magnetic field and the corresponding total power of ion outflow decreases as $P_{esc} \propto B^{0.6}$. Thus, if the average energy of escaping particles remains constant, the P_{esc} relationship is determined by the escape flux relationship, and will have the same upper and lower limits. As the escape energy is determined by the stellar wind velocity and corresponding motional electric field, this is likely to be true as long as the wind maintains its momentum through an encounter with the planetary obstacle. This will be true in the absence of significant mass-loading.

The interaction area is found to scale as $A \propto B^{0.41}$, which is shallower than one might expect for an interaction area that scales with a length scale (R_S) squared, or $A \propto B^{2/3}$. While we recover the standoff radius relationship as expected (see Figure 5.3), the interaction area is more sensitive to the stellar wind parameters and corresponding shock properties. Furthermore, the shape of the shock will be affected by the shape of the obstacle; the assumption of a spherically symmetric obstacle is particularly poor for small magnetic field values (as shown in Section 5.4).

5.7 Conclusions

Understanding the influence of planetary magnetic field on ion escape is a critical area for assessing the potential habitability of exoplanets. Here we have presented a systematic study of the influence of a weak magnetic dipole on the plasma environment and corresponding ion escape from a Mars-like exoplanet using a hybrid plasma model.

Parameter	Scaling	Lower Limit	Upper Limit
Ω	$\propto B^{-0.33}$	$R_s < R_P$	N/A
$\dot{M}$	$\propto B^{-0.67}$	$R_s \sim R_{IMB}$, $B \sim B_{max}$	a) may flatten beyond $P_B \sim 35 P_{sw}$ b) cusp dynamics past $P_B \sim (5.26)^6 P_{sw}$
P	$\propto B^{-0.60}$	$R_s \sim R_{IMB}$, $B \sim B_{max}$	a), b)
A	$\propto B^{0.41}$	$R_s \sim R_{IMB}$, $B \sim B_{max}$	Bow shock models needed

Table 5.2: Summary of derived scaling relationships for polar cap solid angle (Ω), mass outflow ($\dot{M}$), escape power (P_{esc}), and bow shock interaction area (A) with magnetic field along with upper and lower limits of the scaling law. Lower limits are calculated empirically from the simulations while upper limits are postulated as in the text.

We have found that an intrinsic magnetic field does not always act to decrease the ion escape rate, and instead leads to an increase in escape rate up until the point where the magnetic standoff reaches the terminator IMB before then beginning to decrease again. This reflects a balance between southern hemisphere shielding of ions from the motional electric field and increased plasmasphere trapping due to smaller polar cap area. The value of the magnetic field associated with maximum ion escape is therefore dependent on the stellar wind pressure.

Where possible we have calculated scaling laws for the relationship of various fundamental quantities and magnetic field. The scaling laws are interpreted in the global context of planetary atmospheric escape theory. Lower limits for these scaling laws have been derived from the simulation results, while upper limits are postulated via predicted limits on the observed processes.

Going forward, more study is needed to assess effects associated with the dynamics of the stellar wind for planets with weak magnetospheres due to the extreme influence of the stellar wind on these systems, as well as a larger array of IMF configurations relative to the planetary dipole. Furthermore, the effects of stronger planetary magnetic fields must be assessed using a simulation platform that fully couples a polar wind model.

Chapter 6

Conclusions

In this thesis I have summarized the state of terrestrial planetary atmospheric escape modeling for solar system planets and exoplanets, compared a variety of Martian plasma models to each other and to MAVEN data to understand how the choice in model affects the interpretation of results, used a global hybrid plasma model to examine the influence of the stellar drivers on the plasma environment and ion escape, and used the same model to analyze the effect of an intrinsic planetary magnetic field on the plasma environment and ion escape. These studies have key implications for both planetary and exoplanetary science. Here I discuss these conclusions and opportunities for future work.

6.1 Exoplanetary Science

6.1.1 Stellar Influence

Chapter 4 describes a study where a global hybrid plasma model was used to analyze the influence of stellar drivers on the plasma environment and ion escape from a Mars-like terrestrial exoplanet. The stellar drivers were selected such that they changed from the well understood case of the nominal Martian solar wind today, to stellar conditions experienced by a planet in the habitable zone of an M-dwarf. First the IMF was rotated to be quasi-parallel to the subsolar line, then the stellar dynamic and magnetic pressure were increased by a factor of ~ 700, then the dynamic pressure increased another order of magnitude, and finally the EUV was increased by a factor of 100. Our conclusions were:

- Changing the IMF cone angle has critical effects on ion loss rates and morphology
- Quasi-parallel IMFs drive East-West loss asymmetry. This asymmetry may have observable consequences for the atmospheres of tidally locked planets
- With increased stellar wind dynamic pressure by two orders of magnitude ion loss began to be limited by the available supply of of ions to the ionosphere with roughly half of all produced ions being lost
- Increasing EUV from the star minimizes the effect of ion production limitations by driving more ion production and allowing increased escape

While other studies have been performed looking at ion loss for exoplanets around M-dwarfs [e.g. Dong et al., 2017b, Cohen et al., 2015, Garcia-Sage et al., 2017], this is the first study to systematically examine the individual effects of each physical parameter associated with the stellar driving. This approach has the advantage of allowing us to understand the scaling and the limitations, rather than computing a single predicted escape rate. This allows our results to be generalized beyond a single system.

6.1.2 Magnetic Field Influence

In Chapter 5 I discuss a study of the influence of a weak intrinsic planetary magnetic field on the planetary plasma environment and ion escape for an equatorial IMF. We have found that:

- An intrinsic magnetic field does not always act to decrease the ion escape rate, and instead leads to an increase in escape rate up until the point where the magnetic standoff reaches the terminator IMB before then beginning to decrease again
- The escape rate increase at lower magnetic field strengths is driven by southern ($-\vec{E_{SW}}$) hemisphere shielding of ions from the motional electric field
- The escape rate decrease at larger magnetic field strengths is caused by increased plasmasphere trapping due to smaller polar cap area

- Due to the relationship between escape and the magnetic standoff distance and the IMB, the value of the magnetic field associated with maximum ion escape is dependent on the solar wind pressure as $R_S \propto P_{SW}^{-1/6}$.

- Scaling laws for ion escape rate, escape power, effective interaction area, and polar cap area with magnetic field were calculated and interpreted in the global context of planetary atmospheric escape theory.

- The polar cap area follows a power law distribution that follows from expectations for a standoff distance large compared to the planet, even for small magnetic fields

- After the magnetic standoff distance reaches the IMB the escape rates and escape power show slightly steeper decreases with magnetic field than expected from theory due to the variation in ion production with SZA

- Lower limits for these scaling laws have been derived from the simulation results, while upper limits are postulated via predicted limits on the observed processes

Finding an increase in escape rate for small magnetic fields contradicts conventional wisdom that a planetary magnetic field always acts to shield a planet from atmospheric erosion (the "planetary umbrella hypothesis"). They also do not agree with a more recent idea that ion escape will scale with energy input from the the stellar wind, and therefore with effective collecting area. While these patterns of ion increase or decrease with magnetic field are seen in certain regimes, understanding the overall behavior requires a deeper understanding of the physics that is driving the acceleration of ions.

This is important for understanding the connection of a planetary magnetic field (or lack thereof) with habitability of exoplanets. While there have been previous studies using both global plasma models [e.g. Dong et al., 2017b, Kallio and Barabash, 2012a, Sakai et al., 2018] and analytic methods [e.g. Gunell, Herbert et al., 2018, Blackman and Tarduno, 2018] on the influence of planetary magnetic fields on ion escape, this is the most systematic modeling study over a range of weak

magnetic fields and the first determination of scaling laws with magnetic field from simulations.

6.2 Planetary Science

6.2.1 Model Comparison

Chapter 3 describes the model comparison study where a variety of plasma models were run with identical input conditions and compared to each other and corresponding MAVEN data. This study includes models that have been substantially updated since the last model comparison challenge [Brain et al., 2010], compares a wider variety of models than Regoli et al. [2018], and is the first study to also compare a variety of models to in-situ MAVEN data. We summarize our conclusions as follows:

- Most models showed little boundary asymmetry due to the IMF being nearly completely in the $+y$ direction
- The overall extent of the shocked region was larger in the fluid models than both the empirical boundaries and the MAVEN results, while the hybrid models matched the outbound crossing very well
- Low altitude ion data on the dayside from NGIMS is well produced (both in overall normalization and scale height) by all models have an inner boundary lower than $\sim$200 km, including all BATSRUS models and HELIOSARES
- Outflow of cold ions in the southern hemisphere varied substantially across models; this outflow was much denser and more localized in the HELIOSARES model than the BATSRUS model
- All models that allow for finite ion gyroradii effects show a plume feature; this feature varies substantially accross the models
- Despite these differences overall global escape rates were relatively constant

Together these conclusions imply that while there is remarkable consistency across models in some well-studied regimes where simple physics dominates (e.g. low altitude dayside ions), there is still substantial variability in other features (e.g. southern hemisphere or tail escape). These differences arise from both lower boundary implementations and model physics. It is imperative that the choice of model must be carefully considered for the region and relevant physics one is interested in.

6.2.2 Early Solar System

The conclusions listed in Sections 6.1.1 and 6.1.2 are also relevant to understanding planetary atmospheric evolution in the early solar system. Solar drivers have evolved substantially over system timescales, as discussed in Section 1.4. While the stellar wind discussed in Chapter 4 was selected to be appropriate for a planet in the habitable zone of an M-dwarf, many of the parameters (such as increase in EUV and dynamic pressure) may also be relevant for Mars in the early solar system. Therefore, all arguments about understanding the limitations of scaling ion loss with stellar drivers are also important to consider when tracing Mars' atmospheric evolution back in time.

Similarly, remnant crustal fields on Mars may imply that Mars may have had an intrinsic global magnetic field in the past [Acuna et al., 1998, Connerney et al., 2001]. Thus, determining the influence of a weak global magnetic field on ion escape is important to understanding Martian atmospheric evolution. Chapter 5 describes the effects of varying the magnetic field of a Mars-like planet encountering a nominal solar wind, and is therefore applicable to the study of ancient Mars.

6.3 Future Work

6.3.1 Model Comparison

The model challenge described in Chapter 3 focused specifically on one orbit with a moderate solar wind and +y directed IMF. Changing input conditions will vary how the solar wind interacts with the ionosphere and likely how variations in model physics appear. Furthermore, we have

limited our analysis to certain regions; more analysis and comparisons with data from additional MAVEN orbits will be necessary to probe other regions such as the tail. Extending our analysis to other regions will allow a more complete understanding of how variations in global morphology are dependent on model choice, and what impact these variations have on global escape rates.

6.3.2 Stellar Influence

Chapter 4 concentrated specifically on understanding the change in stellar parameters from a nominal Martian solar wind to a reconstructed stellar wind experienced by a Trappist-1 exoplanet in the habitable zone. This analysis is inherently limited by considering only a single stellar wind end state. Further study could involve varying the stellar wind parameters in the extreme limit, as well as the planetary parameters. Furthermore, stellar variability is especially important for active M-dwarfs [France et al., 2016]. Future work should focus on modeling the planetary atmospheric response to stellar activity related to flares, coronal mass ejections, and orbital variation. Finally, our model is limited by the simple ionospheric production method; future work should employ a more complete ionospheric coupling to more completely examine the stellar driving effects.

6.3.3 Planetary Magnetic Field

Similar steps are necessary to extend the study of intrinsic planetary magnetic fields. Additional IMF orientations should be studied, including both changes in clock angle and cone angle relative to the planetary dipole. Clock angle, particularly the direction of the motional electric field in comparison with the dipole magnetic field, will change the size of the magnetosphere and the efficiency of mis-aligned ion pickup resulting in an increase in ion escape with magnetic field. Dynamics of the solar wind should be considered due to the extreme influence of the solar wind on these systems. A more detailed ionospheric coupling model should be used to assess the influence of the magnetic field on the ionosphere, and the subsequent connection to ion escape. Furthermore, the effects of stronger planetary magnetic fields must be assessed using a simulation platform that fully couples a polar wind model [Garcia-Sage et al., 2017, e.g].

6.3.4 Planetary Properties

In addition to follow-up studies varying external influences, additional planetary properties should be considered. All chapters presented here consider a base case of Mars today, as it is a comparatively well-understood and well-observed system; however, to truly understand ion escape a larger variety of planetary systems should be studied. The planetary mass and radius as well as the atmospheric composition and pressure are important parameters to understand. Using Earth and Venus as additional data points in the magnetic field/planetary radius/atmospheric composition parameter space will allow constraints of such models.

6.3.5 Understanding Evolution through Time

Thus far we have discussed the straightforward follow up studies necessary to extend the work we have discussed here; however, to truly understand planetary atmospheric evolution these models of ion escape must be connected to the larger picture. As described in Section 1.4, the current state of solar system atmospheric loss estimates involve scaling current loss rates with predicted variations in stellar drivers. Here we quantify some of the scaling expected with stellar drivers and magnetic field. Additionally, this work points out various limitations in those scaling estimates due to ion production or diffusion. Future models of atmospheric evolution should take these relationships and limitations into account.

Furthermore, our models primarily consider ion pickup and bulk escape processes, similar models specifically studying the variation of other escape processes with stellar conditions and planetary properties and the limitations therein must also be created. More broadly, integrated models coupling various escape processes, planetary evolution, and stellar evolution will be necessary to fully understand atmospheric evolution and planetary habitability. In the application of such models to exoplanets, the full range of variability must be taken into account such that the discussion of atmospheric sustainability can be more nuanced and include error estimates, rather than a simple binary determinations of whether an atmosphere is stable or not.

Bibliography

M. H. Acuna, J. E. P. Connerney, P. Wasilewski, R. P. Lin, K. A. Anderson, C. W. Carlson, J. McFadden, D. W. Curtis, D. Mitchell, H. Reme, C. Mazelle, J. A. Sauvaud, C. D'Uston, A. Cros, J. L. Medale, S. J. Bauer, P. Cloutier, M. Mayhew, D. Winterhalter, and N. F. Ness. Magnetic Field and Plasma Observations at Mars: Initial Results of. Science, 279:1676, March 1998. doi: 10.1126/science.279.5357.1676.

V. S. Airapetian, A. Glocer, G. V. Khazanov, R. O. P. Loyd, K. France, J. Sojka, W. C. Danchi, and M. W. Liemohn. How Hospitable Are Space Weather Affected Habitable Zones? The Role of Ion Escape. ApJ, 836:L3, February 2017. doi: 10.3847/2041-8213/836/1/L3.

R. Allart, V. Bourrier, C. Lovis, D. Ehrenreich, J. J. Spake, A. Wyttenbach, L. Pino, F. Pepe, D. K. Sing, and A. Lecavelier des Etangs. Spectrally resolved helium absorption from the extended atmosphere of a warm neptune-mass exoplanet. Science, 362(6421):1384–1387, 2018. ISSN 0036-8075. doi: 10.1126/science.aat5879. URL `http://science.sciencemag.org/content/362/6421/1384`.

E. Anders and T. Owen. Mars and Earth: Origin and Abundance of Volatiles. Science, 198:453–465, Nov 1977. doi: 10.1126/science.198.4316.453.

D. E. Anderson, Jr. Mariner 6, 7, and 9 Ultraviolet Spectrometer Experiment: Analysis of hydrogen Lyman alpha data. J. Geophys. Res., 79:1513, 1974. doi: 10.1029/JA079i010p01513.

Jonathon Anderson, Patrick J. Burns, Daniel Milroy, Peter Ruprecht, Thomas Hauser, and Howard Jay Siegel. Deploying rmacc summit: An hpc resource for the rocky mountain region. In Proceedings of the Practice and Experience in Advanced Research Computing 2017 on Sustainability, Success and Impact, PEARC17, pages 8:1–8:7, New York, NY, USA, 2017. ACM. ISBN 978-1-4503-5272-7. doi: 10.1145/3093338.3093379. URL `http://doi.acm.org/10.1145/3093338.3093379`.

G. Anglada-Escudé, P. J. Amado, J. Barnes, Z. M. Berdiñas, R. P. Butler, G. A. L. Coleman, I. de La Cueva, S. Dreizler, M. Endl, B. Giesers, S. V. Jeffers, J. S. Jenkins, H. R. A. Jones, M. Kiraga, M. Kürster, M. J. López-González, C. J. Marvin, N. Morales, J. Morin, R. P. Nelson, J. L. Ortiz, A. Ofir, S.-J. Paardekooper, A. Reiners, E. Rodríguez, C. Rodríguez-López, L. F. Sarmiento, J. P. Strachan, Y. Tsapras, M. Tuomi, and M. Zechmeister. A terrestrial planet candidate in a temperate orbit around Proxima Centauri. Nature, 536:437–440, August 2016. doi: 10.1038/nature19106.

J. Arkani-Hamed. A coherent model of the crustal magnetic field of Mars. Journal of Geophysical Research (Planets), 109:E09005, September 2004. doi: 10.1029/2004JE002265.

Sushil K Atreya, Melissa G Trainer, Heather B Franz, Michael H Wong, Heidi LK Manning, Charles A Malespin, Paul R Mahaffy, Pamela G Conrad, Anna E Brunner, Laurie A Leshin, et al. Primordial argon isotope fractionation in the atmosphere of mars measured by the sam instrument on curiosity and implications for atmospheric loss. Geophysical Research Letters, 40 (21):5605–5609, 2013.

W. I. Axford. The polar wind and the terrestrial helium budget. Journal of Geophysical Research (1896-1977), 73(21):6855–6859, 1968. doi: 10.1029/JA073i021p06855. URL https://agupubs.onlinelibrary.wiley.com/doi/abs/10.1029/JA073i021p06855.

Utkarsh Ayachit. The ParaView Guide: A Parallel Visualization Application. Kitware, Inc., USA, 2015. ISBN 1930934300, 9781930934306.

S. I. Babichenko, E. V. Deregusov, V. G. Kurt, N. N. Romanova, V. A. Skliankin, A. S. Smirnov, J. J. Bertaux, and J. Blamont. Measurements in interplanetary space and in the Martian upper atmosphere with a hydrogen absorption-cell spectrophotometer for L-alpha radiation on-board Mars 4-7 spaceprobes. Space Science Instrumentation, 3:271–286, November 1977.

Thorsten Bagdonat and Uwe Motschmann. From a Weak to a Strong Comet - 3d Global Hybrid Simulation Studies. Earth Moon and Planets, 90:305–321, Jun 2002. doi: 10.1023/A:1021578232282.

F. Bagenal. Planetary Magnetospheres, pages 251–307. Springer Netherlands, Dordrecht, 2013. ISBN 978-94-007-5606-9. doi: 10.1007/978-94-007-5606-9_6. URL https://doi.org/10.1007/978-94-007-5606-9_6.

Faez Bakalian and Richard E. Hartle. Monte Carlo computations of the escape of atomic nitrogen from Mars. Icarus, 183:55–68, Jul 2006. doi: 10.1016/j.icarus.2006.02.004.

P. M. Banks and T. E. Holzer. Charge exchange and ion diffusion for thermal nonequilibrium conditions. Planet. Space Sci., 16:1019–1022, August 1968. doi: 10.1016/0032-0633(68)90018-4.

Peter M. Banks and Thomas E. Holzer. The polar wind. Journal of Geophysical Research (1896-1977), 73(21):6846–6854, 1968. doi: 10.1029/JA073i021p06846. URL https://agupubs.onlinelibrary.wiley.com/doi/abs/10.1029/JA073i021p06846.

S. Barabash, A. Fedorov, J. J. Sauvaud, R. Lundin, C. T. Russell, Y. Futaana, T. L. Zhang, H. Andersson, K. Brinkfeldt, A. Grigoriev, M. Holmström, M. Yamauchi, K. Asamura, W. Baumjohann, H. Lammer, A. J. Coates, D. O. Kataria, D. R. Linder, C. C. Curtis, K. C. Hsieh, B. R. Sandel, M. Grande, H. Gunell, H. E. J. Koskinen, E. Kallio, P. Riihelä, T. Säles, W. Schmidt, J. Kozyra, N. Krupp, M. Fränz, J. Woch, J. Luhmann, S. McKenna-Lawlor, C. Mazelle, J.-J. Thocaven, S. Orsini, R. Cerulli-Irelli, M. Mura, M. Milillo, M. Maggi, E. Roelof, P. Brandt, K. Szego, J. D. Winningham, R. A. Frahm, J. Scherrer, J. R. Sharber, P. Wurz, and P. Bochsler. The loss of ions from Venus through the plasma wake. Nature, 450:650–653, November 2007a. doi: 10.1038/nature06434.

Saas Barabash, Andrei Fedorov, Rickrdd Lundin, and J.-A. Sauvaud. Martian Atmospheric Erosion Rates. Science, 315:501, January 2007b. doi: 10.1126/science.1134358.

Saas Barabash, Andrei Fedorov, Rickrdd Lundin, and J.-A. Sauvaud. Martian Atmospheric Erosion Rates. Science, 315:501, January 2007c. doi: 10.1126/science.1134358.

Stas Barabash, Andrei Fedorov, Rickard Lundin, and Jean-Andre Sauvaud. Martian atmospheric erosion rates. Science, 315(5811):501–503, 2007. ISSN 0036-8075. doi: 10.1126/science.1134358. URL http://science.sciencemag.org/content/315/5811/501.

R. Barnes, V. S. Meadows, and N. Evans. Comparative Habitability of Transiting Exoplanets. ApJ, 814:91, December 2015. doi: 10.1088/0004-637X/814/2/91.

R. Barnes, R. Deitrick, R. Luger, P. E. Driscoll, T. R. Quinn, D. P. Fleming, B. Guyer, D. V. McDonald, V. S. Meadows, G. Arney, D. Crisp, S. D. Domagal-Goldman, D. Foreman-Mackey, N. A. Kaib, A. Lincowski, J. Lustig-Yaeger, and E. Schwieterman. The Habitability of Proxima Centauri b I: Evolutionary Scenarios. ArXiv e-prints, August 2016.

R. Barnes, R. Deitrick, R. Luger, P. Driscoll, D. Fleming, T. Quinn, H. Smotherman, R. Garcia, D. McDonald, C. Wilhelm, and B. Guyer. Vplanet: Virtual planet simulator. Astrophysics Source Code Library, November 2018.

W. Baumjohann and R. A. Treumann. Basic space plasma physics. 1996. doi: 10.1142/p015.

M. Benna, P. R. Mahaffy, J. M. Grebowsky, J. L. Fox, R. V. Yelle, and B. M. Jakosky. First measurements of composition and dynamics of the Martian ionosphere by MAVEN's Neutral Gas and Ion Mass Spectrometer. Geophysical Research Letters, 42:8958–8965, Nov 2015. doi: 10.1002/2015GL066146.

Mehdi Benna, Mario H. Acuña, Brian J. Anderson, Stanislav Barabash, Scott A. Boardsen, George Gloeckler, Robert E. Gold, George C. Ho, Haje Korth, Stamatios M. Krimigis, Ralph L. McNutt, Jim M. Raines, Menelaos Sarantos, James A. Slavin, Sean C. Solomon, Tielong L. Zhang, and Thomas H. Zurbuchen. Modeling the response of the induced magnetosphere of Venus to changing IMF direction using MESSENGER and Venus Express observations. Geophysical Research Letters, 36:L04109, Feb 2009. doi: 10.1029/2008GL036718.

J. L. Bertaux and J. T. Clarke. Deuterium content of the Venus atmosphere. Nature, 338:567–568, Apr 1989. doi: 10.1038/338567a0.

Jean-Loup Bertaux, Oleg Korablev, Severine Perrier, Eric Quemerais, Franck Montmessin, François Leblanc, Sébastien Lebonnois, Pascal Rannou, Franck Lefèvre, François Forget, et al. Spicam on mars express: Observing modes and overview of uv spectrometer data and scientific results. Journal of Geophysical Research: Planets, 111(E10), 2006.

C Bertucci, C Mazelle, MH Acuña, CT Russell, and JA Slavin. Structure of the magnetic pileup boundary at mars and venus. J Geophys Res Space Phys 1978 2012, 110(A1), 2005. ISSN 2156-2202. doi: 10.1029/2004JA010592.

Anil Bhardwaj, SV Mohankumar, Tirtha Pratim Das, P Pradeepkumar, P Sreelatha, B Sundar, Amarnath Nandi, Dinakar Prasad Vajja, MB Dhanya, Neha Naik, et al. Menca experiment aboard indias mars orbiter mission. Current Science, 109(6):1106–1113, 2015.

D. Bhattacharyya, J. T. Clarke, J.-L. Bertaux, J.-Y. Chaufray, and M. Mayyasi. A strong seasonal dependence in the Martian hydrogen exosphere. Geophys. Res. Lett., 42:8678–8685, October 2015. doi: 10.1002/2015GL065804.

D. Bhattacharyya, J. T. Clarke, J. Y. Chaufray, M. Mayyasi, J. L. Bertaux, M. S. Chaffin, N. M. Schneider, and G. L. Villanueva. Seasonal Changes in Hydrogen Escape From Mars Through Analysis of HST Observations of the Martian Exosphere Near Perihelion. Journal of Geophysical Research (Space Physics), 122:11,756–11,764, Nov 2017. doi: 10.1002/2017JA024572.

K. Biemann, T. Owen, D. R. Rushneck, A. L. Lafleur, and D. W. Howarth. The Atmosphere of Mars near the Surface: Isotope Ratios and Upper Limits on Noble Gases. Science, 194:76–78, Oct 1976. doi: 10.1126/science.194.4260.76.

H. K. Biernat, N. V. Erkaev, and C. J. Farrugia. MHD Effects in the Venus Magnetosheath. Advances in Space Research, 26:1587–1591, Jan 2000. doi: 10.1016/S0273-1177(00)00085-5.

J. B. Biersteker and H. E. Schlichting. Atmospheric mass loss due to giant impacts: the importance of the thermal component for hydrogen-helium envelopes. arXiv e-prints, September 2018.

E. G. Blackman and J. A. Tarduno. Mass, energy, and momentum capture from stellar winds by magnetized and unmagnetized planets: implications for atmospheric erosion and habitability. MNRAS, 481:5146–5155, December 2018. doi: 10.1093/mnras/sty2640.

A. Boesswetter, H. Lammer, Y. Kulikov, U. Motschmann, and S. Simon. Non-thermal water loss of the early Mars: 3D multi-ion hybrid simulations. Planet. Space Sci., 58:2031–2043, December 2010. doi: 10.1016/j.pss.2010.10.003.

A. Boesswetter, H. Lammer, Y. Kulikov, U. Motschmann, and S. Simon. Non-thermal water loss of the early mars: 3d multi-ion hybrid simulations. Planetary and Space Science, 58(14):2031 – 2043, 2010. ISSN 0032-0633. doi: https://doi.org/10.1016/j.pss.2010.10.003. URL `http://www.sciencedirect.com/science/article/pii/S0032063310003107`.

A. Boesswetter, H. Lammer, Y. Kulikov, U. Motschmann, and S. Simon. Non-thermal water loss of the early Mars: 3D multi-ion hybrid simulations. Planet. Space Sci., 58:2031–2043, December 2010. doi: 10.1016/j.pss.2010.10.003.

William J. Borucki, David Koch, Gibor Basri, Natalie Batalha, Timothy Brown, Douglas Caldwell, John Caldwell, Jørgen Christensen-Dalsgaard, William D. Cochran, Edna DeVore, Edward W. Dunham, Andrea K. Dupree, Thomas N. Gautier, John C. Geary, Ronald Gilliland, Alan Gould, Steve B. Howell, Jon M. Jenkins, Yoji Kondo, David W. Latham, Geoffrey W. Marcy, Søren Meibom, Hans Kjeldsen, Jack J. Lissauer, David G. Monet, David Morrison, Dimitar Sasselov, Jill Tarter, Alan Boss, Don Brownlee, Toby Owen, Derek Buzasi, David Charbonneau, Laurance Doyle, Jonathan Fortney, Eric B. Ford, Matthew J. Holman, Sara Seager, Jason H. Steffen, William F. Welsh, Jason Rowe, Howard Anderson, Lars Buchhave, David Ciardi, Lucianne Walkowicz, William Sherry, Elliott Horch, Howard Isaacson, Mark E. Everett, Debra Fischer, Guillermo Torres, John Asher Johnson, Michael Endl, Phillip MacQueen, Stephen T. Bryson, Jessie Dotson, Michael Haas, Jeffrey Kolodziejczak, Jeffrey Van Cleve, Hema Chandrasekaran, Joseph D. Twicken, Elisa V. Quintana, Bruce D. Clarke, Christopher Allen, Jie Li, Haley Wu, Peter Tenenbaum, Ekaterina Verner, Frederick Bruhweiler, Jason Barnes, and Andrej Prsa. Kepler Planet-Detection Mission: Introduction and First Results. Science, 327:977, Feb 2010. doi: 10.1126/science.1185402.

A. Bößwetter, T. Bagdonat, U. Motschmann, and K. Sauer. Plasma boundaries at Mars: a 3-D simulation study. Annales Geophysicae, 22:4363–4379, December 2004. doi: 10.5194/angeo-22-4363-2004.

S. Bougher, G. Keating, R. Zurek, J. Murphy, R. Haberle, J. Hollingsworth, and R. T. Clancy. Mars global surveyor aerobraking : atmospheric trends and model interpretation. Advances in Space Research, 23:1887–1897, January 1999. doi: 10.1016/S0273-1177(99)00272-0.

S. W. Bougher, S. Engel, R. G. Roble, and B. Foster. Comparative terrestrial planet thermospheres 3. Solar cycle variation of global structure and winds at solstices. J. Geophys. Res., 105:17669–17692, July 2000. doi: 10.1029/1999JE001232.

S. W. Bougher, J. M. Bell, J. R. Murphy, M. A. Lopez-Valverde, and P. G. Withers. Polar warming in the Mars thermosphere: Seasonal variations owing to changing insolation and dust distributions. Geophysical Research Letters, 33:L02203, Jan 2006. doi: 10.1029/2005GL024059.

S. W. Bougher, T. M. McDunn, K. A. Zoldak, and J. M. Forbes. Solar cycle variability of Mars dayside exospheric temperatures: Model evaluation of underlying thermal balances. Geophys. Res. Lett., 36:L05201, March 2009. doi: 10.1029/2008GL036376.

S. W. Bougher, D. Pawlowski, J. M. Bell, S. Nelli, T. McDunn, J. R. Murphy, M. Chizek, and A. Ridley. Mars Global Ionosphere-Thermosphere Model: Solar cycle, seasonal, and diurnal variations of the Mars upper atmosphere. Journal of Geophysical Research (Planets), 120:311–342, February 2015. doi: 10.1002/2014JE004715.

L. H. Brace, R. F. Theis, and W. R. Hoegy. Plasma clouds above the ionopause of Venus and their implications. Planet. Space Sci., 30:29–37, January 1982. doi: 10.1016/0032-0633(82)90069-1.

D. Brain, S. Barabash, A. Boesswetter, S. Bougher, S. Brecht, G. Chanteur, D. Hurley, E. Dubinin, X. Fang, M. Fraenz, J. Halekas, E. Harnett, M. Holmstrom, E. Kallio, H. Lammer, S. Ledvina, M. Liemohn, K. Liu, J. Luhmann, Y. Ma, R. Modolo, A. Nagy, U. Motschmann, H. Nilsson, H. Shinagawa, S. Simon, and N. Terada. A comparison of global models for the solar wind interaction with Mars. Icarus, 206:139–151, March 2010. doi: 10.1016/j.icarus.2009.06.030.

D. Brain, S. Barabash, A. Boesswetter, S. Bougher, S. Brecht, G. Chanteur, D. Hurley, E. Dubinin, X. Fang, M. Fraenz, J. Halekas, E. Harnett, M. Holmstrom, E. Kallio, H. Lammer, S. Ledvina, M. Liemohn, K. Liu, J. Luhmann, Y. Ma, R. Modolo, A. Nagy, U. Motschmann, H. Nilsson, H. Shinagawa, S. Simon, and N. Terada. A comparison of global models for the solar wind interaction with mars. Icarus, 206(1):139 – 151, 2010. ISSN 0019-1035. doi: https://doi.org/10.1016/j.icarus.2009.06.030. URL `http://www.sciencedirect.com/science/article/pii/S0019103509002723`. Solar Wind Interactions with Mars.

D. Brain, J. McFadden, J. Halekas, J. Connerney, F. Eparvier, D. Mitchell, L. Andersson, B. Jakosky, Y. Dong, H. Egan, T. Weber, Y. Ma, C. Dong, R. Modolo, S. Bougher, and J. Luhmann. Ion Escape Rates from Mars. In EGU General Assembly Conference Abstracts, volume 19 of EGU General Assembly Conference Abstracts, page 11139, April 2017.

D. A. Brain, A. H. Baker, J. Briggs, J. P. Eastwood, J. S. Halekas, and T. D. Phan. Episodic detachment of Martian crustal magnetic fields leading to bulk atmospheric plasma escape. Geophysical Research Letters, 37:L14108, Jul 2010. doi: 10.1029/2010GL043916.

D. A. Brain, F. Leblanc, J. G. Luhmann, T. E. Moore, and F. Tian. Planetary Magnetic Fields and Climate Evolution, pages 487–501. 2013. doi: 10.2458/azu_uapress_9780816530595-ch20.

D. A. Brain, J. P. McFadden, J. S. Halekas, J. E. P. Connerney, S. W. Bougher, S. Curry, C. F. Dong, Y. Dong, F. Eparvier, X. Fang, K. Fortier, T. Hara, Y. Harada, B. M. Jakosky, R. J. Lillis, R. Livi, J. G. Luhmann, Y. Ma, R. Modolo, and K. Seki. The spatial distribution of planetary ion fluxes near Mars observed by MAVEN. Geophys. Res. Lett., 42:9142–9148, November 2015. doi: 10.1002/2015GL065293.

D. A. Brain, F. Bagenal, Y. J. Ma, H. Nilsson, and G. Stenberg Wieser. Atmospheric escape from unmagnetized bodies. Journal of Geophysical Research (Planets), 121:2364–2385, Dec 2016. doi: 10.1002/2016JE005162.

DA Brain, McFadden, JP, JS Halekas, JEP Connerney, SW Bougher, S Curry, CF Dong, Y Dong, F Eparvier, X Fang, K Fortier, T Hara, Y Harada, BM Jakosky, RJ Lillis, R Livi, JG Luhmann, Y Ma, R Modolo, and K Seki. The spatial distribution of planetary ion fluxes near mars observed by MAVEN. Geophys. Res. Lett., 42(21):9142–9148, 2015. ISSN 1944-8007. doi: 10.1002/2015GL065293.

S. H. Brecht and J. R. Ferrante. Global hybrid simulation of unmagnetized planets - Comparison of Venus and Mars. J. Geophys. Res., 96:11, July 1991. doi: 10.1029/91JA00671.

S. H. Brecht and S. A. Ledvina. The loss of water from Mars: Numerical results and challenges. Icarus, 206:164–173, March 2010. doi: 10.1016/j.icarus.2009.04.028.

S. H. Brecht and S. A. Ledvina. Control of ion loss from Mars during solar minimum. Earth, Planets, and Space, 64:165–178, February 2012. doi: 10.5047/eps.2011.05.037.

S. H. Brecht and S. A. Ledvina. The role of the Martian crustal magnetic fields in controlling ionospheric loss. Geophys. Res. Lett., 41:5340–5346, August 2014. doi: 10.1002/2014GL060841.

S. H. Brecht, S. A. Ledvina, and S. W. Bougher. Ionospheric loss from Mars as predicted by hybrid particle simulations. Journal of Geophysical Research (Space Physics), 121:10, October 2016. doi: 10.1002/2016JA022548.

Stephen Brecht and Stephen Ledvina. The loss of water from mars: Numerical results and challenges. Icarus, 206(1):164–173, 2010. ISSN 0019-1035. doi: 10.1016/j.icarus.2009.04.028.

Stephen Brecht and Stephen Ledvina. Control of ion loss from mars during solar minimum. Earth Planets Space, 64(2):12, 2012. ISSN 1880-5981. doi: 10.5047/eps.2011.05.037.

Stephen H. Brecht and Stephen A. Ledvina. The solar wind interaction with the martian ionosphere/atmosphere. Space Science Reviews, 126(1):15–38, Oct 2006. ISSN 1572-9672. doi: 10.1007/s11214-006-9084-z. URL https://doi.org/10.1007/s11214-006-9084-z.

Stephen H. Brecht, Stephen A. Ledvina, and Stephen W. Bougher. Ionospheric loss from mars as predicted by hybrid particle simulations. Journal of Geophysical Research: Space Physics, 121 (10):10,190–10,208, 2016. ISSN 2169-9402. doi: 10.1002/2016JA022548. URL http://dx.doi.org/10.1002/2016JA022548. 2016JA022548.

H. S. Bridge, A. J. Lazarus, C. W. Snyder, E. J. Smith, Jr. Davis, L., Jr. Coleman, P. J., and D. E. Jones. Mariner V: Plasma and Magnetic Fields Observed near Venus. Science, 158:1669–1673, Dec 1967. doi: 10.1126/science.158.3809.1669.

Henry C. Brinton, Joseph M. Grebowsky, and Hans G. Mayr. Altitude variation of ion composition in the midlatitude trough region: Evidence for upward plasma flow. Journal of Geophysical Research (1896-1977), 76(16):3738–3745, 1971. doi: 10.1029/JA076i016p03738. URL https://agupubs.onlinelibrary.wiley.com/doi/abs/10.1029/JA076i016p03738.

J. C. Cain, B. B. Ferguson, and D. Mozzoni. An n = 90 internal potential function of the Martian crustal magnetic field. Journal of Geophysical Research (Planets), 108:5008, February 2003. doi: 10.1029/2000JE001487.

M. S. Chaffin, J.-Y. Chaufray, I. Stewart, F. Montmessin, N. M. Schneider, and J.-L. Bertaux. Unexpected variability of Martian hydrogen escape. Geophys. Res. Lett., 41:314–320, January 2014. doi: 10.1002/2013GL058578.

M. S. Chaffin, J. Y. Chaufray, J. Deighan, N. M. Schneider, M. Mayyasi, J. T. Clarke, E. Thiemann, S. K. Jain, M. M. J. Crismani, A. Stiepen, F. G. Eparvier, W. E. McClintock, A. I. F. Stewart, G. M. Holsclaw, F. Montmessin, and B. M. Jakosky. Mars h escape rates derived from maven/iuvs lyman alpha brightness measurements and their dependence on model assumptions. Journal of Geophysical Research: Planets, 123(8):2192–2210, 2018. doi: 10.1029/2018JE005574. URL https://agupubs.onlinelibrary.wiley.com/doi/abs/10.1029/2018JE005574.

L. Chai, W. Wan, Y. Wei, T. Zhang, W. Exner, M. Fraenz, E. Dubinin, M. Feyerabend, U. Motschmann, Y. Ma, J. S. Halekas, Y. Li, Z. Rong, and J. Zhong. The Induced Global Looping Magnetic Field on Mars. ApJ, 871:L27, February 2019. doi: 10.3847/2041-8213/aaff6e.

J. W. Chamberlain. Planetary coronae and atmospheric evaporation. Planet. Space Sci., 11:901–960, August 1963. doi: 10.1016/0032-0633(63)90122-3.

J. W. Chamberlain. Charge exchange in a planetary corona - Its effect on the distribution and escape of hydrogen. J. Geophys. Res., 82:1–9, January 1977. doi: 10.1029/JA082i001p00001.

Joseph W. Chamberlain. Charge exchange in a planetary corona: Its effect on the distribution and escape of hydrogen. Journal of Geophysical Research (1896-1977), 82(1):1–9, 1977. doi: 10.1029/JA082i001p00001. URL https://agupubs.onlinelibrary.wiley.com/doi/abs/10.1029/JA082i001p00001.

S. Chapman and H. Zirin. Notes on the Solar Corona and the Terrestrial Ionosphere. Smithsonian Contributions to Astrophysics, 2:1, 1957.

D. Charbonneau, T. M. Brown, R. W. Noyes, and R. L. Gilliland. Detection of an Extrasolar Planet Atmosphere. ApJ, 568:377–384, March 2002. doi: 10.1086/338770.

Eric Chassefire, Benoit Langlais, Yoann Quesnel, and Franois Leblanc. The fate of early mars' lost water: The role of serpentinization. Journal of Geophysical Research: Planets, 118(5):1123–1134, 2013. doi: 10.1002/jgre.20089. URL https://agupubs.onlinelibrary.wiley.com/doi/abs/10.1002/jgre.20089.

J. Y. Chaufray, J. L. Bertaux, F. Leblanc, and E. Quémerais. Observation of the hydrogen corona with SPICAM on Mars Express. Icarus, 195:598–613, June 2008. doi: 10.1016/j.icarus.2008.01.009.

Yue Chen. Effects of the charge exchange of solar wind with the martian exosphere. PhD thesis, RICE UNIVERSITY, Nov 2003.

J. T. Clarke, J.-L. Bertaux, J.-Y. Chaufray, G. R. Gladstone, E. Quemerais, J. K. Wilson, and D. Bhattacharyya. A rapid decrease of the hydrogen corona of Mars. Geophys. Res. Lett., 41: 8013–8020, November 2014. doi: 10.1002/2014GL061803.

P. A. Cloutier, C. C. Law, D. H. Crider, P. W. Walker, Y. Chen, M. H. Acuña, J. E. P. Connerney, R. P. Lin, K. A. Anderson, D. L. Mitchell, C. W. Carlson, J. McFadden, D. A. Brain, H. Rème, C. Mazelle, J. A. Sauvaud, C. d'Uston, D. Vignes, S. J. Bauer, and N. F. Ness. Venus-like interaction of the solar wind with Mars. Geophys. Res. Lett., 26:2685–2688, 1999. doi: 10.1029/1999GL900591.

P.A. Cloutier, R.E. Daniell, and D.M. Butler. Atmospheric ion wakes of venus and mars in the solar wind. Planetary and Space Science, 22(6):967 – 990, 1974. ISSN 0032-0633. doi: https://doi.org/10.1016/0032-0633(74)90166-4. URL http://www.sciencedirect.com/science/article/pii/0032063374901664.

A. J. Coates, A. Wellbrock, G. R. Lewis, C. S. Arridge, F. J. Crary, D. T. Young, M. F. Thomsen, D. B. Reisenfeld, Jr. Sittler, E. C., R. E. Johnson, K. Szego, Z. Bebesi, and G. H. Jones. Cassini in Titan's tail: CAPS observations of plasma escape. Journal of Geophysical Research (Space Physics), 117:A05324, May 2012. doi: 10.1029/2012JA017595.

O. Cohen, J. J. Drake, A. Glocer, C. Garraffo, K. Poppenhaeger, J. M. Bell, A. J. Ridley, and T. I. Gombosi. Magnetospheric Structure and Atmospheric Joule Heating of Habitable Planets Orbiting M-dwarf Stars. ApJ, 790:57, July 2014. doi: 10.1088/0004-637X/790/1/57.

O. Cohen, Y. Ma, J. J. Drake, A. Glocer, C. Garraffo, J. M. Bell, and T. I. Gombosi. The Interaction of Venus-like, M-dwarf Planets with the Stellar Wind of Their Host Star. ApJ, 806:41, June 2015. doi: 10.1088/0004-637X/806/1/41.

K. D. Cole. Theory of some Quiet Magnetospheric [Phenomena related to the Geomagnetic Tail. Nature, 211:1385–1387, September 1966. doi: 10.1038/2111385a0.

J. E. P. Connerney, M. H. Acuña, P. J. Wasilewski, G. Kletetschka, N. F. Ness, H. Rème, R. P. Lin, and D. L. Mitchell. The global magnetic field of Mars and implications for crustal evolution. Geophysical Research Letters, 28:4015–4018, Jan 2001. doi: 10.1029/2001GL013619.

J. E. P. Connerney, J. Espley, P. Lawton, S. Murphy, J. Odom, R. Oliversen, and D. Sheppard. The maven magnetic field investigation. Space Science Reviews, 195(1):257–291, Dec 2015. ISSN 1572-9672. doi: 10.1007/s11214-015-0169-4. URL https://doi.org/10.1007/s11214-015-0169-4.

J. E. P. Connerney, J. Espley, P. Lawton, S. Murphy, J. Odom, R. Oliversen, and D. Sheppard. The MAVEN Magnetic Field Investigation. Space Sci. Rev., 195:257–291, December 2015. doi: 10.1007/s11214-015-0169-4.

T. E. Cravens. A magnetohydrodynamical model of the inner coma of Comet Halley. Journal of Geophysical Research, 94:15025–15040, Nov 1989. doi: 10.1029/JA094iA11p15025.

T. E. Cravens. Physics of Solar System Plasmas. November 2004.

T. E. Cravens, E. Howell, J. H. Waite, and G. R. Gladstone. Auroral oxygen precipitation at Jupiter. Journal of Geophysical Research, 100:17153–17162, Sep 1995. doi: 10.1029/95JA00970.

T. E. Cravens, C. J. Lindgren, and S. A. Ledvina. A two-dimensional multifluid MHD model of Titans plasma environment. Planetary and Space Science, 46:1193–1205, Oct 1998. doi: 10.1016/S0032-0633(98)00051-8.

T. E. Cravens, A. Hoppe, S. A. Ledvina, and S. McKenna-Lawlor. Pickup ions near Mars associated with escaping oxygen atoms. Journal of Geophysical Research (Space Physics), 107:1170, August 2002. doi: 10.1029/2001JA000125.

T. E. Cravens, A. Hoppe, S. A. Ledvina, and S. McKenna-Lawlor. Pickup ions near mars associated with escaping oxygen atoms. Journal of Geophysical Research: Space Physics, 107(A8):SMP 7–1–SMP 7–10, 2002. ISSN 2156-2202. doi: 10.1029/2001JA000125. URL http://dx.doi.org/10.1029/2001JA000125.

J. Cui, X. S. Wu, H. Gu, F. Y. Jiang, and Y. Wei. Photochemical escape of atomic C and N on Mars: clues from a multi-instrument MAVEN dataset. A&A, 621:A23, Jan 2019. doi: 10.1051/0004-6361/201833749.

S. M. Curry, M. Liemohn, X. Fang, Y. Ma, and J. Espley. The influence of production mechanisms on pick-up ion loss at Mars. Journal of Geophysical Research (Space Physics), 118:554–569, Jan 2013. doi: 10.1029/2012JA017665.

S. M. Curry, M. Liemohn, X. Fang, Y. Ma, J. Slavin, J. Espley, S. Bougher, and C. F. Dong. Test particle comparison of heavy atomic and molecular ion distributions at Mars. Journal of Geophysical Research (Space Physics), 119:2328–2344, Mar 2014. doi: 10.1002/2013JA019221.

Shannon M. Curry, Janet Luhmann, Yingjuan Ma, Michael Liemohn, Chuanfei Dong, and Takuya Hara. Comparative pick-up ion distributions at Mars and Venus: Consequences for atmospheric deposition and escape. Planetary and Space Science, 115:35–47, Sep 2015. doi: 10.1016/j.pss.2015.03.026.

Margaret O. Dayhoff, Richard V. Eck, Ellis R. Lippincott, and Carl Sagan. Venus: Atmospheric evolution. Science, 155(3762):556–558, 1967. ISSN 0036-8075. doi: 10.1126/science.155.3762.556. URL http://science.sciencemag.org/content/155/3762/556.

C. de Bergh, B. Bezard, T. Owen, D. Crisp, J. P. Maillard, and B. L. Lutz. Deuterium on Venus: Observations from Earth. Science, 251:547–549, Feb 1991. doi: 10.1126/science.251.4993.547.

C. S. Deehr, G. G. Sivjee, A. Egeland, K. Henriksen, P. E. Sandholt, R. Smith, P. Sweeney, C. Duncan, and J. Gilmer. Ground-based observations of F region aurora associated with the magnetospheric cusp. Journal of Geophysical Research, 85:2185–2192, May 1980. doi: 10.1029/JA085iA05p02185.

P. A. Delamere. Hybrid code simulations of the solar wind interaction with Comet 19P/Borrelly. Journal of Geophysical Research (Space Physics), 111:A12217, Dec 2006. doi: 10.1029/2006JA011859.

G. A. DiBraccio, J. G. Luhmann, S. M. Curry, J. R. Espley, S. Xu, D. L. Mitchell, Y. Ma, C. Dong, J. R. Gruesbeck, J. E. P. Connerney, Y. Harada, S. Ruhunusiri, J. S. Halekas, Y. Soobiah, T. Hara, D. A. Brain, and B. M. Jakosky. The Twisted Configuration of the Martian Magnetotail: MAVEN Observations. Geophys. Res. Lett., 45:4559–4568, May 2018. doi: 10.1029/2018GL077251.

Gina A. DiBraccio, Julian Dann, Jared R. Espley, Jacob R. Gruesbeck, Yasir Soobiah, John E. P. Connerney, Jasper S. Halekas, Yuki Harada, Charles F. Bowers, David A. Brain, Suranga Ruhunusiri, Takuya Hara, and Bruce M. Jakosky. Maven observations of tail current sheet flapping at mars. Journal of Geophysical Research: Space Physics, 122(4):4308–4324, 2017. doi: 10.1002/2016JA023488. URL https://agupubs.onlinelibrary.wiley.com/doi/abs/10.1002/2016JA023488.

C. Dival, E. Kallio, S. Barabash, G. Stenberg, H. Nilsson, Y. Futaana, M. Holmstrm, A. Fedorov, R. A. Frahm, R. Jarvinen, and D. A. Brain. A case study of proton precipitation at mars: Mars express observations and hybrid simulations. Journal of Geophysical Research: Space Physics, 117(A6):n/a–n/a, 2012. ISSN 2156-2202. doi: 10.1029/2012JA017537. URL http://dx.doi.org/10.1029/2012JA017537. A06222.

J.-D. do Nascimento, Jr., A. A. Vidotto, P. Petit, C. Folsom, M. Castro, S. C. Marsden, J. Morin, G. F. Porto de Mello, S. Meibom, S. V. Jeffers, E. Guinan, and I. Ribas. Magnetic Field and Wind of Kappa Ceti: Toward the Planetary Habitability of the Young Sun When Life Arose on Earth. ApJ, 820:L15, March 2016. doi: 10.3847/2041-8205/820/1/L15.

T. M. Donahue and Jr. Hodges, R. R. Past and Present Water Budget of Venus. Journal of Geophysical Research, 97:6083–6091, Apr 1992. doi: 10.1029/92JE00343.

C. Dong, S. W. Bougher, Y. Ma, G. Toth, A. F. Nagy, and D. Najib. Solar wind interaction with Mars upper atmosphere: Results from the one-way coupling between the multifluid MHD model and the MTGCM model. Geophys. Res. Lett., 41:2708–2715, April 2014. doi: 10.1002/2014GL059515.

C. Dong, Y. Ma, S. W. Bougher, G. Toth, A. F. Nagy, J. S. Halekas, Y. Dong, S. M. Curry, J. G. Luhmann, D. Brain, J. E. P. Connerney, J. Espley, P. Mahaffy, M. Benna, J. P. McFadden, D. L. Mitchell, G. A. DiBraccio, R. J. Lillis, B. M. Jakosky, and J. M. Grebowsky. Multifluid MHD study of the solar wind interaction with Mars' upper atmosphere during the 2015 March 8th ICME event. Geophys. Res. Lett., 42:9103–9112, November 2015a. doi: 10.1002/2015GL065944.

C. Dong, Z. Huang, M. Lingam, G. Tóth, T. Gombosi, and A. Bhattacharjee. The Dehydration of Water Worlds via Atmospheric Losses. ApJ, 847:L4, September 2017a. doi: 10.3847/2041-8213/aa8a60.

C. Dong, M. Lingam, Y. Ma, and O. Cohen. Is Proxima Centauri b Habitable? A Study of Atmospheric Loss. ApJ, 837:L26, March 2017b. doi: 10.3847/2041-8213/aa6438.

C. Dong, M. Jin, M. Lingam, V. S. Airapetian, Y. Ma, and B. van der Holst. Atmospheric escape from the TRAPPIST-1 planets and implications for habitability. Proceedings of the National Academy of Science, 115:260–265, January 2018. doi: 10.1073/pnas.1708010115.

Chuanfei Dong, Stephen W. Bougher, Yingjuan Ma, Gabor Toth, Andrew F. Nagy, and Dalal Najib. Solar wind interaction with mars upper atmosphere: Results from the one-way coupling between the multifluid mhd model and the mtgcm model. Geophysical Research Letters, 41(8):2708–2715, 2014. doi: 10.1002/2014GL059515. URL https://agupubs.onlinelibrary.wiley.com/doi/abs/10.1002/2014GL059515.

Chuanfei Dong, Stephen W. Bougher, Yingjuan Ma, Gabor Toth, Yuni Lee, Andrew F. Nagy, Valeriy Tenishev, Dave J. Pawlowski, Michael R. Combi, and Dalal Najib. Solar wind interaction

with the Martian upper atmosphere: Crustal field orientation, solar cycle, and seasonal variations. Journal of Geophysical Research (Space Physics), 120:7857–7872, Sep 2015b. doi: 10.1002/2015JA020990.

Chuanfei Dong, Stephen W. Bougher, Yingjuan Ma, Gabor Toth, Yuni Lee, Andrew F. Nagy, Valeriy Tenishev, Dave J. Pawlowski, Michael R. Combi, and Dalal Najib. Solar wind interaction with the martian upper atmosphere: Crustal field orientation, solar cycle, and seasonal variations. Journal of Geophysical Research: Space Physics, 120(9):7857–7872, 2015. ISSN 2169-9402. doi: 10.1002/2015JA020990. URL http://dx.doi.org/10.1002/2015JA020990. 2015JA020990.

Chuanfei Dong, Yingjuan Ma, Stephen W. Bougher, Gabor Toth, Andrew F. Nagy, Jasper S. Halekas, Yaxue Dong, Shannon M. Curry, Janet G. Luhmann, David Brain, Jack E. P. Connerney, Jared Espley, Paul Mahaffy, Mehdi Benna, James P. McFadden, David L. Mitchell, Gina A. DiBraccio, Robert J. Lillis, Bruce M. Jakosky, and Joseph M. Grebowsky. Multifluid MHD study of the solar wind interaction with Mars' upper atmosphere during the 2015 March 8th ICME event. Geophysical Research Letters, 42:9103–9112, Nov 2015a. doi: 10.1002/2015GL065944.

Y. Dong, X. Fang, D. A. Brain, J. P. McFadden, J. S. Halekas, J. E. Connerney, S. M. Curry, Y. Harada, J. G. Luhmann, and B. M. Jakosky. Strong plume fluxes at Mars observed by MAVEN: An important planetary ion escape channel. Geophysical Research Letters, 42:8942–8950, Nov 2015b. doi: 10.1002/2015GL065346.

Y. Dong, X. Fang, D. A. Brain, J. P. McFadden, J. S. Halekas, J. E. Connerney, S. M. Curry, Y. Harada, J. G. Luhmann, and B. M. Jakosky. Strong plume fluxes at Mars observed by MAVEN: An important planetary ion escape channel. Geophys. Res. Lett., 42:8942–8950, November 2015c. doi: 10.1002/2015GL065346.

Y. Dong, X. Fang, D. A. Brain, J. P. McFadden, J. S. Halekas, J. E. Connerney, S. M. Curry, Y. Harada, J. G. Luhmann, and B. M. Jakosky. Strong plume fluxes at mars observed by maven: An important planetary ion escape channel. Geophysical Research Letters, 42(21):8942–8950, 2015. doi: 10.1002/2015GL065346. URL https://agupubs.onlinelibrary.wiley.com/doi/abs/10.1002/2015GL065346.

Y. Dong, X. Fang, D. A. Brain, J. P. McFadden, J. S. Halekas, J. E. P. Connerney, F. Eparvier, L. Andersson, D. Mitchell, and B. M. Jakosky. Seasonal variability of Martian ion escape through the plume and tail from MAVEN observations. Journal of Geophysical Research (Space Physics), 122:4009–4022, Apr 2017c. doi: 10.1002/2016JA023517.

S. B. Dostovalov and S. D. Chuvakhin. On the Distribution of Neutral Hydrogen in the Upper Atmosphere of Mars. Cosmic Research, 11:687, September 1973.

P. Driscoll and D. Bercovici. Divergent evolution of earth and venus: Influence of degassing, tectonics, and magnetic fields. Icarus, 226(2):1447 – 1464, 2013. ISSN 0019-1035. doi: https://doi.org/10.1016/j.icarus.2013.07.025. URL http://www.sciencedirect.com/science/article/pii/S0019103513003266.

Peter E. Driscoll. Planetary Interiors, Magnetic Fields, and Habitability, pages 2917–2935. Springer International Publishing, Cham, 2018. ISBN 978-3-319-55333-7. doi: 10.1007/978-3-319-55333-7_76. URL https://doi.org/10.1007/978-3-319-55333-7_76.

M Dryer and GR Heckman. On the hypersonic analogue as applied to planetary interaction with the solar plasma. Planet. Space Sci., 1967.

E. Dubinin, M. Fränz, J. Woch, E. Roussos, S. Barabash, R. Lundin, J. D. Winningham, R. A. Frahm, and M. Acuña. Plasma Morphology at Mars. Aspera-3 Observations. Space Sci. Rev., 126:209–238, October 2006. doi: 10.1007/s11214-006-9039-4.

E Dubinin, R Modolo, M Fraenz, J Woch, G Chanteur, F Duru, F Akalin, D Gurnett, R Lundin, S Barabash, et al. Plasma environment of mars as observed by simultaneous mex-aspera-3 and mex-marsis observations. Journal of Geophysical Research: Space Physics, 113(A10), 2008.

E. Dubinin, M. Fraenz, A. Fedorov, R. Lundin, N. Edberg, F. Duru, and O. Vaisberg. Ion Energization and Escape on Mars and Venus. Space Sci. Rev., 162:173–211, Dec 2011. doi: 10.1007/s11214-011-9831-7.

E Dubinin, M Fraenz, M Pätzold, D Andrews, O Vaisberg, L Zelenyi, and S Barabash. Martian ionosphere observed by mars express. 2. influence of solar irradiance on upper ionosphere and escape fluxes. Planetary and Space Science, 145:1–8, 2017.

E. Dubinin, M. Fraenz, M. Pätzold, J. McFadden, J. S. Halekas, G. A. DiBraccio, J. E. P. Connerney, F. Eparvier, D. Brain, B. M. Jakosky, O. Vaisberg, and L. Zelenyi. The Effect of Solar Wind Variations on the Escape of Oxygen Ions From Mars Through Different Channels: MAVEN Observations. Journal of Geophysical Research (Space Physics), 122:11,285–11,301, Nov 2017. doi: 10.1002/2017JA024741.

E. Dubinin, M. Fraenz, M. Ptzold, J. McFadden, J.S. Halekas, J.E.P. Connerney, B.M. Jakosky, O. Vaisberg, and L. Zelenyi. Martian ionosphere observed by maven. 3. influence of solar wind and imf on upper ionosphere. Planetary and Space Science, 160:56 – 65, 2018. ISSN 0032-0633. doi: https://doi.org/10.1016/j.pss.2018.03.016. URL `http://www.sciencedirect.com/science/article/pii/S0032063317304361`.

H. Egan, R. Jarvinen, and D. Brain. Stellar Influence on Heavy Ion Escape from Unmagnetized Exoplanets. MNRAS, March 2019. doi: 10.1093/mnras/stz788.

Hilary Egan, Yingjuan Ma, Chuanfei Dong, Ronan Modolo, Riku Jarvinen, Stephen Bougher, Jasper Halekas, David Brain, James Mcfadden, John Connerney, David Mitchell, and Bruce Jakosky. Comparison of global martian plasma models in the context of maven observations. Journal of Geophysical Research: Space Physics, 123(5):3714–3726, 2018. doi: 10.1029/2017JA025068. URL `https://agupubs.onlinelibrary.wiley.com/doi/abs/10.1029/2017JA025068`.

Hilary Egan, Yingjuan Ma, Chuanfei Dong, Ronan Modolo, Riku Jarvinen, Stephen Bougher, Jasper Halekas, David Brain, James Mcfadden, John Connerney, David Mitchell, and Bruce Jakosky. Comparison of Global Martian Plasma Models in the Context of MAVEN Observations. Journal of Geophysical Research (Space Physics), 123:3714–3726, May 2018. doi: 10.1029/2017JA025068.

Hilary Egan, Riku Jarvinen, and David Brain. Stellar influence on heavy ion escape from unmagnetized exoplanets. submitted 2019.

S. L. England, G. Liu, E. Yiit, P. R. Mahaffy, M. Elrod, M. Benna, H. Nakagawa, N. Terada, and B. Jakosky. Maven ngims observations of atmospheric gravity waves in the martian thermosphere. Journal of Geophysical Research: Space Physics, 122(2):2310–2335, 2017. doi: 10.1002/2016JA023475. URL https://agupubs.onlinelibrary.wiley.com/doi/abs/10.1002/2016JA023475.

E Engwall, A I. Eriksson, C M. Cully, M Andr, Roy Torbert, and H Vaith. Earth's ionospheric outflow dominated by hidden cold plasma. Nature Geoscience, 2:24–27, 01 2009. doi: 10.1038/ngeo387.

J. S. Evans, M. H. Stevens, J. D. Lumpe, N. M. Schneider, A. I. F. Stewart, J. Deighan, S. K. Jain, M. S. Chaffin, M. Crismani, A. Stiepen, W. E. McClintock, G. M. Holsclaw, F. Lefèvre, D. Y. Lo, J. T. Clarke, F. G. Eparvier, E. M. B. Thiemann, P. C. Chamberlin, S. W. Bougher, J. M. Bell, and B. M. Jakosky. Retrieval of CO_2 and N_2 in the Martian thermosphere using dayglow observations by IUVS on MAVEN. Geophys. Res. Lett., 42:9040–9049, November 2015. doi: 10.1002/2015GL065489.

Donald H. Fairfield. Average and unusual locations of the Earth's magnetopause and bow shock. Journal of Geophysical Research, 76:6700, Jan 1971. doi: 10.1029/JA076i028p06700.

X. Fang, M. W. Liemohn, A. F. Nagy, Y. Ma, D. L. De Zeeuw, J. U. Kozyra, and T. H. Zurbuchen. Pickup oxygen ion velocity space and spatial distribution around Mars. Journal of Geophysical Research (Space Physics), 113:A02210, February 2008. doi: 10.1029/2007JA012736.

X. Fang, Y. Ma, D. Brain, Y. Dong, and R. Lillis. Control of Mars global atmospheric loss by the continuous rotation of the crustal magnetic field: A time-dependent MHD study. Journal of Geophysical Research (Space Physics), 120:10, December 2015a. doi: 10.1002/2015JA021605.

Xiaohua Fang, Michael W. Liemohn, Andrew F. Nagy, Yingjuan Ma, Darren L. De Zeeuw, Janet U. Kozyra, and Thomas H. Zurbuchen. Pickup oxygen ion velocity space and spatial distribution around mars. Journal of Geophysical Research: Space Physics, 113(A2):n/a–n/a, 2008a. ISSN 2156-2202. doi: 10.1029/2007JA012736. URL http://dx.doi.org/10.1029/2007JA012736. A02210.

Xiaohua Fang, Michael W. Liemohn, Andrew F. Nagy, Yingjuan Ma, Darren L. De Zeeuw, Janet U. Kozyra, and Thomas H. Zurbuchen. Pickup oxygen ion velocity space and spatial distribution around mars. Journal of Geophysical Research: Space Physics, 113(A2), 2008b. doi: 10.1029/2007JA012736. URL https://agupubs.onlinelibrary.wiley.com/doi/abs/10.1029/2007JA012736.

Xiaohua Fang, Michael W. Liemohn, Andrew F. Nagy, Janet G. Luhmann, and Yingjuan Ma. On the effect of the martian crustal magnetic field on atmospheric erosion. Icarus, 206:130–138, Mar 2010. doi: 10.1016/j.icarus.2009.01.012.

Xiaohua Fang, Michael W Liemohn, Andrew F Nagy, Janet G Luhmann, and Yingjuan Ma. On the effect of the martian crustal magnetic field on atmospheric erosion. pages 130–138, 2010. ISSN 0019-1035. doi: 10.1016/j.icarus.2009.01.012.

Xiaohua Fang, Yingjuan Ma, David Brain, Yaxue Dong, and Robert Lillis. Control of Mars global atmospheric loss by the continuous rotation of the crustal magnetic field: A time-dependent

MHD study. Journal of Geophysical Research (Space Physics), 120:10,926–10,944, Dec 2015b. doi: 10.1002/2015JA021605.

A Fedorov, S Barabash, J-A Sauvaud, Y Futaana, TL Zhang, R Lundin, and C Ferrier. Measurements of the ion escape rates from venus for solar minimum. Journal of Geophysical Research: Space Physics, 116(A7), 2011.

FMI. Rhybrid. URL `https://github.com/fmihpc/rhybrid`.

F. Forget, F. Montmessin, J.-L. Bertaux, F. González-Galindo, S. Lebonnois, E. Quémerais, A. Reberac, E. Dimarellis, and M. A. López-Valverde. Density and temperatures of the upper Martian atmosphere measured by stellar occultations with Mars Express SPICAM. Journal of Geophysical Research (Planets), 114:E01004, January 2009. doi: 10.1029/2008JE003086.

C. M. Fowler, L. Andersson, R. E. Ergun, Y. Harada, T. Hara, G. Collinson, W. K. Peterson, J. Espley, J. Halekas, J. Mcfadden, D. L. Mitchell, C. Mazelle, M. Benna, and B. M. Jakosky. MAVEN Observations of Solar Wind-Driven Magnetosonic Waves Heating the Martian Dayside Ionosphere. Journal of Geophysical Research (Space Physics), 123:4129–4149, May 2018. doi: 10.1029/2018JA025208.

J. L. Fox. The production and escape of nitrogen atoms on Mars. Journal of Geophysical Research, 98:3297–3310, Feb 1993. doi: 10.1029/92JE02289.

J. L. Fox and F. M. Bakalian. Photochemical escape of atomic carbon from Mars. Journal of Geophysical Research, 106:28785–28796, Dec 2001. doi: 10.1029/2001JA000108.

J. L. Fox and A. B. Hać. Photochemical escape of oxygen from Mars: A comparison of the exobase approximation to a Monte Carlo method. Icarus, 204:527–544, December 2009. doi: 10.1016/j.icarus.2009.07.005.

Jane L Fox and Katherine E Yeager. Morphology of the near-terminator martian ionosphere: A comparison of models and data. Journal of Geophysical Research: Space Physics, 111(A10), 2006.

K. France, R. O. P. Loyd, A. Youngblood, A. Brown, P. C. Schneider, S. L. Hawley, C. S. Froning, J. L. Linsky, A. Roberge, A. P. Buccino, J. R. A. Davenport, J. M. Fontenla, L. Kaltenegger, A. F. Kowalski, P. J. D. Mauas, Y. Miguel, S. Redfield, S. Rugheimer, F. Tian, M. C. Vieytes, L. M. Walkowicz, and K. L. Weisenburger. The MUSCLES Treasury Survey. I. Motivation and Overview. ApJ, 820:89, April 2016. doi: 10.3847/0004-637X/820/2/89.

M. Fränz, E. Dubinin, D. Andrews, S. Barabash, H. Nilsson, and A. Fedorov. Cold ion escape from the Martian ionosphere. Planet. Space Sci., 119:92–102, December 2015. doi: 10.1016/j.pss.2015.07.012.

M. Frnz, E. Dubinin, D. Andrews, S. Barabash, H. Nilsson, and A. Fedorov. Cold ion escape from the martian ionosphere. Planetary and Space Science, 119:92 – 102, 2015. ISSN 0032-0633. doi: https://doi.org/10.1016/j.pss.2015.07.012. URL `http://www.sciencedirect.com/science/article/pii/S0032063315002305`.

T. J. Fuller-Rowell and D. S. Evans. Height-integrated Pedersen and Hall conductivity patterns inferred from the TIROS-NOAA satellite data. J. Geophys. Res., 92:7606–7618, July 1987. doi: 10.1029/JA092iA07p07606.

E. Gaidos, C. P. Conrad, M. Manga, and J. Hernlund. Thermodynamic Limits on Magnetodynamos in Rocky Exoplanets. ApJ, 718:596–609, August 2010. doi: 10.1088/0004-637X/718/2/596.

K. Garcia-Sage, A. Glocer, J. J. Drake, G. Gronoff, and O. Cohen. On the Magnetic Protection of the Atmosphere of Proxima Centauri b. ApJ, 844:L13, July 2017. doi: 10.3847/2041-8213/aa7eca.

C. Garraffo, J. J. Drake, and O. Cohen. The Space Weather of Proxima Centauri b. ApJ, 833:L4, December 2016. doi: 10.3847/2041-8205/833/1/L4.

C. Garraffo, J. J. Drake, O. Cohen, J. D. Alvarado-Gómez, and S. P. Moschou. The Threatening Magnetic and Plasma Environment of the TRAPPIST-1 Planets. ApJ, 843:L33, July 2017. doi: 10.3847/2041-8213/aa79ed.

M. Gillon, E. Jehin, S. M. Lederer, L. Delrez, J. de Wit, A. Burdanov, V. Van Grootel, A. J. Burgasser, A. H. M. J. Triaud, C. Opitom, B.-O. Demory, D. K. Sahu, D. Bardalez Gagliuffi, P. Magain, and D. Queloz. Temperate Earth-sized planets transiting a nearby ultracool dwarf star. Nature, 533:221–224, May 2016. doi: 10.1038/nature17448.

M. Gillon, A. H. M. J. Triaud, B.-O. Demory, E. Jehin, E. Agol, K. M. Deck, S. M. Lederer, J. de Wit, A. Burdanov, J. G. Ingalls, E. Bolmont, J. Leconte, S. N. Raymond, F. Selsis, M. Turbet, K. Barkaoui, A. Burgasser, M. R. Burleigh, S. J. Carey, A. Chaushev, C. M. Copperwheat, L. Delrez, C. S. Fernandes, D. L. Holdsworth, E. J. Kotze, V. Van Grootel, Y. Almleaky, Z. Benkhaldoun, P. Magain, and D. Queloz. Seven temperate terrestrial planets around the nearby ultracool dwarf star TRAPPIST-1. Nature, 542:456–460, February 2017. doi: 10.1038/nature21360.

S. Ginzburg, H. E. Schlichting, and R. Sari. Super-Earth Atmospheres: Self-consistent Gas Accretion and Retention. ApJ, 825:29, July 2016. doi: 10.3847/0004-637X/825/1/29.

S. Ginzburg, H. E. Schlichting, and R. Sari. Core-powered mass-loss and the radius distribution of small exoplanets. MNRAS, 476:759–765, May 2018. doi: 10.1093/mnras/sty290.

A. Glocer, G. Tóth, T. Gombosi, and D. Welling. Modeling ionospheric outflows and their impact on the magnetosphere, initial results. Journal of Geophysical Research (Space Physics), 114: A05216, May 2009a. doi: 10.1029/2009JA014053.

A. Glocer, G. Tóth, Y. Ma, T. Gombosi, J.-C. Zhang, and L. M. Kistler. Multifluid Block-Adaptive-Tree Solar wind Roe-type Upwind Scheme: Magnetospheric composition and dynamics during geomagnetic storms: Initial results. Journal of Geophysical Research (Space Physics), 114:A12203, December 2009b. doi: 10.1029/2009JA014418.

T. I. Gombosi. Preshock region acceleration of implanted cometary H^+ and O^+. Journal of Geophysical Research, 93:35–47, Jan 1988. doi: 10.1029/JA093iA01p00035.

F. González-Galindo, F. Forget, M. A. López-Valverde, M. Angelats I Coll, and S. W. Bougher. LMD-MGCM: The First Ground-to-Exosphere General Circulation Model of the Martian Atmosphere. In Seventh International Conference on Mars, volume 1353 of LPI Contributions, page 3099, July 2007.

F. González-Galindo, F. Forget, M. Angelats I Coll, and M. A. López-Valverde. The Martian upper atmosphere. Lecture Notes and Essays in Astrophysics, 3:151–162, December 2008.

F González-Galindo, F Forget, MA López-Valverde, M Angelats i Coll, and E Millour. A ground-to-exosphere martian general circulation model: 1. seasonal, diurnal, and solar cycle variation of thermospheric temperatures. Journal of Geophysical Research: Planets, 114(E4), 2009.

H. Gröller, R. V. Yelle, T. T. Koskinen, F. Montmessin, G. Lacombe, N. M. Schneider, J. Deighan, A. I. F. Stewart, S. K. Jain, M. S. Chaffin, M. M. J. Crismani, A. Stiepen, F. Lefèvre, W. E. McClintock, J. T. Clarke, G. M. Holsclaw, P. R. Mahaffy, S. W. Bougher, and B. M. Jakosky. Probing the Martian atmosphere with MAVEN/IUVS stellar occultations. Geophys. Res. Lett., 42:9064–9070, November 2015. doi: 10.1002/2015GL065294.

H. Gröller, F. Montmessin, R. V. Yelle, F. Lefèvre, F. Forget, N. M. Schneider, T. T. Koskinen, J. Deighan, and S. K. Jain. MAVEN/IUVS Stellar Occultation Measurements of Mars Atmospheric Structure and Composition. Journal of Geophysical Research (Planets), 123:1449–1483, June 2018. doi: 10.1029/2017JE005466.

H. Gunell, M. Holmstrm, E. Kallio, P. Janhunen, and K. Dennerl. X rays from solar wind charge exchange at mars: A comparison of simulations and observations. Geophysical Research Letters, 31(22):n/a–n/a, 2004. ISSN 1944-8007. doi: 10.1029/2004GL020953. URL `http://dx.doi.org/10.1029/2004GL020953`. L22801.

H. Gunell, M. Holmström, S. Barabash, E. Kallio, P. Janhunen, A. F. Nagy, and Y. Ma. Planetary ENA imaging: Effects of different interaction models for Mars. Planet. Space Sci., 54:117–131, February 2006. doi: 10.1016/j.pss.2005.04.002.

Gunell, Herbert, Maggiolo, Romain, Nilsson, Hans, Stenberg Wieser, Gabriella, Slapak, Rikard, Lindkvist, Jesper, Hamrin, Maria, and De Keyser, Johan. Why an intrinsic magnetic field does not protect a planet against atmospheric escape. A&A, 614:L3, 2018. doi: 10.1051/0004-6361/201832934. URL `https://doi.org/10.1051/0004-6361/201832934`.

D. A. Gurnett, F. L. Scarf, and W. S. Kurth. The structure of Titan's wake from plasma wave observations. J. Geophys. Res., 87:1395–1403, March 1982. doi: 10.1029/JA087iA03p01395.

DA Gurnett, DL Kirchner, RL Huff, DD Morgan, AM Persoon, TF Averkamp, F Duru, E Nielsen, A Safaeinili, JJ Plaut, et al. Radar soundings of the ionosphere of mars. Science, 310(5756): 1929–1933, 2005.

DA Gurnett, DD Morgan, F Duru, F Akalin, JD Winningham, RA Frahm, E Dubinin, and S Barabash. Large density fluctuations in the martian ionosphere as observed by the mars express radar sounder. Icarus, 206(1):83–94, 2010.

R. M. Haberle, D. Tyler, C. P. McKay, and W. L. Davis. A model for the evolution of CO2 on Mars. Icarus, 109:102–120, May 1994. doi: 10.1006/icar.1994.1079.

P. K. Haff and C. C. Watson. The erosion of planetary and satellite atmospheres by energetic atomic particles. J. Geophys. Res., 84:8436–8442, December 1979. doi: 10.1029/JB084iB14p08436.

J. S. Halekas. Seasonal variability of the hydrogen exosphere of Mars. Journal of Geophysical Research (Planets), 122:901–911, May 2017. doi: 10.1002/2017JE005306.

J. S. Halekas, E. R. Taylor, G. Dalton, G. Johnson, D. W. Curtis, J. P. McFadden, D. L. Mitchell, R. P. Lin, and B. M. Jakosky. The Solar Wind Ion Analyzer for MAVEN. Space Sci. Rev., 195: 125–151, December 2015. doi: 10.1007/s11214-013-0029-z.

J. S. Halekas, S. Ruhunusiri, Y. Harada, G. Collinson, D. L. Mitchell, C. Mazelle, J. P. McFadden, J. E. P. Connerney, J. R. Espley, F. Eparvier, J. G. Luhmann, and B. M. Jakosky. Structure, dynamics, and seasonal variability of the mars-solar wind interaction: Maven solar wind ion analyzer in-flight performance and science results. Journal of Geophysical Research: Space Physics, 122(1):547–578, 2017. ISSN 2169-9402. doi: 10.1002/2016JA023167. URL http://dx.doi.org/10.1002/2016JA023167. 2016JA023167.

E. M. Harnett and R. M. Winglee. Three-dimensional multifluid simulations of ionospheric loss at Mars from nominal solar wind conditions to magnetic cloud events. Journal of Geophysical Research (Space Physics), 111:A09213, September 2006. doi: 10.1029/2006JA011724.

E. M. Harnett and R. M. Winglee. High-resolution multifluid simulations of the plasma environment near the martian magnetic anomalies. Journal of Geophysical Research: Space Physics, 112(A5): n/a–n/a, 2007. ISSN 2156-2202. doi: 10.1029/2006JA012001. URL http://dx.doi.org/10.1029/2006JA012001. A05207.

C. A. Haswell, L. Fossati, T. Ayres, K. France, C. S. Froning, S. Holmes, U. C. Kolb, R. Busuttil, R. A. Street, L. Hebb, A. Collier Cameron, B. Enoch, V. Burwitz, J. Rodriguez, R. G. West, D. Pollacco, P. J. Wheatley, and A. Carter. Near-ultraviolet Absorption, Chromospheric Activity, and Star-Planet Interactions in the WASP-12 system. ApJ, 760:79, November 2012. doi: 10.1088/0004-637X/760/1/79.

Xiangqun He. Hydrogen Escape from the Earth's Atmosphere. PhD thesis, BOSTON UNIVERSITY., Jan 1995.

DP Hinson, RA Simpson, JD Twicken, GL Tyler, and FM Flasar. Initial results from radio occultation measurements with mars global surveyor. Journal of Geophysical Research: Planets, 104(E11):26997–27012, 1999.

J. H. Hoffman, W. H. Dodson, C. R. Lippincott, and H. D. Hammack. Initial ion composition results from the isis 2 satellite. Journal of Geophysical Research (1896-1977), 79(28):4246–4251, 1974. doi: 10.1029/JA079i028p04246. URL https://agupubs.onlinelibrary.wiley.com/doi/abs/10.1029/JA079i028p04246.

J. H. Hoffman, R. R. Hodges, M. B. McElroy, T. M. Donahue, and M. Kolpin. Composition and Structure of the Venus Atmosphere: Results from Pioneer Venus. Science, 205:49–52, Jul 1979. doi: 10.1126/science.205.4401.49.

John H. Hoffman. Studies of the composition of the ionosphere with a magnetic deflection mass spectrometer. International Journal of Mass Spectrometry and Ion Physics, 4(4):315 – 322, 1970. ISSN 0020-7381. doi: https://doi.org/10.1016/0020-7381(70)85047-1. URL http://www.sciencedirect.com/science/article/pii/0020738170850471.

J. L. Hollingsworth, R. M. Haberle, and J. Schaeffer. Seasonal variations of storm zones on Mars. Advances in Space Research, 19:1237–1240, May 1997. doi: 10.1016/S0273-1177(97)00275-5.

MM Huddleston, CR Chappell, DC Delcourt, TE Moore, BL Giles, and MO Chandler. An examination of the process and magnitude of ionospheric plasma supply to the magnetosphere. Journal of Geophysical Research: Space Physics, 110(A12), 2005.

D. L. Huestis, T. G. Slanger, B. D. Sharpee, and J. L. Fox. Chemical origins of the Mars ultraviolet dayglow. Faraday Discussions, 147:307, 2010. doi: 10.1039/c003456h.

D. M. Hunten. The Escape of Light Gases from Planetary Atmospheres. Journal of Atmospheric Sciences, 30:1481–1494, November 1973. doi: 10.1175/1520-0469(1973)030⟨1481:TEOLGF⟩2.0.CO;2.

D. M. Hunten. Thermal and nonthermal escape mechanisms for terrestrial bodies. Planet. Space Sci., 30:773–783, August 1982. doi: 10.1016/0032-0633(82)90110-6.

D. M. Hunten and T. M. Donahue. Hydrogen Loss from the Terrestrial Planets. Annual Review of Earth and Planetary Sciences, 4:265, Jan 1976. doi: 10.1146/annurev.ea.04.050176.001405.

D. M. Hunten, R. O. Pepin, and J. C. G. Walker. Mass fractionation in hydrodynamic escape. Icarus, 69:532–549, March 1987. doi: 10.1016/0019-1035(87)90022-4.

James W. Hurrell. Comparison of ncar community climate model (ccm) climates. Climate Dynamics, 11(1):25–50, Jan 1995. ISSN 1432-0894. doi: 10.1007/BF00220675. URL https://doi.org/10.1007/BF00220675.

Kevin S. Hutchins, Bruce M. Jakosky, and Janet G. Luhmann. Impact of a paleomagnetic field on sputtering loss of Martian atmospheric argon and neon. Journal of Geophysical Research, 102:9183–9190, Jan 1997. doi: 10.1029/96JE03838.

Wing-Huen Ip and Andreas Kopp. MHD simulations of the solar wind interaction with Mercury. Journal of Geophysical Research (Space Physics), 107:1348, Nov 2002. doi: 10.1029/2001JA009171.

B. M. Jakosky and R. J. Phillips. Mars' volatile and climate history. Nature, 412:237–244, July 2001.

B. M. Jakosky, R. O. Pepin, R. E. Johnson, and J. L. Fox. Mars atmospheric loss and isotopic fractionation by solar-wind-induced sputtering and photochemical escape. Icarus, 111:271–288, October 1994. doi: 10.1006/icar.1994.1145.

B. M. Jakosky, R. P. Lin, J. M. Grebowsky, J. G. Luhmann, D. F. Mitchell, G. Beutelschies, T. Priser, M. Acuna, L. Andersson, D. Baird, D. Baker, R. Bartlett, M. Benna, S. Bougher, D. Brain, D. Carson, S. Cauffman, P. Chamberlin, J.-Y. Chaufray, O. Cheatom, J. Clarke, J. Connerney, T. Cravens, D. Curtis, G. Delory, S. Demcak, A. DeWolfe, F. Eparvier, R. Ergun, A. Eriksson, J. Espley, X. Fang, D. Folta, J. Fox, C. Gomez-Rosa, S. Habenicht, J. Halekas, G. Holsclaw, M. Houghton, R. Howard, M. Jarosz, N. Jedrich, M. Johnson, W. Kasprzak, M. Kelley, T. King, M. Lankton, D. Larson, F. Leblanc, F. Lefevre, R. Lillis, P. Mahaffy, C. Mazelle, W. McClintock, J. McFadden, D. L. Mitchell, F. Montmessin, J. Morrissey, W. Peterson, W. Possel, J.-A. Sauvaud, N. Schneider, W. Sidney, S. Sparacino, A. I. F. Stewart, R. Tolson, D. Toublanc, C. Waters, T. Woods, R. Yelle, and R. Zurek. The Mars Atmosphere and Volatile Evolution (MAVEN) Mission. Space Science Reviews, 195:3–48, December 2015a. doi: 10.1007/s11214-015-0139-x.

B. M. Jakosky, R. P. Lin, J. M. Grebowsky, J. G. Luhmann, D. F. Mitchell, G. Beutelschies, T. Priser, M. Acuna, L. Andersson, D. Baird, D. Baker, R. Bartlett, M. Benna, S. Bougher, D. Brain, D. Carson, S. Cauffman, P. Chamberlin, J.-Y. Chaufray, O. Cheatom, J. Clarke,

J. Connerney, T. Cravens, D. Curtis, G. Delory, S. Demcak, A. DeWolfe, F. Eparvier, R. Ergun, A. Eriksson, J. Espley, X. Fang, D. Folta, J. Fox, C. Gomez-Rosa, S. Habenicht, J. Halekas, G. Holsclaw, M. Houghton, R. Howard, M. Jarosz, N. Jedrich, M. Johnson, W. Kasprzak, M. Kelley, T. King, M. Lankton, D. Larson, F. Leblanc, F. Lefevre, R. Lillis, P. Mahaffy, C. Mazelle, W. McClintock, J. McFadden, D. L. Mitchell, F. Montmessin, J. Morrissey, W. Peterson, W. Possel, J.-A. Sauvaud, N. Schneider, W. Sidney, S. Sparacino, A. I. F. Stewart, R. Tolson, D. Toublanc, C. Waters, T. Woods, R. Yelle, and R. Zurek. The Mars Atmosphere and Volatile Evolution (MAVEN) Mission. Space Sci. Rev., 195:3–48, December 2015b. doi: 10.1007/s11214-015-0139-x.

B. M. Jakosky, D. Brain, M. Chaffin, S. Curry, J. Deighan, J. Grebowsky, J. Halekas, F. Leblanc, R. Lillis, J. G. Luhmann, L. Andersson, N. Andre, D. Andrews, D. Baird, D. Baker, J. Bell, M. Benna, D. Bhattacharyya, S. Bougher, C. Bowers, P. Chamberlin, J.-Y. Chaufray, J. Clarke, G. Collinson, M. Combi, J. Connerney, K. Connour, J. Correira, K. Crabb, F. Crary, T. Cravens, M. Crismani, G. Delory, R. Dewey, G. DiBraccio, C. Dong, Y. Dong, P. Dunn, H. Egan, M. Elrod, S. England, F. Eparvier, R. Ergun, A. Eriksson, T. Esman, J. Espley, S. Evans, K. Fallows, X. Fang, M. Fillingim, C. Flynn, A. Fogle, C. Fowler, J. Fox, M. Fujimoto, P. Garnier, Z. Girazian, H. Groeller, J. Gruesbeck, O. Hamil, K. G. Hanley, T. Hara, Y. Harada, J. Hermann, M. Holmberg, G. Holsclaw, S. Houston, S. Inui, S. Jain, R. Jolitz, A. Kotova, T. Kuroda, D. Larson, Y. Lee, C. Lee, F. Lefevre, C. Lentz, D. Lo, R. Lugo, Y.-J. Ma, P. Mahaffy, M. L. Marquette, Y. Matsumoto, M. Mayyasi, C. Mazelle, W. McClintock, J. McFadden, A. Medvedev, M. Mendillo, K. Meziane, Z. Milby, D. Mitchell, R. Modolo, F. Montmessin, A. Nagy, H. Nakagawa, C. Narvaez, K. Olsen, D. Pawlowski, W. Peterson, A. Rahmati, K. Roeten, N. Romanelli, S. Ruhunusiri, C. Russell, S. Sakai, N. Schneider, K. Seki, R. Sharrar, S. Shaver, D. E. Siskind, M. Slipski, Y. Soobiah, M. Steckiewicz, M. H. Stevens, I. Stewart, A. Stiepen, S. Stone, V. Tenishev, N. Terada, K. Terada, E. Thiemann, R. Tolson, G. Toth, J. Trovato, M. Vogt, T. Weber, P. Withers, S. Xu, R. Yelle, E. Yiğit, and R. Zurek. Loss of the Martian atmosphere to space: Present-day loss rates determined from MAVEN observations and integrated loss through time. Icarus, 315:146–157, November 2018. doi: 10.1016/j.icarus.2018.05.030.

B.M. Jakosky, D. Brain, M. Chaffin, S. Curry, J. Deighan, J. Grebowsky, J. Halekas, F. Leblanc, R. Lillis, J.G. Luhmann, L. Andersson, N. Andre, D. Andrews, D. Baird, D. Baker, J. Bell, M. Benna, D. Bhattacharyya, S. Bougher, C. Bowers, P. Chamberlin, J.-Y. Chaufray, J. Clarke, G. Collinson, M. Combi, J. Connerney, K. Connour, J. Correira, K. Crabb, F. Crary, T. Cravens, M. Crismani, G. Delory, R. Dewey, G. DiBraccio, C. Dong, Y. Dong, P. Dunn, H. Egan, M. Elrod, S. England, F. Eparvier, R. Ergun, A. Eriksson, T. Esman, J. Espley, S. Evans, K. Fallows, X. Fang, M. Fillingim, C. Flynn, A. Fogle, C. Fowler, J. Fox, M. Fujimoto, P. Garnier, Z. Girazian, H. Groeller, J. Gruesbeck, O. Hamil, K.G. Hanley, T. Hara, Y. Harada, J. Hermann, M. Holmberg, G. Holsclaw, S. Houston, S. Inui, S. Jain, R. Jolitz, A. Kotova, T. Kuroda, D. Larson, Y. Lee, C. Lee, F. Lefevre, C. Lentz, D. Lo, R. Lugo, Y.-J. Ma, P. Mahaffy, M.L. Marquette, Y. Matsumoto, M. Mayyasi, C. Mazelle, W. McClintock, J. McFadden, A. Medvedev, M. Mendillo, K. Meziane, Z. Milby, D. Mitchell, R. Modolo, F. Montmessin, A. Nagy, H. Nakagawa, C. Narvaez, K. Olsen, D. Pawlowski, W. Peterson, A. Rahmati, K. Roeten, N. Romanelli, S. Ruhunusiri, C. Russell, S. Sakai, N. Schneider, K. Seki, R. Sharrar, S. Shaver, D.E. Siskind, M. Slipski, Y. Soobiah, M. Steckiewicz, M.H. Stevens, I. Stewart, A. Stiepen, S. Stone, V. Tenishev, N. Terada, K. Terada, E. Thiemann, R. Tolson, G. Toth, J. Trovato, M. Vogt, T. Weber, P. Withers, S. Xu, R. Yelle, E. Yiit, and R. Zurek. Loss of the martian atmosphere to space: Present-day loss rates determined from maven observations and integrated loss through time.

Icarus, 315:146 – 157, 2018. ISSN 0019-1035. doi: https://doi.org/10.1016/j.icarus.2018.05.030. URL http://www.sciencedirect.com/science/article/pii/S0019103517306917.

Bruce M. Jakosky. MAVEN observations of the Mars upper atmosphere, ionosphere, and solar wind interactions. Journal of Geophysical Research (Space Physics), 122:9552–9553, Sep 2017. doi: 10.1002/2017JA024324.

Bruce M. Jakosky. Maven observations of the mars upper atmosphere, ionosphere, and solar wind interactions. Journal of Geophysical Research: Space Physics, 122(9):9552–9553, 2017. doi: 10.1002/2017JA024324. URL https://agupubs.onlinelibrary.wiley.com/doi/abs/10.1002/2017JA024324.

Bruce M Jakosky, Robert O Pepin, Robert E Johnson, and Jane L Fox. Mars atmospheric loss and isotopic fractionation by solar-wind-induced sputtering and photochemical escape. Icarus, 111 (2):271–288, 1994.

Bruce M. Jakosky, Joseph M. Grebowsky, Janet G. Luhmann, and David A. Brain. Initial results from the MAVEN mission to Mars. Geophysical Research Letters, 42:8791–8802, Nov 2015c. doi: 10.1002/2015GL065271.

R. Jarvinen and E. Kallio. Energization of planetary pickup ions in the solar system. Journal of Geophysical Research: Planets, 119(1):219–236, 2013. doi: 10.1002/2013JE004534. URL https://agupubs.onlinelibrary.wiley.com/doi/abs/10.1002/2013JE004534.

R. Jarvinen and E. Kallio. Energization of planetary pickup ions in the solar system. Journal of Geophysical Research (Planets), 119:219–236, January 2014. doi: 10.1002/2013JE004534.

R. Jarvinen and A. Sandroos. Solar wind interaction with Venus and Mars in a parallel hybrid code. In EGU General Assembly Conference Abstracts, volume 15 of EGU General Assembly Conference Abstracts, pages EGU2013–4352, April 2013.

R. Jarvinen, E. Kallio, P. Janhunen, S. Barabash, T. L. Zhang, V. Pohjola, and I. Sillanpää. Oxygen ion escape from Venus in a global hybrid simulation: role of the ionospheric O^+ ions. Annales Geophysicae, 27:4333–4348, November 2009. doi: 10.5194/angeo-27-4333-2009.

R. Jarvinen, E. Kallio, and S. Dyadechkin. Hemispheric asymmetries of the Venus plasma environment. Journal of Geophysical Research (Space Physics), 118:4551–4563, July 2013. doi: 10.1002/jgra.50387.

R. Jarvinen, D. A. Brain, and J. G. Luhmann. Dynamics of planetary ions in the induced magnetospheres of Venus and Mars. Planet. Space Sci., 127:1–14, August 2016a. doi: 10.1016/j.pss.2015.08.012.

R. Jarvinen, D. A. Brain, and J. G. Luhmann. Dynamics of planetary ions in the induced magnetospheres of Venus and Mars. Planet. Space Sci., 127:1–14, August 2016b. doi: 10.1016/j.pss.2015.08.012.

R. Jarvinen, D.A. Brain, and J.G. Luhmann. Dynamics of planetary ions in the induced magnetospheres of venus and mars. Planetary and Space Science, 127:1 – 14, 2016. ISSN 0032-0633. doi: https://doi.org/10.1016/j.pss.2015.08.012. URL http://www.sciencedirect.com/science/article/pii/S0032063315002421.

R. Jarvinen, D. A. Brain, R. Modolo, A. Fedorov, and M. Holmström. Oxygen Ion Energization at Mars: Comparison of MAVEN and Mars Express Observations to Global Hybrid Simulation. Journal of Geophysical Research (Space Physics), 123:1678–1689, February 2018. doi: 10.1002/2017JA024884.

James Jeans. The Dynamical Theory of Gases. Cambridge Library Collection - Physical Sciences. Cambridge University Press, 4 edition, 1925. doi: 10.1017/CBO9780511694370.

H. Jin, K. Maezawa, and T. Mukai. Effects of charge exchange and electron impact ionization on the formation of the magnetic pileup boundary at Mars. Journal of Geophysical Research (Space Physics), 111:A05306, May 2006. doi: 10.1029/2005JA011127.

E. P. G. Johansson, J. Mueller, and U. Motschmann. Interplanetary magnetic field orientation and the magnetospheres of close-in exoplanets. A&A, 525:A117, January 2011. doi: 10.1051/0004-6361/201014802.

R. E. Johnson. Plasma ion heating of an SO2 atmosphere on Io. Geophys. Res. Lett., 16:1117–1120, October 1989. doi: 10.1029/GL016i010p01117.

R. E. Johnson, D. Schnellenberger, and M. C. Wong. The sputtering of an oxygen thermosphere by energetic O^+. Journal of Geophysical Research, 105:1659–1670, Jan 2000. doi: 10.1029/1999JE001058.

K. Kabin, T. I. Gombosi, D. L. DeZeeuw, and K. G. Powell. Interaction of Mercury with the Solar Wind. Icarus, 143:397–406, Feb 2000. doi: 10.1006/icar.1999.6252.

K. Kabin, T.I. Gombosi, D.L. DeZeeuw, and K.G. Powell. Interaction of mercury with the solar wind. Icarus, 143(2):397 – 406, 2000. ISSN 0019-1035. doi: https://doi.org/10.1006/icar.1999.6252. URL http://www.sciencedirect.com/science/article/pii/S0019103599962528.

K. Kabin, R. Rankin, G. Rostoker, R. Marchand, I. J. Rae, A. J. Ridley, T. I. Gombosi, C. R. Clauer, and D. L. Dezeeuw. Open-closed field line boundary position: A parametric study using an MHD model. Journal of Geophysical Research (Space Physics), 109:A05222, May 2004. doi: 10.1029/2003JA010168.

E. Kallio and S. Barabash. Magnetized Mars: Spatial distribution of oxygen ions. Earth, Planets, and Space, 64:149–156, February 2012a. doi: 10.5047/eps.2011.07.008.

E. Kallio and S. Barabash. Magnetized Mars: Spatial distribution of oxygen ions. Earth, Planets, and Space, 64:149–156, February 2012b. doi: 10.5047/eps.2011.07.008.

E. Kallio and P. Janhunen. Ion escape from Mars in a quasi-neutral hybrid model. Journal of Geophysical Research (Space Physics), 107:1035, March 2002. doi: 10.1029/2001JA000090.

E. Kallio and P. Janhunen. Modelling the solar wind interaction with Mercury by a quasi-neutral hybrid model. Annales Geophysicae, 21:2133–2145, November 2003. doi: 10.5194/angeo-21-2133-2003.

E. Kallio and P. Janhunen. Modelling the solar wind interaction with mercury by a quasi-neutral hybrid model. Annales Geophysicae, 21(11):2133–2145, 2003. doi: 10.5194/angeo-21-2133-2003. URL https://www.ann-geophys.net/21/2133/2003/.

E. Kallio, J. G. Luhmann, and J. G. Lyon. Magnetic field near Venus - A comparison between Pioneer Venus Orbiter magnetic field observations and an MHD simulation. J. Geophys. Res., 103:4723, March 1998. doi: 10.1029/97JA02862.

E. Kallio, S. Barabash, K. Brinkfeldt, H. Gunell, M. Holmström, Y. Futaana, W. Schmidt, T. Säles, H. Koskinen, P. Riihelä, R. Lundin, H. Andersson, M. Yamauchi, A. Grigoriev, J.D. Winningham, R.A. Frahm, J.R. Sharber, J.R. Scherrer, A.J. Coates, D.R. Linder, D.O. Kataria, J. Kozyra, J.G. Luhmann, E. Roelof, D. Williams, S. Livi, P. Brandt, C.C. Curtis, K.C. Hsieh, B.R. Sandel, M. Grande, M. Carter, J.-A. Sauvaud, A. Fedorov, J.-J. Thocaven, McKenna-Lawler, S., S. Orsini, Cerulli-Irelli, R., M. Maggi, P. Wurz, P. Bochsler, N. Krupp, J. Woch, M. Fränz, K. Asamura, and C. Dierker. Energetic neutral atoms (ENA) at mars: Properties of the hydrogen atoms produced upstream of the martian bow shock and implications for ENA sounding technique around non-magnetized planets. Icarus, 182(2):448–463, 2006a. ISSN 0019-1035. doi: 10.1016/j.icarus.2005.12.019.

E. Kallio, A. Fedorov, E. Budnik, T. Säles, P. Janhunen, W. Schmidt, H. Koskinen, P. Riihelä, S. Barabash, R. Lundin, M. Holmström, H. Gunell, K. Brinkfeldt, Y. Futaana, H. Andersson, M. Yamauchi, A. Grigoriev, J.-A. Sauvaud, J.-J. Thocaven, J.D. Winningham, R.A. Frahm, J.R. Sharber, J.R. Scherrer, A.J. Coates, D.R. Linder, D.O. Kataria, J. Kozyra, J.G. Luhmann, E. Roelof, D. Williams, S. Livi, C.C. Curtis, K.C. Hsieh, B.R. Sandel, M. Grande, M. Carter, McKenna-Lawler, S., S. Orsini, Cerulli-Irelli, R., M. Maggi, P. Wurz, P. Bochsler, N. Krupp, J. Woch, M. Fränz, K. Asamura, and C. Dierker. Ion escape at mars: Comparison of a 3-D hybrid simulation with mars express IMA/ASPERA-3 measurements. Icarus, 182(2):350–359, 2006b. ISSN 0019-1035. doi: 10.1016/j.icarus.2005.09.018.

E. Kallio, A. Fedorov, E. Budnik, T. Säles, P. Janhunen, W. Schmidt, H. Koskinen, P. Riihelä, S. Barabash, R. Lundin, M. Holmström, H. Gunell, K. Brinkfeldt, Y. Futaana, H. Andersson, M. Yamauchi, A. Grigoriev, J.-A. Sauvaud, J.-J. Thocaven, J. D. Winningham, R. A. Frahm, J. R. Sharber, J. R. Scherrer, A. J. Coates, D. R. Linder, D. O. Kataria, J. Kozyra, J. G. Luhmann, E. Roelof, D. Williams, S. Livi, C. C. Curtis, K. C. Hsieh, B. R. Sandel, M. Grande, M. Carter, S. McKenna-Lawler, S. Orsini, R. Cerulli-Irelli, M. Maggi, P. Wurz, P. Bochsler, N. Krupp, J. Woch, M. Fränz, K. Asamura, and C. Dierker. Ion escape at Mars: Comparison of a 3-D hybrid simulation with Mars Express IMA/ASPERA-3 measurements. Icarus, 182: 350–359, June 2006. doi: 10.1016/j.icarus.2005.09.018.

E. Kallio, I. Sillanpää, R. Jarvinen, P. Janhunen, M. Dougherty, C. Bertucci, and F. Neubauer. Morphology of the magnetic field near Titan: Hybrid model study of the Cassini T9 flyby. Geophys. Res. Lett., 34:L24S09, October 2007. doi: 10.1029/2007GL030827.

E. Kallio, S. Barabash, P. Janhunen, and R. Jarvinen. Magnetized Mars: Transformation of Earth-like magnetosphere to Venus-like induced magnetosphere. Planet. Space Sci., 56:823–827, May 2008. doi: 10.1016/j.pss.2007.12.005.

E. Kallio, K. Liu, R. Jarvinen, V. Pohjola, and P. Janhunen. Oxygen ion escape at Mars in a hybrid model: High energy and low energy ions. Icarus, 206:152–163, March 2010. doi: 10.1016/j.icarus.2009.05.015.

E. Kallio, J.-Y. Chaufray, R. Modolo, D. Snowden, and R. Winglee. Modeling of Venus, Mars, and Titan. Space Sci. Rev., 162:267–307, December 2011. doi: 10.1007/s11214-011-9814-8.

Esa Kallio and Pekka Janhunen. Atmospheric effects of proton precipitation in the martian atmosphere and its connection to the mars-solar wind interaction. Journal of Geophysical Research: Space Physics, 106(A4):5617–5634, 2001.

Esa Kallio and Pekka Janhunen. Ion escape from mars in a quasineutral hybrid model. pages SIA 1–1–SIA 1–21, 2002. ISSN 2156-2202. doi: 10.1029/2001JA000090.

Esa Kallio, Kaijun Liu, Riku Jarvinen, Valter Pohjola, and Pekka Janhunen. Oxygen ion escape at mars in a hybrid model: High energy and low energy ions. Icarus, 206(1):152–163, 2010. ISSN 0019-1035. doi: 10.1016/j.icarus.2009.05.015.

L. Kaltenegger. How to Characterize Habitable Worlds and Signs of Life. ARA&A, 55:433–485, August 2017. doi: 10.1146/annurev-astro-082214-122238.

Jeffrey S. Kargel, Jonathan Z. Kaye, James W. Head, Giles M. Marion, Roger Sassen, James K. Crowley, Olga Prieto Ballesteros, Steven A. Grant, and David L. Hogenboom. Europa's Crust and Ocean: Origin, Composition, and the Prospects for Life. Icarus, 148:226–265, Nov 2000. doi: 10.1006/icar.2000.6471.

D. M. Kass and Y. L. Yung. Loss of Atmosphere from Mars Due to Solar Wind-Induced Sputtering. Science, 268:697–699, May 1995. doi: 10.1126/science.7732377.

J. F. Kasting and J. B. Pollack. Loss of water from Venus. I - Hydrodynamic escape of hydrogen. Icarus, 53:479–508, March 1983. doi: 10.1016/0019-1035(83)90212-9.

J. F. Kasting, O. B. Toon, and J. B. Pollack. How climate evolved on the terrestrial planets. Scientific American, 258:46–53, May 1988.

James Kasting. How to find a habitable planet. Princeton University Press, 2012.

James F. Kasting, Daniel P. Whitmire, and Ray T. Reynolds. Habitable Zones around Main Sequence Stars. Icarus, 101:108–128, Jan 1993. doi: 10.1006/icar.1993.1010.

J.-h. Kim, O. Agertz, R. Teyssier, M. J. Butler, D. Ceverino, J.-H. Choi, R. Feldmann, B. W. Keller, A. Lupi, T. Quinn, Y. Revaz, S. Wallace, N. Y. Gnedin, S. N. Leitner, S. Shen, B. D. Smith, R. Thompson, M. J. Turk, T. Abel, K. S. Arraki, S. M. Benincasa, S. Chakrabarti, C. DeGraf, A. Dekel, N. J. Goldbaum, P. F. Hopkins, C. B. Hummels, A. Klypin, H. Li, P. Madau, N. Mandelker, L. Mayer, K. Nagamine, S. Nickerson, B. W. O'Shea, J. R. Primack, S. Roca-Fàbrega, V. Semenov, I. Shimizu, C. M. Simpson, K. Todoroki, J. W. Wadsley, J. H. Wise, and AGORA Collaboration. The AGORA High-resolution Galaxy Simulations Comparison Project. II. Isolated Disk Test. ApJ, 833:202, December 2016. doi: 10.3847/1538-4357/833/2/202.

K. G. Kislyakova, H. Lammer, M. Holmström, M. Panchenko, P. Odert, N. V. Erkaev, M. Leitzinger, M. L. Khodachenko, Y. N. Kulikov, M. Güdel, and A. Hanslmeier. XUV-Exposed, Non-Hydrostatic Hydrogen-Rich Upper Atmospheres of Terrestrial Planets. Part II: Hydrogen Coronae and Ion Escape. Astrobiology, 13:1030–1048, November 2013. doi: 10.1089/ast.2012.0958.

K. G. Kislyakova, C. P. Johnstone, P. Odert, N. V. Erkaev, H. Lammer, T. Lüftinger, M. Holmström, M. L. Khodachenko, and M. Güdel. Stellar wind interaction and pick-up ion escape of the Kepler-11 "super-Earths". A&A, 562:A116, February 2014. doi: 10.1051/0004-6361/201322933.

M. G. Kivelson, K. K. Khurana, F. V. Coroniti, S. Joy, C. T. Russell, R. J. Walker, J. Warnecke, L. Bennett, and C. Polanskey. The magnetic field and magnetosphere of ganymede. Geophysical Research Letters, 24(17):2155–2158, 1997. doi: 10.1029/97GL02201. URL https://agupubs.onlinelibrary.wiley.com/doi/abs/10.1029/97GL02201.

C. Koenders, K. H. Glassmeier, I. Richter, H. Ranocha, and U. Motschmann. Dynamical features and spatial structures of the plasma interaction region of 67P/Churyumov-Gerasimenko and the solar wind. Planetary and Space Science, 105:101–116, Jan 2015. doi: 10.1016/j.pss.2014.11.014.

R. K. Kopparapu. A Revised Estimate of the Occurrence Rate of Terrestrial Planets in the Habitable Zones around Kepler M-dwarfs. ApJ, 767:L8, April 2013. doi: 10.1088/2041-8205/767/1/L8.

Ravi Kumar Kopparapu, Ramses Ramirez, James F. Kasting, Vincent Eymet, Tyler D. Robinson, Suvrath Mahadevan, Ryan C. Terrien, Shawn Domagal-Goldman, Victoria Meadows, and Rohit Deshpande. Habitable Zones around Main-sequence Stars: New Estimates. ApJ, 765:131, Mar 2013. doi: 10.1088/0004-637X/765/2/131.

J. U. Kozyra, T. E. Cravens, and A. F. Nagy. Energetic O/+/ precipitation. J. Geophys. Res., 87: 2481–2486, April 1982. doi: 10.1029/JA087iA04p02481.

V. A. Krasnopolskii. On the structure of Mars' atmosphere at 120-220 km. Icarus, 24:28–35, January 1975. doi: 10.1016/0019-1035(75)90155-4.

V. A. Krasnopolsky. Hydrodynamic flow of N_2 from Pluto. J. Geophys. Res., 104:5955–5962, March 1999. doi: 10.1029/1998JE900052.

V. A. Krasnopolsky, O. B. Likin, F. Farnik, and B. Valnicek. Solar occultation observations of the Martian atmosphere in the ranges of 2-4 and 4-8 keV measured by PHOBOS 2. Icarus, 89: 147–151, January 1991. doi: 10.1016/0019-1035(91)90094-A.

Vladimir A. Krasnopolsky. Atmospheric chemistry on Venus, Earth, and Mars: Main features and comparison. Planetary and Space Science, 59:952–964, Aug 2011. doi: 10.1016/j.pss.2010.02.011.

Vladimir A. Krasnopolsky, Michael J. Mumma, and G. Rand all Gladstone. Detection of Atomic Deuterium in the Upper Atmosphere of Mars. Science, 280:1576, Jun 1998. doi: 10.1126/science.280.5369.1576.

Vladimir A. Krasnopolsky, Jean Pierre Maillard, Tobias C. Owen, Robert A. Toth, and Michael D. Smith. Oxygen and carbon isotope ratios in the martian atmosphere. Icarus, 192:396–403, Dec 2007. doi: 10.1016/j.icarus.2007.08.013.

Yu. N. Kulikov, H. Lammer, H. I. M. Lichtenegger, N. Terada, I. Ribas, C. Kolb, D. Langmayr, R. Lundin, E. F. Guinan, S. Barabash, and H. K. Biernat. Atmospheric and water loss from early Venus. Planetary and Space Science, 54:1425–1444, Nov 2006. doi: 10.1016/j.pss.2006.04.021.

Yu.N. Kulikov, H. Lammer, H.I.M. Lichtenegger, N. Terada, I. Ribas, C. Kolb, D. Langmayr, R. Lundin, E.F. Guinan, S. Barabash, and H.K. Biernat. Atmospheric and water loss from early venus. Planetary and Space Science, 54(13):1425 – 1444, 2006. ISSN 0032-0633. doi: https://doi.org/10.1016/j.pss.2006.04.021. URL http://www.sciencedirect.com/science/article/pii/S0032063306001693. The Planet Venus and the Venus Express Mission.

S. Kumar. Venus nightside ionosphere: A model with KeV electron impact ionization. Geophysical Research Letters, 9:595–598, May 1982. doi: 10.1029/GL009i005p00595.

S. Kumar, D. M. Hunten, and J. B. Pollack. Nonthermal escape of hydrogen and deuterium from Venus and implications for loss of water. Icarus, 55:369–389, Sep 1983. doi: 10.1016/0019-1035(83)90109-4.

H. Lammer and S. J. Bauer. Atmospheric mass loss from Titan by sputtering. Planet. Space Sci., 41:657–663, September 1993. doi: 10.1016/0032-0633(93)90049-8.

H. Lammer, C. Kolb, T. Penz, U.V. Amerstorfer, H.K. Biernat, and B. Bodiselitsch. Estimation of the past and present martian water-ice reservoirs by isotopic constraints on exchange between the atmosphere and the surface. International Journal of Astrobiology, 2(3):195202, 2003. doi: 10.1017/S1473550403001605.

H. Lammer, F. Selsis, I. Ribas, E. F. Guinan, S. J. Bauer, and W. W. Weiss. Atmospheric Loss of Exoplanets Resulting from Stellar X-Ray and Extreme-Ultraviolet Heating. ApJ, 598:L121–L124, December 2003. doi: 10.1086/380815.

F. Leblanc and R. E. Johnson. Sputtering of the Martian atmosphere by solar wind pick-up ions. Planet. Space Sci., 49:645–656, May 2001. doi: 10.1016/S0032-0633(01)00003-4.

F. Leblanc and R. E. Johnson. Role of molecular species in pickup ion sputtering of the Martian atmosphere. Journal of Geophysical Research (Planets), 107:5010, Feb 2002. doi: 10.1029/2000JE001473.

François Leblanc, Jean-Yves Chaufray, Jean Lilensten, Olivier Witasse, and J-L Bertaux. Martian dayglow as seen by the spicam uv spectrograph on mars express. Journal of Geophysical Research: Planets, 111(E9), 2006.

A. Lecavelier Des Etangs, D. Ehrenreich, A. Vidal-Madjar, G. E. Ballester, J.-M. Désert, R. Ferlet, G. Hébrard, D. K. Sing, K.-O. Tchakoumegni, and S. Udry. Evaporation of the planet HD 189733b observed in H I Lyman-α. A&A, 514:A72, May 2010. doi: 10.1051/0004-6361/200913347.

S. Ledvina, Y.-J. Ma, and E. Kallio. Modeling and simulating flowing plasmas and related phenomena. Space Sci Rev, 139(1-4):143–189, 2008. ISSN 0038-6308. doi: 10.1007/s11214-008-9384-6.

S. A. Ledvina and T. E. Cravens. A three-dimensional MHD model of plasma flow around Titan. Planetary and Space Science, 46:1175–1191, Oct 1998. doi: 10.1016/S0032-0633(98)00052-X.

S. A. Ledvina, T. E. Cravens, and K. KecskeméTy. Ion distributions in Saturn's magnetosphere near Titan. Journal of Geophysical Research (Space Physics), 110:A06211, June 2005. doi: 10.1029/2004JA010771.

S. A. Ledvina, Y.-J. Ma, and E. Kallio. Modeling and Simulating Flowing Plasmas and Related Phenomena. Space Sci. Rev., 139:143–189, August 2008. doi: 10.1007/s11214-008-9384-6.

S. A. Ledvina, S. H. Brecht, D. A. Brain, and B. M. Jakosky. Ion escape rates from Mars: Results from hybrid simulations compared to MAVEN observations. Journal of Geophysical Research (Space Physics), 122:8391–8408, August 2017. doi: 10.1002/2016JA023521.

Stephen A. Ledvina, Stephen H. Brecht, and Janet G. Luhmann. Ion distributions of 14 amu pickup ions associated with Titan's plasma interaction. Geophysical Research Letters, 31:L17S10, Aug 2004. doi: 10.1029/2004GL019861.

O. R. Lehmer and D. C. Catling. Rocky Worlds Limited to 1.8 Earth Radii by Atmospheric Escape during a Star's Extreme UV Saturation. ApJ, 845:130, August 2017. doi: 10.3847/1538-4357/aa8137.

K. Li, S. Haaland, A. Eriksson, M. André, E. Engwall, Y. Wei, E. A. Kronberg, M. Fränz, P. W. Daly, H. Zhao, and Q. Y. Ren. On the ionospheric source region of cold ion outflow. Geophysical Research Letters, 39:L18102, Sep 2012. doi: 10.1029/2012GL053297.

O. Lie-Svendsen, M. H. Rees, and K. Stamnes. Helium escape from the Earth's atmosphere: The charge exchange mechanism revisited. Planetary and Space Science, 40:1639–1662, Dec 1992. doi: 10.1016/0032-0633(92)90123-6.

M. W. Liemohn, Y. Ma, R. A. Frahm, X. Fang, J. U. Kozyra, A. F. Nagy, J. D. Winningham, J. R. Sharber, S. Barabash, and R. Lundin. Mars Global MHD Predictions of Magnetic Connectivity Between the Dayside Ionosphere and the Magnetospheric Flanks. Space Sci. Rev., 126:63–76, October 2006. doi: 10.1007/s11214-006-9116-8.

M. W. Liemohn, S. M. Curry, X. Fang, and Y. Ma. Comparison of high-altitude production and ionospheric outflow contributions to O^+ loss at Mars. Journal of Geophysical Research (Space Physics), 118:4093–4107, July 2013. doi: 10.1002/jgra.50388.

Robert J. Lillis, Justin Deighan, Jane L. Fox, Stephen W. Bougher, Yuni Lee, Michael R. Combi, Thomas E. Cravens, Ali Rahmati, Paul R. Mahaffy, Mehdi Benna, Meredith K. Elrod, James P. McFadden, Robert. E. Ergun, Laila Andersson, Christopher M. Fowler, Bruce M. Jakosky, Ed Thiemann, Frank Eparvier, Jasper S. Halekas, Franois Leblanc, and Jean-Yves Chaufray. Photochemical escape of oxygen from mars: First results from maven in situ data. Journal of Geophysical Research: Space Physics, 122(3):3815–3836, 2017. doi: 10.1002/2016JA023525. URL `https://agupubs.onlinelibrary.wiley.com/doi/abs/10.1002/2016JA023525`.

Y. Lin. Global hybrid simulation of hot flow anomalies near the bow shock and in the magnetosheath. Planetary and Space Science, 50:577–591, Apr 2002. doi: 10.1016/S0032-0633(02)00037-5.

M. J. Lindenfield and B. Shizgal. Non-Maxwellian effects associated with the thermal escape of a planetary atmosphere. Planetary and Space Science, 27:739–751, Jun 1979. doi: 10.1016/0032-0633(79)90003-5.

K. Liu, E. Kallio, R. Jarvinen, H. Lammer, H. I. M. Lichtenegger, Y. N. Kulikov, N. Terada, T. L. Zhang, and P. Janhunen. Hybrid simulations of the O^+ ion escape from Venus: Influence of the solar wind density and the IMF x component. Advances in Space Research, 43:1436–1441, May 2009. doi: 10.1016/j.asr.2009.01.005.

S. C. Liu and T. M. Donahue. The Regulation of Hydrogen and Oxygen Escape from Mars. Icarus, 28:231–246, Jun 1976. doi: 10.1016/0019-1035(76)90035-X.

S.-F. Liu, Y. Hori, D. N. C. Lin, and E. Asphaug. Giant Impact: An Efficient Mechanism for the Devolatilization of Super-Earths. ApJ, 812:164, October 2015. doi: 10.1088/0004-637X/812/2/164.

Y Liu, A.F. Nagy, T.I. Gombosi, DeZeeuw, D.L., and K.G. Powell. The solar wind interaction with mars: results of three-dimensional three-species MHD studies. pages 1837–1846, 2001. ISSN 0273-1177. doi: 10.1016/S0273-1177(01)00301-5.

M. Lockwood, J. H. Waite Jr., T. E. Moore, J. F. E. Johnson, and C. R. Chappell. A new source of suprathermal o+ ions near the dayside polar cap boundary. Journal of Geophysical Research: Space Physics, 90(A5):4099–4116, 1985. doi: 10.1029/JA090iA05p04099. URL https://agupubs.onlinelibrary.wiley.com/doi/abs/10.1029/JA090iA05p04099.

J. G. Luhmann and J. U. Kozyra. Dayside pickup oxygen ion precipitation at Venus and Mars - Spatial distributions, energy deposition and consequences. J. Geophys. Res., 96:5457–5467, April 1991a. doi: 10.1029/90JA01753.

J. G. Luhmann and J. U. Kozyra. Dayside pickup oxygen ion precipitation at venus and mars: Spatial distributions, energy deposition and consequences. Journal of Geophysical Research: Space Physics, 96(A4):5457–5467, 1991b. doi: 10.1029/90JA01753. URL https://agupubs.onlinelibrary.wiley.com/doi/abs/10.1029/90JA01753.

J. G. Luhmann and K. Schwingenschuh. A model of the energetic ion environment of mars. Journal of Geophysical Research: Space Physics, 95(A2):939–945, 1990. doi: 10.1029/JA095iA02p00939. URL https://agupubs.onlinelibrary.wiley.com/doi/abs/10.1029/JA095iA02p00939.

J. G. Luhmann, R. E. Johnson, and M. H. G. Zhang. Evolutionary impact of sputtering of the Martian atmosphere by O(+) pickup ions. Geophys. Res. Lett., 19:2151–2154, November 1992. doi: 10.1029/92GL02485.

J. G. Luhmann, R. E. Johnson, and M. H. G. Zhang. Evolutionary impact of sputtering of the martian atmosphere by o+ pickup ions. Geophysical Research Letters, 19(21):2151–2154, 1992. doi: 10.1029/92GL02485. URL https://agupubs.onlinelibrary.wiley.com/doi/abs/10.1029/92GL02485.

J. G. Luhmann, C. T. Russell, and N. A. Tsyganenko. Disturbances in mercury's magnetosphere: Are the mariner 10 substorms simply driven? Journal of Geophysical Research: Space Physics, 103(A5):9113–9119, 1998. doi: 10.1029/97JA03667. URL https://agupubs.onlinelibrary.wiley.com/doi/abs/10.1029/97JA03667.

J. G. Luhmann, S. A. Ledvina, J. G. Lyon, and C. T. Russell. Venus O $^+$ pickup ions: Collected PVO results and expectations for Venus Express. Planetary and Space Science, 54:1457–1471, Nov 2006. doi: 10.1016/j.pss.2005.10.009.

J. G. Luhmann, A. Fedorov, S. Barabash, E. Carlsson, Y. Futaana, T. L. Zhang, C. T. Russell, J. G. Lyon, S. A. Ledvina, and D. A. Brain. Venus Express observations of atmospheric oxygen escape during the passage of several coronal mass ejections. Journal of Geophysical Research (Planets), 113:E00B04, Aug 2008. doi: 10.1029/2008JE003092.

J. G. Luhmann, C. Dong, Y. Ma, S. M. Curry, D. Mitchell, J. Espley, J. Connerney, J. Halekas, D. A. Brain, B. M. Jakosky, and C. Mazelle. Implications of MAVEN Mars near-wake measurements and models. Geophys. Res. Lett., 42:9087–9094, November 2015. doi: 10.1002/2015GL066122.

J.G. Luhmann, S.A. Ledvina, J.G. Lyon, and C.T. Russell. Venus o+ pickup ions: Collected pvo results and expectations for venus express. Planetary and Space Science, 54(13-14):1457–1471, 2006. doi: 10.1016/j.pss.2005.10.009.

R. Lundin. Ion Acceleration and Outflow from Mars and Venus: An Overview. Space Sci. Rev., 162:309–334, December 2011. doi: 10.1007/s11214-011-9811-y.

R. Lundin and E. M. Dubinin. Phobos-2 results on the ionospheric plasma escape from Mars. Advances in Space Research, 12:255–263, Sep 1992. doi: 10.1016/0273-1177(92)90338-X.

R. Lundin, A. Zakharov, R. Pellinen, H. Borg, B. Hultqvist, N. Pissarenko, E. M. Dubinin, S. W. Barabash, I. Liede, and H. Koskinen. First measurements of the ionospheric plasma escape from Mars. Nature, 341:609–612, October 1989a. doi: 10.1038/341609a0.

R. Lundin, A. Zakharov, R. Pellinen, H. Borg, B. Hultqvist, N. Pissarenko, E. M. Dubinin, S. W. Barabash, I. Liede, and H. Koskinen. First measurements of the ionospheric plasma escape from Mars. Nature, 341:609–612, October 1989b. doi: 10.1038/341609a0.

R Lundin, A Zakharov, R Pellinen, SW Barabasj, H Borg, EM Dubinin, B Hultqvist, H Koskinen, I Liede, and N Pissarenko. Aspera/phobos measurements of the ion outflow from the martian ionosphere. Geophysical Research Letters, 17(6):873–876, 1990.

R. Lundin, S. Barabash, A. Fedorov, M. Holmström, H. Nilsson, J. A. Sauvaud, and M. Yamauchi. Solar forcing and planetary ion escape from Mars. Geophysical Research Letters, 35:L09203, May 2008. doi: 10.1029/2007GL032884.

R. Lundin, S. Barabash, M. Yamauchi, H. Nilsson, and D. Brain. On the relation between plasma escape and the Martian crustal magnetic field. Geophysical Research Letters, 38:L02102, Jan 2011. doi: 10.1029/2010GL046019.

R. Lundin, S. Barabash, M. Holmström, H. Nilsson, Y. Futaana, R. Ramstad, M. Yamauchi, E. Dubinin, and M. Fraenz. Solar cycle effects on the ion escape from Mars. Geophysical Research Letters, 40:6028–6032, Dec 2013. doi: 10.1002/2013GL058154.

Rickard Lundin, Helmut Lammer, and Ignasi Ribas. Planetary magnetic fields and solar forcing: Implications for atmospheric evolution. Space Science Reviews, 129(1):245–278, Mar 2007. ISSN 1572-9672. doi: 10.1007/s11214-007-9176-4. URL https://doi.org/10.1007/s11214-007-9176-4.

Y. Ma, A. F. Nagy, K. C. Hansen, D. L. Dezeeuw, T. I. Gombosi, and K. G. Powell. Three-dimensional multispecies MHD studies of the solar wind interaction with Mars in the presence of crustal fields. Journal of Geophysical Research (Space Physics), 107:1282, October 2002. doi: 10.1029/2002JA009293.

Y. Ma, C. T. Russell, A. F. Nagy, G. Toth, C. Dong, and S. W. Bougher. Multi-fluid MHD Study of the Solar Wind Induced Plasma Escape from the Martian Atmosphere. AGU Fall Meeting Abstracts, December 2013a.

Y. J. Ma, C. T. Russell, A. F. Nagy, G. Toth, M. K. Dougherty, A. Wellbrock, A. J. Coates, P. Garnier, J.-E. Wahlund, T. E. Cravens, M. S. Richard, and F. J. Crary. The importance of thermal electron heating in titan's ionosphere: Comparison with cassini t34 flyby. Journal of Geophysical Research: Space Physics, 116(A10):n/a–n/a, 2011. ISSN 2156-2202. doi: 10.1029/2011JA016657. URL http://dx.doi.org/10.1029/2011JA016657. A10213.

Y. J. Ma, A. F. Nagy, C. T. Russell, R. J. Strangeway, H. Y. Wei, and G. Toth. A global multispecies single-fluid MHD study of the plasma interaction around Venus. Journal of Geophysical Research (Space Physics), 118:321–330, January 2013b. doi: 10.1029/2012JA018265.

Y. J. Ma, X. Fang, A. F. Nagy, C. T. Russell, and Gabor Toth. Martian ionospheric responses to dynamic pressure enhancements in the solar wind. Journal of Geophysical Research: Space Physics, 119(2):1272–1286, 2014. ISSN 2169-9402. doi: 10.1002/2013JA019402. URL http://dx.doi.org/10.1002/2013JA019402. 2013JA019402.

Y. J. Ma, C. T. Russell, X. Fang, Y. Dong, A. F. Nagy, G. Toth, J. S. Halekas, J. E. P. Connerney, J. R. Espley, P. R. Mahaffy, M. Benna, J. P. McFadden, D. L. Mitchell, and B. M. Jakosky. MHD model results of solar wind interaction with Mars and comparison with MAVEN plasma observations. Geophysical Research Letters, 42:9113–9120, Nov 2015. doi: 10.1002/2015GL065218.

Y. J. Ma, C. T. Russell, X. Fang, C. F. Dong, A. F. Nagy, G. Toth, J. S. Halekas, J. E. P. Connerney, J. R. Espley, P. R. Mahaffy, M. Benna, J. McFadden, D. L. Mitchell, L. Andersson, and B. M. Jakosky. Variations of the Martian plasma environment during the ICME passage on 8 March 2015: A time-dependent MHD study. Journal of Geophysical Research (Space Physics), 122:1714–1730, Feb 2017. doi: 10.1002/2016JA023402.

Y. J. Ma, C. T. Russell, X. Fang, C. F. Dong, A. F. Nagy, G. Toth, J. S. Halekas, J. E. P. Connerney, J. R. Espley, P. R. Mahaffy, M. Benna, J. McFadden, D. L. Mitchell, L. Andersson, and B. M. Jakosky. Variations of the martian plasma environment during the icme passage on 8 march 2015: A time-dependent mhd study. Journal of Geophysical Research: Space Physics, 122(2): 1714–1730, 2017. ISSN 2169-9402. doi: 10.1002/2016JA023402. URL http://dx.doi.org/10.1002/2016JA023402. 2016JA023402.

Ying-Juan Ma and Andrew F. Nagy. Ion escape fluxes from mars. Geophysical Research Letters, 34(8):n/a–n/a, 2007. ISSN 1944-8007. doi: 10.1029/2006GL029208. URL http://dx.doi.org/10.1029/2006GL029208. L08201.

Ying-Juan Ma, Andrew F. Nagy, Thomas E. Cravens, Igor V. Sokolov, John Clark, and Kenneth C. Hansen. 3-D global MHD model prediction for the first close flyby of Titan by Cassini. Geophysical Research Letters, 31:L22803, Nov 2004. doi: 10.1029/2004GL021215.

Ying-Juan Ma, Andrew F. Nagy, Gabor Toth, Thomas E. Cravens, Christopher T. Russell, Tamas I. Gombosi, Jan-Erik Wahlund, Frank J. Crary, Andrew J. Coates, César L. Bertucci, and Fritz M. Neubauer. 3D global multi-species Hall-MHD simulation of the Cassini T9 flyby. Geophysical Research Letters, 34:L24S10, Dec 2007. doi: 10.1029/2007GL031627.

Yingjuan Ma, Andrew F. Nagy, Kenneth C. Hansen, Darren L. DeZeeuw, Tamas I. Gombosi, and K. G. Powell. Three-dimensional multispecies mhd studies of the solar wind interaction with mars in the presence of crustal fields. Journal of Geophysical Research: Space Physics, 107 (A10):SMP 6–1–SMP 6–7, 2002. ISSN 2156-2202. doi: 10.1029/2002JA009293. URL http://dx.doi.org/10.1029/2002JA009293. 1282.

Yingjuan Ma, Andrew F. Nagy, Igor V. Sokolov, and Kenneth C. Hansen. Three-dimensional, multispecies, high spatial resolution mhd studies of the solar wind interaction with mars. Journal of Geophysical Research: Space Physics, 109(A7):n/a–n/a, 2004a. ISSN 2156-2202. doi: 10.1029/2003JA010367. URL http://dx.doi.org/10.1029/2003JA010367. A07211.

Yingjuan Ma, Andrew F. Nagy, Igor V. Sokolov, and Kenneth C. Hansen. Three-dimensional, multispecies, high spatial resolution mhd studies of the solar wind interaction with mars. Journal of Geophysical Research: Space Physics, 109(A7), 2004b. doi: 10.1029/2003JA010367. URL https://agupubs.onlinelibrary.wiley.com/doi/abs/10.1029/2003JA010367.

Yingjuan Ma, Xiaohua Fang, Christopher T. Russell, Andrew F. Nagy, Gabor Toth, Janet G. Luhmann, Dave A. Brain, and Chuanfei Dong. Effects of crustal field rotation on the solar wind plasma interaction with Mars. Geophysical Research Letters, 41:6563–6569, Oct 2014. doi: 10.1002/2014GL060785.

Yingjuan Ma, Xiaohua Fang, Christopher T. Russell, Andrew F. Nagy, Gabor Toth, Janet G. Luhmann, Dave A. Brain, and Chuanfei Dong. Effects of crustal field rotation on the solar wind plasma interaction with mars. Geophysical Research Letters, 41(19):6563–6569, 2014. ISSN 1944-8007. doi: 10.1002/2014GL060785. URL http://dx.doi.org/10.1002/2014GL060785. 2014GL060785.

YJ Ma, CT Russell, X Fang, and Y Dong. MHD model results of solar wind interaction with mars and comparison with MAVEN plasma observations. Geophysical , 2015. doi: 10.1002/2015GL065218.

J. A. Magalhães, J. T. Schofield, and A. Seiff. Results of the Mars Pathfinder atmospheric structure investigation. J. Geophys. Res., 104:8943–8956, April 1999. doi: 10.1029/1998JE900041.

P. R. Mahaffy, M. Benna, M. Elrod, R. V. Yelle, S. W. Bougher, S. W. Stone, and B. M. Jakosky. Structure and composition of the neutral upper atmosphere of mars from the maven ngims investigation. Geophysical Research Letters, 42(21):8951–8957, 2015. doi: 10.1002/2015GL065329. URL https://agupubs.onlinelibrary.wiley.com/doi/abs/10.1002/2015GL065329.

P. R. Mahaffy, M. Benna, T. King, D. N. Harpold, R. Arvey, M. Barciniak, M. Bendt, D. Carrigan, T. Errigo, V. Holmes, C. S. Johnson, J. Kellogg, P. Kimvilakani, M. Lefavor, J. Hengemihle, F. Jaeger, E. Lyness, J. Maurer, A. Melak, F. Noreiga, M. Noriega, K. Patel, B. Prats, E. Raaen, F. Tan, E. Weidner, C. Gundersen, S. Battel, B. P. Block, K. Arnett, R. Miller, C. Cooper, C. Edmonson, and J. T. Nolan. The Neutral Gas and Ion Mass Spectrometer on the Mars Atmosphere and Volatile Evolution Mission. Space Sci. Rev., 195:49–73, December 2015. doi: 10.1007/s11214-014-0091-1.

L. J. Maher and B. A. Tinsley. Atomic hydrogen escape rate due to charge exchange with hot plasmaspheric ions. Journal of Geophysical Research, 82:689, Feb 1977. doi: 10.1029/JA082i004p00689.

G. P. Mantas and W. B. Hanson. Photoelectron fluxes in the Martian ionosphere. Journal of Geophysical Research, 84:369–386, Feb 1979. doi: 10.1029/JA084iA02p00369.

Carlos R Martinis, Jody K Wilson, and Michael J Mendillo. Modeling day-to-day ionospheric variability on mars. Journal of Geophysical Research: Space Physics, 108(A10), 2003.

Majd Mayyasi, Dolon Bhattacharyya, John Clarke, Amy Catalano, Mehdi Benna, Paul Mahaffy, Edward Thiemann, Christina O. Lee, Justin Deighan, Sonal Jain, Michael Chaffin, Matteo Crismani, William McClintock, Ian Stewart, Greg Holsclaw, Arnaud Stiepen, Franck Montmessin, Nick Schneider, and Bruce Jakosky. Significant Space Weather Impact on the

Escape of Hydrogen From Mars. Geophysical Research Letters, 45:8844–8852, Sep 2018. doi: 10.1029/2018GL077727.

M. B. McElroy, T. Y. Kong, Y. L. Yung, and A. O. Nier. Composition and structure of the Martian upper atmosphere - Analysis of results from Viking. Science, 194:1295–1298, December 1976. doi: 10.1126/science.194.4271.1295.

M. B. McElroy, T. Y. Kong, and Y. L. Yung. Photochemistry and evolution of Mars' atmosphere: A Viking perspective. Journal of Geophysical Research, 82:4379–4388, Sep 1977. doi: 10.1029/JS082i028p04379.

Michael B. McElroy. Mars: An Evolving Atmosphere. Science, 175:443–445, Jan 1972. doi: 10.1126/science.175.4020.443.

Tess Rose McEnulty. Oxygen Loss from Venus and the Influence of Extreme Solar Wind Conditions. PhD thesis, University of California, Berkeley, Jun 2012.

J. P. McFadden, O. Kortmann, D. Curtis, G. Dalton, G. Johnson, R. Abiad, R. Sterling, K. Hatch, P. Berg, C. Tiu, D. Gordon, S. Heavner, M. Robinson, M. Marckwordt, R. Lin, and B. Jakosky. MAVEN SupraThermal and Thermal Ion Compostion (STATIC) Instrument. Space Sci. Rev., 195:199–256, December 2015. doi: 10.1007/s11214-015-0175-6.

V. S. Meadows, G. N. Arney, E. W. Schwieterman, J. Lustig-Yaeger, A. P. Lincowski, T. Robinson, S. D. Domagal-Goldman, R. Deitrick, R. K. Barnes, D. P. Fleming, R. Luger, P. E. Driscoll, T. R. Quinn, and D. Crisp. The Habitability of Proxima Centauri b: Environmental States and Observational Discriminants. Astrobiology, 18:133–189, February 2018. doi: 10.1089/ast.2016.1589.

Michael Mendillo, Clara Narvaez, Marissa F. Vogt, Majd Mayyasi, Jeffrey Forbes, Marina Galand, Edward Thiemann, Mehdi Benna, Francis Eparvier, Phillip Chamberlin, Paul Mahaffy, and Laila Andersson. Sources of ionospheric variability at mars. Journal of Geophysical Research: Space Physics, 122(9):9670–9684, 2017. doi: 10.1002/2017JA024366. URL `https://agupubs.onlinelibrary.wiley.com/doi/abs/10.1002/2017JA024366`.

V. G. Merkin and C. C. Goodrich. Does the polar cap area saturate? Geophysical Research Letters, 34(9), 2007. doi: 10.1029/2007GL029357. URL `https://agupubs.onlinelibrary.wiley.com/doi/abs/10.1029/2007GL029357`.

M. Michael, R. E. Johnson, F. Leblanc, M. Liu, J. G. Luhmann, and V. I. Shematovich. Ejection of nitrogen from Titan's atmosphere by magnetospheric ions and pick-up ions. Icarus, 175:263–267, May 2005. doi: 10.1016/j.icarus.2004.11.004.

D. L. Mitchell, C. Mazelle, J.-A. Sauvaud, J.-J. Thocaven, J. Rouzaud, A. Fedorov, P. Rouger, D. Toublanc, E. Taylor, D. Gordon, M. Robinson, S. Heavner, P. Turin, M. Diaz-Aguado, D. W. Curtis, R. P. Lin, and B. M. Jakosky. The MAVEN Solar Wind Electron Analyzer. Space Sci. Rev., 200:495–528, April 2016. doi: 10.1007/s11214-015-0232-1.

DL Mitchell, RP Lin, C Mazelle, H Rème, PA Cloutier, JEP Connerney, MH Acuña, and NF Ness. Probing mars' crustal magnetic field and ionosphere with the mgs electron reflectometer. Journal of Geophysical Research: Planets, 106(E10):23419–23427, 2001.

R. Modolo and G. M. Chanteur. A global hybrid model for Titan's interaction with the Kronian plasma: Application to the Cassini Ta flyby. Journal of Geophysical Research (Space Physics), 113:A01317, January 2008. doi: 10.1029/2007JA012453.

R. Modolo, G. M. Chanteur, E. Dubinin, and A. P. Matthews. Influence of the solar EUV flux on the Martian plasma environment. Annales Geophysicae, 23:433–444, February 2005a. doi: 10.5194/angeo-23-433-2005.

R. Modolo, G. M. Chanteur, E. Dubinin, and A. P. Matthews. Influence of the solar EUV flux on the Martian plasma environment. Annales Geophysicae, 23:433–444, February 2005b. doi: 10.5194/angeo-23-433-2005.

R. Modolo, G. M. Chanteur, E. Dubinin, and A. P. Matthews. Simulated solar wind plasma interaction with the Martian exosphere: influence of the solar EUV flux on the bow shock and the magnetic pile-up boundary. Annales Geophysicae, 24:3403–3410, December 2006. doi: 10.5194/angeo-24-3403-2006.

R. Modolo, G. M. Chanteur, E. Dubinin, and A. P. Matthews. Simulated solar wind plasma interaction with the martian exosphere: influence of the solar euv flux on the bow shock and the magnetic pile-up boundary. Annales Geophysicae, 24(12):3403–3410, 2006. doi: 10.5194/angeo-24-3403-2006. URL https://www.ann-geophys.net/24/3403/2006/.

R. Modolo, G. M. Chanteur, and E. Dubinin. Dynamic martian magnetosphere: Transient twist induced by a rotation of the imf. Geophysical Research Letters, 39(1):n/a–n/a, 2012. ISSN 1944-8007. doi: 10.1029/2011GL049895. URL http://dx.doi.org/10.1029/2011GL049895. L01106.

R. Modolo, S. Hess, M. Mancini, F. Leblanc, J.-Y. Chaufray, D. Brain, L. Leclercq, R. Esteban-Hernández, G. Chanteur, P. Weill, F. González-Galindo, F. Forget, M. Yagi, and C. Mazelle. Mars-solar wind interaction: LatHyS, an improved parallel 3-D multispecies hybrid model. Journal of Geophysical Research (Space Physics), 121:6378–6399, July 2016. doi: 10.1002/2015JA022324.

Ronan Modolo, Sebastien Hess, Marco Mancini, Francois Leblanc, Jean-Yves Chaufray, David Brain, Ludivine Leclercq, Rosa Esteban-Hernndez, Gerard Chanteur, Philippe Weill, Francisco Gonzlez-Galindo, Francois Forget, Manabu Yagi, and Christian Mazelle. Mars-solar wind interaction: Lathys, an improved parallel 3-d multispecies hybrid model. Journal of Geophysical Research: Space Physics, 121(7):6378–6399, 2016. ISSN 2169-9402. doi: 10.1002/2015JA022324. URL http://dx.doi.org/10.1002/2015JA022324. 2015JA022324.

J. Moen and A. Brekke. The solar flux influence on quiet time conductances in the auroral ionosphere. Geophys. Res. Lett., 20:971–974, May 1993. doi: 10.1029/92GL02109.

U. Motschmann and E. Kührt. Interaction of the Solar Wind with Weak Obstacles: Hybrid Simulations for Weakly Active Comets and for Mars. Space Sci. Rev., 122:197–208, Feb 2006. doi: 10.1007/s11214-006-6218-2.

Joachim Müller, Sven Simon, Uwe Motschmann, Josef Schüle, Karl-Heinz Glassmeier, and Gavin J. Pringle. A.I.K.E.F.: Adaptive hybrid model for space plasma simulations. Computer Physics Communications, 182:946–966, Apr 2011. doi: 10.1016/j.cpc.2010.12.033.

A. F. Nagy, D. Winterhalter, K. Sauer, T. E. Cravens, S. Brecht, C. Mazelle, D. Crider, E. Kallio, A. Zakharov, E. Dubinin, M. Verigin, G. Kotova, W. I. Axford, C. Bertucci, and J. G. Trotignon. The plasma Environment of Mars. Space Sci. Rev., 111:33–114, March 2004a. doi: 10.1023/B:SPAC.0000032718.47512.92.

A. F. Nagy, D. Winterhalter, K. Sauer, T. E. Cravens, S. Brecht, C. Mazelle, D. Crider, E. Kallio, A. Zakharov, E. Dubinin, M. Verigin, G. Kotova, W. I. Axford, C. Bertucci, and J. G. Trotignon. The plasma Environment of Mars. Space Science Reviews, 111:33–114, March 2004b. doi: 10.1023/B:SPAC.0000032718.47512.92.

D. Najib, A. F. Nagy, G. Tóth, and Y. Ma. Three-dimensional, multifluid, high spatial resolution MHD model studies of the solar wind interaction with Mars. Journal of Geophysical Research (Space Physics), 116:A05204, May 2011. doi: 10.1029/2010JA016272.

Dalal Najib, Andrew F. Nagy, Gbor Tth, and Yingjuan Ma. Three-dimensional, multifluid, high spatial resolution mhd model studies of the solar wind interaction with mars. Journal of Geophysical Research: Space Physics, 116(A5):n/a–n/a, 2011a. ISSN 2156-2202. doi: 10.1029/2010JA016272. URL http://dx.doi.org/10.1029/2010JA016272. A05204.

Dalal Najib, Andrew F. Nagy, Gbor Tth, and Yingjuan Ma. Three-dimensional, multifluid, high spatial resolution mhd model studies of the solar wind interaction with mars. Journal of Geophysical Research: Space Physics, 116(A5), 2011b. doi: 10.1029/2010JA016272. URL https://agupubs.onlinelibrary.wiley.com/doi/abs/10.1029/2010JA016272.

R. Nakamura, W. Baumjohann, Y. Asano, A. Runov, A. Balogh, C. J. Owen, A. N. Fazakerley, M. Fujimoto, B. Klecker, and H. RèMe. Dynamics of thin current sheets associated with magnetotail reconnection. Journal of Geophysical Research (Space Physics), 111:A11206, November 2006. doi: 10.1029/2006JA011706.

E Nielsen, X-D Wang, DA Gurnett, DL Kirchner, R Huff, R Orosei, A Safaeinili, JJ Plaut, and G Picardi. Vertical sheets of dense plasma in the topside martian ionosphere. Journal of Geophysical Research: Planets, 112(E2), 2007.

A. O. Nier, W. B. Hanson, M. B. McElroy, A. Seiff, and N. W. Spencer. Entry Science Experiments: the Viking Mars Lander. Icarus, 16:74–91, February 1972. doi: 10.1016/0019-1035(72)90138-8.

A. O. Nier, W. B. Hanson, A. Seiff, M. B. McElroy, N. W. Spencer, R. J. Duckett, T. C. D. Knight, and W. S. Cook. Composition and structure of the Martian atmosphere - Preliminary results from Viking 1. Science, 193:786–788, August 1976. doi: 10.1126/science.193.4255.786.

AO Nier and Michael B McElroy. Composition and structure of mars' upper atmosphere: Results from the neutral mass spectrometers on viking 1 and 2. Journal of Geophysical Research, 82(28): 4341–4349, 1977.

Hans Nilsson, Ella Carlsson, David A. Brain, Masatoshi Yamauchi, Mats Holmström, Stas Barabash, Rickard Lundin, and Yoshifumi Futaana. Ion escape from Mars as a function of solar wind conditions: A statistical study. Icarus, 206:40–49, Mar 2010. doi: 10.1016/j.icarus.2009.03.006.

Hans Nilsson, Niklas JT Edberg, Gabriella Stenberg, Stas Barabash, Mats Holmström, Yoshifumi Futaana, Rickard Lundin, and Andrei Fedorov. Heavy ion escape from mars, influence from solar wind conditions and crustal magnetic fields. Icarus, 215(2):475–484, 2011.

T. NordströM, G. Stenberg, H. Nilsson, S. Barabash, and T. L. Zhang. Venus ion outflow estimates at solar minimum: Influence of reference frames and disturbed solar wind conditions. Journal of Geophysical Research (Space Physics), 118:3592–3601, June 2013. doi: 10.1002/jgra.50305.

Lisa Nortmann, Enric Pallé, Michael Salz, Jorge Sanz-Forcada, Evangelos Nagel, F. Javier Alonso-Floriano, Stefan Czesla, Fei Yan, Guo Chen, Ignas A. G. Snellen, Mathias Zechmeister, Jürgen H. M. M. Schmitt, Manuel López-Puertas, Núria Casasayas-Barris, Florian F. Bauer, Pedro J. Amado, José A. Caballero, Stefan Dreizler, Thomas Henning, Manuel Lampón, David Montes, Karan Molaverdikhani, Andreas Quirrenbach, Ansgar Reiners, Ignasi Ribas, Alejand ro Sánchez-López, P. Christian Schneider, and María R. Zapatero Osorio. Ground-based detection of an extended helium atmosphere in the Saturn-mass exoplanet WASP-69b. Science, 362:1388–1391, Dec 2018. doi: 10.1126/science.aat5348.

Office of Science and U.S. Department of Energy. National energy research scientific computing center (nersc). URL `http://www.nersc.gov/users/accounts/user-accounts/acknowledge-nersc/`.

T. Ogino. A three-dimensional MHD simulation of the interaction of the solar wind with the earth's magnetosphere: The generation of field-aligned currents. Journal of Geophysical Research, 91: 6791–6806, Jun 1986. doi: 10.1029/JA091iA06p06791.

H. J. Opgenoorth, R. S. Dhillon, L. Rosenqvist, M. Lester, N. J. T. Edberg, S. E. Milan, P. Withers, and D. Brain. Day-side ionospheric conductivities at Mars. Planetary and Space Science, 58: 1139–1151, Aug 2010. doi: 10.1016/j.pss.2010.04.004.

J. E. Owen and Y. Wu. The Evaporation Valley in the Kepler Planets. ApJ, 847:29, September 2017. doi: 10.3847/1538-4357/aa890a.

Tobias Owen, Jean Pierre Maillard, Catherine de Bergh, and Barry L. Lutz. Deuterium on Mars: The Abundance of HDO and the Value of D/H. Science, 240:1767–1770, Jun 1988. doi: 10.1126/science.240.4860.1767.

M Pätzold, S Tellmann, B Häusler, D Hinson, R Schaa, and GL Tyler. A sporadic third layer in the ionosphere of mars. Science, 310(5749):837–839, 2005.

T. Penz, N. V. Erkaev, H. K. Biernat, H. Lammer, U. V. Amerstorfer, H. Gunell, E. Kallio, S. Barabash, S. Orsini, A. Milillo, and W. Baumjohann. Ion loss on Mars caused by the Kelvin Helmholtz instability. Planet. Space Sci., 52:1157–1167, November 2004. doi: 10.1016/j.pss.2004.06.001.

R. O. Pepin. On the origin and early evolution of terrestrial planet atmospheres and meteoritic volatiles. Icarus, 92:2–79, July 1991. doi: 10.1016/0019-1035(91)90036-S.

R. O. Pepin. Evolution of the martian atmosphere. Icarus, 111:289–304, October 1994. doi: 10.1006/icar.1994.1146.

J. L. Phillips, J. G. Luhmann, C. T. Russell, and K. R. Moore. Finite Larmor radius effect on ion pickup at Venus. Journal of Geophysical Research, 92:9920–9930, Sep 1987. doi: 10.1029/JA092iA09p09920.

V. Pierrard. Evaporation of hydrogen and helium atoms from the atmospheres of Earth and Mars. Planetary and Space Science, 51:319–327, Apr 2003. doi: 10.1016/S0032-0633(03)00014-X.

V. Pohjola and E. Kallio. On the modeling of planetary plasma environments by a fully kinetic electromagnetic global model HYB-em. Annales Geophysicae, 28:743–751, March 2010. doi: 10.5194/angeo-28-743-2010.

A. Rahmati, D. E. Larson, T. E. Cravens, R. J. Lillis, P. A. Dunn, J. S. Halekas, J. E. Connerney, F. G. Eparvier, E. M. B. Thiemann, and B. M. Jakosky. MAVEN insights into oxygen pickup ions at Mars. Geophys. Res. Lett., 42:8870–8876, November 2015. doi: 10.1002/2015GL065262.

A. Rahmati, D. E. Larson, T. E. Cravens, R. J. Lillis, J. S. Halekas, J. P. McFadden, D. L. Mitchell, E. M. B. Thiemann, J. E. P. Connerney, P. A. Dunn, C. O. Lee, F. G. Eparvier, G. A. DiBraccio, J. R. Espley, J. G. Luhmann, C. Mazelle, and B. M. Jakosky. Seasonal Variability of Neutral Escape from Mars as Derived From MAVEN Pickup Ion Observations. Journal of Geophysical Research (Planets), 123:1192–1202, May 2018. doi: 10.1029/2018JE005560.

R. Ramstad, S. Barabash, Y. Futaana, H. Nilsson, X.-D. Wang, and M. Holmström. The Martian atmospheric ion escape rate dependence on solar wind and solar EUV conditions: 1. Seven years of Mars Express observations. Journal of Geophysical Research (Planets), 120:1298–1309, July 2015a. doi: 10.1002/2015JE004816.

R. Ramstad, S. Barabash, Y. Futaana, H. Nilsson, and M. Holmström. Effects of the crustal magnetic fields on the Martian atmospheric ion escape rate. Geophys. Res. Lett., 43:10, October 2016a. doi: 10.1002/2016GL070135.

Robin Ramstad, Stas Barabash, Yoshifumi Futaana, Hans Nilsson, Xiao-Dong Wang, and Mats Holmström. The Martian atmospheric ion escape rate dependence on solar wind and solar EUV conditions: 1. Seven years of Mars Express observations. Journal of Geophysical Research (Planets), 120:1298–1309, Jul 2015b. doi: 10.1002/2015JE004816.

Robin Ramstad, Stas Barabash, Yoshifumi Futaana, Hans Nilsson, and Mats Holmström. Effects of the crustal magnetic fields on the Martian atmospheric ion escape rate. Geophysical Research Letters, 43:10,574–10,579, Oct 2016b. doi: 10.1002/2016GL070135.

Robin Ramstad, Stas Barabash, Yoshifumi Futaana, and Mats Holmstrm. Solar wind- and euv-dependent models for the shapes of the martian plasma boundaries based on mars express measurements. Journal of Geophysical Research: Space Physics, 122(7):7279–7290, 2017. doi: 10.1002/2017JA024098. URL https://agupubs.onlinelibrary.wiley.com/doi/abs/10.1002/2017JA024098.

Robin Ramstad, Stas Barabash, Yoshifumi Futaana, Hans Nilsson, and Mats Holmström. Global Mars-solar wind coupling and ion escape. Journal of Geophysical Research (Space Physics), 122:8051–8062, Aug 2017. doi: 10.1002/2017JA024306.

Robin Ramstad, Stas Barabash, Yoshifumi Futaana, Hans Nilsson, and Mats Holmstrm. Global mars-solar wind coupling and ion escape. Journal of Geophysical Research: Space Physics, 122(8):8051–8062, 2017. doi: 10.1002/2017JA024306. URL https://agupubs.onlinelibrary.wiley.com/doi/abs/10.1002/2017JA024306.

Robin Ramstad, Stas Barabash, Yoshifumi Futaana, Hans Nilsson, and Mats Holmström. Ion Escape From Mars Through Time: An Extrapolation of Atmospheric Loss Based on 10 Years of Mars Express Measurements. Journal of Geophysical Research (Planets), 123:3051–3060, Nov 2018. doi: 10.1029/2018JE005727.

S. I. Rasool and C. de Bergh. The Runaway Greenhouse and the Accumulation of CO_2 in the Venus Atmosphere. Nature, 226:1037–1039, June 1970. doi: 10.1038/2261037a0.

Seth Redfield, Michael Endl, William D. Cochran, and Lars Koesterke. Sodium Absorption from the Exoplanetary Atmosphere of HD 189733b Detected in the Optical Transmission Spectrum. ApJ, 673:L87, Jan 2008. doi: 10.1086/527475.

L. H. Regoli, A. J. Coates, M. F. Thomsen, G. H. Jones, E. Roussos, J. H. Waite, N. Krupp, and G. Cox. Survey of pickup ion signatures in the vicinity of Titan using CAPS/IMS. Journal of Geophysical Research (Space Physics), 121:8317–8328, Sep 2016. doi: 10.1002/2016JA022617.

L. H. Regoli, C. Dong, Y. Ma, E. Dubinin, W. B. Manchester, S. W. Bougher, and D. T. Welling. Multispecies and Multifluid MHD Approaches for the Study of Ionospheric Escape at Mars. Journal of Geophysical Research (Space Physics), 123:7370–7383, September 2018. doi: 10.1029/2017JA025117.

I. Ribas, E. Bolmont, F. Selsis, A. Reiners, J. Leconte, S. N. Raymond, S. G. Engle, E. F. Guinan, J. Morin, M. Turbet, F. Forget, and G. Anglada-Escudé. The habitability of Proxima Centauri b. I. Irradiation, rotation and volatile inventory from formation to the present. A&A, 596:A111, December 2016. doi: 10.1051/0004-6361/201629576.

P. G. Richards, J. A. Fennelly, and D. G. Torr. Euvac: A solar euv flux model for aeronomic calculations. Journal of Geophysical Research: Space Physics, 99(A5):8981–8992, 1994. ISSN 2156-2202. doi: 10.1029/94JA00518. URL `http://dx.doi.org/10.1029/94JA00518`.

George R. Ricker, Joshua N. Winn, Roland Vanderspek, David W. Latham, Gáspár Á. Bakos, Jacob L. Bean, Zachory K. Berta-Thompson, Timothy M. Brown, Lars Buchhave, Nathaniel R. Butler, R. Paul Butler, William J. Chaplin, David Charbonneau, Jørgen Christensen-Dalsgaard, Mark Clampin, Drake Deming, John Doty, Nathan De Lee, Courtney Dressing, Edward W. Dunham, Michael Endl, Francois Fressin, Jian Ge, Thomas Henning, Matthew J. Holman, Andrew W. Howard, Shigeru Ida, Jon M. Jenkins, Garrett Jernigan, John Asher Johnson, Lisa Kaltenegger, Nobuyuki Kawai, Hans Kjeldsen, Gregory Laughlin, Alan M. Levine, Douglas Lin, Jack J. Lissauer, Phillip MacQueen, Geoffrey Marcy, Peter R. McCullough, Timothy D. Morton, Norio Narita, Martin Paegert, Enric Palle, Francesco Pepe, Joshua Pepper, Andreas Quirrenbach, Stephen A. Rinehart, Dimitar Sasselov, Bun'ei Sato, Sara Seager, Alessandro Sozzetti, Keivan G. Stassun, Peter Sullivan, Andrew Szentgyorgyi, Guillermo Torres, Stephane Udry, and Joel Villasenor. Transiting Exoplanet Survey Satellite (TESS). Journal of Astronomical Telescopes, Instruments, and Systems, 1:014003, Jan 2015. doi: 10.1117/1.JATIS.1.1.014003.

A. Ridley, T. Gombosi, and D. Dezeeuw. Ionospheric control of the magnetosphere: conductance. Annales Geophysicae, 22:567–584, February 2004. doi: 10.5194/angeo-22-567-2004.

W. Riedler, D. Möhlmann, V. N. Oraevsky, K. Schwingenschuh, Ye. Yeroshenko, J. Rustenbach, Oe. Aydogar, G. Berghofer, H. Lichtenegger, M. Delva, G. Schelch, K. Pirsch, G. Fremuth, M. Steller, H. Arnold, T. Raditsch, U. Auster, K. H. Fornacon, H. J. Schenk, H. Michaelis, U. Motschmann, T. Roatsch, K. Sauer, R. Schröter, J. Kurths, D. Lenners, J. Linthe, V. Kobzev, V. Styashkin, J. Achache, J. Slavin, J. G. Luhmann, and C. T. Russell. Magnetic fields near Mars: first results. Nature, 341:604–607, Oct 1989. doi: 10.1038/341604a0.

J. A. Riousset, C. S. Paty, R. J. Lillis, M. O. Fillingim, S. L. England, P. G. Withers, and J. P. M. Hale. Three-dimensional multifluid modeling of atmospheric electrodynamics in Mars' dynamo region. Journal of Geophysical Research (Space Physics), 118:3647–3659, June 2013. doi: 10.1002/jgra.50328.

Jeremy A. Riousset, Carol S. Paty, Robert J. Lillis, Matthew O. Fillingim, Scott L. England, Paul G. Withers, and John P. M. Hale. Electrodynamics of the Martian dynamo region near magnetic cusps and loops. Geophysical Research Letters, 41:1119–1125, Feb 2014. doi: 10.1002/2013GL059130.

Henry Rishbeth and Owen K Garriott. Introduction to ionospheric physics. IEEE Transactions on Image Processing, 1969.

R. M. Robinson, R. R. Vondrak, K. Miller, T. Dabbs, and D. Hardy. On calculating ionospheric conductances from the flux and energy of precipitating electrons. J. Geophys. Res., 92:2565–2569, March 1987. doi: 10.1029/JA092iA03p02565.

R. G. Roble, R. E. Dickinson, and E. C. Ridley. Global circulation and temperature structure of thermosphere with high-latitude plasma convection. J. Geophys. Res., 87:1599–1614, March 1982. doi: 10.1029/JA087iA03p01599.

N. Romanelli, R. Modolo, F. Leblanc, J. Y. Chaufray, A. Martinez, Y. Ma, C. O. Lee, J. G. Luhmann, J. Halekas, D. Brain, G. DiBraccio, J. Espley, J. Mcfadden, B. Jakosky, and M. Holmström. Responses of the Martian Magnetosphere to an Interplanetary Coronal Mass Ejection: MAVEN Observations and LatHyS Results. Geophysical Research Letters, 45:7891–7900, Aug 2018. doi: 10.1029/2018GL077714.

A. Romantan, V. Mercea, D. Ristoiu, and D. Ursu. Hydrogen dynamics in the earth atmosphere. Studii si Cercetari de Fizica, 33:389–400, Jan 1981.

R. Z. Sagdeev, V. D. Shapiro, V. I. Shevchenko, and K. Szego. MHD turbulence in the solar wind-comet interaction region. Geophysical Research Letters, 13:85–88, Feb 1986. doi: 10.1029/GL013i002p00085.

Shotaro Sakai, Kanako Seki, Naoki Terada, Hiroyuki Shinagawa, Takashi Tanaka, and Yusuke Ebihara. Effects of a weak intrinsic magnetic field on atmospheric escape from mars. Geophysical Research Letters, 45(18):9336–9343, 2018. doi: 10.1029/2018GL079972. URL `https://agupubs.onlinelibrary.wiley.com/doi/abs/10.1029/2018GL079972`.

M. Schmidt-Voigt. Time-dependent MHD simulations for cometary plasmas. A&A, 210:433–454, Feb 1989.

J. T. Schofield, J. R. Barnes, D. Crisp, R. M. Haberle, S. Larsen, J. A. Magalhaes, J. R. Murphy, A. Seiff, and G. Wilson. The Mars Pathfinder Atmospheric Structure Investigation/Meteorology. Science, 278:1752, December 1997. doi: 10.1126/science.278.5344.1752.

Robert Schunk and Andrew Nagy. Ionospheres: physics, plasma physics, and chemistry. Cambridge university press, 2009.

R.W. Schunk and A.F. Nagy. Ionospheres: Physics, Plasma Physics, and Chemistry. Cambridge Atmospheric and Space Science Series. Cambridge University Press, 2000. ISBN 9780521632379. URL `https://books.google.com/books?id=sBpaHlSxkF4C`.

K. Seki, R. C. Elphic, M. Hirahara, T. Terasawa, and T. Mukai. On Atmospheric Loss of Oxygen Ions from Earth Through Magnetospheric Processes. Science, 291:1939–1941, March 2001. doi: 10.1126/science.1058913.

A. L. Shields, S. Ballard, and J. A. Johnson. The habitability of planets orbiting M-dwarf stars. Phys. Rep., 663:1, December 2016. doi: 10.1016/j.physrep.2016.10.003.

H Shinagawa and TE Cravens. A one-dimensional multispecies magnetohydrodynamic model of the dayside ionosphere of mars. Journal of Geophysical Research: Space Physics, 94(A6):6506–6516, 1989.

H. Shinagawa, J. Kim, A. F. Nagy, and T. E. Cravens. A comprehensive magnetohydrodynamic model of the Venus ionosphere. Journal of Geophysical Research, 96:11083–11095, Jul 1991. doi: 10.1029/90JA02505.

Bernie D. Shizgal and Gregory G. Arkos. Nonthermal escape of the atmospheres of Venus, Earth, and Mars. Reviews of Geophysics, 34:483–505, Jan 1996. doi: 10.1029/96RG02213.

S. Simon and U. Motschmann. Titan's induced magnetosphere under non-ideal upstream conditions: 3D multi-species hybrid simulations. Planet. Space Sci., 57:2001–2015, December 2009. doi: 10.1016/j.pss.2009.08.010.

S. Simon, A. Boesswetter, T. Bagdonat, and U. Motschmann. Physics of the Ion Composition Boundary: a comparative 3-D hybrid simulation study of Mars and Titan. Annales Geophysicae, 25:99–115, February 2007. doi: 10.5194/angeo-25-99-2007.

Rikard Slapak, Maria Hamrin, Timo Pitkänen, Masatoshi Yamauchi, Hans Nilsson, Tomas Karlsson, and Audrey Schillings. Quantification of the total ion transport in the near-Earth plasma sheet. Annales Geophysicae, 35:869–877, Jul 2017. doi: 10.5194/angeo-35-869-2017.

J.A. Slavin. Mercury's magnetosphere. Advances in Space Research, 33(11):1859 – 1874, 2004. ISSN 0273-1177. doi: https://doi.org/10.1016/j.asr.2003.02.019. URL http://www.sciencedirect.com/science/article/pii/S0273117704000092. Comparative Magnetospheres.

M. Slipski, B. M. Jakosky, M. Benna, M. Elrod, P. Mahaffy, D. Kass, S. Stone, and R. Yelle. Variability of martian turbopause altitudes. Journal of Geophysical Research: Planets, 123(11): 2939–2957, 2018. doi: 10.1029/2018JE005704. URL https://agupubs.onlinelibrary.wiley.com/doi/abs/10.1029/2018JE005704.

Marek Slipski and Bruce M. Jakosky. Argon isotopes as tracers for martian atmospheric loss. Icarus, 272:212–227, Jul 2016. doi: 10.1016/j.icarus.2016.02.047.

W. H. Smyth and M. R. Combi. A general model for Io's neutral gas clouds. II - Application to the sodium cloud. ApJ, 328:888–918, May 1988. doi: 10.1086/166346.

T. W. Speiser and N. F. Ness. The neutral sheet in the geomagnetic tail: Its motion, equivalent currents, and field line connection through it. Journal of Geophysical Research, 72(1):131–141, 1967. doi: 10.1029/JZ072i001p00131. URL https://agupubs.onlinelibrary.wiley.com/doi/abs/10.1029/JZ072i001p00131.

John R. Spreiter, Audrey L. Summers, and Alberta Y. Alksne. Hydromagnetic flow around the magnetosphere. Planetary and Space Science, 14:223,IN1,251–250,IN2,253, Mar 1966. doi: 10.1016/0032-0633(66)90124-3.

JR Spreiter, AL Summers, and AW Rizzi. Solar wind flow past nonmagnetic planetsVenus and mars. Planet. Space Sci., 1970.

A. I. Stewart. Mariner 6 and 7 Ultraviolet Spectrometer Experiment: Implications of CO_2 $^+$, CO and O Airglow. J. Geophys. Res., 77:54, 1972. doi: 10.1029/JA077i001p00054.

Shane W. Stone, Roger V. Yelle, Mehdi Benna, Meredith K. Elrod, and Paul R. Mahaffy. Thermal structure of the martian upper atmosphere from maven ngims. Journal of Geophysical Research: Planets, 123(11):2842–2867, 2018. doi: 10.1029/2018JE005559. URL https://agupubs.onlinelibrary.wiley.com/doi/abs/10.1029/2018JE005559.

R. J. Strangeway, R. E. Ergun, Y.-J. Su, C. W. Carlson, and R. C. Elphic. Factors controlling ionospheric outflows as observed at intermediate altitudes. Journal of Geophysical Research (Space Physics), 110:A03221, March 2005. doi: 10.1029/2004JA010829.

D. F. Strobel. Chemistry and evolution of Titan's atmosphere. Planetary and Space Science, 30:839–848, Aug 1982. doi: 10.1016/0032-0633(82)90116-7.

Daniel W. Swift. Use of a Hybrid Code for Global-Scale Plasma Simulation. Journal of Computational Physics, 126:109–121, Jun 1996. doi: 10.1006/jcph.1996.0124.

N. D. Sze and M. B. McElroy. Some problems in Venus' aeronomy. Planetary and Space Science, 23:763–786, May 1975. doi: 10.1016/0032-0633(75)90014-8.

T. Tanaka. Generation mechanisms for magnetosphere-ionosphere current systems deduced from a three-dimensional MHD simulation of the solar wind-magnetosphere-ionosphere coupling processes. Journal of Geophysical Research, 100:12057–12074, Jul 1995. doi: 10.1029/95JA00419.

Yuki A. Tanaka, Takeru K. Suzuki, and Shu-ichiro Inutsuka. Atmospheric Escape by Magnetically Driven Wind from Gaseous Planets. II. Effects of Magnetic Diffusion. ApJ, 809:125, Aug 2015. doi: 10.1088/0004-637X/809/2/125.

N. Terada, S. Machida, and H. Shinagawa. Global hybrid simulation of the Kelvin-Helmholtz instability at the Venus ionopause. Journal of Geophysical Research (Space Physics), 107:1471, December 2002. doi: 10.1029/2001JA009224.

N. Terada, H. Shinagawa, T. Tanaka, K. Murawski, and K. Terada. A three-dimensional, multispecies, comprehensive MHD model of the solar wind interaction with the planet Venus. Journal of Geophysical Research (Space Physics), 114:A09208, September 2009. doi: 10.1029/2008JA013937.

N. Terada, H. Shinagawa, T. Tanaka, K. Murawski, and K. Terada. A three-dimensional, multispecies, comprehensive mhd model of the solar wind interaction with the planet venus. Journal of Geophysical Research: Space Physics, 114(A9):n/a–n/a, 2009a. ISSN 2156-2202. doi: 10.1029/2008JA013937. URL http://dx.doi.org/10.1029/2008JA013937. A09208.

Naoki Terada, Yuri N. Kulikov, Helmut Lammer, Herbert I.M. Lichtenegger, Takashi Tanaka, Hiroyuki Shinagawa, and Tielong Zhang. Atmosphere and water loss from early mars under extreme solar wind and extreme ultraviolet conditions. Astrobiology, 9(1):55–70, 2009b. doi: 10.1089/ast.2008.0250. URL https://doi.org/10.1089/ast.2008.0250. PMID: 19216683.

F. Tian, E. Chassefière, F. Leblanc, and D. Brain. Atmospheric Escape and Climate Evolution of Terrestrial Planets, pages 567–581. 2013. doi: 10.2458.

Feng Tian and Owen B. Toon. Hydrodynamic escape of nitrogen from Pluto. Geophysical Research Letters, 32:L18201, Sep 2005. doi: 10.1029/2005GL023510.

Feng Tian, James F. Kasting, Han-Li Liu, and Raymond G. Roble. Hydrodynamic planetary thermosphere model: 1. Response of the Earth's thermosphere to extreme solar EUV conditions and the significance of adiabatic cooling. Journal of Geophysical Research (Planets), 113:E05008, May 2008. doi: 10.1029/2007JE002946.

B. A. Tinsley. Energetic neutral atom precipitation during magnetic storms: optical emission, ionization, and energy deposition at low and middle latitudes. Journal of Geophysical Research, 84:1855–1864, May 1979. doi: 10.1029/JA084iA05p01855.

R. Tolson, A. M. Dwyer, P. E. Escalera, B. E. George, J. L. Hanna, G. M. Keating, and M. R. Werner. Application of Accelerometer Data to Mars Odyssey Aerobraking and Atmospheric Modeling. Journal of Spacecraft and Rockets, 42:435–443, May 2005. doi: 10.2514/1.15173.

RH Tolson, GM Keating, SN Noll, DT Baird, and TJ Shellenberg. Utilization of mars global surveyor accelerometer data for atmospheric modeling. Astrodynamics 1999, pages 1329–1346, 2000.

Pavel Trávníček, Petr Hellinger, and David Schriver. Structure of Mercury's magnetosphere for different pressure of the solar wind: Three dimensional hybrid simulations. Geophysical Research Letters, 34:L05104, Mar 2007. doi: 10.1029/2006GL028518.

R. A. Treumann and C. H. Jaroschek. Fundamentals of Non-relativistic Collisionless Shock Physics: II. Basic Equations and Models. ArXiv e-prints, May 2008a.

R. A. Treumann and C. H. Jaroschek. Fundamentals of Non-relativistic Collisionless Shock Physics: IV. Quasi-Parallel Supercritical Shocks. ArXiv e-prints, May 2008b.

J. G. Trotignon, C. Mazelle, C. Bertucci, and M. H. Acuña. Martian shock and magnetic pile-up boundary positions and shapes determined from the Phobos 2 and Mars Global Surveyor data sets. Planet. Space Sci., 54:357–369, April 2006a. doi: 10.1016/j.pss.2006.01.003.

J. G. Trotignon, C. Mazelle, C. Bertucci, and M. H. Acuña. Martian shock and magnetic pile-up boundary positions and shapes determined from the Phobos 2 and Mars Global Surveyor data sets. Planet. Space Sci., 54:357–369, April 2006b. doi: 10.1016/j.pss.2006.01.003.

M. J. Turk, B. D. Smith, J. S. Oishi, S. Skory, S. W. Skillman, T. Abel, and M. L. Norman. yt: A Multi-code Analysis Toolkit for Astrophysical Simulation Data. ApJS, 192:9, January 2011. doi: 10.1088/0067-0049/192/1/9.

Arnaud Valeille, Stephen W. Bougher, Valeriy Tenishev, Michael R. Combi, and Andrew F. Nagy. Water loss and evolution of the upper atmosphere and exosphere over martian history. Icarus, 206(1):28 – 39, 2010. ISSN 0019-1035. doi: https://doi.org/10.1016/j.icarus.2009.04.036. URL http://www.sciencedirect.com/science/article/pii/S0019103509002358. Solar Wind Interactions with Mars.

Ellen Van den Acker, Tim Van Hoolst, Olivier de Viron, Pascale Defraigne, François Forget, Fréderic Hourdin, and Véronique Dehant. Influence of the seasonal winds and the CO_2 mass exchange between atmosphere and polar caps on Mars' rotation. Journal of Geophysical Research (Planets), 107:5055, Jul 2002. doi: 10.1029/2000JE001539.

B. van der Holst, I. V. Sokolov, X. Meng, M. Jin, W. B. Manchester, IV, G. Tóth, and T. I. Gombosi. Alfvén Wave Solar Model (AWSoM): Coronal Heating. ApJ, 782:81, February 2014. doi: 10.1088/0004-637X/782/2/81.

A. Vidal-Madjar, A. Lecavelier des Etangs, J.-M. Désert, G. E. Ballester, R. Ferlet, G. Hébrard, and M. Mayor. An extended upper atmosphere around the extrasolar planet HD209458b. Nature, 422:143–146, March 2003. doi: 10.1038/nature01448.

A. Vidal-Madjar, D. K. Sing, A. Lecavelier Des Etangs, R. Ferlet, J. M. Désert, G. Hébrard, I. Boisse, D. Ehrenreich, and C. Moutou. The upper atmosphere of the exoplanet HD 209458 b revealed by the sodium D lines. Temperature-pressure profile, ionization layer, and thermosphere. A&A, 527:A110, Mar 2011. doi: 10.1051/0004-6361/201015698.

A. Vidal-Madjar, C. M. Huitson, V. Bourrier, J. M. Désert, G. Ballester, A. Lecavelier des Etangs, D. K. Sing, D. Ehrenreich, R. Ferlet, G. Hébrard, and J. C. McConnell. Magnesium in the atmosphere of the planet HD 209458 b: observations of the thermosphere-exosphere transition region. A&A, 560:A54, Dec 2013. doi: 10.1051/0004-6361/201322234.

A. A. Vidotto, R. Fares, M. Jardine, C. Moutou, and J.-F. Donati. On the environment surrounding close-in exoplanets. MNRAS, 449:4117–4130, June 2015. doi: 10.1093/mnras/stv618.

G. L. Villanueva, M. J. Mumma, R. E. Novak, H. U. Käufl, P. Hartogh, T. Encrenaz, A. Tokunaga, A. Khayat, and M. D. Smith. Strong water isotopic anomalies in the martian atmosphere: Probing current and ancient reservoirs. Science, 348:218–221, Apr 2015. doi: 10.1126/science.aaa3630.

M. F. Vogt, P. Withers, P. R. Mahaffy, M. Benna, M. K. Elrod, J. S. Halekas, J. E. P. Connerney, J. R. Espley, D. L. Mitchell, C. Mazelle, and B. M. Jakosky. Ionopause-like density gradients in the Martian ionosphere: A first look with MAVEN. Geophys. Res. Lett., 42:8885–8893, November 2015. doi: 10.1002/2015GL065269.

J.-E. Wahlund, R. Boström, G. Gustafsson, D. A. Gurnett, W. S. Kurth, A. Pedersen, T. F. Averkamp, G. B. Hospodarsky, A. M. Persoon, P. Canu, F. M. Neubauer, M. K. Dougherty, A. I. Eriksson, M. W. Morooka, R. Gill, M. André, L. Eliasson, and I. Müller-Wodarg. Cassini Measurements of Cold Plasma in the Ionosphere of Titan. Science, 308:986–989, May 2005. doi: 10.1126/science.1109807.

L. Wallace. Analysis of the lyman-alpha observations of venus made from mariner 5. Journal of Geophysical Research (1896-1977), 74(1):115–131, 1969. doi: 10.1029/JA074i001p00115. URL https://agupubs.onlinelibrary.wiley.com/doi/abs/10.1029/JA074i001p00115.

X. Wang, A. Bhattacharjee, and Z. W. Ma. Collisionless reconnection: Effects of Hall current and electron pressure gradient. J. Geophys. Res., 105:27633–27648, December 2000. doi: 10.1029/1999JA000357.

X.-D. Wang, S. Barabash, Y. Futaana, A. Grigoriev, and P. Wurz. Influence of Martian crustal magnetic anomalies on the emission of energetic neutral hydrogen atoms. Journal of Geophysical Research (Space Physics), 119:8600–8609, October 2014. doi: 10.1002/2014JA020307.

X.-D. Wang, M. Alho, R. Jarvinen, E. Kallio, S. Barabash, and Y. Futaana. Emission of hydrogen energetic neutral atoms from the Martian subsolar magnetosheath. Journal of Geophysical Research (Space Physics), 121:190–204, January 2016. doi: 10.1002/2015JA021653.

D. Winske, L. Yin, N. Omidi, and et al. Hybrid Simulation Codes: Past, Present and Future - A Tutorial. In J. Büchner, C. Dum, and M. Scholer, editors, Space Plasma Simulation, volume 615 of Lecture Notes in Physics, Berlin Springer Verlag, pages 136–165, 2003.

Paul Withers, M Mendillo, H Rishbeth, DP Hinson, and J Arkani-Hamed. Ionospheric characteristics above martian crustal magnetic anomalies. Geophysical research letters, 32(16), 2005.

Paul Withers, Michael Mendillo, DP Hinson, and Kerri Cahoy. Physical characteristics and occurrence rates of meteoric plasma layers detected in the martian ionosphere by the mars global surveyor radio science experiment. Journal of Geophysical Research: Space Physics, 113(A12), 2008.

Paul Withers, M. Felici, M. Mendillo, L. Moore, C. Narvaez, M. F. Vogt, and B. M. Jakosky. First Ionospheric Results From the MAVEN Radio Occultation Science Experiment (ROSE). Journal of Geophysical Research (Space Physics), 123:4171–4180, May 2018. doi: 10.1029/2018JA025182.

R. S. Wolff, B. E. Goldstein, and C. M. Yeates. The onset and development of Kelvin-Helmholtz instability at the Venus ionopause. J. Geophys. Res., 85:7697–7707, December 1980. doi: 10.1029/JA085iA13p07697.

J. H. Yatteau. Some issues related to evolution of planetary atmospheres. PhD thesis, Harvard University, Cambridge, MA., Jan 1983.

A. W. Yau, T. Abe, and W. K. Peterson. The polar wind: Recent observations. Journal of Atmospheric and Solar-Terrestrial Physics, 69:1936–1983, November 2007. doi: 10.1016/j.jastp.2007.08.010.

R. V. Yelle. Aeronomy of extra-solar giant planets at small orbital distances. Icarus, 170:167–179, July 2004. doi: 10.1016/j.icarus.2004.02.008.

R. V. Yelle, J. Cui, and I. C. F. Müller-Wodarg. Methane escape from Titan's atmosphere. Journal of Geophysical Research (Planets), 113:E10003, Oct 2008. doi: 10.1029/2007JE003031.

Y. L. Yung, J.-S. Wen, J. P. Pinto, M. Allen, K. K. Pierce, and S. Paulson. HDO in the Martian atmosphere - Implications for the abundance of crustal water. Icarus, 76:146–159, October 1988. doi: 10.1016/0019-1035(88)90147-9.

Yuk L. Yung, Jun-Shan Wen, Julianne I. Moses, Bridget M. Land ry, Mark Allen, and Kuang-Jung Hsu. Hydrogen and deuterium loss from the terrestrial atmosphere: A quantitative assessment of nonthermal escape fluxes. Journal of Geophysical Research, 94:14971–14989, Oct 1989. doi: 10.1029/JD094iD12p14971.

J. Zendejas, A. Segura, and A. C. Raga. Atmospheric mass loss by stellar wind from planets around main sequence M stars. Icarus, 210:539–544, December 2010. doi: 10.1016/j.icarus.2010.07.013.

M. H. G. Zhang, J. G. Luhmann, S. W. Bougher, and A. F. Nagy. The ancient oxygen exosphere of mars: Implications for atmosphere evolution. Journal of Geophysical Research: Planets, 98(E6): 10915–10923, 1993. doi: 10.1029/93JE00231. URL https://agupubs.onlinelibrary.wiley.com/doi/abs/10.1029/93JE00231.

M. H. G. Zhang, J. G. Luhmann, A. F. Nagy, J. R. Spreiter, and S. S. Stahara. Oxygen ionization rates at Mars and Venus: Relative contributions of impact ionization and charge exchange. Journal of Geophysical Research, 98:3311–3318, Feb 1993. doi: 10.1029/92JE02229.

T. L. Zhang, J. Du, Y. J. Ma, H. Lammer, W. Baumjohann, C. Wang, and C. T. Russell. Disappearing induced magnetosphere at venus: Implications for close-in exoplanets. Geophysical Research Letters, 36(20), 2009. doi: 10.1029/2009GL040515. URL https://agupubs.onlinelibrary.wiley.com/doi/abs/10.1029/2009GL040515.

J. I. Zuluaga, S. Bustamante, P. A. Cuartas, and J. H. Hoyos. The Influence of Thermal Evolution in the Magnetic Protection of Terrestrial Planets. ApJ, 770:23, June 2013. doi: 10.1088/0004-637X/770/1/23.